UNIVERSITI SAINS MALAYSIA

Laporan Akhir Projek Penyelidikan Jangka Pendek

Fundamental Studies of Lead Free Rare Earth Doped – BiXNa1-XTiO3 (BNT) Piezoelectric Material Synthesize using a Wet Chemical Technique

By
Dr. Khairunisak Abdul Razak
Assoc. Prof. Srimala Sreekantan
Mr. Teng Wan Dung
Prof. Wei Gao

2011

E. **ABSTRACT OF RESEARCH**

In this work, bismuth-based lead free piezoelectric has been successfully produced using soft combustion technique. Two basic compounds; bismuth sodium titanate ($Bi_{0.5}Na_{0.5}TiO_3$) (BNT) and bismuth potassium titanate ($Bi_{0.5}K_{0.5}TiO_3$) (BKT) with lanthanide doping have been produced. Pure Pr-doped BNT was obtained in all samples containing 5, 10 and 20 mol% Pr after calcination at 800°C for 3 hours. The crystallite size and grain size decreased with increasing Pr amount because Pr acted as grain growth inhibitor. Maximum density was obtained in 5 mol% Pr-doped BNT. The maximum dielectric constant of 756 was obtained in 5 mol% Pr-doped BNT and decreased at higher levels of Pr doping. Pr doped into BNT also caused a decrease in dielectric loss. In the case of BKT, a single phase BKT was obtained with a minimum of 0.5 mol of glycine. Various compounds of $Bi_{0.5(1-x)}Pr_xK_{0.5}TiO_3$ where x = 0.01, 0.03, 0.05, 0.10, 0.15 and 0.20 were prepared. Pure BKT and BPKT powders were obtained after calcination at 800°C for 3 h. After sintering at 1050°C for 5 h, pure BKT and Pr-doped BKT pellets were obtained for x = 0 and 0.01. However, for BPKT with x = 0.03, 0.05, 0.10, 0.15 and 0.20, a minor amount of $Bi_4Ti_3O_{12}$ (BIT) secondary phase was present after sintering at 1050 °C for 5 h. The crystallite size and grain size of all the samples followed similar trends, first increasing from x = 0 (undoped BKT) to x = 0.05 and then decreasing above x = 0.05. BPKT with x = 0.05 had the highest dielectric properties (ε_r = 713.87) due to its large crystallite size (68.66 nm), large grain size (435 nm) and high relative density (93.39%).

Abstrak Penyelidikan

Dalam kajian ini piezoelektrik tanpa plumbum berasaskan bismuth telah berjaya disintesis dengan menggunakan teknik pembakaran lembut. Dua sebatian asas bismuth sodium titanat ($Bi_{0.5}Na_{0.5}TiO_3$) (BNT) dan bismuth potasium titanat ($Bi_{0.5}K_{0.5}TiO_3$) (BKT) dengan pendopan unsur lantanida telah dihasilkan. Pr terdop BNT telah diperolehi untuk semua sampel yang mengandungi 5, 10 and 20 mol% Pr selepas proses pengkalsinan pada 800°C selama 3 h. Saiz kristal dan butiran mengecil dengan pertambahan amaun Pr terdop kerana Pr bertindak sebagai perencat pertumbuhan butiran. Ketumpatan maksima diperolehi dengan 5 mol % Pr terdop BNT. Pemalar dielektrik maksima sebanyak 756 telah dicapai untuk sampel 5 mol % Pr terdop BNT dan berkurangan dengan pertambahan Pr terdop melebihi 5 mol %. Pr terdop BNT turut menyebabkan penurunan kehilangan dielektrik. Untuk BKT, fasa tunggal BKT dapat diperolehi dengan menambah 0.5 mol glisin sebagai agen pembakar. Pelbagai sebatian $Bi_{0.5(1-x)}Pr_xK_{0.5}TiO_3$ dengan x = 0.01, 0.03, 0.05, 0.10, 0.15 and 0.20 telah dihasilkan. Fasa tulen BKT dan Pr terdop BKT telah dihasilkan selepas proses pengkalsinan pada 800°C selama 3 jam. Selepas pensinteran pada 1050°C selama 5 jam, palet berfasa tulen BKT dan BPKT telah dapat dihasilkan untuk x= 0 and 0.01. Walaubagaimanapun, untuk BPKT x = 0.03, 0.05, 0.10, 0.15 and 0.20 sedikit fasa sekunder $Bi_4Ti_3O_{12}$ (BIT) terbentuk selepas proses pensinteran. Saiz kristal dan butiran untuk semua sampel turut meningkat dari x=0 (BKT) hingga x=0.05 dan mengecil apabila x melebihi 0.05. BPKT dengan x=0.05 mempunyai pemalar dielektrik tertinggi (ε_r = 713.87) kerana saiz kristal (68.66 nm) yang besar, saiz butiran (435 nm) yang besar dan ketumpatan relatif yang tinggi (93.39%).

F. **SUMMARY OF RESEARCH FINDINGS**
Ringkasan dapatan Projek Penyelidikan

- Pure BNT and Pr-doped BNT ceramic powders were successfully synthesized using the wet chemical technique after calcination at 800 °C. However, after sintering at 1100 °C for 3 h, only 5mol% Pr-doped BNT showed a single phase while 10 and 20 mol% Pr-doped BNT showed the presence of secondary phase $Bi_4Ti_3O_{12}$.
- Grain size and crystallite size decreased with increasing Pr doping level because Pr acted at grain growth inhibitor. Optimum density was obtained with 10% Pr doping.
- The highest dielectric constant was obtained for 5mol% Pr-doped BNT. The result could be due to the optimum grain size of the sample and the presence of a single phase in the compound.
- BKT and Pr doped BKT were successfully produced using the wet chemical technique.
- The optimum amount of glycine added to aid the combustion reaction was found to be 0.5 M.
- Pure BPKT was obtained up to $x = 0.01$. Above that level, the ferroelectric compound BIT was formed. BPKT with $x = 0.05$ showed the optimum dielectric properties with a dielectric constant of 713.87 and tan δ of 0.1391.

G. **COMPREHENSIVE TECHNICAL REPORT**

Laporan Teknikal Lengkap

Applicants are required to prepare a comprehensive technical report explaining the project.
(This report must be attached separately)
Sila sediakan laporan teknikal lengkap yang menerangkan keseluruhan projek ini.

TECHNICAL REPORT IS ENCLOSED

List the key words that reflectour research:

Senaraikan kata kunci yang mencerminkan penyelidikan anda:

English	Bahasa Malaysia
Lead free piezoelectric	Piezoelectrik tanpa plumbum
Ferroelectric	feroelektrik
Wet chemical technique	Teknik kimia basah
Soft combustion technique	Teknik pembakaran lembut

Final Report

Fundamental Studies of Lead Free Rare Earth Doped BixNa1-xTiO3 (BNT) Piezoelectric Material Synthesize Using A Wet Chemical Technique

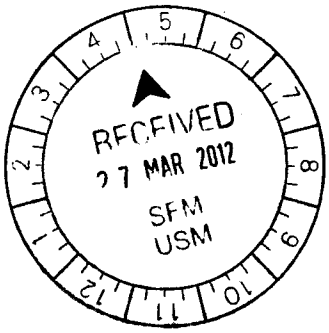

Team members:

Dr. Khairunisak Abdul Razak

Dr. Srimala Sreekantan

Dr. Teng Wan Dung

Prof. Wei Gao

School of Materials and Mineral Resources Engineering

Universiti Sains Malaysia

ABSTRACT OF RESEARCH

In this work, bismuth-based lead free piezoelectric has been successfully produced using soft combustion technique. Two basic compounds; bismuth sodium titanate ($Bi_{0.5}Na_{0.5}TiO_3$) (BNT) and bismuth potassium titanate ($Bi_{0.5}K_{0.5}TiO_3$) (BKT) with lanthanide doping have been produced. Pure Pr-doped BNT was obtained in all samples containing 5, 10 and 20 mol% Pr after calcination at 800°C for 3 hours. The crystallite size and grain size decreased with increasing Pr amount because Pr acted as grain growth inhibitor. Maximum density was obtained in 5 mol% Pr-doped BNT. The maximum dielectric constant of 756 was obtained in 5 mol% Pr-doped BNT and decreased at higher levels of Pr doping. Pr doped into BNT also caused a decrease in dielectric loss. In the case of BKT, a single phase BKT was obtained with a minimum of 0.5 mol of glycine. Various compounds of $Bi_{0.5(1-x)}Pr_xK_{0.5}TiO_3$ where x = 0.01, 0.03, 0.05, 0.10, 0.15 and 0.20 were prepared. Pure BKT and BPKT powders were obtained after calcination at 800°C for 3 h. After sintering at 1050°C for 5 h, pure BKT and Pr-doped BKT pellets were obtained for x = 0 and 0.01. However, for BPKT with x = 0.03, 0.05, 0.10, 0.15 and 0.20, a minor amount of $Bi_4Ti_3O_{12}$ (BIT) secondary phase was present after sintering at 1050 °C for 5 h. The crystallite size and grain size of all the samples followed similar trends, first increasing from x = 0 (undoped BKT) to x = 0.05 and then decreasing above x = 0.05. BPKT with x = 0.05 had the highest dielectric properties (ε_r = 713.87) due to its large crystallite size (68.66 nm), large grain size (435 nm) and high relative density (93.39%).

Abstrak Penyelidikan

Dalam kajian ini piezoelektrik tanpa plumbum berasaskan bismuth telah berjaya disintesis dengan menggunakan teknik pembakaran lembut. Dua sebatian asas bismuth sodium titanat ($Bi_{0.5}Na_{0.5}TiO_3$) (BNT) dan bismuth potasium titanat ($Bi_{0.5}K_{0.5}TiO_3$) (BKT) dengan pendopan unsur lantanida telah dihasilkan. Pr terdop BNT telah diperolehi untuk semua sampel yang mengandungi 5, 10 and 20 mol% Pr selepas proses pengkalsinan pada 800°C selama 3 h. Saiz kristal dan butiran mengecil dengan pertambahan amaun Pr terdop kerana Pr bertindak sebagai perencat pertumbuhan butiran. Ketumpatan maksima diperolehi dengan 5 mol % Pr terdop BNT. Pemalar dielektrik maksima sebanyak 756 telah dicapai untuk sampel 5 mol % Pr terdop BNT dan berkurangan dengan pertambahan Pr terdop melebihi 5 mol %. Pr terdop BNT turut menyebabkan penurunan kehilangan dielektrik. Untuk BKT, fasa tunggal BKT dapat diperolehi dengan menambah 0.5 mol glisin sebagai agen pembakar. Pelbagai sebatian $Bi_{0.5(1-x)}Pr_xK_{0.5}TiO_3$ dengan x = 0.01, 0.03, 0.05, 0.10, 0.15 and 0.20 telah dihasilkan. Fasa tulen BKT dan Pr terdop BKT telah dihasilkan selepas proses pengkalsinan pada 800°C selama 3 jam. Selepas pensinteran pada 1050°C selama 5 jam, palet berfasa tulen BKT dan BPKT telah dapat dihasilkan untuk x= 0 and 0.01. Walaubagaimanapun, untuk BPKT x = 0.03, 0.05, 0.10, 0.15 and 0.20 sedikit fasa sekunder $Bi_4Ti_3O_{12}$ (BIT) terbentuk selepas proses pensinteran. Saiz kristal dan butiran untuk semua sampel turut meningkat dari x=0 (BKT) hingga x=0.05 dan mengecil apabila x melebihi 0.05. BPKT dengan x=0.05 mempunyai pemalar dielektrik tertinggi (ε_r = 713.87) kerana saiz kristal (68.66 nm) yang besar, saiz butiran (435 nm) yang besar dan ketumpatan relatif yang tinggi (93.39%).

Project objectives vs actual achievement

	Objectives	Actual Progress
1	To determine the optimum processing parameters to synthesis Pb-free piezoelectric $(Bi_xNa_{1-x})TiO_3$ (BNT) using wet-chemical technique.	100%
2	To investigate the effects of rare-earth doping on stoichiometry and microstructure of BNT.	100%
3	To produce Pb-free piezoelectric thick film using Electrophoretic Deposition (EPD) technique. • Due to limitation of equipment for characterization the objective was changed to (approved during progress report monitoring): To study the effects of Pr doping on BKT using soft combustion approach	100%
4	To study electrical properties of bulk disc and thick film of Pb-free piezoelectric. • Due to limitation of equipment for characterization the objective was changed to (approved during progress report monitoring): To study electrical properties of Pr doped BKT	100%

Chapters in book:

1. Umar Al-Amani, S. Sreekantan, M. N. Ahmad Fauzi, K. A. Razak, Current Progress In Synthesis and Properties of Doped Bismuth Titanate For Advanced Electronic Applications, in Bismuth: Characteristics, Production and Applications, 2011, ISBN: 978-1-61470-640-3, Editor: Kamakhya Prasad Ghatak, Nova Publishing
2. Umar Al-Amani, S. Sreekantan, M.N. Ahmad Fauzi, K. A. Razak, Synthesis and Properties of Nd-Doped $Bi_4Ti_3O_{12}$ Using the Soft Combustion Technique, in Bismuth: Characteristics, Production and Applications, 2011, ISBN: 978-1-61470-640-3, Editor: Kamakhya Prasad Ghatak, Nova Publishing
3. Umar Al-Amani Azlan , Warapong Krengvirat, Ahmad Fauzi Mohd Noor, **Khairunisak Abd. Razak** and Srimala Sreekantan, Sintering and Characterization of Rare Earth Doped Bismuth Titanate Ceramics Prepared by Soft Combustion Synthesis, in Sintering, 2011, ISBN 978-953-308-4-8, Intech

Journals

1. **Razak, K.A.,** C.J. Yip, and S. Sreekantan, Synthesis of (Bi0.5Na0.5)TiO3 (BNT) and Pr doped BNT using the soft combustion technique and its properties. Journal of Alloys and Compounds. 2011, **509**(6): p. 2936-2941.

2. Ng, C.Y. and **K.A. Razak**, Properties of praseodymium-doped bismuth potassium titanate (Bi 0.5K0.5TiO3) synthesised using the soft combustion technique. Journal of Alloys and Compounds. 2011, **509**(3): p. 942-947.

3. Yip, C.J., **K.A. Razak**, and S. Sreekantan, Synthesis and properties study of Pr doped (Bi0.5Na 0.5)TiO3 produced using the soft combustion technique, in Advanced Materials Research. 2011, p. 1619-1622.

4. Khoo Khai Ling, Khairunisak Abdul Razak, Azlan Abdul Aziz, Seed mediated growth of gold nanorods for diagnostic applications, Revistas CENIC Ciencias Químicas, 2010: 1-13

5. Khairunisak Abdul Razak, Azlan Abdul Aziz, Shaharum Shamsuddin, Properties of silica nanocolloids synthesized via micelle formation approach, Journal of Industrial Technology (JIT), accepted

Conferences

1. Khairunisak Abdul Razak and Mohamad Afifi Anuar, The effects of combustion agent on the formation of Bi-based compounds synthesized using the soft combustion technique, International Conference on X-ray and Related Techniques 2012, Vistana Hotel Penang, 3-5 July 2012
2. Ng Chai Yan and Khairunisak Abdul Razak, Praseodymium doped bismuth potasium titanate ($Bi_{0.5}K_{0.5}TiO_3$) synthesized using the glycine-assisted soft combustion technique, the 3rd Regional Conference on Natural Resources and Materials Engineering (3rd RC-NRM), 25-26 October 2010, 183-188
3. Khairunisak Abdul Razak, Azlan Abdul Aziz , Shaharum Shamsuddin, Seed-mediated Growth of Gold Nanorods for Diagnostic Applications, 15th International Scientific Congress, 28 June - 1July , 2010, Havana, Cuba
4. Khairunisak Abdul Razak, Azlan Abdul Aziz , Shaharum Shamsuddin, Properties of silica nanocolloids synthesized via micelle formation approach, International conference on nanotechnology-research and commercialization (ICONT2009), Bayview Hotel, Langkawi, Malaysia, 14-17 Dec 2009.

MSc thesis

1. Ng Chai Yan, "Pr doped lead free piezoelectric ($Bi_{0.5}K_{0.5}$)TiO3 prepared by soft combustion technique", MSc, 2010
2. Chiah Jun Yip, "Pr doped lead free piezoelectric (Bi0.5Na0.5)TiO3 prepared by soft combustion technique" MSc, 2010

Undergraduate final year thesis

1) Mohd Afifi, The effects of combustion agent on $Bi_{0.5}Na_{0.5}TiO_3$ properties synthesize using the soft combustion technique, 2011

2) Norhidasalini bte Zailani, "Processing of rare earth doped lead free piezoelectric (Na0.5Bi0.5)TiO3 (NBT) using wet chemical route", 2010

3) Lim Ee Sin, Structural and property of samarium and neodymium doped bismuth titanate using wet chemical technique, 2009

1. SYNTHESIS AND PROPERTIES STUDIES OF BNT AND Pr-DOPED BNT USING THE SOFT COMBUSTION METHOD

In this work, $(Bi_{0.5}Na_{0.5})TiO_3$ (BNT) and Pr doped BNT were produced using the soft combustion technique. The SEM morphologies of BNT powder are shown in Figure 1. Figure 1 (a) shows the SEM micrograph of BNT powder before calcination whereby the shape of particle BNT is in plate-like shaped and pin shaped. Lack of mutual solubility between bismuth layer structure phase and perovskite phase can be observed in Figure 1. The plate-like shape is the bismuth-layered phase whereas the smaller cubic or round particles with a size of 100nm are regarded as perovskite (Ma *et al.,* 2009). In Figure 1(b), SEM micrograph of BNT powder after calcination shows nearly cubical or round shaped particle distribution. There is no plate-like shaped particle appeared. It can be concluded that all bismuth layered phase were fully transformed into perovskite grains. The average particles size is around 140 nm. It is obvious that particle size increased after calcination process.

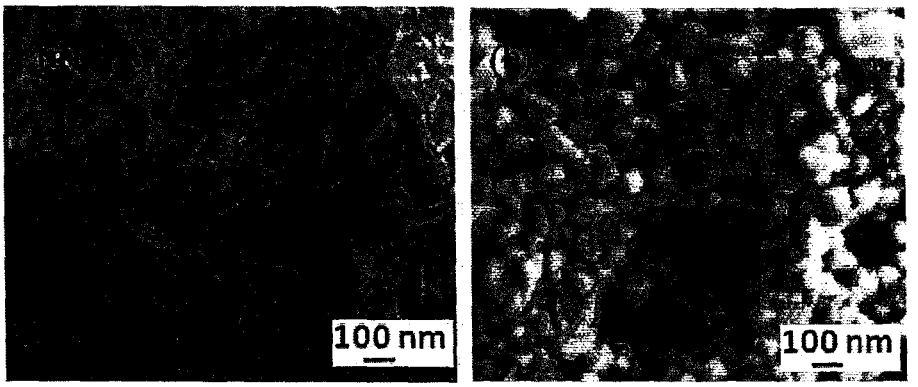

Figure 1: SEM micrographs of BNT; (a) as synthesized powders and (b) after calcination at 800°C.

TEM observation shown in Figure 2 is in agreement with SEM observation. The average particle size is in the range of 80-150nm. It shows that the soft combustion method able to produce nearly nano-scale powder. Bismuth layered structure unable to be observed under TEM but it can be observed using SEM as shown in Figure 1(a).

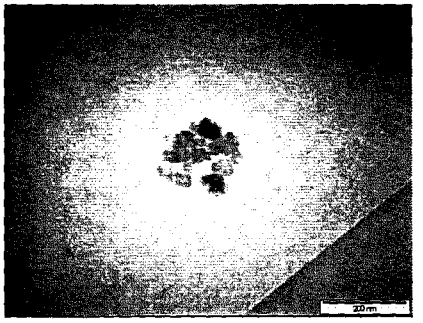

Figure 2: TEM observation of undoped BNT powder before calcined at 800°C.

The XRD spectra of BNT and $(Bi_{0.5}Na_{0.5})_{(1-x)}Pr_xTiO_3$ (x = 0.02, 0.05, 0.10, 0.20) powder calcined in air at 800°C for 3 hours are shown in Figure 3. Generally, a single perovskite phase without secondary phase is observed for Pr doped BNT (JCPDS No. 36-340). At room temperature, BNT and Pr doped BNT powders have rhombohedral symmetry. However, it was hard to observe due to peak overlapping and that could be due to nearly cubic lattice. Fukuchi *et al.*, (2002) have reported that although the crystal structure of BNT was rhombohedral, the diffraction lines were indexed based on the pseudocubic unit cell because of the small degree of rhombohedral distortion.

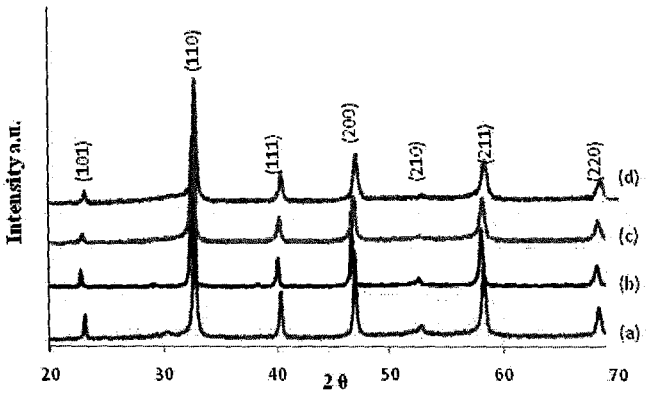

Figure 3: XRD spectra of samples after calcination at 800°C, (a) BNT, (b) 5% of Pr doped BNT, (c) 10% of Pr doped BNT, (d) 20% of Pr doped BNT.

From the XRD spectra Figure 3, the reflection peaks can be indexed as a bismuth-layered perovskite structure. BNT powders did not show any peak that belong to praseodymium oxide.

This observation proved that the praseodymium ions were substituted inside the perovskite lattice. The ionic radii of Pr^{3+}, Bi^{3+}, and Na^{+} were very close. Their measurements are 0.99 nm, 0.96 nm and 0.99 nm respectively (Shannon, 1976). The close values made Pr^{3+} ion were readily substituted out Bi^{3+} ion or Na^{+} ion in the perovskite lattice. It is because the charge of Pr ions can be 2+ or 3+ and it can substitute into A-site or B-site in BNT perovskite structure (Watcharapasorn *et al.*, 2007).

The spectra of doped and undoped BNT (x = 0.05, 0.10, 0.20) calcined powders at the peak position (200) are shown in Figure 4. From Figure 4, the peak position (200) of BNT shifted to the left side which is proportional to the amount of Pr added. This is indicative of a change in the unit cell size (McLaughlin, 2008). Lattice distortion occurred in this case. There are some micro strain occurred when Pr was added into BNT. This can be explained by Vegard's law which suggest a linear relationship existed between the crystal lattice parameter and the concentration of the Pr dopant added. The increase of ion shift will results in an increasing of lattice energy to stabilize the structure (Lee *et al.*, 2009). However, this trend stop at 5% of Pr doped BNT and start to shift to the right side with further addition of Pr. The result is in agreement with Lee *et al.* (2009) and Liu *et al.* (2009).

According to McLaughlin, (2008), BNT is A-site complex perovskite, with the composition $A'A''BO_3$. A complex perovskite has a tendency to be disordered and it is no regular long range arrangement of the complex-site ions (at A-site). This lack of order creates many micro regions of slightly different compositions. The presence of these many different phases and thus different transition temperatures lead to a broadening of the overall phase transition temperature of the bulk material. In each of the systems studied, a second and for some a third ion were added to the B-site, creating an even more complex perovskite, $A'A''B'B''B'''O_3$.

From Figure 4, it also showed that the intensity of the peak position (200) is decreased with the increasing concentration of Pr dopant. Compared to the undoped BNT, Pr doped BNT have a broader peak. It was mainly due to compositional fluctuation or substitution disordering in the arrangement of cations at crystallographic sites in the lattice structure (Xu *et al.*, 2008). Broaden in the peak indicates the crystallite size decreased. It is agreement with Figure 5 which were calculated using Scherrer's equation, $k= (0.9 \times \lambda) / (B \cos \theta)$.

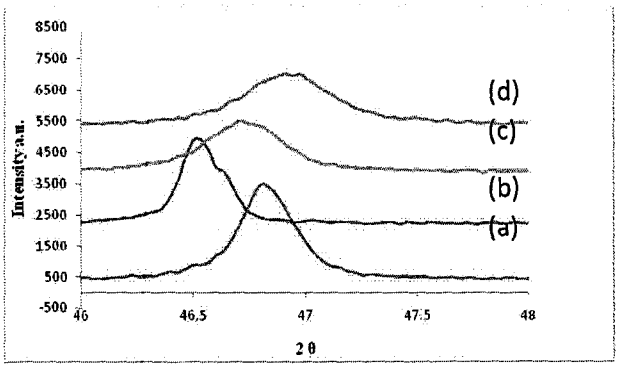

Figure 4: XRD spectra of a) BNTS b) 5% of Pr doped BNT, c) 10% of Pr doped BNT, d) 20% of Pr doped BNT after calcined at 800°C at (200) peak position.

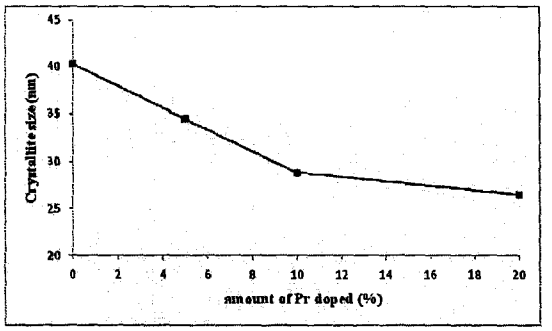

Figure 5: Crystallite size of BNT doped with various amount of Pr after calcined at 800°C.

Figure 6 shows the SEM micrographs of doped and undoped BNT. There are a lot of flakes inside the powder. The grain sizes of the flakes decreased gradually with increasing the amount of Pr doped. Undoped BNT shows the highest average grain size which is around 215.86 nm. Grain size of 5% of Pr doped BNT is around 157.12 nm which is smaller compared to undoped BNT. It proved that grain size decreased by doping with Pr. 10% of Pr doped BNT and 20% of Pr doped BNT shows 76.47 nm and 70.77 nm respectively. It is because Pr acts as an inhibitor during the growth process. Slower diffusion rate of Pr than Bi ions cause Pr to inhibit the growth of grains. According to Liu *et al.,* (2009), this happened is due to the particles coalescence or aggregation during the growth process. Calcination process is very important for sintering process later. Not only purity of phase of calcined powder, grain size that obtained during calcination also will affect the result of sintering.

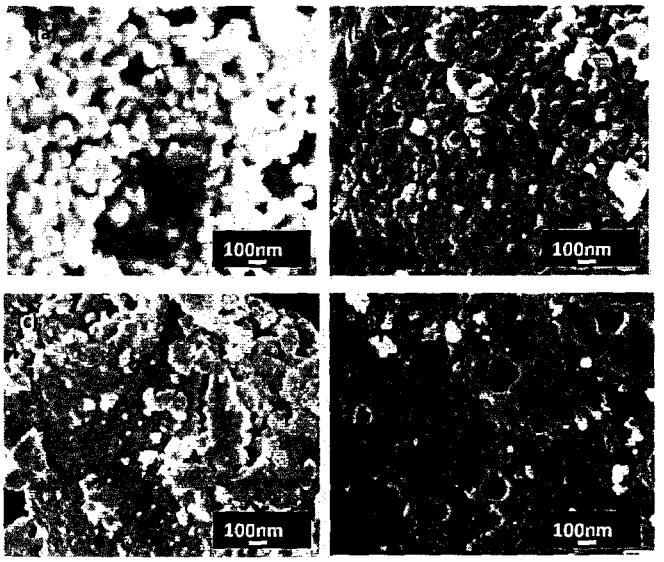

Figure 6: SEM micrographs of Pr doped BNT after calcination at 800°C, (a) BNT, (b) 5% of Pr doped BNT, (c) 10% of Pr doped BNT, and (d) 20% of Pr doped BNT.

From Figure 6, it shows quasi-cubical shaped-like of the particle. It indicates that cubical shaped like particle is produced using the soft combustion technique. These are regarded as perovskite grains and it has been discussed in early section. The shape of the particle is not much different with concentration of Pr doped on BNT. The average of the particle size of various Pr concentration doped on BNT is shown in Table 1.

Table 1: Average of grain size of various amount of Pr doped on BNT.

Sample	Average of grain size (nm)
BNT	215.86
5% of Pr doped BNT	157.12
10% of Pr doped BNT	76.47
20% of Pr doped BNT	70.77

The XRD spectra of BNT and $(Bi_{0.5}Na_{0.5})_{(1-x)}$ Pr_xTiO3 (x = 0, 0.05, 0.10, 0.20) sintered pellet in air at 1100°C for 3 hours are shown in Figure 1. Generally, there are secondary phases appeared in 10% of Pr doped and 20% of Pr doped BNT. Figure 7 (a) and (c) shows a single perovskite phase without extra peak (JCPDS No. 36-340). The extra peaks appeared at about 30°, 34°, 38°,

53°, 59° and also 64°. According to XRD, secondary phase which is bismuth titanate ($Bi_4Ti_3O_{12}$) appeared at (117), (201), (208) and (220) peak positions (JCPDS No. 00-047-0398).

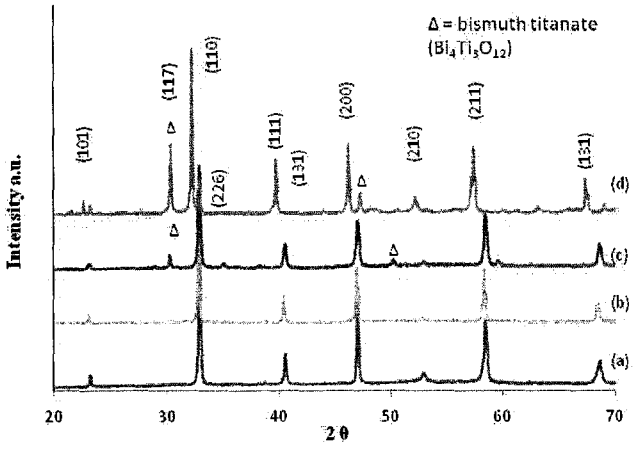

Figure 7: XRD spectra of BNT and Pr doped BNT after sintering at 1100°C, (a) BNT, (b) 5% of Pr doped BNT, (c) 10% of Pr doped BNT, and (d) 20% of Pr doped BNT.

Figure 8 shows that the XRD spectra of BNT at ~ 2θ = 47°C shows the splitting of *(h0l)* - and *(0kl)* - type reflections. On the contrary, the BNT (x= 0, 0.10) do not show any peak splitting caused by *(h0l)* - and *(0kl)* - type reflections. Splitting normally is because of lattice distortion (McLaughlin, 2008). They can be assigned to a (200/020) peak splitting according to a rhombohedral symmetry and a tetragonal symmetry. This means that addition of Pr doped has a tendency to change the lattice parameter. This also indicates that the substitution of Pr ions for Bi ions may distort the positions of ions in the lattice (Goh *et al.*, 2009). The result proved the coexistence of rhombohedral and tetragonal phases, which is consistent with the nature of the specimen with an MPB composition (Zhou *et al.*, 2008).

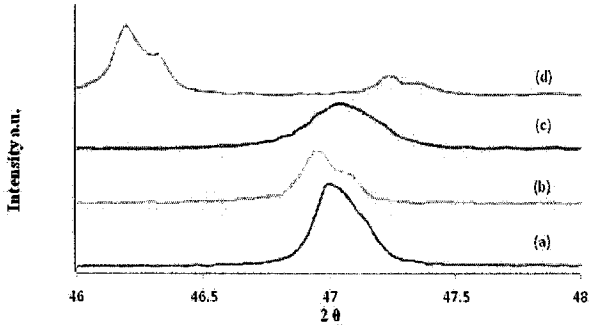

Figure 8: XRD spectra of BNT (x= 0, 0.05, 0.10, and 0.20) powder, showing the splitting of *(h0l)* - and *(0kl)* - type reflections in the peak postion ~ 2θ = 47°C.

Figure 9 shows the crystallite sizes of BNT with different amount of Pr after sintering at 1100°C. In general, crystallite sizes of BNT after sintering increased compared to powder after calcination. From Figure 9, for each composition, crystallite size decreased with increasing Pr doped in BNT. Crystallite size of undoped BNT is 71.4 nm whereas crystallite size of 5% of Pr doped BNT is 57.2 nm. When amount of Pr doped on BNT increased to 10% and 20%, crystallite sizes decreased to 55.6 nm and 46.5 nm.

Watcharapasorn *et al.,* (2007) has reported that that Dysprosium doped in BNT can lead grain of BNT becomes smaller. However, McLaughlin (2008) also has reported that grain growth during sintering was suppressed with small amounts of additives, but larger amounts of additives increased the grain size. However, in this study it was observed that Pr doped BNT up to 20% still suppressed the crystallite size.

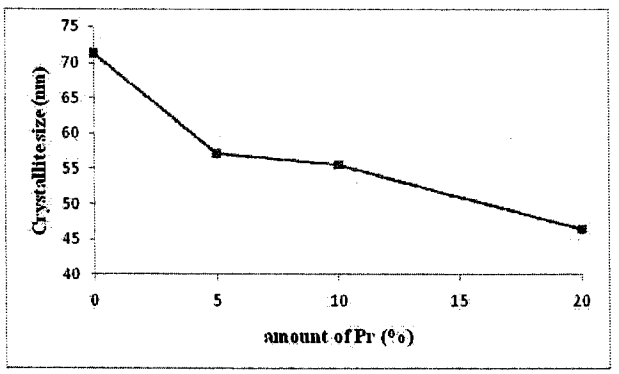

Figure 9: Crystallite size of various amount of Pr doped BNT after sintered at 1100°C.

Figure 10 shows the SEM micrographs of different amount of Pr doped on BNT after sintering at 1100°C. It was obvious that the grain size of Pr doped BNT was smaller compared to undoped BNT. BNT had a large grain size > 10μm whereas 5% of Pr doped showed much smaller grain size (683.152nm) compared to BNT. From here we can conclude that Pr doped in BNT lead to reduce the grain size. By comparing with amount of Pr doped, grain size decreased with increasing in Pr amount. In this case, Pr as a grain growth inhibitor that influences the diffusion happened during sintering process. The result is in agreement with Watcharapasorn (2007) where the addition of Dy ions into BNT lattice inhibited grain growth. The effects of these dopants were attributed to segregation of cation vacancies as well as acceptor solutes at the grain boundaries in which the space charge region was induced and this limited the movement of grain boundaries. By doping a small amount of Pr, the grain size can be reduced due to the diffusivity of Pr being lower compared to Bi. Pr^{3+} ion could substitute either A-site or B-site and it seemed to suggest a complex role in densification and grain growth behavior of BNT.

However, until 20% of Pr doped BNT, it shows larger grain size compared to samples that has lower amount of Pr. When amount of additive added is above the optimum amount it will lead the grain size growth (McLaughlin, 2008). By doping a small amount of Pr, the grain size can reduced due to the diffusivity of Pr is lower compared to Bi. Pr doped as an inhibitor to slow down the grain growth rate. Furthermore, the grain size indicated that the grain growth rate decrease with increasing Pr concentration (Fukuchi *et al.,* 2002). Furthermore, the agglomeration state of the calcined powders influenced the grain size of the sintered ceramic. This is why 5% of Pr shows the highest average grain size among the samples. Figure 11 shows the decline trend of grain size with increasing Pr amount. It is a large drop for undoped BNT compared to Pr doped BNT.

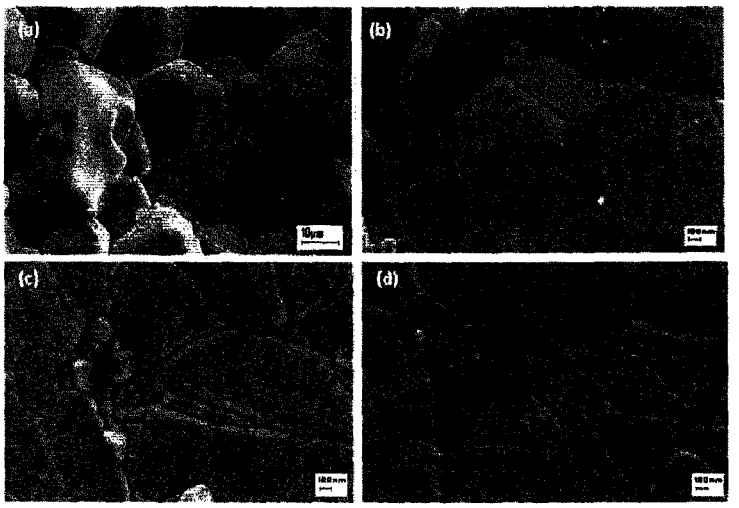

Figure 10: SEM micrographs of samples sintered at 1100°C, (a) BNT, (b) 5% of Pr doped BNT, (c) 10% of Pr doped BNT, and (d) 20% of Pr doped BNT.

It is seems contradict with the crystallite size result in previous discussion that 20% of Pr doped BNT gives smaller crystallite size but bigger grain size. It can be explained with agglomerated particle occurred in the sample before sintering process. It is known that in smaller particle, it is harder to control the degree of agglomeration of particles. Agglomerated particle leads grain growth faster due to shorter distance among the particles.

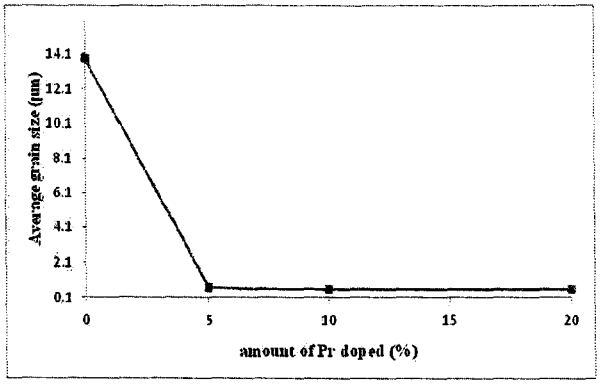

Figure 11: Average grain size of various amount of Pr doped BNT after sintered at 1100°C.

The relative density of each of the compositions was calculated by dividing the theoretical density which is 5.998g/cm^3 (Figure 12). Sample 10% of Pr doped shows the highest relative density value which is 96.64% whereas undoped BNT sample shows the lowest relative density value which is 86.69%. This indicates that Pr doped has improved the density of BNT.

However, the amount of Pr added also influence the density of BNT. Above 10% of Pr doped BNT, density starts to decrease. 20% of Pr doped BT gives only 93.92% relative density. For each composition, the density of the sintered samples increased with increasing amount of Pr doped up to the optimum amount, and then decreased beyond that amount.

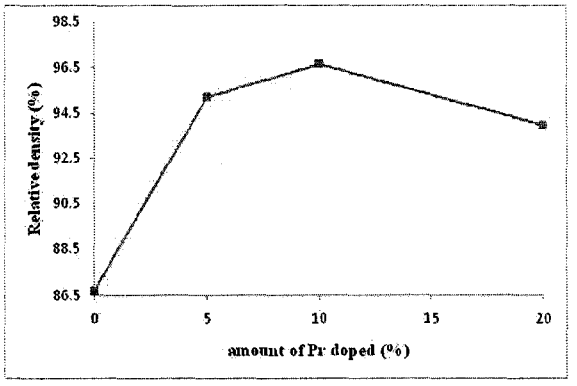

Figure 12: Relative density of various amount of Pr doped BNT after sintered at 1100°C.

The relative dielectric permittivity and loss tangent were measured at 25°C with electric field of 1V as shown in Figure 13. BNT shows the lowest dielectric constant value which is only 347 whereas 5% of Pr doped BNT gives the highest dielectric constant value which is 756. For each composition, the dielectric permittivity of the sintered samples increased with increasing the amount of Pr doped up to the optimum amount which is 10% of Pr doped BNT, and then decreased beyond that. It can be concluded that Pr doped on BNT improved the dielectric constant and reduced the loss tangent.

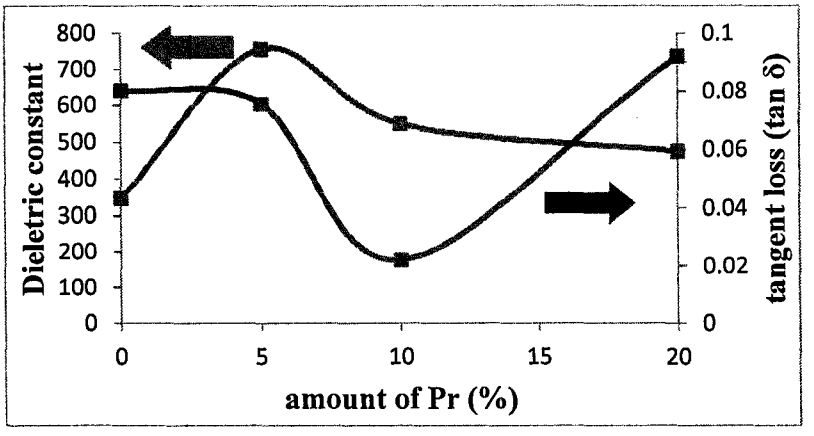

Figure 13: Relative dielectric constant and loss tangent (tan δ) of a) BNTS, b) 5% of Pr doped BNT, c) 10% of Pr doped BNT, d) 20% of Pr doped BNT after sintered at 1100°C.

This phenomenon is much related with domains and the grain size of the samples. In general, a domain is proportional to the grain size which means that when grain size increases, domain will become larger. However, increasing until 20% of Pr doped BNT the degradation of dielectric constant suddenly happen and loss tangent also increase. The larger concentration of additive has an adverse effect on both the dielectric constants and the losses (McLaughlin, 2008). Oshato and Imaeda (2003) have reported that the quality factor, which is the inverse of the loss tangent, increases with a decrease of the ionic radius of rare earth (La, Nd, Sm, Pr, etc.). In this case, it can be concluded that 5% of Pr doped BNT gives the optimum properties in terms of phase, grain size, density and also electrical properties.

From previous section, the optimum amount of Pr doped BNT is 5% which shows excellent overall properties. Therefore, in this section, the study on various sintering temperature s of BNT is performed on 5% of Pr doped BNT. The XRD spectra of 5% of Pr doped BNT powder sintered in air at (a) 1050°C (b) 1100°C (c) 1120°C (d) 1200°C for 3 hours is shown in Figure 14. Generally, a single perovskite phase without secondary phases was observed for Pr doped BNT (JCPDS No. 36-340) in various sintering temperature. However, there is still extra one peak appeared for 5% of Pr doped BNT 1050°C. Based on XRD, secondary phase which is bismuth titanate ($Bi_4Ti_3O_{12}$) appeared at (117) peak positions (JCPDS No. 00-047-0398). At room temperature, BNT and Pr doped BNT are rhombohedral symmetry. However, it is hard to observe due to overlapping peak and it is known that its lattice dimension is nearly cubic (Watcharapasorn *et al*, 2007). Fukuchi *et al.,* (2002) reported that although the crystal structure of BNT was rhormbohedral, the diffraction lines are indexed based on the pseudocubic unit cell because of the small degree of rhombohedral distortion.

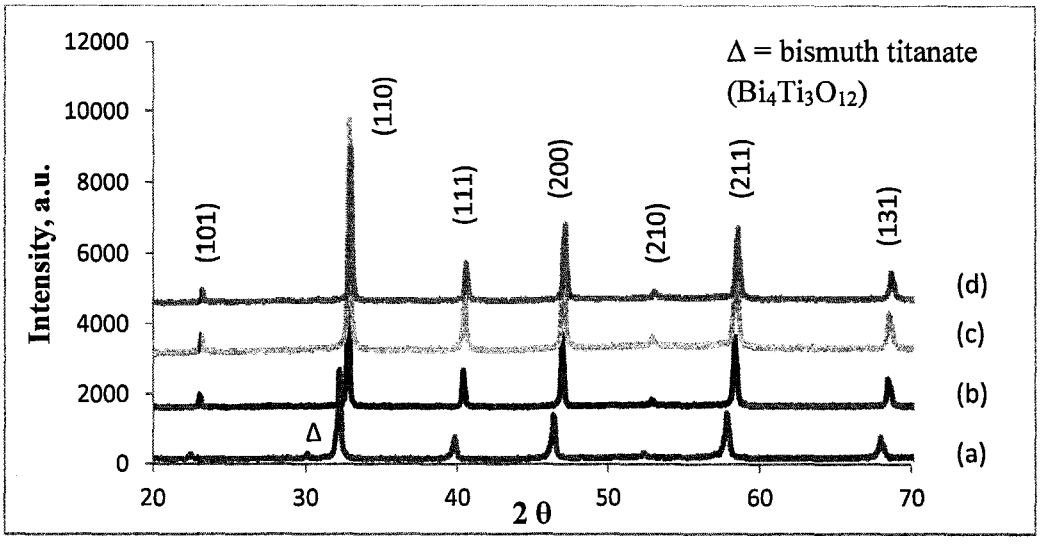

Figure 14: XRD pattern of 5% of Pr doped BNT sintered at (a) 1050°C, (b) 1100°C, (c) 1120°C and (d) 1200°C.

As shown in Figure 15, the presence of BIT secondary phase is only observed in sample 5% of Pr doped BNT sintered at 1050°C. It shows very low intensity in Figure 15(a). However, it is not observed in samples that were sintered at 1100°C and above. It proved that this secondary phase (bismuth titanate) can be eliminated after sintering above 1100°C. The XRD peaks become narrower with increasing sintering temperature. The results show that the crystallinity of particles improves with increasing in sintering temperature. Lu and Lai (1998) also reported that the narrower the peak, the higher crystallinity.

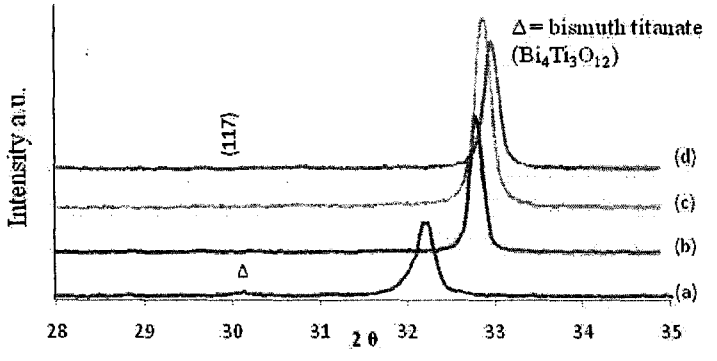

Figure 15: XRD spectra of 5% of Pr doped BNT sintered at (a) 1050°C, (b) 1100°C, (c) 1120°C and (d) 1200°C at (110) peak position.

The XRD spectra of 5% of Pr doped BNT doped sintered at different temperature (T=1050°C, 1100°C, 1120°C, 1200°C) at the (200) peak position which are shown in Figure 16. In Figure 16, the (200) peak positions of BNT are shifted to the right side when increased the sintering temperature. It is because of lattice distortion happened (Gao *et al.*, 2007). There are some micro strain occurred when Pr is added into BNT. This can be explained by Vegard's law which holds that a linear relation exists between the crystal lattice parameter and the different sintering temperature (Cullity, 2001). The increase of ion shift results in an increasing of lattice energy to stabilize the structure. Liu *et al.* (2006) also reported that it reached until certain amount of additive the peak will be shifted to the left again.

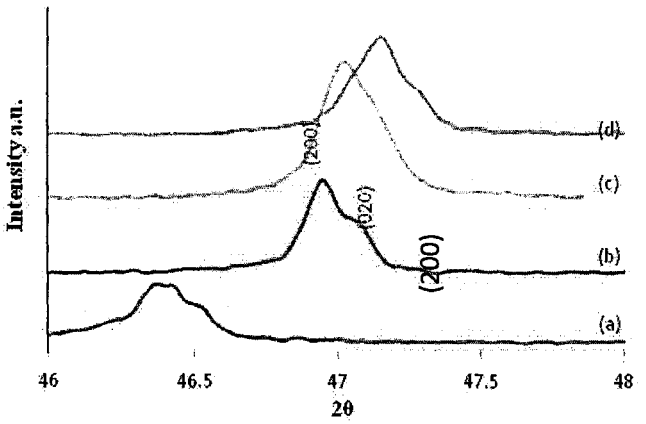

Figure 16: XRD spectra of 5% of Pr doped BNT sintered at (a) 1050°C, (b) 1100°C, (c) 1120°C, and (d) 1200°C at (200) peak position.

Figure 17 shows the SEM micrographs of 5% of Pr doped BNT sintered at different temperature (T= 1050°C, 1100°C, 1120°C, 1200°C). Sintering at 1200°C of Pr doped BNT shows the largest average grain size which is 1064.4 nm whereas sintering 1050 °C shows the smallest average grain size which is 601.32 nm. In general, the average grain size increased with arising temperature as shown in Figure 18.

The sintering temperature has influenced on the morphology and microstructure of sintered BNT (Pookmanee *et al.*, 2004). Diffusion among the grains occurred during sintering process. When ions gained adequate energy, mobility of ions also become more frequent. It

started to diffuse to adjacent grain and larger grain is formed. Diffusion is a time consuming process. In this case, factor of Pr as inhibitor is no longer considered and grain also grow gradually following with other ceramic sintering behavior. The driving force for sintering is the reduction in total particle surface area; surface energies are larger in magnitude than grain boundary energies. The finer powder, the necessary diffusion length of the atoms for sintering becomes shorter, which accelerates pore diffusion. This results in higher density ceramic.

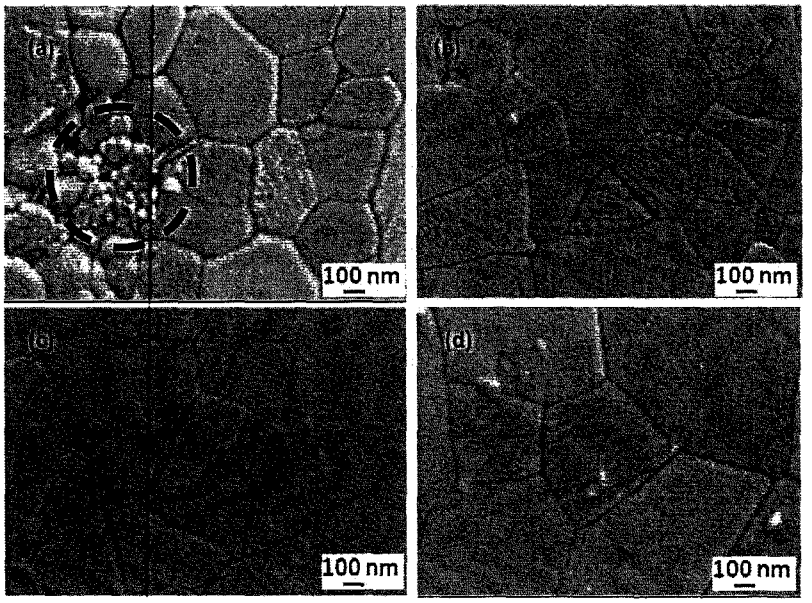

Figure 17: SEM micrographs of 5% of Pr doped BNT sintered at (a) 1050°C, (b) 1100°C, (c) 1120°C and (d) 1200°C.

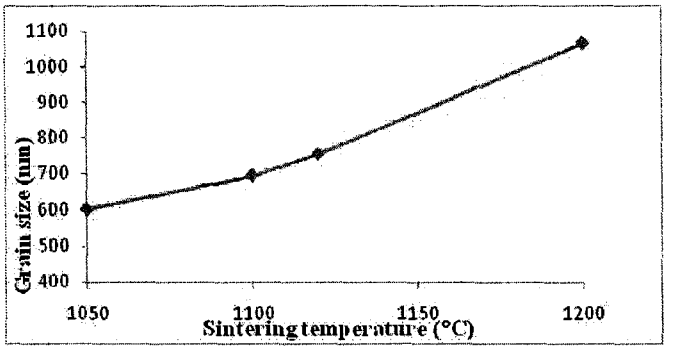

Figure 18: Average grain size of 5% of Pr doped BNT sintered various sintering temperature.

The relative density of each of the compositions was calculated by dividing the theoretical density which is 5.998g/cm^3. The grain size increased and density of the pellets decreased with increasing the sintering temperature (Cernea *et al.,* 2010). 5% of Pr doped BNT sintered at 1050°C shows the lowest relative density which is 88.80% (Figure 19). It is because the energy was insufficient for the ions to diffuse completely as circled in Figure 17(a) whereby some small grains and pores are observed. However, 5% of Pr doped BNT 1100°C shows the highest relative density value which is 95.21%. This result shows that the optimum sintering temperature for 5% of Pr doped BNT ceramic was around 1100°C. Above the optimum sintering temperature (1100°C), the density of the sintered samples decreased that could be due to degradation of grains and evaporation of Bi ions occur. This result is in agreement with Li *et al.,* (2005).

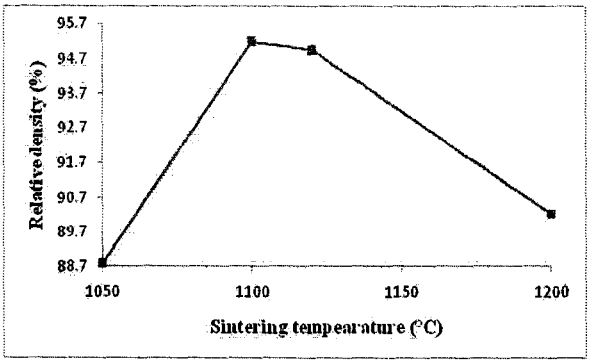

Figure 19: Relative density of 5% of Pr doped BNT sintered various sintering tempearature.

The relative dielectric permittivity and tangent loss were measured at 25°C with electric field of 1V as shown in Figure 20. For each composition, the dielectric permittivity of the sintered samples increased with increasing sintering temperature up to the optimum temperature which is 1150°C, and then decreased at the temperature above it. 5% of Pr doped BNT sintered at 1200°C shows the highest dielectric constant value (836) whereas 5% of Pr doped BNT 1050°C shows the lowest dielectric constant which is 712 only. The result shows that dielectric constant increased with arising sintering temperature that could be explained by the grain size. From Figure 18, grain size increased with arising sintering temperature. In terms of grain size, a domain is proportional to the grain size which means that when grain size increased, domain will became larger (Wang *et al.,* 2004). The square root of grain size is directly proportional to the domain width. A large grain size gives a large amount of domains. Takasu *et al.,* (1986) stated that domain size decreases with decreasing grain size. The dielectric constant and loss tangent of

5% of Pr doped BNT at various sintering temperature are shown in Figure 20. In term of loss tangent, it is also increased proportional to the sintering temperature.

The small grains consisted of small domains, as the width of domain is directly proportional to the square of the grain size. The small grain has difficulties to release the internal stress by this mechanism. The dielectric constant decreases as a result of the unreleased internal stress. Larger grain size with more number of domains contributes to large permittivity (Bahel *et al.*, 2007).

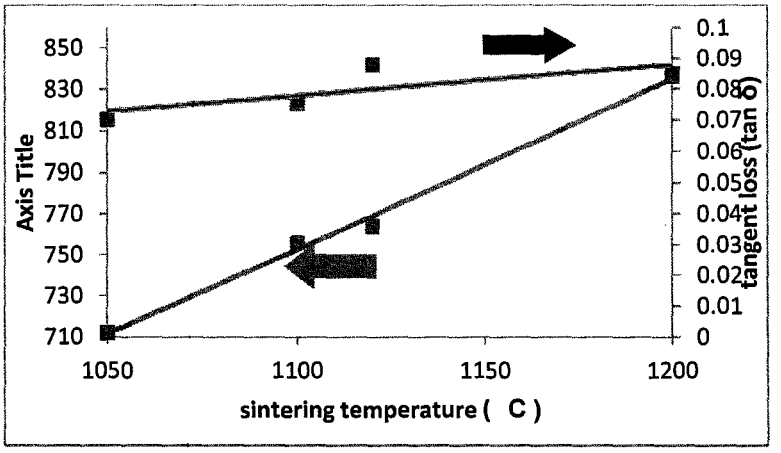

Figure 20: Dielectric constant and tangent loss (tan δ) of 5% of Pr doped BNT sintered at (a) 1050°C, (b) 1100°C, (c) 1120°C, (d) 1200°C.

2. Synthesis and properties of Lanthanum doped $(Na_{0.5}Bi_{0.5})TiO_3$ (BNT) using wet chemical technique

In this project, the effect of lanthanum doped in BNT was studied. Similar method to produce BNT is used to synthesize BNTL. The La doped was added during the synthesis. Phases presence in different composition of La (x = 0, 0.2, 0.4 and 0.6) before calcination and after calcinations were observed using XRD.

Figures 21-23 show the XRD spectra of BNT doped with the different amount of La. The result shows that the calcination process can eliminate secondary phases in the BNTL compounds. From the figure, we can observe that BNT with amount of La (x=0.2) has the lowest secondary phases while BNT with amount of La (x=0.6) has the higher amount of secondary phases. From this result, we can conclude that the increasing amount of dopant will increase the amount of secondary phases. According to Dunmin et al. (2003), the ceramics possess almost pure single phase of perovskite structure with a little dopant. The high amount of dopant makes the diffusion of doped in BNT lattices does not completely occur. This is due to the lower diffusivity of La compared to Bi.

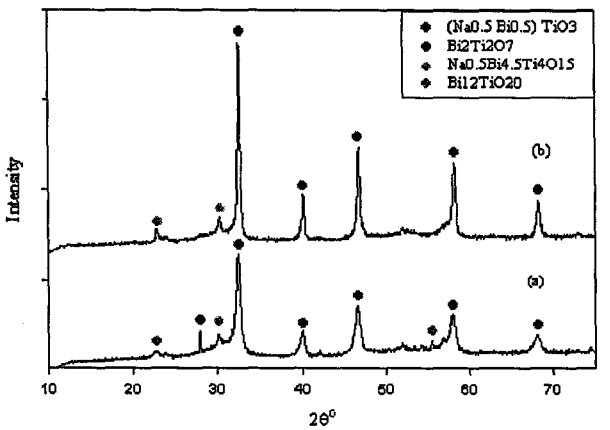

Figure 21: XRD spectra of BNTL (x=0.2) (a) before calcination (b) after calcination at 800°C

2θ°

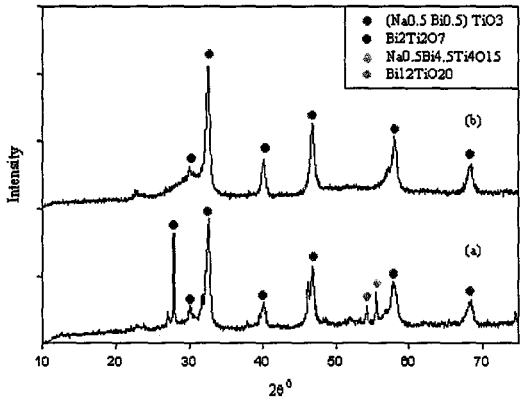

Figure 22: XRD spectra of BNTL (x=0.4) (a) before calcination (b) after calcination at 800°C

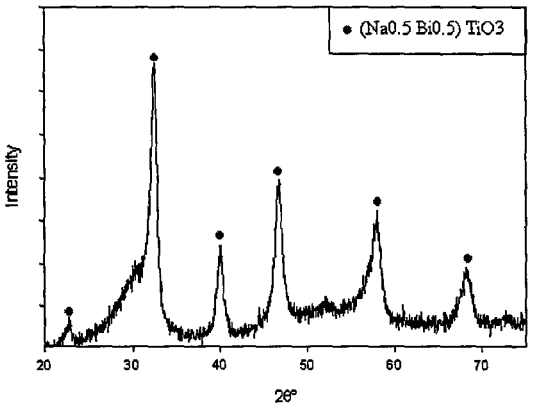

Figure 23: XRD spectra of BNTL (x=0.6) after calcination at 800°C

Figure 24 shows the comparison between BNTL (x=0.4) with the addition of glycine and without glycine as combustion agent. The addition of glycine in BNTL does not eliminate the second phase in sample unlike BNT.

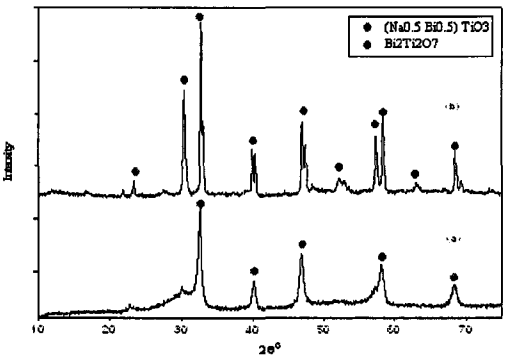

Figure 24: BNTL (x=0.4) after calcination at 800°C (a) without glycine, and (b) with glycine

Figure 25 shows SEM micrographs at BNTL after calcination at 800°C and soaking time is 3 hours. The particle size of sample decreased with increasing the amount of dopant. La plays the role as grain growth inhibitor. Lanthanum can replace the bismuth in BNT in perovskite structure due to their similarity of ionic radius (3^+ ion = 117pm). Considering the well-known volatility of bismuth, one does expect that the diffusivity of bismuth is significantly higher than lanthanum. La^{3+}, as donor dopant, took the place of A, induced the appearance of A ($(Bi_{0.5}Na_{0.5})^{2+}$) vacancy, reduced cell volume, weakened B - 0 bond strength (along *a* axis) and decreased *c I a* (Goh et al., 2008).

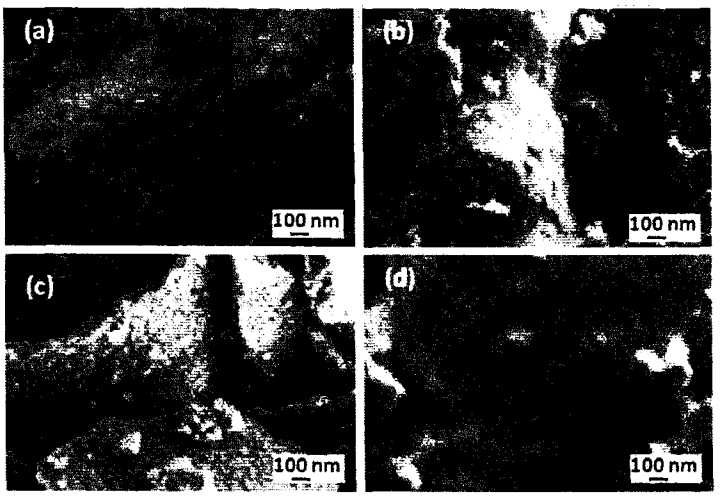

Figure 25: SEM micrographs of BNTL with varying x after calcination at 800°C, (a) BNT undoped (x=0), (b) BNTL (x=0.2), (c) BNTL (x=0.4), and, (d) BNTL (x=0.6).

Figure 26 shows the density of sintered BNT and BNTL pellets. Increasing the composition of La in the sample caused the density to decrease. The density of the sample was influenced by the particle size. The density of the samples slightly increased with the addition of 0.2 La. Further increase in La amount caused the density to decrease.

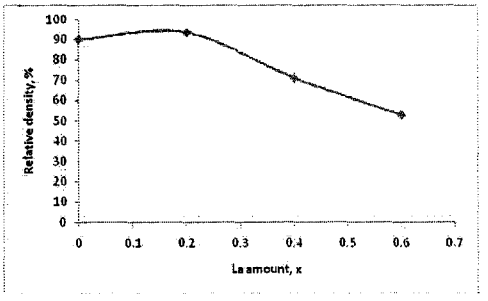

Figure 26: Density of BNT and BNTL pellet sintered at 1050°C.

Figure 27 shows dielectric properties of BNTL with varying La content. Dielectric constant reaches maximum with 0.2 La doping. Beyond 0.2 La content, dielectric constant values degrading. On the other hand, dielectric loss increases with increasing La doping. The result could be due to phase distortion from rhombohedral to pseudo cubic phase (Panda, 2009).

From this result, it was observed that BNTL_0.2S has the higher permittivity and lower loss tangent while BNTL_0.6S has lower permittivity and the higher loss tangent. La^{3+}, as donor dopant, took the place of A, induced the appearance of A ($(Bi_{0.5}Na_{0.5})^{2+}$) vacancy, reduced cell volume, weakened B - 0 bond strength (along *a* axis) and decreased *c I a* . The domain turned easily and dielectric constant increased, enhancing the piezoelectric strain constant. But if the amount of La^{3+} was excessive, the distortion enlarged, increasing the difficulty of polarization, decreasing the dielectric constant and piezoelectric strain constant of materials (Xinyou et al., 2006).

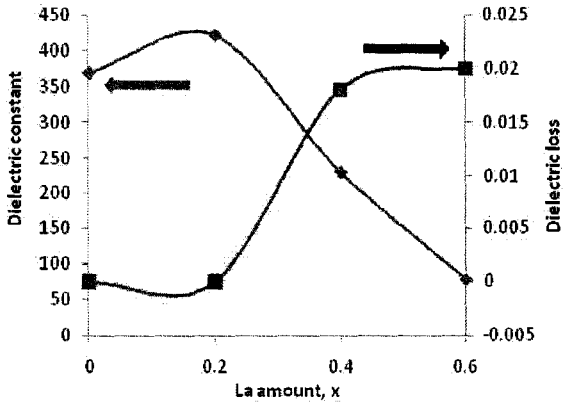

Figure 27: Dielectric properties of BNTL with varying La content.

3. PRASEODYMIUM-DOPED BISMUTH POTASSIUM TITANATE ($Bi_{0.5}K_{0.5}TiO_3$) PREPARED BY THE SOFT COMBUSTION TECHNIQUE

Firstly, the BKT powder was produced by directly dissolved potassium nitrate (KNO_3) in 2-methoxyethanol ($CH_3OCH_2CH_2OH$). Figure 28 (a) and (b) show the XRD pattern of the powder as produced and after calcination at 800°C, respectively. XRD spectra show the presence of secondary phase in the compounds. However, after calcination, the BKT powders still did not form a single phase BKT. The BKT phase was matched with the ICDD number of 36-0339, whereas, for the secondary phase, it was matched with the ICDD number of 72-1019, which was bismuth titanate, $Bi_4Ti_3O_{12}$, (BIT) phase. It was believed that the KNO_3 which was not fully dissolved in the solution could be one of the reasons that caused the formation of the secondary phase.

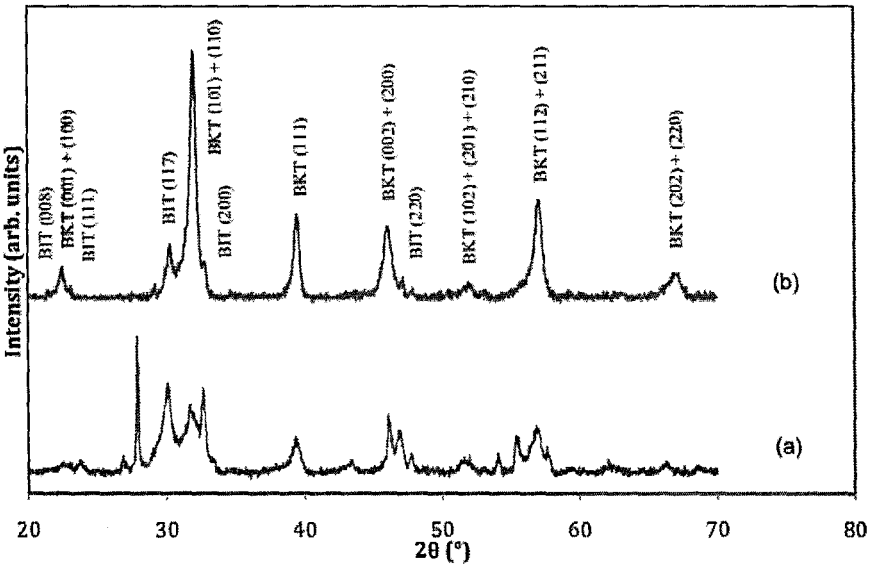

Figure 28: XRD spectra of the BKT without H_2O: (a) synthesized powder; (b) powder calcined at 800°C.

To solve the problem of limited solubility of KNO_3 in $CH_3OCH_2CH_2OH$, KNO_3 was first dissolved in 5 ml H_2O. The XRD spectra of these BKT synthesized powder and calcined powder are shown in Figure 29. As the synthesized powder without H_2O, the BKT dissolved in 5 ml

H_2O also contained the secondary phase. For the calcined powder, the peaks showed the presence of the secondary phase of BIT. However, this BIT peaks were not obvious in the spectrum. The most obvious peak was (117). This could be due to a very small amount of the BIT phase that resulted in low intensity XRD peak. By comparing the calcined powders of BKT without H_2O and BKT dissolved in 5 ml H_2O (Figure 30), it can be seen that, the BKT dissolved in 5 ml H_2O contained less amount of the secondary phase than the BKT without dissolving in H_2O. With this, all the subsequent powders were then produced by dissolving KNO_3 in 5 ml H_2O during preparation steps of BKT.

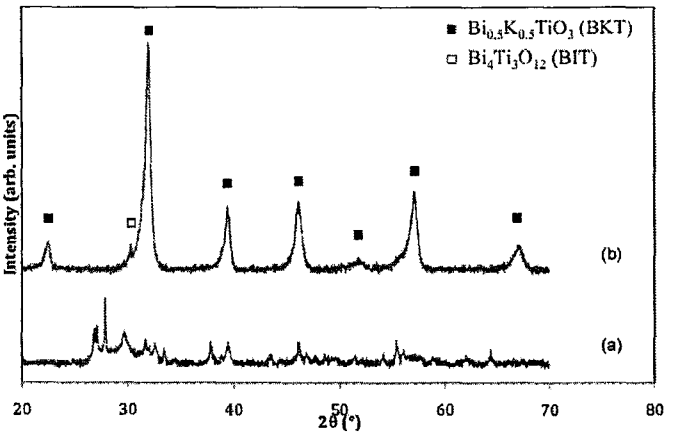

Figure 29: XRD spectra of the BKT dissolved in 5 ml H_2O: (a) synthesized powder; (b) powder calcined at 800°C.

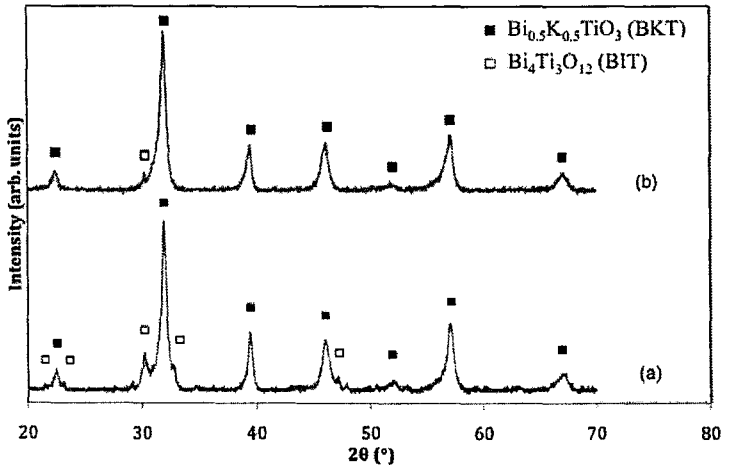

Figure 30: XRD spectra of the BKT powders: (a) without dissolving in H_2O and (b) dissolving in 5 ml H_2O calcined at 800°C.

Up to this step, the calcined powder which contained only single BKT phase had not been obtained yet. It was believed that the presence of the secondary phase was due to the incomplete combustion of the starting materials (Michael *et al.*, 2000). With this, glycine (H_2NCH_2COOH) which acted as a combustion fuel was added into the starting materials. Glycine is one of the most popular and attractive fuels to produce uniform composition and precise control stoichiometry of complex oxide ceramic powders (Aruna and Mukasyan, 2008).

Various molar fractions of glycine were used and the XRD spectra of the calcined powders are shown in Figure 31. From these XRD spectra, it can be observed that the BKT synthesized with the addition of 0.1 and 0.3 mol of glycine showed the presence of the secondary BIT phase as in the BKT synthesized without glycine. Whereas, the BKT with 0.5, 1.0 and 1.5 mol of glycine showed only the presence of single phase BKT. The result proved that the addition of a small amount of glycine (0.1 and 0.3 mol) was insufficient to aid in the combustion process. Whereas, a higher amount of glycine (0.5 mol and above) was sufficient and capable to obtain the pure phase BKT. With this, 0.5 mol of glycine was used to prepare the subsequent powders.

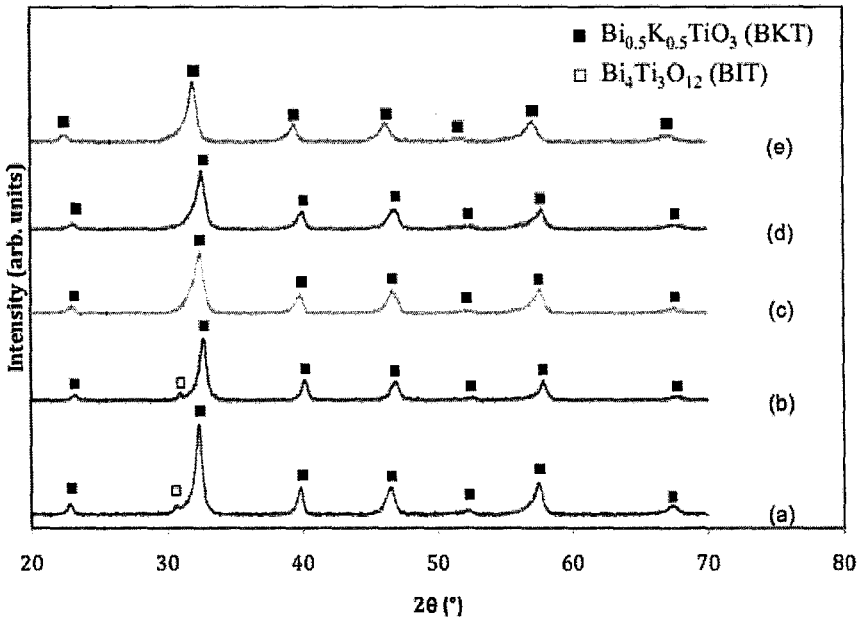

Figure 31: XRD spectra of the BKT powders with: (a) 0.1; (b) 0.3; (c) 0.5; (d) 1.0 and (e) 1.5 mol of glycine. All samples were calcined at 800°C

Figure 32 shows the TGA curve of BKT powder with 0.5 mol of glycine. It can be observed that a step weight loss occurred at 100-120°C. Since water vaporizes at this temperature range, this weight loss was due to the loss of moisture from the sample. At 320-380°C, the weight loss could be due to the decomposition of the organic substances. Besides that, a gradual weight loss is occurred at the temperature range of 380-550°C was also attributed to decomposition of physical and chemical absorb water. Moreover, the decomposition of nitrate materials of $Bi(NO_3)_3.5H_2O$ and KNO_3 also took place at this temperature (Hao *et al.*, 2005).

In addition, a weight loss was also observed at 550-700°C. This could be due to the solid state reaction of the starting materials to form BKT powder. Above 700°C, there was no obvious weight change of the powder. This result implied that the BKT powder started to crystallize and form the perovskite structure above this temperature (Chou *et al.*, 2010; Hao *et al.*, 2005; Yu *et al.*, 2007). Hence, the calcination temperature of BKT powder in current work was conducted above 700°C.

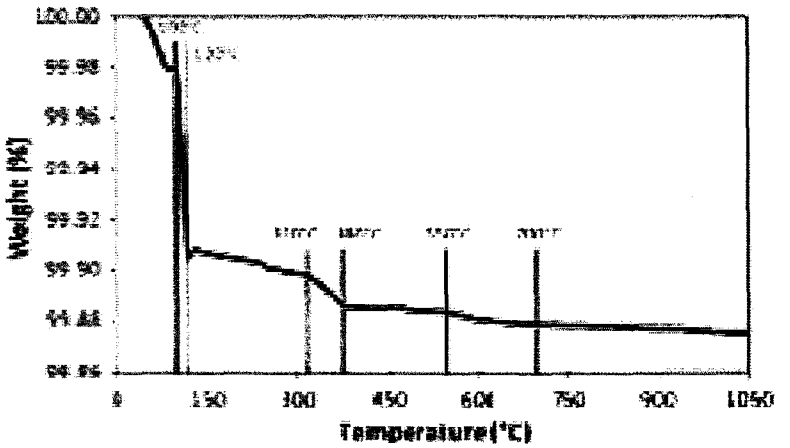

Figure 32: TGA curve of the BKT powder with 0.5 mol of glycine

Figure 33 shows the XRD spectra of the as synthesized and calcined powders of BKT with the addition of 0.5 mol glycine. Before calcination, the BKT contained the secondary phase, whereas after calcination, all the secondary phases were eliminated. This BKT powder was calcined at 800°C and 850°C for 3 h, respectively. From the XRD spectra, it can be seen that a single phase BKT was obtained after calcination at 800°C and 850°C. Moreover, the powder calcined at 800°C possesses higher cyrstallinity. Besides that, the powder calcined at 800°C has finer

powder and smaller crystallite size (9.66 nm) compared to powder calcined at 850°C (11.89 nm). Thus, the lower temperature of 800°C was adopted to calcine all of the following powders.

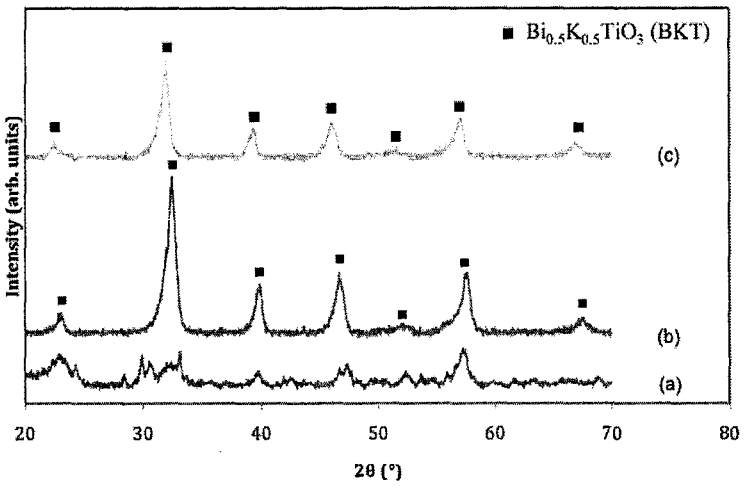

Figure 33: XRD spectra of the BKT with 0.5 mol glycine: (a) synthesized powder; (b) powder calcined at 800°C and (c) powder calcined at 850°C

Beside calcination temperature, the sintering temperature of the BKT with 0.5 mol of glycine was studied as well. After calcination, this powder was pressed into pellets and they were sintered at 1000°C, 1030°C and 1050°C for 3 h. The pellet sintered at 1050°C melted, that could be due to volatilization of potassium and bismuth (Huang *et al.*, 2009; Hou *et al.*, 2005; Konig *et al.*, 2009; Rao and Sankaram, 2009; Rao *et al.*, 2009; Wada *et al.*, 2001 and 2002; Zhang *et al.*, 2010). The XRD spectra of this BKT sintered at 1000°C and 1030°C are shown in Figure 34. From this figure, it can be seen that the pellets sintered at 1000°C and 1030°C contained the secondary phase of BIT. The result was due to the high volatility of the potassium component at the sintering temperatures (Konig *et al.*, 2009; Wada *et al.*, 2001 and 2002).

To minimize the volatilization of the potassium component, the pellets were then sintered in an alumina crucible. Since sintering carried out in the closed crucible required higher heating temperature than the opened crucible, the pellets were then sintered at 1050°C and 1100°C. The

pellets were sintered for 5 h rather than 3 h to obtain the denser pellets. However, the pellet sintered at 1100°C melted. Figure 35 shows the XRD spectrum of the BKT with 0.5 mol of glycine sintered at 1050°C. This sample contained a single phase BKT and thus the sintering temperature of 1050°C was applied on all subsequent pellets.

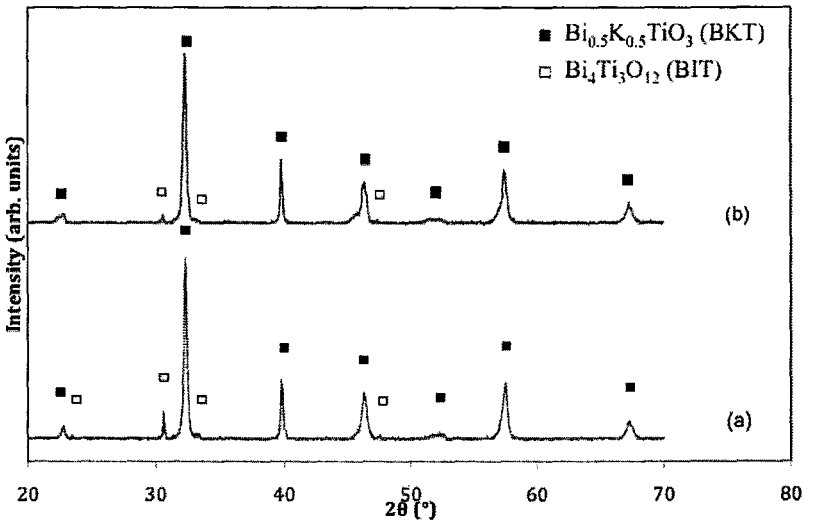

Figure 34: XRD spectra of the BKT pellets with 0.5 mol of glycine sintered at: (a) 1000°C and (b) 1030°C for 3 h

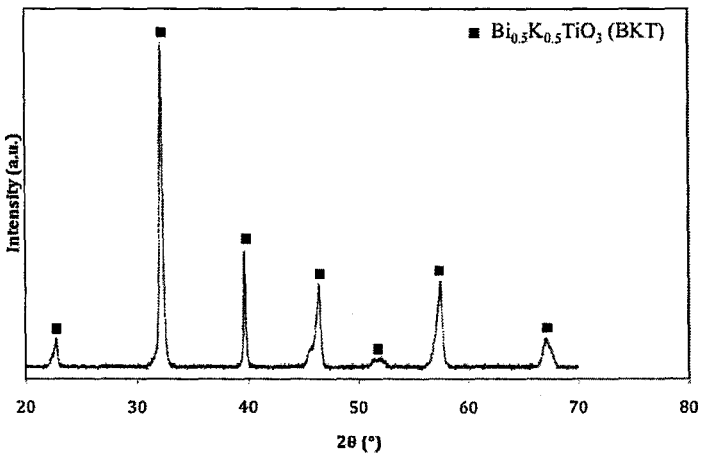

Figure 35: XRD spectrum of the BKT pellets with 0.5 mol of glycine sintered at 1050°C for 5 h

Figure 36 shows the XRD spectra of the BKT with optimum amount of glycine (0.5 mol), calcination temperature (800°C) and sintering temperature (1050°C). The intensities of the XRD peaks increased as the sample was calcined and it was even higher as the sample was sintered. The spectra showed that the crystallinity of the BKT improved after calcination and sintering processes. By using Rietveld refinement, it was obtained that the BKT sintered at 1050°C had the lattice parameters of a = 3.929 Å, b = 3.929 Å, c = 3.976 Å, and the α, β, γ angles of 90°. Since they had the angles of 90°, and the a and b have the same value, thus prove that BKT sintered at 1050°C had a tetragonal symmetry at room temperature. Furthermore, these results were in agreement with the reported values of a = 3.913 Å and c = 3.993 Å (Rao *et al.*, 2009). Apart from that, the crystallite size of the calcined powder and sintered pellet were obtained as 9.66 nm and 33.98 nm, respectively.

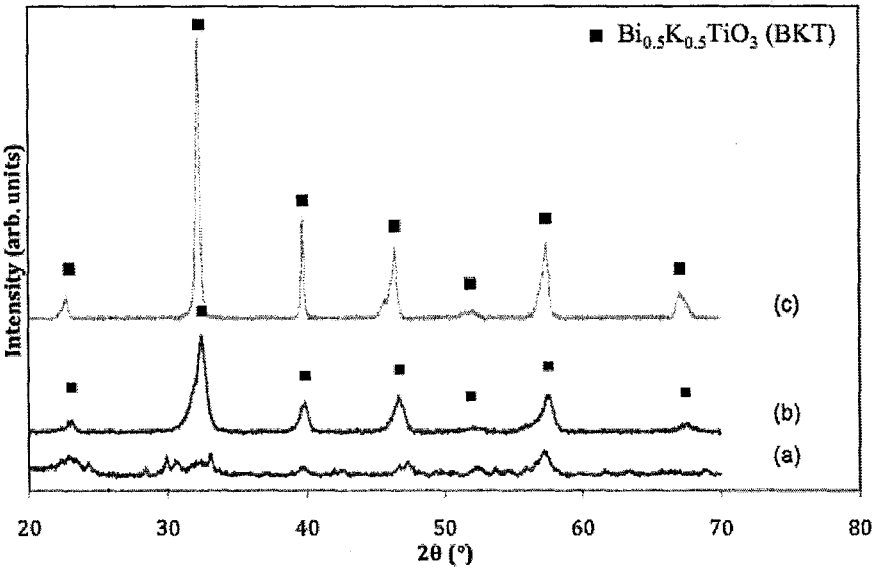

Figure 36: XRD spectra of the BKT with 0.5 mol of glycine: (a) synthesized powder; (b) powder calcined at 800°C and (c) pellet sintered at 1050°C

The FESEM micrographs of the BKT powders; as prepared, after calcination at 800°C and after sintering at 1050°C are illustrated in Figure 37 (a), (b) and (c), respectively. It can be seen that the synthesized BKT powder and powder calcined at 800°C have the flake-like structure particles even though they are agglomerated. For the microstructure of BKT sintered at 1050°C, the grains are hard to discern. However, it can still be seen that the grains are in the range of 100

nm to 300 nm. Figure 38 (a) and (b) show the TEM micrographs of the as synthesized and calcined (800°C) BKT (with 0.5 mol of glycine), respectively. As in the SEM micrographs, the particles show the flake like structure. Besides that, it can be observed that both synthesized and calcined powders have the similar particle sizes, which are in the range of 10 nm to 100 nm.

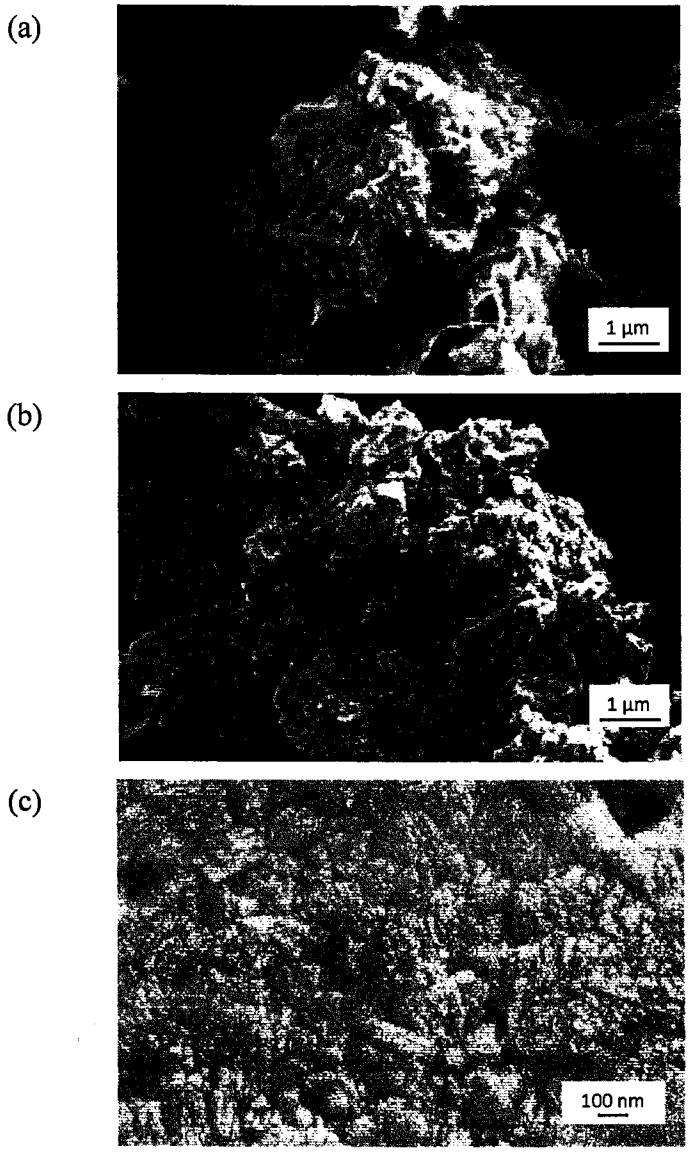

Figure 37: FESEM micrographs of the BKT with 0.5 mol of glycine: (a) synthesized powder; (b) powder calcined at 800°C and (c) pellet sintered at 1050°C.

(a)

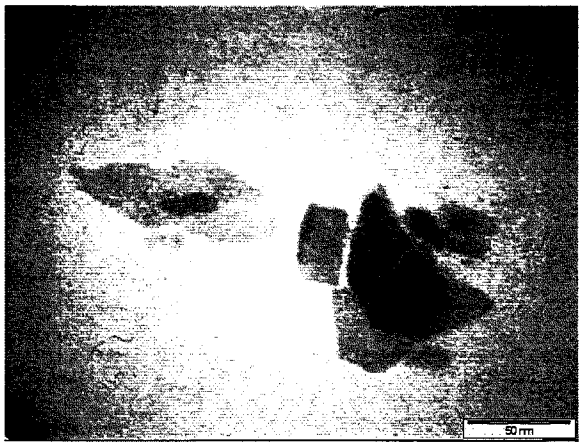

(b)

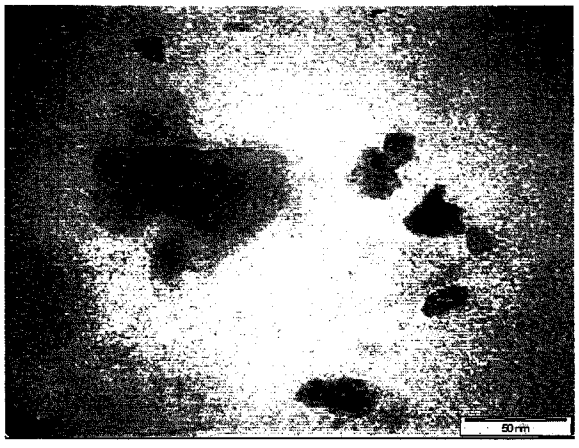

Figure 38: TEM micrographs of the BKT with 0.5 mol of glycine: (a) synthesized powder and (b) powder calcined at 800°C.

To confirm the amount of elements present in calcined powder (800°C) and sintered pellet (1050°C) BKT, the EDX analysis was performed. Their EDX spectra are shown in Figure 39 and Figure 40. It can be observed that as the BKT sam[redacted] e at [redacted] nt [redacted] the Bi and K elements were slightly lower compared [redacted] sa [redacted] cou [redacted] to the slight volatilization of the Bi and K components. Generally, BKT was still able to retain its elements composition ($Bi_{0.5}K_{0.5}TiO_3$) after calcination and sintering processes.

(a)

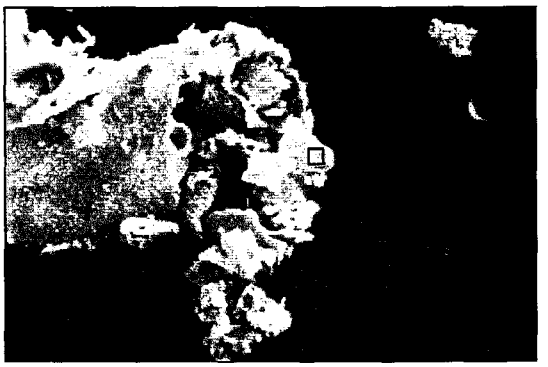

(b)

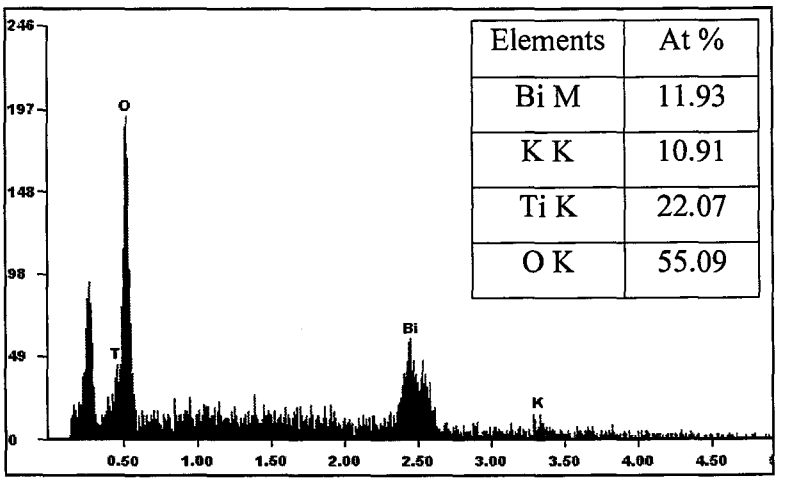

Elements	At %
Bi M	11.93
K K	10.91
Ti K	22.07
O K	55.09

Figure 39: (a) FESEM micrograph and (b) EDX spectrum of the BKT powder with 0.5 mol of glycine calcined at 800°C

(a)

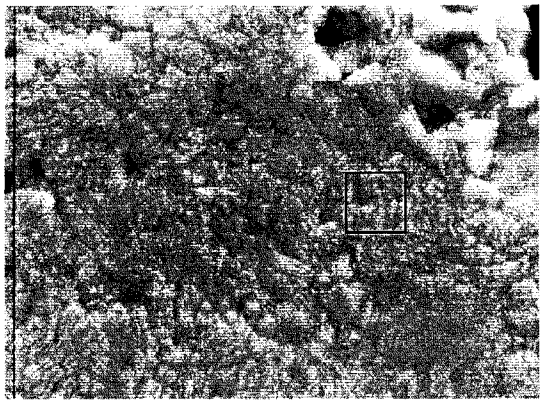

(b)

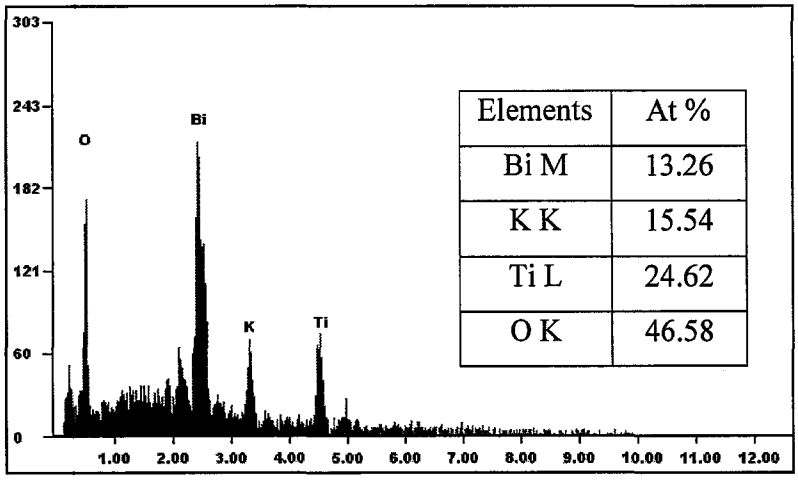

Elements	At %
Bi M	13.26
K K	15.54
Ti L	24.62
O K	46.58

Figure 40: (a) FESEM micrograph and (b) EDX spectrum of the BKT pellet with 0.5 mol of glycine sintered at 1050°C

4. Praseodymium-doped bismuth potassium titanate (BPKT)

The ionic radii of the Pr^{3+}, Bi^{3+}, K^{+} and Ti^{4+} are 0.99 Å, 1.03 Å, 1.38 Å and 0.605 Å, respectively. Since a similar ionic radius is required for a dopant to dope inside the structure, Pr^{3+} is thus preferred to replace the Bi^{3+} ion. With this, the BPKT has the chemical formula of $Bi_{0.5-x}Pr_xK_{0.5}TiO_3$ (Goh *et al.*, 2009).

Various amounts of Pr (x = 0.01, 0.03, 0.05, 0.10, 0.15, 0.20) were added into BKT. Figure 41 shows the XRD spectra of the undoped BKT and various BPKT powders calcined at 800°C. The BPKT with x = 0.01 and 0.03 have a single phase BPKT. This indicated that the Pr^{3+} in the BPKT did not form the secondary phase or separated from the interior grain, but dissolved into the perovskite lattice (Chon *et al.*, 2003). However, when the amount of x was further increased (x = 0.05, 0.10, 0.15, 0.20), the secondary phase of BIT appeared. For the BPKT (x = 0.01) and BPKT (x = 0.03), the amount of Pr added into them was lesser and thus the secondary phase of BIT was not formed. Whereas, for the BPKT with x = 0.05, 0.10, 0.15 and 0.20, a small amount of the secondary phase was formed.

The formation of the secondary BIT phase was due to Pr doping. When Pr was added into BKT, the Pr^{3+} substituted the Bi^{3+}, these bondless Bi^{3+} were then reacted with Ti^{4+} and O^{2-}, and formed BIT. The formation of the secondary BIT phase was in contrast with some works reported the formation of the secondary phases of $Bi_2Ti_2O_7$ (Zhang *et al.*, 2010), $K_4Ti_3O_8$ (Hou *et al.*, 2005; Rao *et al.*, 2009), $K_2Ti_4O_9$ (Konig *et al.*, 2009) and $K_2Ti_6O_{13}$ (Konig *et al.*, 2009). The presence of these secondary phases could be explained by volatilization of K^{+} and Bi^{3+} during sintering process.

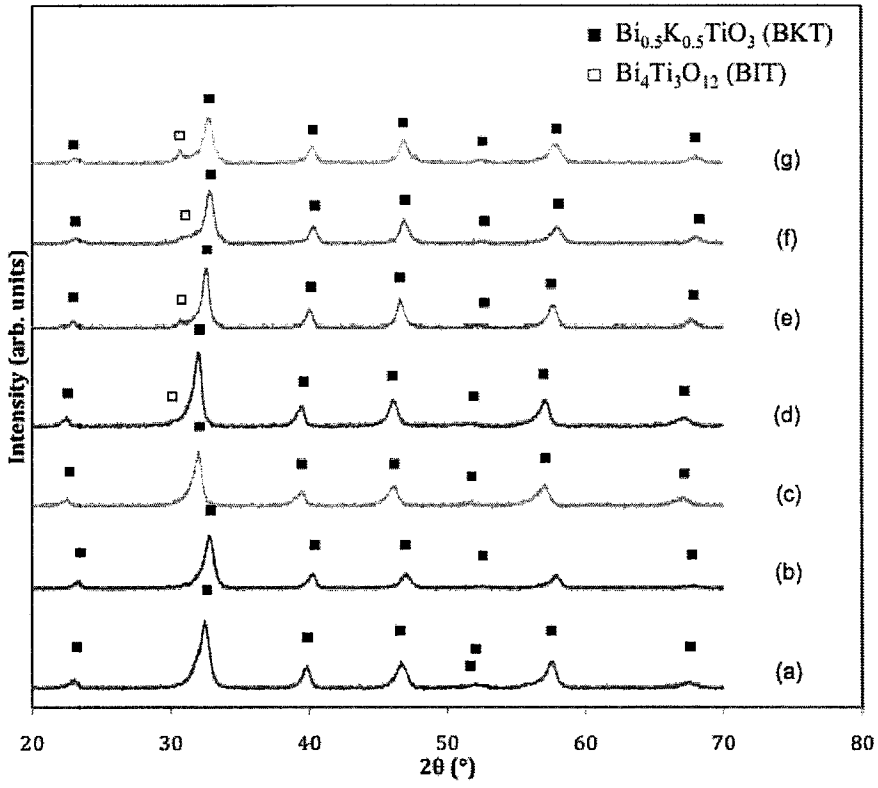

Figure 41: XRD spectra of the powders calcined at 800°C: (a) BKT with 0.5 mol of glycine; BPKT with x are: (b) 0.01; (c) 0.03; (d) 0.05; (e) 0.10; (f) 0.15 and (g) 0.20.

These calcined BPKT powders were then pressed into pellets and sintered at 1050°C for 5 h. Figure 42 shows the XRD spectra of the sintered BPKT pellets. These XRD spectra show that only the BPKT pellet (x = 0.01) contained the pure phase of BPKT and no evidence of the presence of the secondary phase. For the pellets BPKT with x = 0.03, 0.05, 0.10, 0.15 and 0.20, the secondary phase of BIT was present. When the amount of Pr dopant increased, the intensities of the peaks for the BIT phase became stronger. This meant that the secondary BIT phase became more dominant (higher crystallinity) as the amount of dopant increasing. When the amount of Pr dopant increased, more Pr^{3+} were substituted the Bi^{3+}, thus, more bondless Bi^{3+} reacted with Ti^{4+} and O^{2-}, and resulted in more BIT formed.

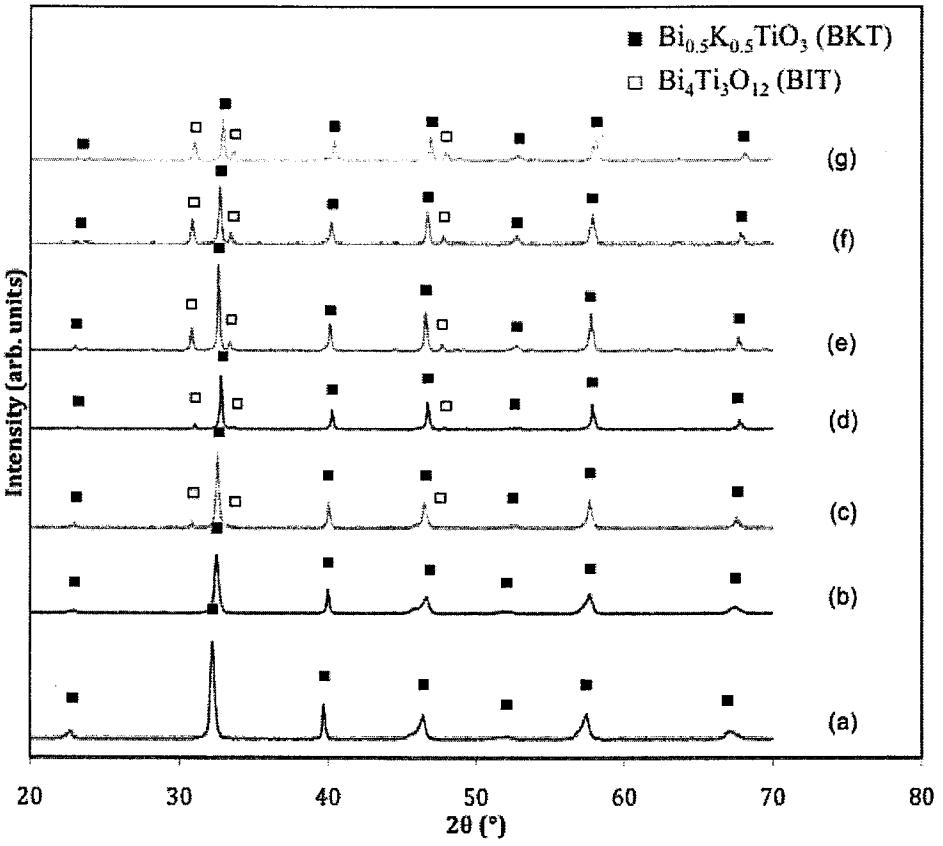

Figure 42: XRD spectra of the pellets sintered at 1050°C: (a) BKT with 0.5 mol of glycine; BPKT with x are: (b) 0.01; (c) 0.03; (d) 0.05; (e) 0.10; (f) 0.15 and (g) 0.20.

Besides that, by comparing the intensities of the peaks after calcination and after sintering, not only the BKT phase became higher crystallinity, but the secondary BIT phase also became higher crystallinity. This is because that, at higher sintering temperature, more Pr^{3+} substituted the Bi^{3+}, and as explained earlier, more Bi^{3+} were then reacted with Ti^{4+} and O^{2-}, and thus more BIT was formed. This can be seen in Figure 4 which taking the BPKT (x = 0.20) as an example.

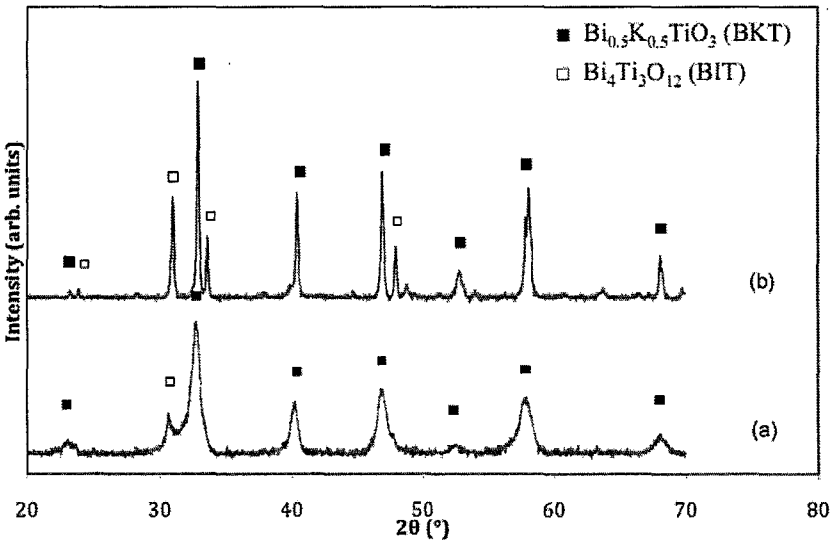

Figure 43: XRD spectra of the BPKT with x is 0.20: (a) powder calcined at 800°C and (b) pellets sintered at 1050°C

The lattice parameters of all the sintered pellets are shown in Table 4.1. All of these pellets have the values of a = b, which showed that the pellets retained the tetragonal symmetry even after doped with Pr. Besides that, these values were in agreement with the reported values (a = 3.913 Å and c = 3.993 Å) as mentioned earlier.

Table 4.1: Lattice parameters of the sintered pellets of BKT and BPKT with various amount of Pr (x)

x	Lattice parameters (Å)	
	a	c
0	3.929	3.976
0.01	3.934	3.978
0.03	3.939	3.958
0.05	3.943	3.949
0.10	3.935	3.939
0.15	3.929	3.935
0.20	3.924	3.931

The crystallite sizes of the calcined powders and sintered pellets are in the range of 9.66 nm to 13.01 nm, and 33.98 nm to 68.66 nm, respectively. The crystallite sizes of calcined BPKT powders with x = 0, 0.01, 0.03, 0.05, 0.10, 0.15 and 0.20 are 9.66, 9.96, 12.49, 13.01, 12.67, 10.36 and 9.93 nm, respectively. Whereas, for the crystallite sizes of sintered BPKT pellets with x = 0, 0.01, 0.03, 0.05, 0.10, 0.15 and 0.20 are 33.98, 35.27, 41.46, 68.66, 51.54, 50.27 and 49.89 nm, respectively. The plots of the crystallite sizes of calcined powders and sintered pellets against amount of Pr (x) are shown in Figure 44 and Figure 45, respectively. It can be observed that the crystallite sizes of both calcined powders and sintered pellets increased from x = 0 to x = 0.05, and then decreased from x = 0.05 to x = 0.20. Besides that, it can be seen that the crystallite sizes of the sintered pellets were larger than the calcined powders. This was due to more ion diffusion occurred during sintering process and caused the crystallite growth.

Figure 44: Crystallite size of the calcined powders of BKT and BPKT

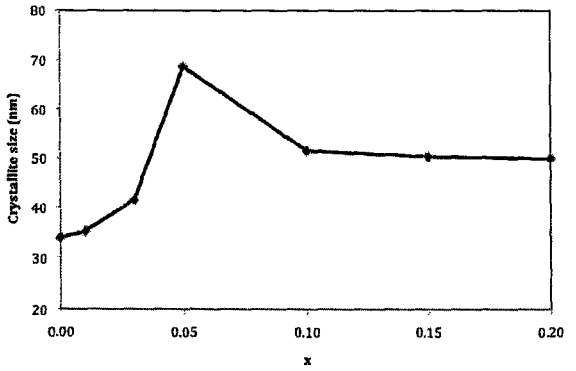

Figure 45: Crystallite size of the sintered pellets of BKT and BPKT

Figure 46 shows the (002) + (200) peaks of the sintered BKT and BPKT pellets. From these peaks, it can be observed that the undoped BKT has the broadest peak among all the pellets. When Pr were added into BKT, the width of the peaks were decreased from x = 0.01 to x = 0.05 and followed by increasing from x = 0.05 to x = 0.20. Since the crystallite size decreased with the broadening of the peaks, this peak broadening trend was in agreement with the crystallite size calculated using Rietveld refinement.

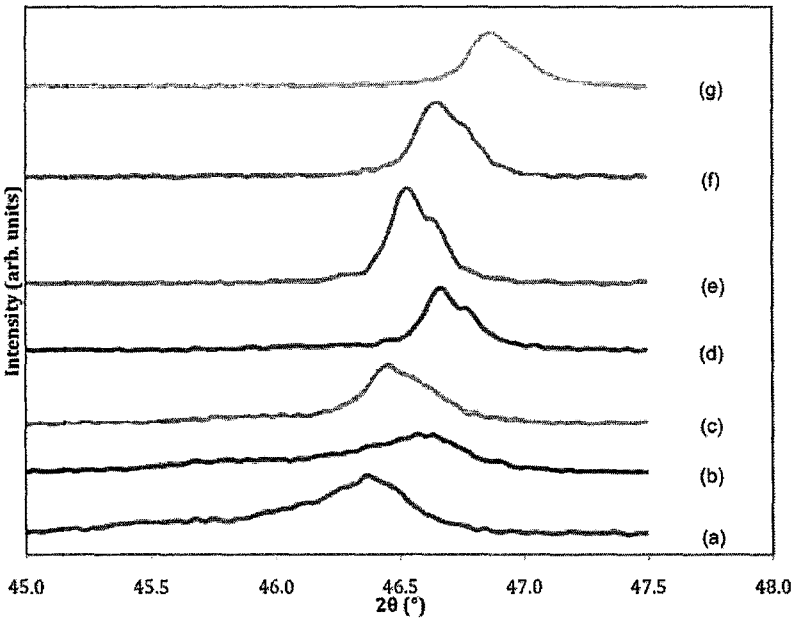

Figure 46: (002) + (200) peaks of the BKT and BPKT pellets sintered at 1050°C: (a) BKT with 0.5 mol of glycine; BPKT with x are: (b) 0.01; (c) 0.03; (d) 0.05; (e) 0.10; (f) 0.15 and (g) 0.20.

Figure 47 shows the FESEM micrographs of the synthesized and calcined powders of BPKT. It can be seen that the particles before and after calcination are similar and having the flake-like structures as in the undoped BKT. Besides that, from all of these micrographs, there was no obvious trend of the particles size or shape can be observed due to agglomeration.

(a) (i)

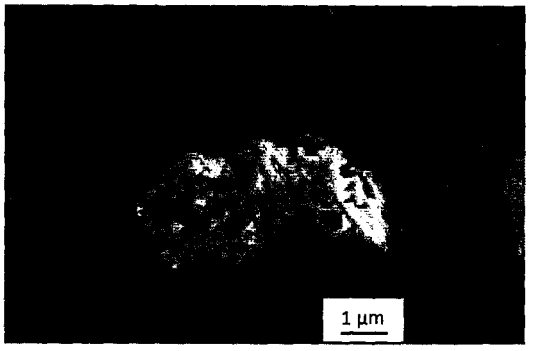

(ii)

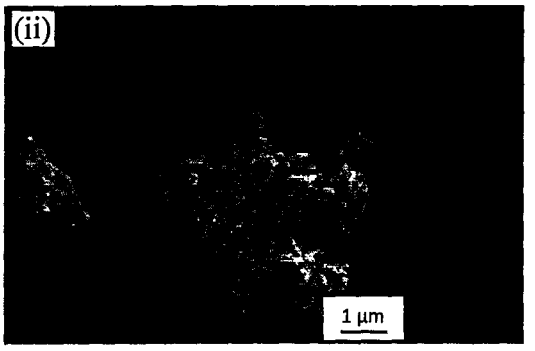

(b) (i)

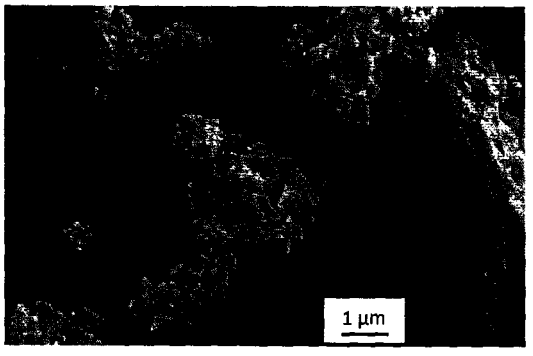

(ii)

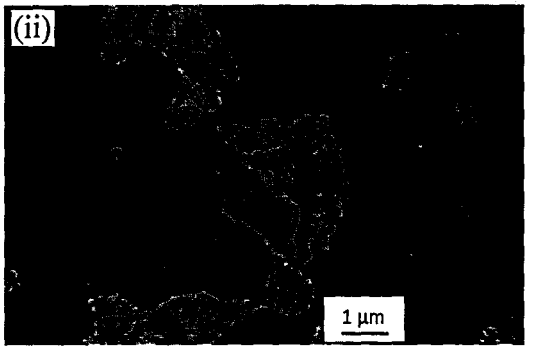

(c) (i)

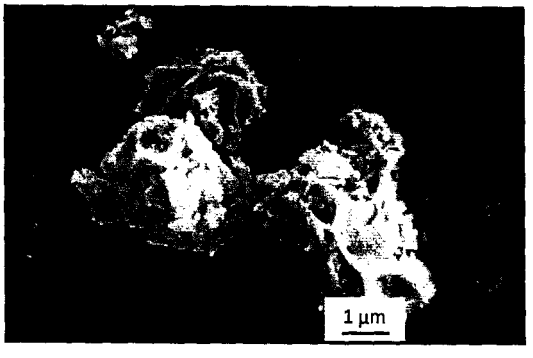

(ii)

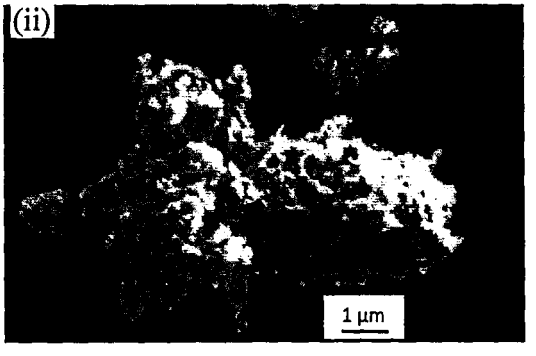

(d) (i)

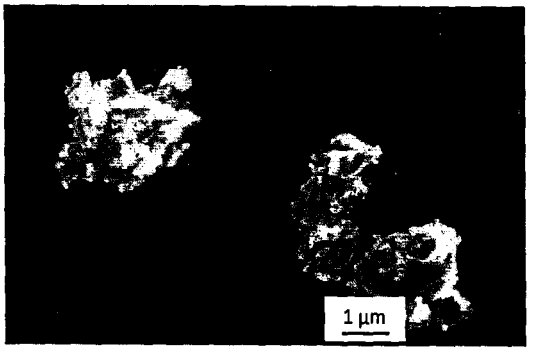

(ii)

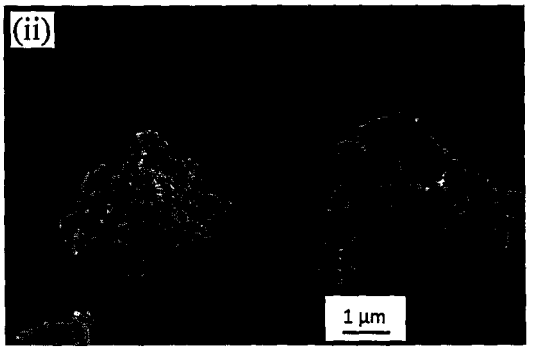

(e) (i)

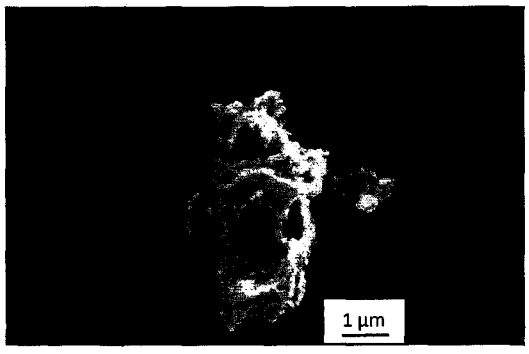

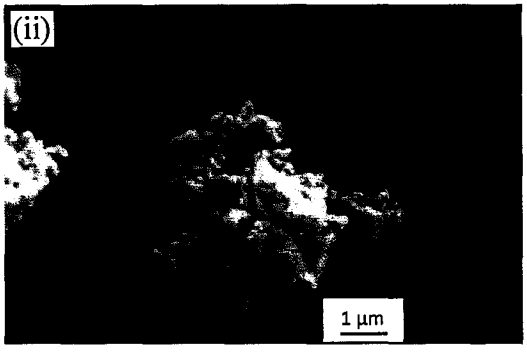

(f) (i)

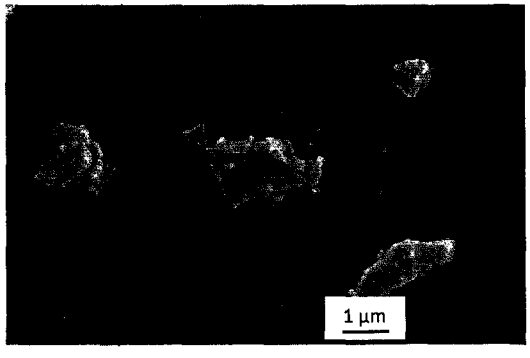

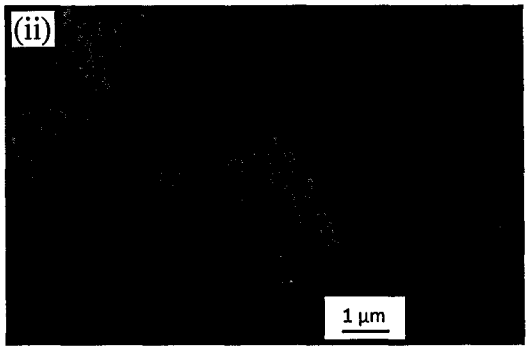

Figure 47: FESEM micrographs of the (i) synthesized and (ii) calcined powders of the BPKT with x are: (a) 0.01; (b) 0.03; (c) 0.05; (d) 0.10; (e) 0.15 and (f) 0.20.

Figure 48 (a) and (b) show the TEM micrographs of the as prepared and calcined (800°C) BPKT (x = 0.01) samples, respectively. The particles have the flake-like structure (similar to undoped BKT) as shown in FESEM images (Figure 47(a)). Apart from that, both powders show similar particle sizes, which are in the range of 10 nm to 100 nm. This particle sizes are also similar to the particle sizes of synthesized and calcined (800°C) BKT with 0.5 mol of glycine (Figure 39).

(a)

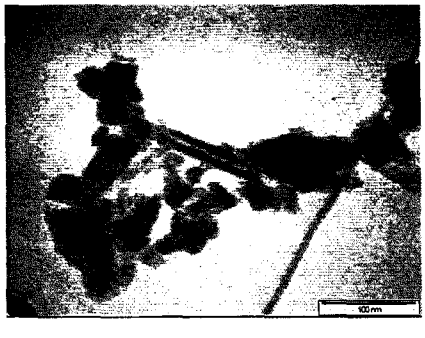

(b)

Figure 48: TEM micrographs of the BPKT with x = 0.01: (a) synthesized powder and (b) powder calcined at 800°C

The FESEM micrographs of the sintered BPKT pellets are illustrated in Figure 49. The grains show no particular shape. By considering the micrograph of the sintered BKT pellet (Figure 37), it is observed that the grain size of the BPKT increased from x = 0 to x = 0.05, and followed by decreasing from x = 0.05 to x = 0.20. BPKT with x = 0.05 has the largest grain sizes and its average grain sizes are 435 nm. As the BKT is doped with small amount of Pr (x = 0.01 to 0.05), the Pr diffuses into BKT and assists the grain growth. However, when the amount of Pr is increased to x = 0.10, there is obvious secondary BIT phase formed. It is believed that this BIT phase acting as a grain growth inhibitor and thus suppresses the grain growth of the BPKT phase (Goh *et al.*, 2009; Kuharuangrong, 2001; Zhang *et al.*, 2010). This grain sizes changing trend is in agreement with the crystallite size changing trend that is obtained from XRD analysis. This is acceptable since crystallite size is normally increasing when the grain size increases (Buscaglia *et al.*, 2006; Goh *et al.*, 2009).

(a)

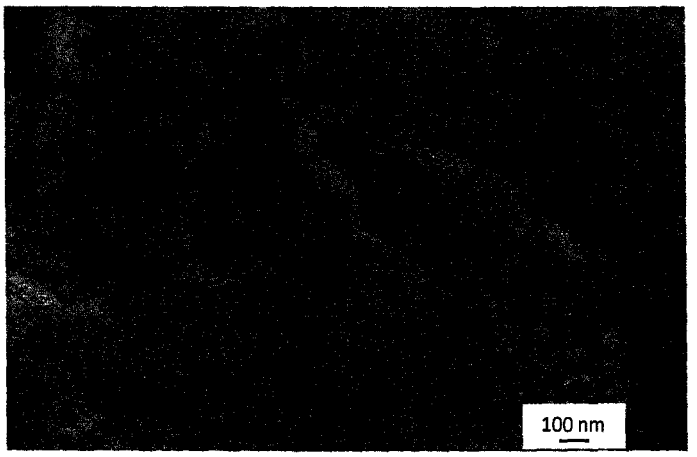

(b)

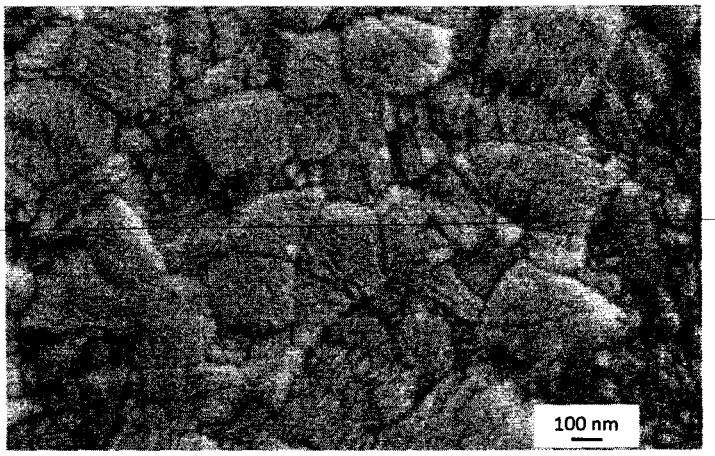

(c)

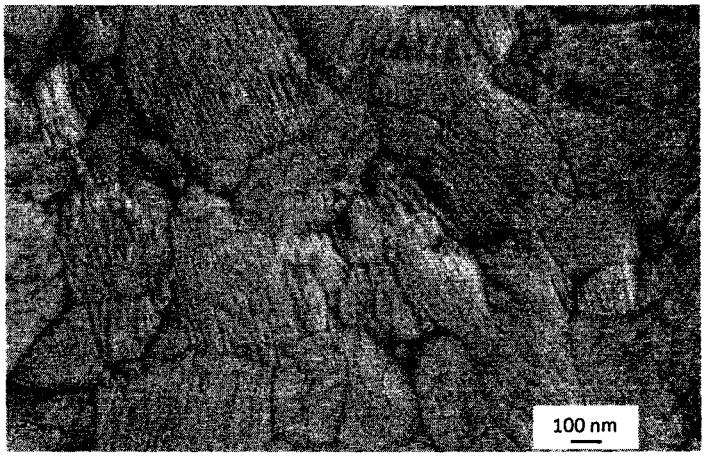

(d)

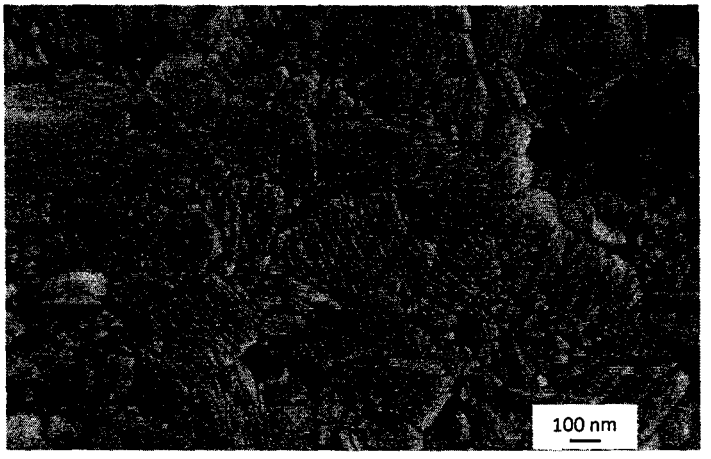

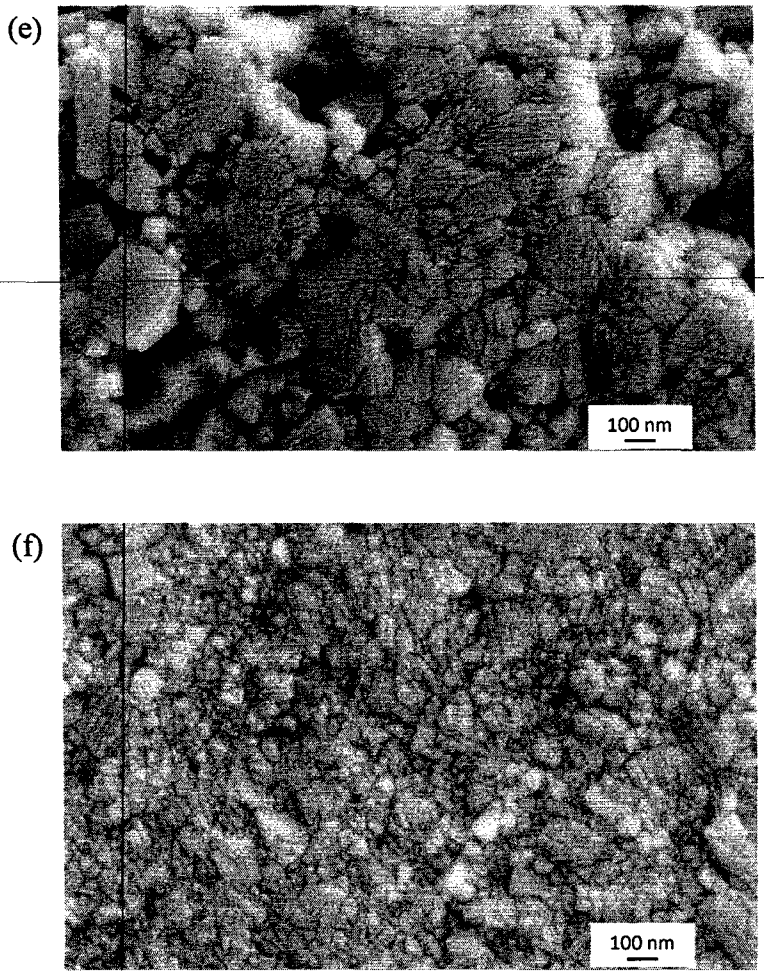

Figure 49: FESEM micrographs of the sintered BPKT pellets with x are: (a) 0.01; (b) 0.03; (c) 0.05; (d) 0.10; (e) 0.15 and (f) 0.20

EDX analysis was performed on the calcined powder (800°C) and sintered pellet (1050°C) BPKT (x = 0.01) to confirm the amount of elements present in them. The EDX spectra are shown in Figure 50 and Figure 51. Similar to BKT, when BPKT (x = 0.01) sample was sintered, the At % of the Bi and K elements were slightly lower compared to as calcined sample. This was due to the slight volatilization of the Bi and K components. Generally, BPKT (x = 0.01) was still able to retain its elements composition ($Bi_{0.49}Pr_{0.01}K0.5TiO_3$) after calcination and sintering processes.

(a)

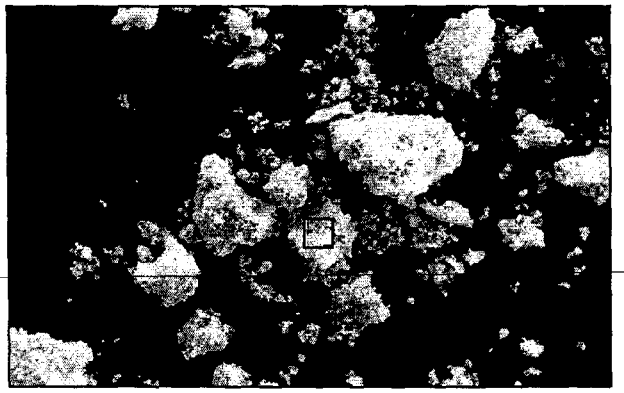

(b)

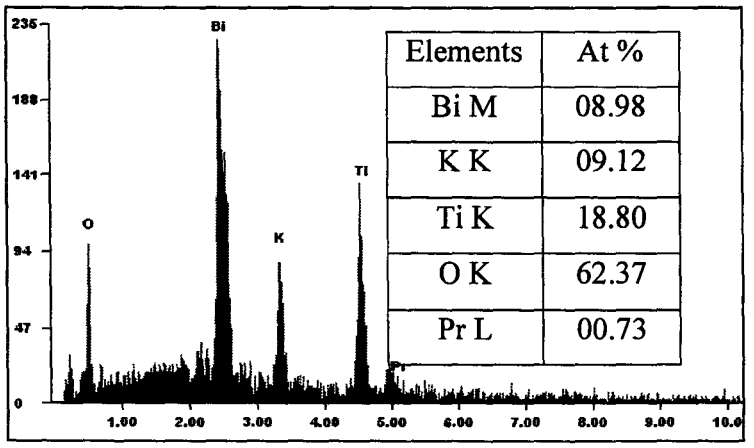

Elements	At %
Bi M	08.98
K K	09.12
Ti K	18.80
O K	62.37
Pr L	00.73

Figure 50: (a) FESEM micrograph and (b) EDX spectrum of the calcined BPKT powder with x = 0.01.

(b)

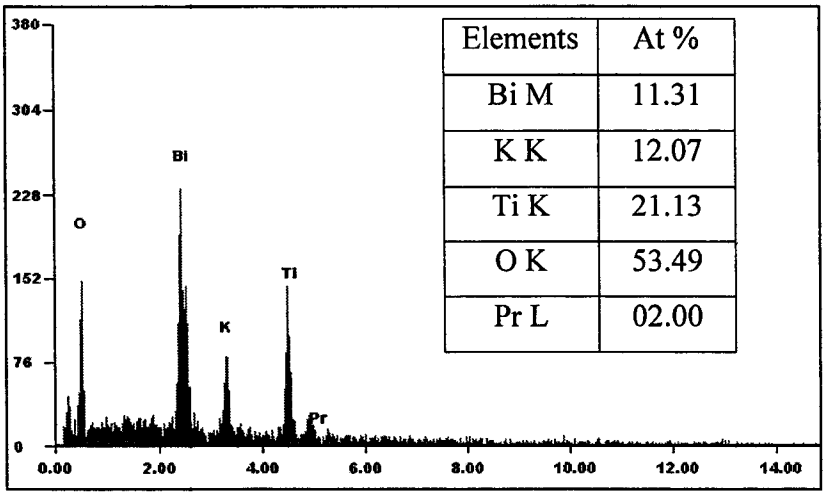

Elements	At %
Bi M	11.31
K K	12.07
Ti K	21.13
O K	53.49
Pr L	02.00

Figure 51: (a) FESEM micrograph and (b) EDX spectrum of the sintered BPKT pellet with x = 0.01.

The densities of the sintered pellets were measured using Archimedes method and they are shown in Table 2 together with their relative densities. Moreover, the plots of density and relative density against x are shown in the Figure 52 and **Error! Reference source not found.**Figure 53, respectively. It can be seen that the densities of the pellets increased from x = 0 to x = 0.05, and then decreased from x = 0.05 to x = 0.20. This could be explained by the

addition of Pr caused the formation of closed-packed microstructure with increasing grain size. However, the density did not increase unlimitedly with the addition of Pr but it started to decrease from x = 0.05. This was due to the decreasing grain size from x = 0.05. When grain size was smaller, it tends to have more pores and thus resulting in lower density. The surface images of these pellets are shown in Figure 54. It can be observed that higher density pellets contained less pores, and vice versa.

Table 2: Density and relative density of the sintered pellets.

x	$Weight_{air}$ (g)	$Weight_{liquid}$ (g)	Density (g cm^{-3})	Average density (g cm^{-3})	Relative density (%)
0	0.7051	0.5755	5.418	5.418	91.37
	0.7046	0.5744	5.390		
	0.7049	0.5760	5.446		
0.01	0.6894	0.5626	5.415	5.422	91.43
	0.6888	0.5623	5.423		
	0.6896	0.5631	5.429		
0.03	0.6576	0.5369	5.426	5.430	91.57
	0.6575	0.5369	5.430		
	0.6573	0.5368	5.433		
0.05	0.7096	0.5815	5.517	5.538	93.39
	0.7098	0.5830	5.575		
	0.7099	0.5819	5.523		
0.10	0.6263	0.4974	4.839	4.818	81.24
	0.6264	0.4960	4.784		
	0.6252	0.4963	4.830		
0.15	0.5454	0.4272	4.595	4.600	77.57
	0.5454	0.4271	4.592		
	0.5451	0.4274	4.612		
0.20	0.5677	0.4414	4.477	4.497	75.83
	0.5679	0.4428	4.521		

	0.5680	0.4421	4.493		

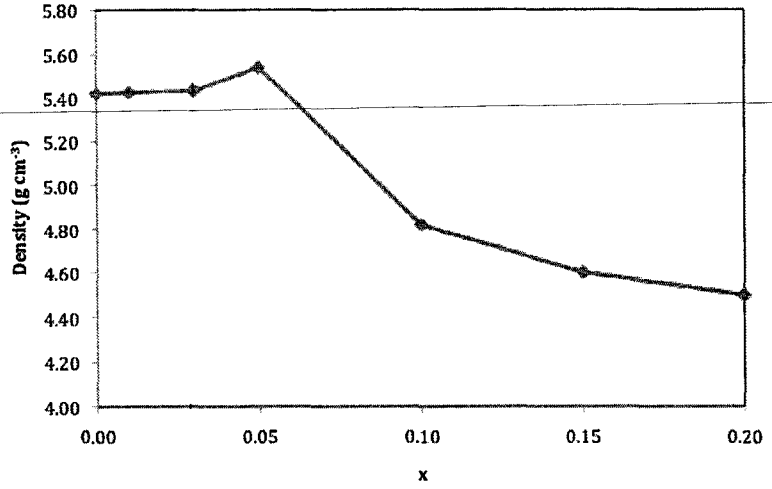

Figure 52: Density of the sintered pellets

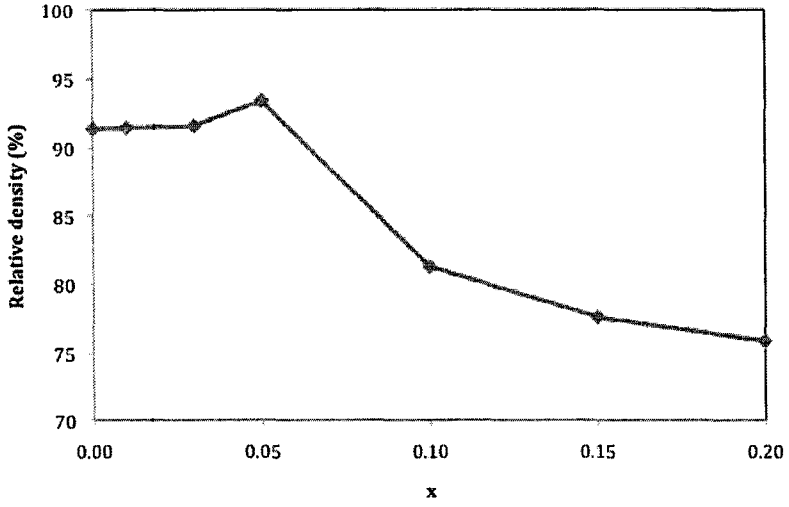

Figure 53: Relative density of the sintered pellets

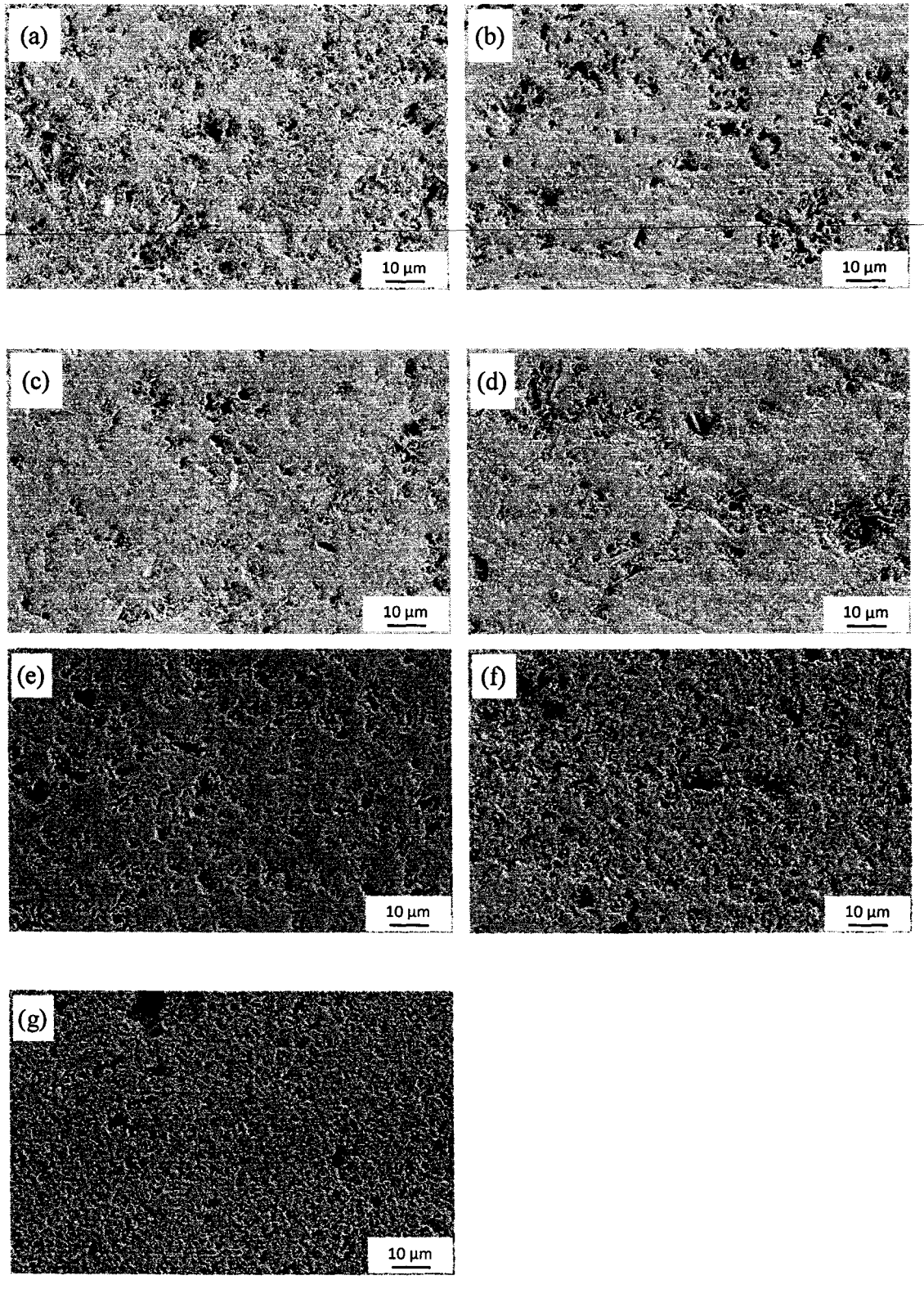

Figure 54: Surface morphology of the sintered BPKT pellets with varying x: (a) 0; (b) 0.01; (c) 0.03; (d) 0.05; (e) 0.10; (f) 0.15 and (g) 0.20

The dielectric test was performed at 1 MHz. The dielectric constant (ε_r) and loss tangent (tan δ) of the sintered pellets are in the range of 437.19 to 713.87, and 0.1014 to 0.1589, respectively. The ε_r of sintered BPKT pellets with x = 0, 0.01, 0.03, 0.05, 0.10, 0.15 and 0.20 are 520.1, 608.11, 643.79, 713.87, 504.99, 477.92 and 437.19, respectively. Whereas, the tan δ of the sintered BPKT pellets with x = 0, 0.01, 0.03, 0.05, 0.10, 0.15 and 0.20 are 0.1051, 0.1182, 0.1383, 0.1391, 0.1589, 0.1545 and 0.1014, respectively. The plots of dielectric constant and loss tangent against x are shown in Figure 55. It can be observed that ε_r increasing from x = 0 to x = 0.05 and decreased beyond x = 0.05. The undoped BKT has the ε_r of 520.1, while the BPKT (x = 0.05) has the highest ε_r of 713.87. This ε_r trend is in agreement with the trends of crystallite sizes and grain sizes. This is acceptable as the ε_r is always increased with increasing grain sizes (Hiruma *et al.*, 2007)

It is known that the electrical properties of the ferroelectric ceramics are highly dependent on the grain size and microstructure of the samples (Goh *et al.*, 2009). As the ferroelectric ceramic is cooled through the Curie temperature (T_c), stress appears in the system. These stresses within the grains can be released or reduced by the formation of an appropriate arrangement of 90° domains. For larger grains, most of the stresses can be relieved with this mechanism. On the other hand, as the grain size decreases, the domains also become smaller. This domain width is roughly proportional to the square root of the grain size. With this, the number of domains in a grain decreases as the square root of the grain size and thus, the smaller the grain; the larger the unrelieved stress (Buscaglia *et al.*, 2006; Moulson and Herbert, 2003; Zhao *et al.*, 2004). Other than that, the decrease of ε_r starting from x = 0.05 to x = 0.20 could also due to the poor density. It is well known the low density ceramics will lead to the low ε_r as well.

For the values of tan δ, they are increased from x = 0 to x = 0.10, and then decreased from x = 0.10 to x = 0.20. The BPKT (x = 0.05) has the highest ε_r and an acceptable tan δ of 0.1391. With this, it can be used as a capacitor, ferroelectric and piezoelectric devices.

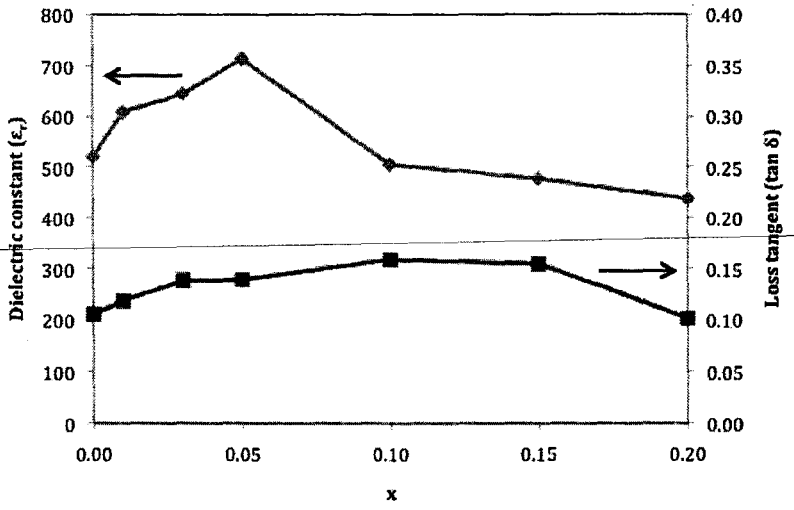

Figure 55: ε_r and tan δ of the sintered pellets

References:

A.Watcharapasorn, S. Jiansirisomboon, T. Tunkasiri, J. Electroceram. (2007) 613.

B.D. Cullity and S.R. Stock (2001) Elements of X-ray diffraction, 3rd edition, Prentice Hall, New Jersey, 678

C.R. Zhou, X.Y. Liu, Mater. Chem. Phys. (2008) 413.

C.S. Chou, Chen, J.H., Yang, R.Y. and Chou, S.W. Powder Technol. (2010), 202[1-3]39.

E. Fukuchi, T. Kimura, J. Am. Ceram. Soc. (2002) 1461.

H. Zhang, S.Jiang, K.Kajiyoshi, and J. Xiao, J. Am. Ceram. Soc. (2010) 93, 750.

J. Hao, X. Wang, R.Chen, and L. Li, Mater. Chem. Phys. (2005) 90, 282.

J. Konig, M. Spreitzer, B. Jancar, D. Suvorov, Z. Samardzija, and A. Popovic, J. Eur. Ceram. Soc. (2009)29, 1695.

L. Ma, K. Zhao, J. Li, Q. Wu, M. Zhao, C. Wang, J. Rare Earth (2009) 496.

M.S. Michael, A. Fauzi, S.R.S. Prabaharan, Int. J. Inorg. Mater. (2000)2, 261.

Moulson, A.J. and Herbert, J.M. (2003). *Electroceramics: Materials, Properties, Applications*, 2nd edition, John Wiley & Sons, Chichester.

P. Pookmanee, P. Uriwilast, S. Phanichpant, Ceram. Int. (2004) 30, 1913.

P. Pookmanee, G. Rujijanagul, S. Ananta, R. B. Heimann, S. Phanichphant J. Eur. Ceram. Soc. (2004) 24, 517.

P.V.B. Rao, and T.B. Sankaram, J. Electroceram. (2009)25[1], 60.

P.V.B. Rao, E.V. Ramana, and T.B. Sankaram, J. Alloys Compd. (2009) 467, 293.

P.Y. Goh, K.A. Razak, S. Sreekantan, J. Alloys Compd. 475 (2009) 758.

Q. Xu, M. Chen, W. Chen, H.-X. Liu, B.-H. Kim, B.-K. Ahn, J. Alloys Compd. 463 (2008) 275

S.R. McLaughlin, PhD thesis, Queen's University Kingston, Ontario, 2008.

S.T. Aruna, and A.S. Mukasyan, Curr. Opin. Solid State Mater. Sci. (2008) 12, 44.

Shannon, R. Acta crystallogr. (1976) Section A[32] 751.

T. Wada, A. Fukui, and Y. Matsuo, Jpn. J. Appl. Phys. (2002)41, 7025.

T. Yu, K.W. Kwok, and H.L.W. Chan, Thin Solid Films (2007), 515, 3563.

T.Wada, K. Toyoike, Y.Imanaka, and Y. Matsuo, Jpn. J. Appl. Phys. (2001)40, 5703.

U., Chon, J.S., Shim, and H.M. Jang, J. Appl. Phys. (2003). 93, pp. 4769-4775.

V., Buscaglia, M.T. Buscaglia, M. Viviani, L. Mitoseriu, P. Nanni, V. Trefiletti, P. Piaggio, I. Gregora, T. Ostapchuk, J. Pokorny, and J. Petzelt, J. Eur. Ceram. Soc. (2006)26, 2889.

W. Li, J. Gu, C. Song, D. Su, J. Zhu, J. Appl. Phys. (2005) *98*, 1.
W.C. Lee, C.Y. Huang, L.K. Tsao, Y.C. Wu, J. Eur. Ceram. Soc. (2009) 1443.

X. Huang, Z.Yang, L. Sun, Q. Xie, B. Li, J. Zhou, and L. Li, Mater. Chem. Phys. (2009)114, 23.

X.X. Wang, K.W. Kwok, X.G. Tang, Solid State Commun. (2004) 129, 319.

Y. Hiruma, H. Nagata, and T. Takenaka, Jpn. J. Appl. Phys. (2007) 46, 1081.

Y.F. Liu, Y.N. Lu, S.H. Dai, J. Alloys Compd. (2009) 484, 801.

Z. Zhao, V. Buscaglia, M.Viviani, M.T.Buscaglia, L.Mitoseriu, A.Testino, M. Nygren, M. Johnsson, and P. Nanni, Phys. Rev. B (2004)70, 024107.

Appendix

Related publications

Quick Find

Use keywords to find the product you are looking for.
Advanced Search

What's New?

Advances in Sociology Research. Volume 10
$129.00

Shopping Cart

0 items

Information

Shipping & Returns
Privacy Notice
Conditions of Use
Contact Us

Bestsellers

01. Built Environment: Design, Management and Applications
02. Computational Mathematics: Theory, Methods and Applications
03. Computational Techniques: The Multiphase CFD Approach to Fluidization and Green Energy Technologies (includes CD-ROM)
04. Electronic Waste Management and Recycling Issues of Old Computers and Electronics
05. Erbium: Compounds, Production and Applications
06. Computational Methods in Applied Science and Engineering
07. Effective Teaching for Intended Learning Outcomes in Science and Technology (Metilost)
08. Electroporation in Laboratory and Clinical Investigations
09. Light Machine Tools for Productive Machining
10. Polymer Morphology

Notifications

Notify me of updates to **Bismuth: Characteristics, Production and Applications**

Bismuth: Characteristics, Production and Applications

Retail Price: ~~$140.00~~
10% Online Discount
You Pay: **$126.00**

Editors: Kamakhya Prasad Ghatak (University of Calcutta, Kolkata, India) Sitangshu Bhattacharya (Indian Institue of Science, Bangalore, India)

Book Description:

Bismuth (Bi) is an important subset of the generalized set of materials science in general and finds wide applications in different aspects of modern technology since its inception. This book presents the different physical properties of bismuth for researchers and engineers, post-graduate students, professionals in the fields of solid state science, nanoscience and technology and nanostructure thermodynamics in addition to materials science. (Imprint: Nova)

Table of Contents:

Special Focus Titles

01. Autoimmunity to Neuronal Proteins in Neurological Disorders
02. Understanding Eating Disorders: Integrating Culture, Psychology and Biology
03. Antimalarial Drugs: Age of the Artemisinins
04. Intentional Learning at its Best: Engaged Learning Strategies in Higher Education
05. The Rise and Fall of China's Last Dynasty: The Deepening of the Chinese Servility
06. Peopling of the Americas, Currents, Canoes, and DNA
07. Globalisation, Governance and Ethics: New Managerial and Economic Insights
08. Self-Management and the Health Care Consumer
09. The Roles of Social Support, Perinatal Depressive Symptomatology and Family Conflicts Among Hong Kong Chinese Women
10. Environmental Chemistry of Animal Manure
11. Medicinal Plants and Sustainable Development
12. Bees in Europe and Sustainable Honey Production (BEE SHOP): Results of a Pan-European Research Network

Tell A Friend

Tell someone you know about this product.

(S.T.Girousi, Z.D.Anastasiadou, P.D.Jannakoudakis)

Index

Series:
Materials Science and Technologies
Binding: Hardcover
Pub. Date: 2011 4th quarter
Pages: 7 x 10 (NBC - C)
ISBN: 978-1-61470-640-3
Status: FP

Status Code	Description
AN	Announcing
FM	Formatting
PP	Page Proofs
FP	Final Production
EP	Editorial Production
PR	At Prepress
AP	At Press
AV	Available

Add to Cart

Sunday 04 September, 2011

Chapter 4

CURRENT PROGRESS IN SYNTHESIS AND PROPERTIES OF DOPED BISMUTH TITANATE FOR ADVANCED ELECTRONIC APPLICATIONS

A. Umar Al-Amani, S. Sreekantan, M. N. Ahmad Fauzi and K. A. Razak[*]

School of Materials and Mineral Resources Engineering, Engineering Campus, Universiti Sains Malaysia, 14300, Nibong Tebal, Seberang Perai Selatan, Penang, Malaysia

ABSTRACT

Lead-free bismuth-layered compounds have been widely studied as alternative materials for advanced electronics applications such as ferroelectric random access memories (FRAM), piezoelectric applications, electro-optic devices, micro-sensors, micro-electro-mechanical systems, actuators, transducers and capacitors. Lead-free bismuth-based materials have been chosen to overcome the toxicity issue produced from lead-based compounds. Various methods have been used to produce bismuth-layered compounds such as solid state reaction, hydrothermal, sol gel and soft combustion techniques. All of these techniques have advantages and disadvantages. In early stage, $Bi_4Ti_3O_{12}$ (BIT) has been widely studied. However, serious issues of low remanent polarization, high leakage current, low fatigue resistance and high processing temperature are obstacles to practical applications. Therefore, various dopants have been used to modify the properties. This review describes the progress in the synthesis of BIT using various methods. The effects of dopants on properties of BIT are also explained. Selected applications of the compounds are also discussed.

Keywords: Synthesis; Doping; A-site; B-site; Ferroelectric; Application; Properties

1. INTRODUCTION

Bismuth-oxide layered perovskite ferroelectric was discovered by Bengt Aurivillius in the late 1949 [1]. In many cases, all compounds which are derived from the general formula $(Bi_2O_2)^{2+}$ $(A_{x-1}B_xO_{3x+1})^{2-}$ are also known as Aurivillius compounds. Newnham et al. [2] claimed that more than 50 ferroelectrics belong to bismuth-based layered compounds and these could exist from one-layer structures to five-layer structures. Among these, bismuth titanate, ($Bi_4Ti_3O_{12}$ or BIT) is one of the interesting subjects for further discussion. As of today, BIT is described in several terms such as bismuth layered structure ferroelectric, bismuth-based ferroelectric compounds, perovskite-based layered structure or layered bismuth oxide [3, 4]. BIT is derived with respective element and value; $(Bi_2O_2)^{2+}$ $(A_{x-1}B_xO_{3x+1})^{2-}$ where A = Bi, B = Ti and x = 3 to become $(Bi_2O_2)^{2+}$ $(Bi_2Ti_3O_{10})^{2-}$, which also corresponds the basic structure of BIT [5-9]. The layered structure of BIT is

[*]khairunisak@eng.usm.my

characterized by the perovskite-like $(Bi_2Ti_3O_{10})^{2-}$ layers sandwiched between $(Bi_2O_2)^{2+}$ layers along its crystallographic c-axis. BIT has a strong anisotropic property with the lattice constant, *c*-axis larger than *a*- and *b*-axes. Based on this, the lattice parameters of BIT can be written $a = 5.450$ Å, $b = 5.4059$ Å and $c = 32.832$ Å, and $\beta = 90.01$ °.

There is some misunderstanding in the crystal structure of BIT. In previous reports, BIT has a monoclinic system, *Pc*, but in practice the structure is often regarded as orthorhombic as the β-angle is very close to 90° [2, 10]. In contrast, Kim and Jeon [11] reported that the monoclinic system is more suitable than the orthorhombic structure at room temperature. In addition, BIT then turns into tetragonal above the Curie temperature [12]. To date, there are a lot of discussions on this particular compound which the improvement has been extensively carried out towards the development for ferroelectric and piezoelectric applications [13-17].

2. PROPERTIES OF BIT CERAMICS AND THIN FILMS

In general, BIT is known to have several outstanding electrical properties. The specific value for each property is different from one to another due to the differences in processing method, materials sources, and environment. However, most researchers agreed that BIT has high remanent polarization (P_r), low coercive field (E_c), high dielectric constant (ε_r), low dielectric loss (tan δ), high Curie temperature (T_c), high breakdown strength, stable piezoelectric response, etc. With this regard, BIT has been used as essential ceramics and films for ferroelectric random access memory (FRAM) and high-precision piezoelectric applications, micro-electromechanical system (MEMS), tunable high-frequency devices, and integrated photonics, optical displays and pyroelectric devices [4, 18-21]. In addition, the use of such technologies is safe since BIT is a lead-free material.

BIT has been widely prepared either in bulk ceramics or thin films using various methods. Bulk BIT has been produced using conventional ball milling, mechanical activation, sol-gel, hydrothermal, molten salt synthesis, chemical synthesis, precipitation, citrate, urea, self-propagation high temperature synthesis, metalorganic decomposition, microemulsion methods etc. [6, 7, 9, 12, 14, 15, 18-20, 22-65]. On the other hand, BIT thin film has been deposited using chemical vapor deposition (CVD), metal-organic chemical vapor deposition (MOCVD), chemical solution deposition (CSD), rf magnetron sputtering, spin-coating technique, sol-gel, polymeric precursor method etc. [13, 66-89].

The conventional ball milling or mixed oxide route often results in high agglomeration and compositional inhomogeneity of powders because of high calcination temperature and repeated grinding. Consequently, the sinterability of BIT derived from the conventional solid-state reaction is poor [19, 29]. As an alternative, several methods from mechanosynthesis and wet-chemical synthesis have been used to solve the conventional issues.

The mechanical activation method is superior compared to the conventional solid-state reaction for several reasons. This technique uses low-cost and widely available oxides as starting materials and skips the calcination step at an intermediate temperature, leading to a simplified process. Furthermore, the mechanically derived powders have higher sinterability than those powders synthesized by the conventional ball milling [22, 30-33, 38, 39]. In addition, the wet chemical synthesis is described into several ways such as sol-gel, hydrothermal, molten salt, chemical synthesis, precipitation, microemulsion methods and etc. These methods are beneficial to reduce the calcination temperature. In addition, these methods lead to improvement in the reactivity of the raw materials and homogeneity of the composition, leading to a decrease in the calcination temperature [23].

Deposition process of thin film is generally divided into two major process; physical vapor deposition (PVD) and chemical vapor deposition methods (CVD). CVD is favourable owing to its capability to produce a high quality thin film compared to PVD. Commonly used techniques for depositing ferroelectric thin films including metal organic chemical vapor deposition (MOCVD), sputtering, and sol-gel methods. Each

technique has merits and drawbacks. For instance MOCVD can be used for large-scale production, but elevated growing temperature is required for cracking the metal-organic (MO) source. Sol-gel method is the simplest method to produce thin films. Sol-gel process involves hydrolysis and polycondensation of relevant molecular precursors. Sol-gel method also offers several advantages including pre- and post-deposition at low temperature, easier compositional control and better uniformity of the films, economical compared to CVD and PVD techniques [81].

Regardless of the method by which they are formed, the process must be economical and the resulted doped BIT must exhibit the following characteristics: (a) high degree of crystallinity and purity, (b) narrow particles size distribution, (c) controlled composition stoichiometries, (d) good electrical properties, (e) excellent adhesion and (f) good deposition coverage. Table 1 shows the comparison of processing parameters from BIT ceramics which were prepared by various methods.

Subbarao [6, 9] prepared the BIT ceramics using the solid state reaction and sintered from 1000 to 1250°C to achieve the theoretical density of about 80%. Macedo et al. [40, 91, 92] reported that the laser sintered BIT ceramics reach 98 to 99% density at significantly lower temperature than that registered for typical conventional process. In their works, the samples were heated up to 350°C at a heating rate of about 50°C min^{-1} with maximum power, P_{max} 10 to 30 W. Watcharapasorn et al. [48] sintered the BIT samples at 1150°C at various sintering times; 4, 10, 24 and 48 h. It was found that the relative density (91 – 94 %) did not vary much with sintering time. According to Kong et al. [38] the reduction in density is believed to be a result of the formation of the plate-like grains. Additionally, high density is needed to produce a better remanent polarization, P_r with low coercive field, E_c. Macedo et al. [40, 92] claimed that P_r was significantly increased with increasing density, reaching $P_r = 6.5$ μC/cm^2. Moreover, the variation in microstructure and grain size is an important factor to determine other electrical properties such as dielectric constant, dissipation factor, piezoelectric coupling coefficient, pyroelectric coefficient, electrical conductivity and so forth.

Table 1. Comparison of processing parameters from BIT ceramics prepared by various methods.

Methods	Calcination, °C	Sintering, °C	Density, %	Remanent polarization, Pr (μC/cm2)	Coercive field, Ec (kV/cm)	References
Conventional	750-800	1000 - 1250	80 - 99	5 – 6.5	3 – 23.5	[6, 9, 40, 48, 90-92]
Mech. Act	*1-20 h	750 - 1100	98	0.23	1.8	[22, 31-34, 38, 39, 50, 53, 63]
Sol-gel	300-750	950 - 1150	-	-	-	[23, 41, 57]
Hydrothermal	150-240	800 - 1000	90 - 95	-	-	[24, 26, 29, 37, 44, 49, 93]
Molten salt	600-1100	-	-	-	-	[25, 27]
Chemical syn.	400-900	850 - 1100	93 - 96	-	-	[12, 36, 54]
Precipitation	500-900	900 - 1000	-	-	-	[14, 35, 52]
Microemulsion	800	-	-	-	-	[28]
Combustion	650 – 1000	1050	98	-	-	[51, 61]

*: milling duration

Kong et al. [38] obtained the large P_r (24 $\mu C/cm^2$) and low E_c (11 kV/cm) for BIT ceramics with better density of 98% after low temperature sintering at 850°C for the powder derived from mechanical activation technique. Stojanovic et al. [43, 53] reported that the BIT powder can be directly synthesized using high impact milling for about 3 to 12 hours and then sintered at 1000°C for 2 h. Lazarevic et al. [30-34] also reported that similar observation was found in their study on mechanically activated BIT powder. Han et al. [39] stated the formation of BIT phase is highly dependent on the processing parameters particularly the impact energy or milling intensity. Zdujic et al. [63] reported that a mixture of α-Bi_2O_3 transformed to $Bi_2O_2CO_3$ at a milling intensity of ~ 0.49 W/g, which in turn was converted directly into a nanocrystalline BIT phase when the intensity was increased to ~ 2.68 W/g.

For the wet chemical synthesis, a number of authors discussed the properties of BIT synthesized powders. Du et al. [23, 57] used the sol-gel route to synthesize the nanoplate-like BIT powders. They found that BIT began to crystallize before 450°C according to thermal analysis and X-ray diffraction (XRD) patterns. Shi et al. [24] reported that BIT fine powders can be synthesized by hydrothermal method at 240°C. They also added that the formation of BIT is dependent on the content of mineralizer KOH, the molar ratio of Bi/Ti, reaction time and temperature. Pookmanee et al. [37] stated that the single phase and the particles size of hydrothermally derived BIT fine powders increased with increasing reaction time, as shown in Fig. 1. Yang et al. [29] reported that the crystallinity and the particle size of BIT powders increased with rising reaction temperature and time. Kan et al. [27] studied the molten salt synthesis method to produce BIT platelets in NaCl-KCl and Na_2SO_4-K_2SO_4 fluxes. They found that the calcination temperature of BIT was influenced by homogeneity of the starting materials. Additionally, the crystallization behavior and particles morphology of BIT showed a strong dependence on the types of the salt flux used.

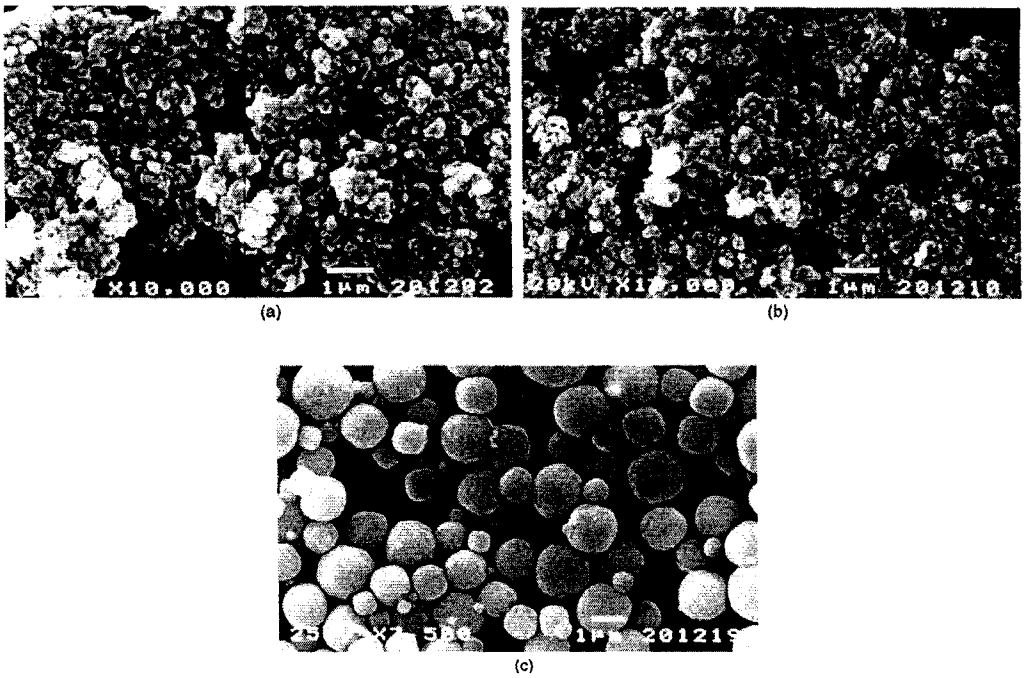

Figure 1. SEM micrographs of BIT powders synthesized by the hydrothermal process at 150°C at different reaction times of (a) 5 h, (b) 10 h, and (c) 15 h [37].

Pookmanee et al. [12] successfully prepared the BIT micro-particles powder using a chemical co-precipitation route with subsequent calcinations process at 500 to 700°C. They found that the average grain size increased with increasing calcination temperature. Pookmanee et al. [36] claimed that BIT single phase was only obtained at 900°C with oxalic acid added. Zhi-hui et al. [54] reported that dispersion of BIT

nanopowders was improved by azeotropic co-precipitation method. Xie et al. [28] compared the particulate properties of BIT derived from co-precipitation method and microemulsion method. They found that the microemulsion method exhibits a narrow size distribution with average particle size of about 35 nm, while co-precipitation method exhibits a wide size distribution with large particle size. Macedo et al. [48, 58] reported that self-propagation high-temperature synthesis (SHS) is beneficial to reduce the processing time in short period. Additionally, the properties of BIT derived from SHS are comparable to that observed for the conventional solid-state reaction.

The physical and ferroelectric properties of BIT thin films are listed in Table 2. A variety of deposition techniques, including sol-gel, metal organic deposition (MOD), rf sputtering, chemical solution deposition (CSD) and polymeric have been used to synthesize BIT films. In general, the deposition technique affects the properties of BIT thin films. As shown in Table 2, the annealing temperature to form crystalline film was in the range of 500 to 700°C, which is lower than the sintering temperature of BIT ceramic. It is essential to obtain the lowest possible processing temperature to comply with silicon technology and to retain the resistance of films. Another important parameter is film thickness whereby it is influenced by several factors such as spin coating parameters, the properties of precursor solution, the deposition temperature and so forth.

Table 2. Physical and ferroelectric properties of BIT thin films.

Deposition technique	Substrate	Annealing, °C	Thickness, nm	Remanent polarization, P_r ($\mu C/cm^2$)	Coercive field, E_c (kV/cm)	References
Sol-gel	Pt/Si	600	400	5	45	[81]
	$Si/SiO_2/Ti/Pt$	700	400	11	160	[82]
	$Pt/Ti/SiO_2/Si$	700	150 - 1000	8 – 13.5	60 - 129	[78, 79]
	Si, Pt/Si	600	400	-	-	[83]
	$Pt/TiO_x/SiO_2/S$	-	300 - 400	-	-	[94]
MOD	Si	600	200	-	-	[76]
	Pt	450	130	15.6	-	[13]
Sputtering	ITO/glass	610 - 700	300 - 700	3.7 - 9.2	50 - 82	[70, 80]
	Si	500	-	2.4	2.3	[69, 74]
CSD	$LaNiO_3/Si$	690	600	7.1	11.27	[88]
	$LaNiO_3/SiO_2/Si$	700	300	10	2.3 V	[71]
	$RuO_2/SiO_2/Si$	700	300	15	1.6 V	[71]
Polymeric	$Pt/Ti/SiO_2/Si$	700	300 - 407	8.5 – 23.7	3.1 V	[68, 71]
	$Pt/Ti/SiO_2/Si$	700	290 (staticair) 240 (oxygen)	15 9	60 40	[75]

Simões et al. [71] investigated the properties of BIT thin films which were deposited on different substrates. They found that substrate with bottom electrodes from $LaNiO_3/SiO_2/Si$ and $RuO_2/SiO_2/Si$ exhibit better ferroelectric properties, high remanent polarization, low drive voltage and good fatigue endurance. For the films deposited on $Pt/SiO_2/Si$ substrates the remanent polarization was low due to stronger contribution of the grain orientation in the *c*-axis direction. Additionally, the grain orientation of films was influenced by annealing temperature [68]. The grain orientation of sol-gel derived films is highly dependent on precursor type, solution synthesis method, film composition, annealing temperature, heat treatment, films thickness and substrates [94].

Kong et al. [78] pointed out that ferroelectric properties are affected by several factors such as grain orientation, properties of the substrate and film thickness. Xu et al. [79] reported that the increase in excess Bi concentration showed a significance increase on the 00*l* and 020/200 crystalline orientation and grain growth. However, the comparison values of P_r, E_c and fatigue behavior with different Bi concentration were not reported. Simões et al. [75] reported that the BIT thin films annealed at different atmosphere also can influence the ferroelectric properties of films. They found that the films annealed in static air were better than the films annealed in oxygen atmosphere.

3. PROPERTIES OF DOPED BIT

There are several reasons why BIT requires further improvement especially for ferroelectric properties. Based on previous reports, BIT has critical drawbacks on its ferroelectric properties such as high leakage current and domain pinning which leads to small remanent polarization and low fatigue endurance [95-98]. All of these limitations are closely related to the vacancies left by Bi^{3+} ions in their structures due to volatilization effect. These can be improved effectively by doping with impurities. The so-called ion doping technique is believed to be an effective method to improve the ferroelectric properties of BIT [99]. Through this way, BIT doped materials have better chemical stability of the adjacent oxide ions and reduces the concentration of oxygen vacancies [100]. As mentioned earlier, BIT with general formula of $(Bi_2O_2)^{2+}(A_{x-1}B_xO_{3x+1})^{2-}$, where A = Bi; B = Ti, x is the number of BO_6 octahedra in the pseudo-perovskite block (x = 3). The ion doping can be performed at A-site, B-site and A- and B-sites.

3.1 Ion Doping on A-Site

In $Bi_4Ti_3O_{12}$ or BIT, the Bi^{3+} ions can be partially substituted by other elements to enhance the ferroelectric properties. In this regard, the lanthanide elements such as lanthanum (La^{3+}), cerium (Ce^{3+}), praseodymium (Pr^{3+}), neodymium (Nd^{3+}), samarium (Sm^{3+}) and gadolinium (Gd^{3+}) ions have been used as the doping elements in BIT materials. Lanthanide doped BIT has been prepared using the conventional solid-state reaction [90, 101-107], sol-gel method [98, 108-117], hydrolysis method [118, 119], polymeric precursor method [120, 121], chemical solution deposition (CSD) [122-125], metal organic solution decomposition (MOD) [95, 126-130], pulsed laser deposition (PLD) [131], and metalorganic chemical vapor deposition (MOCVD) [132].

The ferroelectric properties of doped BIT ceramics at A-site prepared by the conventional solid-state reaction are listed in Table 3. The effects of La dopants on the ferroelectric properties of BIT was studied by Noguchi et al. [100]. La doping was found to be an effective way to reduce the oxygen vacancies and electron holes. Additionally, the remanent polarization of ceramics can be improved with high-pressure oxygen annealing. Chon et al. [133] investigated the effect of La content in BIT on the grain orientation and ferroelectric properties. It was found that the films with La = 0.85 exhibits large remanent polarization with strong grain orientation in c-axis. The fatigue endurance was also improved with La doping.

Table 3 Electrical properties of doped on A-site BIT ceramics using the conventional solid state reaction

Compound	Sintering temperature, °C	Dielectric constant, ε_r	Remanent polarization, P_r ($\mu C/cm^2$)	Coercive field, E_c (kV/cm)	Fatigue cycle	References
$Bi_{4-x}La_xTi_3O_{12}$	800 - 1310	101-391	5 – 36	30 - 50	6.5×10^{10}	[100, 133-137]

$Bi_{4-x}Nd_xTi_3O_{12}$	950 – 1200	140 - 180	5.5 – 29	24 - 45	-	[90, 96, 104, 138, 139]
$Bi_{4-x}Sm_xTi_3O_{12}$	1100	270	16	70	-	[103]

Kim et al. [90] studied the effect of Nd doping on the crystal structure, dielectric, ferroelectric and other electrical properties. They found that the Nd doping exhibits small grain size, high dielectric constant, low dissipation factor, large remanent polarization, P_r and low conductivity. Mao et al. [104] claimed that maximum remanent polarization, P_r was reached with a certain Nd doping. However, the increase in Nd content in BIT showed the increase in coercive field, E_c and decrease in Curie temperature, T_c as well as decrease in dissipation factor. The improved properties are associated to the decrease of the oxygen vacancy concentration and the increase of mobility of domain wall. Chen et al. [103] studied the effect of Sm doping on the ferroelectric properties and microstructures of BIT. The maximum remanent polarization, P_r of about 16 $\mu C/cm^2$ and minimum coercive field, E_c of about 70 kV/cm was obtained for Sm = 0.8. Additionally, the Curie temperature, T_c was also low with Sm doping.

Table 4 shows the electrical properties of various doping on A-site in BIT thin films. In comparison to Table 3, the annealing temperatures of thin films are much lower than the sintering temperature of ceramics. In comparison to Table 2, the ferroelectric properties of doped BIT thin films are much better than that of BIT thin films. According to significant findings by Park et al. [156], the La doping in BIT thin films exhibits better fatigue endurance than lead zirconate titanate, PZT and lower deposition temperature than strontium bismuth tantalite, SBT.

Bae et al. [98] found that La doping in BIT (La content = 0.75) thin films deposited on $Pt/Ti/SiO_2/Si$ substrate using sol-gel spin coating had grain orientation in *c*-axis that was strongly dependent on the annealing temperature, as shown in Fig. 2. The films thickness of La doping was about 400nm at annealing temperature of 650°C. Additionally, the remanent polarization, P_r, coercive field, E_c and fatigue endurance of La-doped BIT films were about 35 $\mu C/cm^2$, 66 kV/cm and 4.5×10^{10} read/write cycles.

Simões et al. [121] studied the La doping in BIT with various La content (0, 0.25, 0.5, 0.75) in BIT thin films deposited on $Pt/Ti/SiO_2/Si$ substrates using a polymeric precursor solution and spin coating method. They observed the change in grain morphology with La doping. The remanent polarization of La doping was better than that of pure BIT. Simões et al. [140] also found that the La doping improved the leakage current densities. The dielectric and ferroelectric properties of the La-doped BIT thin films were reported strongly affected by pH of the solution [141]. The La doped BIT obtained from acid solution and basic solution showed elongated grains around 200 nm in size and spherical grains around 100 nm in size, respectively.

Table 4. Electrical properties of various doping on A-site BIT thin films.

Compound	Film thick-ness (nm)	Anne aling tem-pera-ture, °C	Dielectric constant, ε_r	Remanent polarization, P_r ($\mu C/cm^2$)	Coercive field, E_c (kV/cm)	Fatigue cycle	References
	320	700	148	20.3	0.99V	-	[140]
	208 - 216	700	83-158	20.6-21.5	0.66-1.09V	-	[121]
$Bi_{4-x}La_xTi_3O_{12}$	275-418	700	-	15-20.2	1.35-1.69V	-	[141]
	400	650	-	35	66	4.5×10^{10}	[98]
	50-500	700	230-280	18-25	52-63	10^8	[142]
	200	750	-	3-9	3.5-4V	10^9	[143]
$Bi_{4-x}Nd_xTi_3O_{12}$	280 –	650	395	10 – 50	60 – 100	4.5×10^{10}	[144]

	300						
	300	650	-	35	-	-	[95]
	20	680	-	19	-	-	[124]
	120	750	-	22	80	10^{11}	[145
	500	700	-	60	150	-	[116]
	600	750	343, a-axis 331, random 218, c-axis	19.5 10 6.5	108 95 108	- - -	[115] [115] [115]
	500	600	-	32	73	10^{10}	[146]
	295	-	177	8.8	86	1.44×10^{10}	[131]
	500	700	-	-	-	-	[127
$Bi_{4-x}Sm_xTi_3O_{12}$	280	680	387	29.5	110	4.5×10^{10}	[147]
	500	700	-	-	-	-	[128]
	370	750	202	15.7	-	-	[125]
$Bi_{4-x}Pr_xTi_3O_{12}$	500-680	650-700	-	31	102	1.5×10^{10}	[148], [149], [150]
	700	800	-	29	58	10^8	[153]
$Bi_{4-x}Y_xTi_3O_{12}$	300-400	700	-	10	-	10^{10}	[154]
	450	700	-	16	140	-	
		750		7.5	-	10^{10}	[153]
$Bi_{4-x}Ce_xTi_3O_{12}$	220	700	-	9.9	179	7×10^9	[154]
$Bi_{4-x}Gd_xTi_3O_{12}$	360	700	468	37.5	136	4.5×10^{10}	[155]

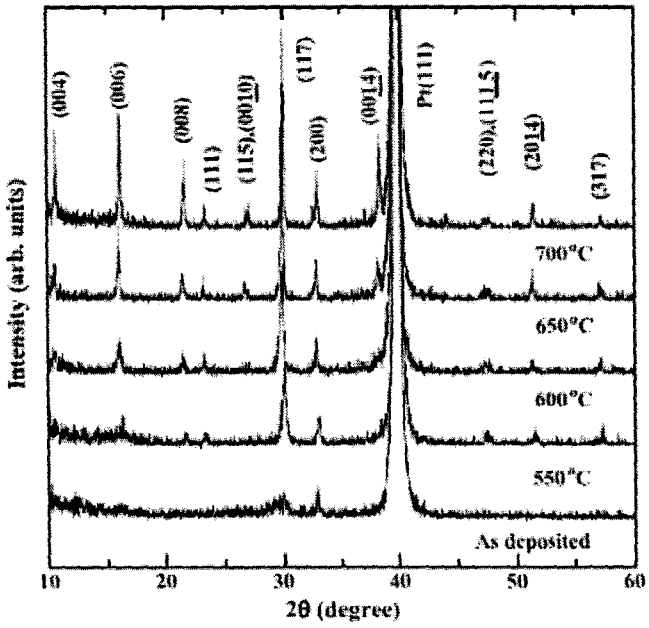

Figure 2. X-ray diffraction patterns of the BLT thin films annealed at different temperatures ranging from 550 to 700°C for 30 min in oxygen [98].

Kao et al. [142] compared the properties of La-doped BIT thin films which were annealed using the conventional thermal annealing (CTA) and rapid thermal annealing (RTA). It was found that the crystallinity, structure, ferroelectric and leakage current properties of films were strongly dependent on the heating rate of

the annealing process. The RTA process showed excellent ferroelectric properties with small leakage current density compared to the CTA process, as shown in Fig. 3.

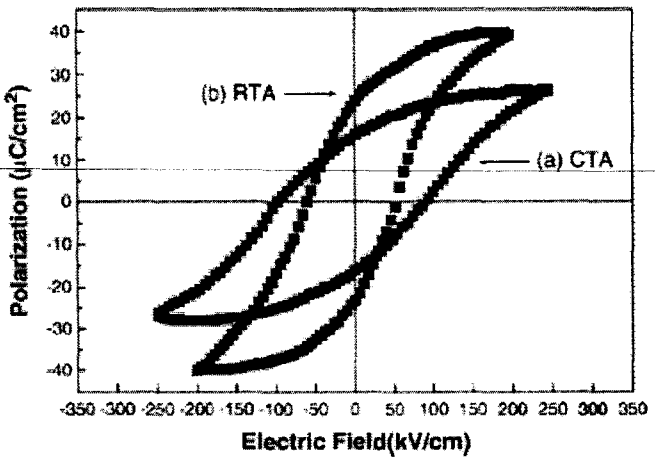

Figure 3. Hysteresis loops of BLT thin films annealed by CTA (a), and RTA methods (b) [142].

The effect of excess Bi_2O_3 content (0%, 2%, 5%, 8%, 10% and 15%) on microstructure and ferroelectric properties of BLT ceramics and thin films was studied by Yunyi et al.[143]. The optimum Bi excess for ceramics and thin films was achieved at 5% and 10% Bi_2O_3, respectively. These optimum values showed the maximum remanent polarization and dielectric constant.

Nd doped BIT has been widely studied by many authors. Xie et al. [145] found that the Nd-doped BIT films exhibits large remanent polarization and small coercive field at high annealing temperature of 750°C. The fatigue endurance of Nd doping showed little changes in polarization up to 10^{11} switching cycles, which were compatible for ferroelectric random access memory, FRAM application. Giridharan and Supriya [95] studied various crystallization parameter for the fabrication of Nd-doped BIT thin films on $Pt/Ti/SiO_2/Si$ using metal organic solution decomposition method (MOCVD) in order to obtain highly *c*-axis oriented and randomly oriented thin films. They found that highly *c*-axis oriented films showed a large remanent polarization. Additionally, the remanent polarization also increases with film thickness.

Lu et al. [115] prepared the polycrystalline Nd-doped BIT thin films of *a*-axis preferential orientation and high *c*-axis orientation on $Pt/Ti/SiO_2/Si$ substrates through a sol-gel method. They found that the ferroelectric and dielectric properties were strongly dependent on the film orientation. Chen et al. [124] studied the difference in crystallization layers of Nd-doped BIT thin films deposited on Pt electrodes using chemical solution deposition (CSD). They found that films prepared by the layer-by-layer crystallization were dominated by *a*-axis-oriented grains and showed high remanent polarization. In contrast, Zhang et al. [131] reported that highly *c*-axis of Nd-doped BIT thin films could enhance the remanent polarization and reduce the coercive field with better fatigue behavior. Chon et al. [144] also found that the maximum remanent polarization was obtained with *c*-axis orientation instead of the a-axis orientation.

Zhong and Shiosaki [157] reported that higher annealing temperature could enhance the intensities of (00*l*) reflections. Similar investigation was also found in other study in which a drastic change of crystallization behavior of films from non-*c*-axis to *c*-axis oriented resulting from high annealing temperature [123]. Both studies suggested that the *c*-axis orientation is significantly governed by the anisotropic growth of BIT grains. In addition, the interfacial energy of *c*-axis is low thus the nucleation of *c*-axis oriented grains would be dominant at high annealing temperature.

Hu et al. [125] studied Sm-doped BIT thin films deposited on $Pt/TiO_x/SiO_2/Si$ substrates using chemical solution deposition (CSD) and pulsed laser deposition (PLD) at various annealing temperatures and 700°C,

respectively. They found that crystallinity, dielectric, ferroelectric and leakage current properties were strongly dependent on the annealing temperature. The remanent polarization, coercive field and leakage current were found better in PLD-grown films. However, both films obtained from CSD and PLD showed fatigue-free behavior up to 10^9 read/write switching cycles.

Liu et al. [127-130] studied different parameters of Sm-doping in BIT thin films. The prepared films were deposited on *n*-type Si (100) substrates using metalorganic decomposition (MOCVD) with subsequent annealing at 700°C. They concluded that the crystallinity of the films increased with increasing annealing temperature. Additionally, the structural distortion could change with Sm content, which could be explained in terms of ionic radius and atomic mass of Sm ions. However, the measurement on ferroelectric properties was not reported. Chon et al. [147] studied the fatigue-free and highly *c*-axis oriented Sm-doped BIT thin films deposited on $Pt/TiO_2/SiO_2/Si$ substrates using metalorganic sol decomposition method. They claimed that the prepared films showed the improved values of the remanent polarization and the nonvolatile charge compared to La-doped BIT films. This was due to the larger distortion was obtained in Sm-doped BIT than La-doped BIT. Hu et al. [125] stated that the degree of enhancement of remanent polarization, P_r in BIT dependent on the extent distortion in the oxygen octahedral within the perovskite block, which was also governed by the difference between ionic size of Bi^{3+} and the doping lanthanide ion.

The improvement in ferroelectric properties could also be performed by other lanthanide elements such as Pr, Y, Ce and Gd as shown in Table 4. In Pr doping, the increase in remanent polarization was found due to randomly oriented films [148, 149]. In Y and Ce doping, the improved ferroelectric properties were attributed to the enhanced degree of (117) orientation [151, 154, 158]. In Gd doping, the increase in annealing temperature from 400 to 700°C showed a highly *c*-axis-oriented preferential growth with a minor fraction of (117) orientation. Thus, the observed *c*-axis-oriented preferential growth of films exhibits the remanent polarization, P_r of about 37.5μC/cm^2, which was significantly higher than that for the highly *c*-axis-oriented La-doped BIT [157].

3.2 Ion Doping on B-Site

In previous section, the trivalent cations were doped at A-site or Bi^{3+} in order to improve the ferroelectric properties of BIT materials. In this section, the ion doping on B-site or Ti^{4+} ions will be discussed. The donor cations from group V (Nb^{5+}, Sb^{5+}, Ta^{5+}) and group VI (e.g. W^{6+}) were used as doping elements for Ti^{4+} at B-site [118]. This technique was preferred to enhance the ferroelectric properties and other electrical properties. Table 5 lists the electrical properties of various donor cations for ion doping on B-site.

Table 5. Electrical properties of ion doping on B-site.

Donor cations	Annealing temperature, °C	Dielectric constant, ε_r	Remanent polarization, P_r (μC/cm^2	Coercive field, E_c (kV/cm)	Fatigue cycle	References
Zr	700 - 950	204 - 493	0.95 – 14.8	7.3 V	1 x 10^8 - 7.22 x 10^9	[159-161]
Mn	700	-	38	25	-	[162]
Nb	500 - 1050	110	3.5 - 14	2.5 V, 55	4.5 x 10^{10}	[163-165]
V	900-950	-	6	32.5	-	[166]
W	700	-	10 – 17.5	45 -160	4.5 - 8 x 10^{10}	[167-169]

Zhang et al. [159] studied the thin films of B-site substituted BIT by various content of Zr deposited on $Pt/Ti/SiO_2/Si$ substrates by pulsed laser deposition (PLD). The remanent polarization was dependent on the Zr

content and the vibration modes of the TiO_6 octahedral weaken greatly. The maximum remanent polarization, P_r was achieved at 14.8 $\mu C/cm^2$ with Zr = 0.2 mol%. Further increase in Zr content resulted in the decrease of remanent polarization. Furthermore, the 0.2 mol% of Zr doping could not improve the fatigue resistance of films.

Du et al. [160] also studied the ceramics of B-site doped BIT by Zr with various content prepared by solid state reaction method. They found that the decrease in remanent polarization of ceramics was due to the hybridization effect instead of the structural distortion. This finding was contradicted to other studies whereby the increase in remanent polarization was attributed to the increase in structural distortion [125]. Additionally, the Zr doping could not decrease oxygen vacancies in BIT ceramics indicating low fatigue resistance.

Kim et al. [165] reported that Nb doping could reduce the oxygen vacancies and enhance ferroelectric properties of BIT films. Additionally, the fatigue behavior of Nb doping could retain the polarization up to 4.5 x 10^{10} cycles. Noguchi et al. [162] found that Mn doping could suppress the leakage current and enhance the polarization properties. Tang et al. [166] studied the properties of BIT with V^{5+} ion doping. They found that the lattice vibration of BIT became weaker with V content. The Curie temperature showed a slight decrease with increasing V content. Furthermore, the sintering behavior was also improved with V doping. The remanent polarization and coercive field were better in V doped BIT compared to undoped BIT. Li et al. [170] studied the effect of different donor dopants with various valences. They found that the increase in remanent polarization was not really dependent on the ionic radius and concentration of oxygen vacancy. However, the decrease in oxygen vacancy and domain pinning effect were important parameters to control the fatigue behavior.

3.3 Ion Doping an A- and B-Sites

Recently, it was reported that ion doping on A- and B-sites in BIT showed a good ferroelectric properties [171-178]. In the case of both doping, the Nd and Mn were partially used in BIT to investigate their effect on microstructure, dielectric and ferroelectric properties of films [171, 176]. It was found that the grain of Nd/Mn doped BIT had different shape and the grain size becomes smaller compared to those of Nd doping, as presented in Fig. 4. The prepared films were dominated with (117) and (00*l*) preferred orientation in polycrystalline structures. The Mn content affected the electrical properties of films such as high remanent polarization, dielectric tunability and dielectric constant and low in coercive field, dissipation factor and leakage current density. Additionally, the Nd/Mn doping exhibited good fatigue properties up to 1.5 x 10^{10} switching cycles.

Zhong et al. [173] reported that Nd/Zr co-doping exhibited greater ferroelectric properties compared to Nd doping. In other reports, the La/Zr doping in BIT thin film could enhance the remanent polarization with better fatigue resistance [174, 179]. Compared to Zr doping, the fatigue endurance was improved with La/Zr doping at low concentration content. However, further increased in Zr content resulted in the decrease of remanent polarization with low fatigue resistant. Additionally, the oxygen vacancy was the predominant factor to determine the ferroelectric fatigue. Uchida et al. [175] compared the properties of BIT with Nd doping, La doping and Nd/V doping. They found that V^{5+} ion doping could enhance the remanent polarization. The coercive field of Nd/V doping was comparable with those of Nd and La doping. Lee et al. [177] also investigated the dielectric and ferroelectric properties of La, Nd and V doping in BIT ceramics. They found that La, Nd, La/V and Nd/V doping could reduce the leakage current density in the high electric field region. Hu et al. [180] studied the effect of Nd/Nb doping on the electrical properties of the BIT ceramics. The remanent polarization, piezoelectric coefficient, and pyroelectric coefficient increased with Nb doping, while dielectric constant, coercive field and leakage current density decreased.

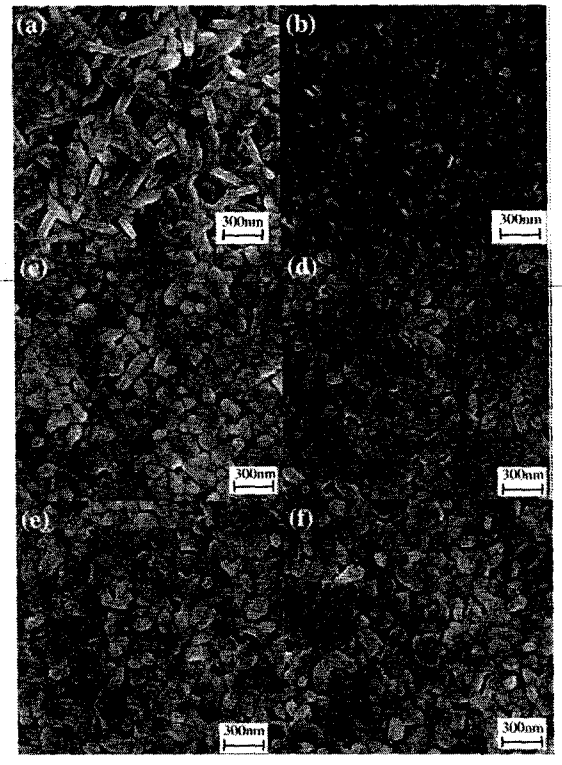

Figure 4. Surface morphologies of (a) BNT, (b) BNTM005, (c) BNTM01, (d) BNTM03, (e) BNTM05, and (f) BNTM1 thin films [176].

4. APPLICATION IN MEMORY DEVICES

Dielectric and ferroelectric based on simple perovskite structure and related Aurivillius-phase layered structure perovskite serves important functions for memory devices applications. Memory devices are generally used in various electronic applications such as cellular phones, note book, internet phone, PDA, MP3 music, and so forth. Among them are known as dynamic random access memory (DRAM), standard random access memory (SRAM), read only memory (ROM), erasable programmable read-only memory (EPROM), flash memory, ferroelectric random access memories (FRAM) etc [181].

Noh et al. [182] described the structure of FRAM was very similar to that of conventional dynamic random access memory (DRAM). They added that in FRAM, the dielectric material in the DRAM capacitor cells was replaced with ferroelectric thin films. In principle, FRAM was designed to store information using the ferroelectric effect in the absence of an applied electric field. Additionally, FRAM exhibited ideal memory properties such as non-volatility, fast access time, and low power consumption [181]. In order to fulfill these requirements, the ferroelectric properties of ceramics or thin films must meet certain criteria such as high remanent polarization, low coercive field and good fatigue resistant as well as low leakage current.

In end of 1999, Park et al. [156] successfully found that La-doped BIT thin films not only exhibited good ferroelectric properties but this films could be used to replace the lead-based thin films for similar applications. From 2000 to 2010, there were many studies on bismuth-layered compound and more than thousand of publications were established within that time. Table 6 shows the comparison of ferroelectric properties for specific compounds. Nowadays, most of the study are focusing on different preparation techniques or use other aid elements and compounds in order to enhance the remanent polarization with minimum losses of current and good fatigue endurance.

For example, Chen et al. [183] studied the effect of annealing atmospheres in different conditions including vacuum, ambient atmosphere and oxygen. They suddenly found that the remanent polarization, P_r of films annealed in oxygen atmosphere was higher than those annealed in ambient atmosphere and vacuum. The P_r for corresponding films annealed at oxygen atmosphere were about 29.5 $\mu C/cm^2$ with low coercive field of about 65 kV/cm and free-fatigue up to $\geq 10^{11}$ switching/cycles. Although the obtained values are still lower than other doping elements such as La, Nd, and Gd, the work must still be continued.

Table 6. Comparison ferroelectric properties with specific compound.

Compound	Remanent polarization, P_r ($\mu C/cm^2$)	Coercive field, E_c (kV/cm)	Fatigue cycle	Leakage current density (A/cm^2)	References
$Bi_{3.25}La_{0.75}Ti_3O_{12}$	35	66	4.5×10^{10}	-	[98]
$Bi_{3.44}Nd_{0.56}Ti_3O_{12}$	60	150	-	10^{-7}	[116]
$Bi_{3.54}Nd_{0.46}Ti_3O_{12}$	32	73	10^{10}	-	[146]
$Bi_{3.15}Sm_{0.85}Ti_3O_{12}$	29.5	110	$4.5 \times 10_{10}$	-	[147]
$Bi_{3.4}Pr_{0.6}Ti_3O_{12}$	31	102	1.5×10^{10}	2.1×10^{-6}	[148]
$Bi_{3.2}Y_{0.8}Ti_3O_{12}$	29	58	10^8	4.38×10^{-8}	[151]
$Bi_{3.25}Ce_{0.75}Ti_3O_{12}$	9.9	179	7×10^9	9×10^{-7}	[154]
$Bi_{3.15}Gd_{0.85}Ti_3O_{12}$	37.5	136	4.5×10^{10}	-	[155]
$Bi_4Ti_{2.97}Mn_{0.03}O_{12-\delta}$	38	25	-	$\sim 10^{-8}$	[162]

5. CONCLUSION

In the early stage of work, BIT seems to be essential material in lead-free category for FRAM application. However, it suffers several issues such as small remanent polarization, non-fatigue-free behavior and high leakage current. The ionic doping is the best solution to improve these limitations. There are many processes have been used in previous studies to prepare the BIT and doped-BIT. Both can be formed in different forms; ceramics and thin films. The increase in remanent polarization is strongly dependent on several parameters including processing method, structural distortion, grain orientation and grain size. Free-fatigue behavior and low leakage current that belong to the doped-BIT can be explained in terms of chemical stability of oxygen ions in the perovskite block resulting from the doping effect.

REFERENCES

[1] B. Aurivillius, *Ark. Kemi* 1949, *1*, 463–471.

[2] R. E. Newnham, R. W. Wolfe, J. F. Dorrian, *Materials Research Bulletin* 1971, *6*, 1029-1039.

[3] S. Kojima, A. Hushur, F. Jiang, S. Hamazaki, M. Takashige, M. S. Jang, S. Shimada, *Journal of Non-Crystalline Solids* 2001, *293-295*, 250-254.

[4] J. Hou, R. V. Kumar, Y. Qu, D. Krsmanovic, *Journal of Nanoparticle Research 12*, 563-571.

[5] L. G. Van Uitert, L. Egerton, *Journal of Applied Physics* 1961, *32*, 959.

[6] E. C. Subbarao, *Physical Review* 1961, *122*, 804-807.

[7] C. H. Hervoches, P. Lightfoot, *Chemistry of Materials* 1999, *11*, 3359-3364.

[8] R. A. Armstrong, R. E. Newnham, *Materials Research Bulletin* 1972, *7*, 1025-1034.

[9] E. C. Subbarao, *Journal of Physics and Chemistry of Solids* 1962, *23*, 665-676.

[10] M. VehkamÃ¤ki, T. HatanpÃ¤Ã¤, M. Kemell, M. Ritala, M. LeskelÃ¤, *Chemistry of Materials* 2006, *18*, 3883-3888.
[11] Y. I. Kim, M. K. Jeon, *Materials Letters* 2004, *58*, 1889-1893.
[12] P. Pookmanee, P. Boonphayak, S. Phanichphant, *Ceramics International* 2004, *30*, 1917-1919.
[13] K. H. Xue, J. Celinska, C. A. Paz De Araujo, *Applied Physics Letters* 2009, *95*.
[14] P. Pookmanee, S. Phanichphant, *Journal of Ceramic Processing Research* 2009, *10*, 448-452.
[15] Y. Noguchi, T. Goto, M. Miyayama, A. Hoshikawa, T. Kamiyama, *Journal of Electroceramics* 2008, *21*, 49-54.
[16] C. M. Wang, J. F. Wang, L. M. Zheng, M. L. Zhao, C. L. Wang, *Materials Science and Engineering: B* 2010, *171*, 79-85.
[17] Z. Xu, R. Chu, J. Hao, Y. Zhang, G. Li, Q. Yin, *Physica B: Condensed Matter* 2009, *404*, 2045-2046.
[18] A. M. Umabala, M. Suresh, A. V. Prasadarao, *Materials Letters* 2000, *44*, 175-180.
[19] S. H. Ng, J. Xue, J. Wang, *Journal of the American Ceramic Society* 2002, *85*, 2660-2665.
[20] W. F. Su, J. F. Lee, M. Y. Chen, R. M. Ho, *Journal of Materials Research* 2004, *19*, 2343-2348.
[21] C. A. P. A. Z. De Araujo, J. Cuchiaro, L. McMillan, M. Scott, J. Scott, 1995.
[22] B. D. StojanoviÄ‡, C. O. Paiva-Santos, M. Cilense, C. JovalekiÄ‡, Z. Z. LazareviÄ‡, *Materials Research Bulletin* 2008, *43*, 1743-1753.
[23] X. Du, Y. Xu, H. Ma, J. Wang, X. Li, *Journal of the American Ceramic Society* 2008, *91*, 2079-2082.
[24] Y. Shi, C. Cao, S. Feng, *Materials Letters* 2000, *46*, 270-273.
[25] H. Hao, H. X. Liu, Y. Liu, M. H. Cao, S. X. Ouyang, *Journal of the American Ceramic Society* 2007, *90*, 1659-1662.
[26] L. Xie, J. Ma, P. Wu, H. Tian, Z. Zhao, J. Zhou, Y. Hu, Y. Wang, J. Tao, X. Zhu, *Materials Research Bulletin* 2007, *42*, 389-393.
[27] Y. Kan, X. Jin, P. Wang, Y. Li, Y.-B. Cheng, D. Yan, *Materials Research Bulletin* 2003, *38*, 567-576.
[28] L. Xie, J. Ma, Z. Zhao, H. Tian, J. Zhou, Y. Wang, J. Tao, X. Zhu, *Colloids and Surfaces A: Physicochemical and Engineering Aspects* 2006, *280*, 232-236.
[29] Q. Yang, Y. Li, Q. Yin, P. Wang, Y. B. Cheng, *Journal of the European Ceramic Society* 2003, *23*, 161-166.
[30] Z. Å. LazareviÄ‡, B. D. StojanoviÄ‡, C. O. Paiva-Santos, N. Å. RomÄ□eviÄ‡, J. A. Varela, *Science of Sintering* 2007, *39*, 267-272.
[31] Z. Å. LazareviÄ‡, B. D. StojanoviÄ‡, M. J. RomÄ□eviÄ‡, N. Å. RomÄ□eviÄ‡, *Science of Sintering* 2009, *41*, 19-26.
[32] Z. Å. LazareviÄ‡, N. Å. RomÄ□eviÄ‡, M. TodoroviÄ‡, B. D. StojanoviÄ‡, *Science of Sintering* 2007, *39*, 177-184.
[33] Z. Å. LazareviÄ‡, B. D. StojanoviÄ‡, C. O. Paiva-Santos, N. Å. RomÄ□eviÄ‡, *Ferroelectrics* 2008, *368*, 154-162.
[34] Z. LazareviÄ‡, B. StojanoviÄ‡, M. RomÄ□eviÄ‡, M. MitriÄ‡, C. JovalekiÄ‡, N. RomÄ□eviÄ‡, *Journal of Alloys and Compounds* 2008, *453*, 499-502.
[35] T. Thongtem, S. Thongtem, *Ceramics International* 2004, *30*, 1463-1470.
[36] P. Pookmanee, *Journal of Ceramic Processing Research* 2008, *9*, 30-33.
[37] P. Pookmanee, P. Uriwilast, S. Phanichpant, *Ceramics International* 2004, *30*, 1913-1915.
[38] L. B. Kong, J. Ma, W. Zhu, O. K. Tan, *Materials Letters* 2001, *51*, 108-114.
[39] K. Han, T. Ko, *Journal of Alloys and Compounds* 2009, *473*, 490-495.
[40] Z. S. Macedo, M. H. Lente, J. A. Eiras, A. C. Hernandes, *Journal of Physics Condensed Matter* 2004, *16*, 2811-2818.
[41] A. V. P. Rao, A. I. Robin, S. Komarneni, *Materials Letters* 1996, *28*, 469-473.
[42] M. AlguerÃ³, P. Ferrer, E. Vila, J. E. Iglesias, A. Castro, *Journal of the American Ceramic Society* 2006, *89*, 3340-3347.

[43] B. D. Stojanovic, A. Z. Simoes, C. O. Paiva-Santos, C. Quinelato, E. Longo, J. A. Varela, *Ceramics International* 2006, *32*, 707-712.
[44] T. Kojima, I. Yoshida, N. Uekawa, K. Kakegawa, *Journal of the European Ceramic Society* 2009, *29*, 431-437.
[45] C. Jovalekic, M. Zdujic, *Ceramics International 36*, 789-792.
[46] Y. Kan, P. Wang, Y. Li, Y.-B. Cheng, D. Yan, *Journal of the European Ceramic Society* 2003, *23*, 2163-2169.
[47] W. Chen, Y. Kinemuchi, K. Watari, T. Tamura, K. Miwa, *Journal of the American Ceramic Society* 2006, *89*, 490-493.
[48] A. Watcharapasorn, P. Siriprapa, S. Jiansirisomboon, *Journal of the European Ceramic Society 30*, 87-93.
[49] D. Chen, X. Jiao, *Materials Research Bulletin* 2001, *36*, 355-363.
[50] M. G. Navarro-Rojero, J. J. Romero, F. Rubio-Marcos, J. F. Fernandez, *Ceramics International 36*, 1319-1325.
[51] Z. S. Macedo, C. R. Ferrari, A. C. Hernandes, *Journal of the European Ceramic Society* 2004, *24*, 2567-2574.
[52] Y. Kan, P. Wang, Y. Li, Y. B. Cheng, D. Yan, *Materials Letters* 2002, *56*, 910-914.
[53] B. D. Stojanovic, C. O. Paiva-Santos, C. Jovalekic, A. Z. Simoes, F. M. Filho, Z. Lazarevic, J. A. Varela, *Materials Chemistry and Physics* 2006, *96*, 471-476.
[54] C. Zhi-hui, Q. Jun-fu, L. Cheng, D. Jian-ning, Z. Yuan-yuan, *Ceramics International 36*, 241-244.
[55] Y. Du, J. Fang, M. Zhang, J. Hong, Z. Yin, Q. Zhang, *Materials Letters* 2002, *57*, 802-806.
[56] S. Luo, Y. Noguchi, M. Miyayama, T. Kudo, *Materials Research Bulletin* 2001, *36*, 531-540.
[57] X. Du, Y. Xu, H. Ma, J. Wang, X. Li, *Journal of the American Ceramic Society* 2007, *90*, 1382-1385.
[58] M. Anilkumar, S. R. Dhage, V. Ravi, *Materials Letters* 2005, *59*, 514-516.
[59] S. R. Dhage, Y. B. Khollam, S. B. Dhespande, H. S. Potdar, V. Ravi, *Materials Research Bulletin* 2004, *39*, 1993-1998.
[60] R. C. Oliveira, L. S. Cavalcante, J. C. Sczancoski, E. C. Aguiar, J. W. M. Espinosa, J. A. Varela, P. S. Pizani, E. Longo, *Journal of Alloys and Compounds* 2009, *478*, 661-670.
[61] Z. S. Macedo, C. R. Ferrari, A. C. Hernandes, *Powder Technology* 2004, *139*, 175-179.
[62] A. Hardy, D. Mondelaers, G. Vanhoyland, M. K. Van Bael, J. Mullens, L. C. Van Poucke, *Journal of Sol-Gel Science and Technology* 2003, *26*, 1103-1107.
[63] M. ZdujiÄ‡, D. Poleti, C. JovalekiÄ‡, L. KaranoviÄ‡, *Journal of Non-Crystalline Solids* 2006, *352*, 3058-3068.
[64] Z. Z. Lazarevic, N. Z. Romcevic, J. D. Bobic, M. J. Romcevic, Z. Dohcevic-Mitrovic, B. D. Stojanovic, *Journal of Alloys and Compounds* 2009, *486*, 848-852.
[65] W. L. Liu, H. R. Xia, H. Han, X. Q. Wang, *Journal of Crystal Growth* 2004, *269*, 499-504.
[66] J. Schwarzkopf, R. Dirsyte, M. Rossberg, G. Wagner, R. Fornari, *Materials Science and Engineering: B* 2007, *144*, 132-137.
[67] E. B. Araújo, V. B. Nunes, S. I. Zanette, J. A. Eiras, *Materials Letters* 2001, *49*, 108-111.
[68] A. Z. Simões, M. A. Ramirez, C. S. Riccardi, A. Ries, E. Longo, J. A. Varela, *Materials Chemistry and Physics* 2005, *92*, 373-378.
[69] M. Yamaguchi, T. Nagatomo, *Thin Solid Films* 1999, *348*, 294-298.
[70] W. K. Chia, Y. C. Chen, C. F. Yang, *Japanese Journal of Applied Physics, Part 1: Regular Papers and Short Notes and Review Papers* 2006, *45*, 5087-5090.
[71] A. Z. Simoìfes, M. P. Cruz, A. Ries, E. Longo, J. A. Varela, R. Ramesh, *Materials Research Bulletin* 2007, *42*, 975-981.
[72] K. S. Hwang, H. A. Park, B. Soojung, B. A. Kang, Y. H. Kim, *Journal of Sol-Gel Science and Technology* 2002, *23*, 67-72.

[73] K.-S. Hwang, C.-K. Kim, S.-B. Kim, J.-T. Kwon, J.-S. Lee, Y.-H. Yun, Y.-H. Kim, B.-A. Kang, *Surface and Coatings Technology* 2002, *150*, 177-181.
[74] M. Yamaguchi, K. Kawanabe, T. Nagatomo, O. Omoto, *Materials Science and Engineering B* 1996, *41*, 138-142.
[75] A. Z. Simoìfes, C. S. Riccardi, A. H. M. Gonzalez, A. Ries, E. Longo, J. A. Varela, *Materials Research Bulletin* 2007, *42*, 967-974.
[76] H. Gu, D. Bao, S. Wang, D. Gao, A. Kuang, X. Li, *Thin Solid Films* 1996, *283*, 81-83.
[77] X. S. Wang, Y. J. Zhang, L. Y. Zhang, X. Yao, *Applied Physics A: Materials Science and Processing* 1999, *68*, 547-552.
[78] L. B. Kong, J. Ma, *Thin Solid Films* 2000, *379*, 89-93.
[79] W. Xianyu, T. Ko, W. I. Lee, *Integrated Ferroelectrics* 2004, *65*, 183-192.
[80] W.-K. Chia, C.-F. Yang, Y.-C. Chen, *Ceramics International* 2008, *34*, 379-384.
[81] S. Madeswaran, N. V. Giridharan, R. Jayavel, *Materials Chemistry and Physics* 2003, *80*, 23-28.
[82] M. Sedlar, M. Sayer, *Ceramics International* 1996, *22*, 241-247.
[83] N. V. Giridharan, S. Madeswaran, R. Jayavel, *Journal of Crystal Growth* 2002, *237-239*, 468-472.
[84] P. H. Xiang, Y. Kinemuchi, K. Watari, *Journal of the European Ceramic Society* 2007, *27*, 663-667.
[85] H. Funakubo, T. Watanabe, T. Kojima, T. Sakai, Y. Noguchi, M. Miyayama, M. Osada, M. Kakihana, K. Saito, *Journal of Crystal Growth* 2003, *248*, 180-185.
[86] S. Sun, P. Lu, P. A. Fuierer, *Journal of Crystal Growth* 1999, *205*, 177-184.
[87] T. Tsukamoto, A. Kakimi, G. Fujihashi, T. Togami, S. Ando, S. Okamura, *Integrated Ferroelectrics* 1998, *20*, 257-258.
[88] C. Jia, Y. Chen, L. Ding, W. Zhang, *Applied Surface Science* 2007, *253*, 9506-9512.
[89] F. Soares-Carvalho, P. Thomas, J. P. Mercurio, B. Frit, S. Parola, *Journal of Sol-Gel Science and Technology* 1997, *8*, 759-763.
[90] J. S. Kim, S. Y. Lee, H. J. Lee, C. W. Ahn, I. W. Kim, M. S. Jang, *Journal of Electroceramics* 2008, *21*, 633-636.
[91] Z. S. Macedo, A. C. Hernandes, *Materials Letters* 2005, *59*, 3456-3461.
[92] Z. S. Macedo, A. C. Hernandes, *Materials Letters* 2002, *55*, 217-220.
[93] H. Gu, Z. Hu, Y. Hu, Y. Yuan, J. You, W. Zou, *Colloids and Surfaces A: Physicochemical and Engineering Aspects* 2008, *315*, 294-298.
[94] J. T. Dawley, R. Radspinner, B. J. J. Zelinski, D. R. Uhlmann, *Journal of Sol-Gel Science and Technology* 2001, *20*, 85-93.
[95] N. Giridharan, S. Supriya, *Thin Solid Films* 2008, *516*, 5244-5247.
[96] J. S. Kim, *Integrated Ferroelectrics* 2006, *79*, 139-145.
[97] N. V. Giridharan, M. Subramanian, R. Jayavel, *Applied Physics A: Materials Science and Processing* 2006, *83*, 123-126.
[98] J. C. Bae, S. S. Kim, E. K. Choi, T. K. Song, W. J. Kim, Y. I. Lee, *Thin Solid Films* 2005, *472*, 90-95.
[99] J. ArreguÃ-n-Zavala, M. E. Villafuerte-CastrejÃ³n, F. GonzÃ¡lez, L. Bucio, O. Novelo-Peralta, R. Y. Sato-BerrÃº, J. OcotlÃ¡n-Flores, *Materials Characterization* 2009, *60*, 219-224.
[100] Y. Noguchi, M. Soga, M. Takahashi, M. Miyayama, *Japanese Journal of Applied Physics, Part 1: Regular Papers and Short Notes and Review Papers* 2005, *44*, 6998-7002.
[101] Y. Y. Yao, C. H. Song, P. Bao, D. Su, X. M. Lu, J. S. Zhu, Y. N. Wang, *Journal of Applied Physics* 2004, *95*, 3126-3130.
[102] M. Chen, Z. L. Liu, Y. Wang, C. C. Wang, X. S. Yang, K. L. Yao, *Physica Status Solidi (A) Applied Research* 2003, *200*, 446-450.
[103] M. Chen, Z. L. Liu, Y. Wang, C. C. Wang, X. S. Yang, K. L. Yao, *Physica B: Condensed Matter* 2004, *352*, 61-65.
[104] X. Y. Mao, F. W. Mao, X. B. Chen, *Integrated Ferroelectrics* 2006, *79*, 155-161.

[105] Q. Y. Tang, Y. M. Kan, Y. G. Li, G. J. Zhang, P. L. Wang, *Solid State Communications* 2007, *142*, 1-5.
[106] W. Wang, J. Zhu, X. Y. Mao, X. B. Chen, *Journal of Physics D: Applied Physics* 2006, *39*, 370-374.
[107] J. L. Pineda-Flores, E. Chavira, J. Reyes-Gasga, A. M. GonzaÌ□lez, A. Huanosta-Tera, *Journal of the European Ceramic Society* 2003, *23*, 839-850.
[108] X. Q. Chen, H. Y. Qi, Y. J. Qi, C. J. Lu, *Physics Letters, Section A: General, Atomic and Solid State Physics* 2005, *346*, 204-208.
[109] L. Cui, Y. J. Hu, *Physica B: Condensed Matter* 2009, *404*, 150-153.
[110] S. Fan, F. Zhang, P. Wang, Y. Ren, *Journal of Rare Earths* 2008, *26*, 575-578.
[111] J. Kim, J. K. Kim, S. Heo, H. S. Lee, *Thin Solid Films* 2006, *503*, 60-63.
[112] H. Ke, W. Wang, L. Chen, J. Xu, D. Jia, Z. Lu, Y. Zhou, *Journal of Sol-Gel Science and Technology 53*, 135-140.
[113] D. Y. Guo, M. Y. Li, J. Liu, L. Fu, J. Wang, B. F. Yu, B. Yang, *Materials Science and Engineering B: Solid-State Materials for Advanced Technology* 2007, *142*, 135-138.
[114] T. Tajiri, K. Sumitani, R. Haruki, A. Kohno, *IEEE Transactions on Ultrasonics, Ferroelectrics, and Frequency Control* 2007, *54*, 2574-2577.
[115] C. J. Lu, Y. Qiao, Y. J. Qi, X. Q. Chen, J. S. Zhu, *Applied Physics Letters* 2005, *87*, 1-3.
[116] M. S. Tomar, R. E. Melgarejo, S. P. Singh, *Microelectronics Journal* 2005, *36*, 574-577.
[117] J. C. Bae, S. S. Kim, M. H. Park, K. W. Jang, Y. I. Lee, J. S. Song, *Journal of Crystal Growth* 2004, *268*, 204-209.
[118] Y. M. Kan, G. J. Zhang, P. L. Wang, Y. B. Cheng, *Journal of the European Ceramic Society* 2008, *28*, 1641-1647.
[119] Y. Kan, X. Jin, G. Zhang, P. Wang, Y. B. Cheng, D. Yan, *Journal of Materials Chemistry* 2004, *14*, 3566-3570.
[120] A. Z. SimÃµes, C. Quinelato, A. Ries, B. D. Stojanovic, E. Longo, J. A. Varela, *Materials Chemistry and Physics* 2006, *98*, 481-485.
[121] A. Z. SimÃµes, B. D. Stojanovic, M. A. Zaghete, C. S. Riccardi, A. Ries, F. Moura, E. Longo, J. A. Varela, *Integrated Ferroelectrics* 2004, *60*, 21-31.
[122] B. Yang, D. M. Zhang, B. Zhou, L. H. Huang, C. D. Zheng, Y. Y. Wu, D. Y. Guo, J. Yu, *Journal of Crystal Growth* 2008, *310*, 4511-4515.
[123] Y. C. Chen, C. P. Hsiung, C. Y. Chen, J. Y. Gan, Y. M. Sun, C. P. Lin, *Thin Solid Films* 2006, *513*, 331-337.
[124] Y. C. Chen, Y. M. Sun, C. P. Lin, J. Y. Gan, *Journal of Crystal Growth* 2004, *268*, 210-214.
[125] X. Hu, A. Garg, Z. H. Barber, *Thin Solid Films* 2005, *484*, 188-195.
[126] H. He, J. Huang, L. Cao, L. Wang, *Microelectronic Engineering* 2008, *85*, 508-511.
[127] W. L. Liu, H. R. Xia, H. Han, X. Q. Wang, *Materials Research Bulletin* 2004, *39*, 1215-1221.
[128] W. L. Liu, H. R. Xia, H. Han, X. Q. Wang, *Journal of Crystal Growth* 2004, *264*, 351-356.
[129] W. L. Liu, H. R. Xia, H. Han, X. Q. Wang, *Materials Letters* 2004, *58*, 2997-3000.
[130] W. L. Liu, H. R. Xia, H. Han, X. Q. Wang, *Journal of Solid State Chemistry* 2004, *177*, 3021-3027.
[131] S. T. Zhang, X. J. Zhang, H. W. Cheng, Y. F. Chen, Z. G. Liu, N. B. Ming, X. B. Hu, J. Y. Wang, *Applied Physics Letters* 2003, *83*, 4378-4380.
[132] T. Kojima, T. Sakai, T. Watanabe, H. Funakubo, K. Saito, M. Osada, *Applied Physics Letters* 2002, *80*, 2746.
[133] U. Chon, H. M. Jang, I. W. Park, *Solid State Communications* 2003, *127*, 469-473.
[134] C. Moriyoshi, S. Klmura, Y. Kuroiwa, S. J. Kim, Y. Noguchi, *Journal of the Korean Physical Society* 2009, *55*, 794-798.
[135] M. K. Jeon, Y. I. Kim, S. H. Nahm, S. I. Woo, *Journal of Physical Chemistry B* 2005, *109*, 968-972.
[136] S. Rachna, S. Bhattacharyya, S. M. Gupta, *Materials Science and Engineering B: Solid-State Materials for Advanced Technology 175*, 207-212.

[137] V. B. Santos, J. C. M'Peko, M. Mir, V. R. Mastelaro, A. C. Hernandes, *Journal of the European Ceramic Society* 2009, *29*, 751-756.
[138] T. Goto, Y. Noguchi, M. Soga, M. Miyayama, *Materials Research Bulletin* 2005, *40*, 1044-1051.
[139] S. N. Achary, S. J. Patwe, P. S. R. Krishna, A. B. Shinde, A. K. Tyagi, *Pramana - Journal of Physics* 2008, *71*, 935-940.
[140] A. Z. SimÃµes, C. S. Riccardi, F. Moura, A. Ries, N. L. A. Junior, M. A. Zaghete, B. Stojanovic, E. Longo, J. A. Varela, *Materials Letters* 2004, *58*, 2842-2847.
[141] A. Z. SimÃµes, A. Ries, F. Moura, C. S. Riccardi, E. Longo, J. A. Varela, *Materials Letters* 2005, *59*, 2759-2764.
[142] M. C. Kao, H. Z. Chen, S. L. Young, *Materials Letters* 2008, *62*, 629-632.
[143] W. Yunyi, Y. Jun, Z. Duanming, Z. Chaodan, Y. Bin, W. Yunbo, *Integrated Ferroelectrics* 2008, *98*, 11-25.
[144] U. Chon, J. S. Shim, H. M. Jang, *Solid State Communications* 2004, *129*, 465-468.
[145] D. Xie, Z. Zhang, T. Ren, T. Liu, Y. Dong, L. Liu, *Integrated Ferroelectrics* 2006, *84*, 67-73.
[146] J. S. Kim, S. S. Kim, *Applied Physics A: Materials Science and Processing* 2005, *81*, 1427-1430.
[147] U. Chon, K. B. Kim, H. M. Jang, G. C. Yi, *Applied Physics Letters* 2001, *79*, 3137.
[148] S. S. Kim, W. J. Kim, *Thin Solid Films* 2005, *484*, 303-309.
[149] W. J. Kim, S. S. Kim, M. H. Park, T. G. Ha, J. K. Chung, E. J. Choi, J. K. Kim, G. P. Hong, Y. N. Choi, *Integrated Ferroelectrics* 2006, *81*, 105-112.
[150] C. H. Yang, Z. Wang, F. Y. Jiang, Y. L. Geng, B. Y. Zhu, X. J. Yi, G. P. Ma, J. R. Han, *Journal of Crystal Growth* 2004, *271*, 171-175.
[151] M. C. Kao, H. Z. Chen, S. L. Young, J. B. Shi, C. H. Lin, *Journal of Crystal Growth* 2008, *310*, 2520-2524.
[152] J. Ma, J. Gu, D. Su, X. M. Wu, C. H. Song, W. Li, X. M. Lu, J. S. Zhu, *Thin Solid Films* 2005, *492*, 264-268.
[153] S. W. Kang, S. W. Rhee, *Journal of Materials Science: Materials in Electronics* 2004, *15*, 231-234.
[154] M. Jeon, H. Chung, K. Kim, K. Oh, S. Woo, *Thin Solid Films* 2005, *489*, 1-4.
[155] U. Chon, H. M. Jang, N. S. Shin, J. S. Kim, D. C. Ahn, Y. S. Kim, K. No, *Physica B: Condensed Matter* 2007, *388*, 190-194.
[156] B. H. Park, B. S. Kang, S. D. Bu, T. W. Noh, J. Lee, W. Jo, *Nature* 1999, *401*, 682-684.
[157] N. Zhong, T. Shiosaki, *Materials Letters* 2007, *61*, 2935-2938.
[158] M. C. Kao, H. Z. Chen, S. L. Young, *Materials Letters* 2008, *62*, 3243-3245.
[159] S. T. Zhang, H. W. Cheng, Y. F. Chen, C. H. Song, J. Wang, Y. D. Xia, X. N. Zhao, Z. G. Liu, N. B. Ming, *Solid State Communications* 2004, *130*, 235-239.
[160] C. L. Du, S. T. Zhang, G. X. Cheng, M. H. Lu, Z. B. Gu, J. Wang, Y. F. Chen, *Physica B: Condensed Matter* 2005, *368*, 157-162.
[161] G. Dong-yun, L. Mei-ya, P. Ling, Y. Ben-fang, W. Geng-zhu, Z. Xing-zhong, W. Yun-bo, J. Yu, *Journal of Physics D: Applied Physics* 2006, *39*, 5033.
[162] Y. Noguchi, K. Yamamoto, Y. Kitanaka, M. Miyayama, *Journal of the European Ceramic Society* 2007, *27*, 4081-4084.
[163] J. H. Park, J. S. Bae, H. J. Park, Y. S. Kim, B. E. Jun, B. C. Choi, J. H. Jeong, *Thin Solid Films* 2008, *516*, 5304-5308.
[164] S. H. Hong, S. Trolier-McKinstry, G. L. Messing, *Journal of the American Ceramic Society* 2000, *83*, 113-118.
[165] J. K. Kim, J. Kim, T. K. Song, S. S. Kim, *Thin Solid Films* 2002, *419*, 225-229.
[166] Q. Y. Tang, Y. M. Kan, Y. G. Li, G. J. Zhang, P. L. Wang, *Scripta Materialia* 2006, *54*, 2075-2080.
[167] T. Sakai, T. Watanabe, M. Osada, M. Kakihana, Y. Noguchi, M. Miyayama, H. Funakubo, *Jpn. J. Appl. Phys* 2003, *42*, 2850-2852.

[168] J. K. Kim, T. K. Song, S. S. Kim, J. Kim, *Materials Letters* 2002, *57*, 964-968.
[169] L. N. Zhang, G. R. Li, S. C. Zhao, A. L. Ding, Q. R. Yin, *Integrated Ferroelectrics* 2006, *79*, 253-263.
[170] W. Li, J. Gu, C. Song, D. Su, J. Zhu, *Journal of Applied Physics* 2005, *98*, 1-4.
[171] X. Zhong, J. Wang, L. Sun, C. Tan, X. Zheng, Y. Zhou, *Applied Physics Letters* 2007, *90*, 012906.
[172] C. M. Wang, J. F. Wang, Z. G. Gai, M. L. Zhao, L. Zhao, J. X. Xu, N. Yin, C. J. Zhang, S. Q. Sun, G. Z. Zang, *Materials Chemistry and Physics* 2008, *110*, 402-405.
[173] X. Zhong, J. Wang, M. Liao, L. Sun, H. Shu, C. Tan, Y. Zhou, *Applied Physics Letters* 2007, *90*, 102906.
[174] S. Zhang, Y. Chen, J. Wang, G. Cheng, Z. Liu, N. Ming, *Applied Physics Letters* 2004, *84*, 3660-3662.
[175] H. Uchida, H. Yoshikawa, I. Okada, H. Matsuda, T. Iijima, T. Watanabe, T. Kojima, H. Funakubo, *Applied Physics Letters* 2002, *81*, 2229.
[176] X. L. Zhong, J. B. Wang, M. Liao, C. B. Tan, H. B. Shu, Y. C. Zhou, *Thin Solid Films* 2008, *516*, 8240-8243.
[177] S. Y. Lee, C. W. Ahn, H. J. Lee, S. H. Kang, J. S. Kim, I. W. Kim, K. S. Lee, *Journal of the Korean Physical Society* 2005, *46*, 337-340.
[178] X. Meng, J. Ma, J. Sun, T. Lin, J. Yu, G. Wang, J. Chu, *Applied Physics A* 2004, *78*, 1089-1091.
[179] L. Lv, S. Zhang, J. Wang, Y. Chen, Z. Liu, X. Zhao, G. Cheng, *Journal of Physics D: Applied Physics* 2005, *38*, 1355.
[180] T. Hu, K. Kwok, H. Chan, C. Choy, *Integrated Ferroelectrics* 2006, *79*, 123-130.
[181] K. Kim, D. J. Jung, *Integrated Ferroelectrics* 2008, *96*, 100-111.
[182] T. W. Noh, B. H. Park, B. S. Kang, S. D. Bu, J. Lee, in *Book A new ferroelectric material for use in FRAM: Lanthanum-substituted bismuth titanate*, ed., ed. by Editor, City, 2000, Vol. 1, Chap. Chapter, pp. 237-242.
[183] G. Wu, K. Ruan, T. Liang, X. Chen, D. Bao, *Thin Solid Films* 2009, *517*, 1563-1566.

Chapter 5

SYNTHESIS AND PROPERTIES OF ND-DOPED $Bi_4Ti_3O_{12}$ USING THE SOFT COMBUSTION TECHNIQUE

*A. Umar Al-Amani, S. Sreekantan, M.N. Ahmad Fauzi and K. A. Razak**

School of Materials and Mineral Resources Engineering, Universiti Sains Malaysia, 14300 Nibong Tebal, Penang, Malaysia

ABSTRACT

Nd-doped $Bi_4Ti_3O_{12}$ ceramics, $Bi_{4-x}Nd_xTi_3O_{12}$ (BNT, x = 0, 0.25, 0.50, 0.75 and 1), were prepared using a soft combustion technique and their phase, structure, thermal behavior, grain morphology, dielectric and ferroelectric properties were investigated. The single phase of BIT was successfully obtained at different synthesis temperature, just after combustion took place at 450°C. The thermal analysis confirmed the phase formation with corresponding temperature. The single phase of BIT was also obtained with different Nd doping. It was also shown that Nd doping had a significance change in Raman and Fourier Transform Infrared spectroscopy (FTIR) spectra. Further increase the sintering temperature at 900°C did not show the presence of secondary phase in X-ray diffraction (XRD) pattern. The average grain length and width decreased with Nd content. The Curie temperature of BNT also reduced to 434°C. The remanent polarization, $2P_r$ and coercive field, $2E_c$ of BNT were higher than BIT, whereby the BNT 075 ceramics exhibited the maximum $2P_r$ and $2E_c$ values of about18.4 $\mu C/cm^2$ and 100.6 kV/cm, respectively.

Keywords: Bismuth titanate; Doping; Soft combustion; Lanthanide

INTRODUCTION

Ion doping technique is a preferable way to enhance the electrical properties of many ceramic materials to date. For instance, bismuth titanate ($Bi_4Ti_3O_{12}$ or BIT) has been reported to exhibit low remanent polarization ($2P_r < 10$ $\mu C/cm^2$), high leakage current, low fatigue resistant, high dielectric loss and high electrical conductivity which limit its application in a non-volatile ferroelectric random access memory technology (NvFRAM) [1-3]. In order to solve these issues, many researchers suggested that ferroelectric properties of BIT can be improved by tuning its composition using ion doping technique. Park et al. [4] found that La^{3+} ion successfully doped in BIT film which the film had enhanced P_r (16 – 20 $\mu C/cm^2$), low leakage current (10^{-7} A/cm^2 at 5V) and good fatigue resistant (3 x 10^{10} switching cycles). Kojima et al. [5] reported that the P_r up to 25 $\mu C/cm^2$ with fatigue free after 2 x 10^{10} cycles could be achieved when Nd was partially doped in BIT thin film. Chon et al. [6] reported that the $Bi_{3.15}Sm_{0.85}Ti_3O_{12}$ thin film has high P_r and good fatigue endurance to reach about 29.5 $\mu C/cm^2$ and 4.5 x 10^{10} switching cycles. However, the increase in these values was strongly

*khairunsak@eng.usm.my

dependent on several things such as the annealing temperature and type of annealing, substrate type, bottom electrode, grain orientation, film thickness etc.

Lanthanide doped BIT has been prepared using the conventional solid-state reaction [7-14], sol-gel method [15-25], hydrolysis method [26, 27], polymeric precursor method [28, 29], chemical solution deposition (CSD) [30-33], metal organic solution decomposition (MOD) [34-39], pulsed laser deposition (PLD) [40], and metalorganic chemical vapor deposition (MOCVD) [41]. Each method has own merits and drawbacks. Conventionally prepared powder often uses high calcination temperature with repeated grinding in its process which then produces hard powder and high agglomeration. As an alternative, wet chemical synthesis is beneficial to reduce the calcination temperature and improve the reactivity and homogeneity of the composition. For deposition process of thin films, the PVD, CVD, MOCVD and rf sputtering are costly and the parameter settings are also complex. Sol-gel method is the simplest method to produce thin films. Sol-gel method also offers several advantages including pre- and post-deposition at low temperature, easier compositional control and better uniformity of the films, economical compared to CVD and PVD techniques [3].

To the best of authors' knowledge, very least works on soft combustion technique have been reported. Previously, this technique has been used extensively to prepare a large number of technologically useful oxide materials such as refractories, magnetic, semiconductors, dielectric, catalyst, sensors, phosphors, etc. and none oxide materials such as carbides, nitrides, borides and silicides [42, 43]. This approach is convenient, requires simple experimental set up and save time as well as requires low energy consumption [44]. This is because this technique is characterized by self-sustaining solution combustion synthesis in which the exothermicity of the redox chemical reaction is used to produce the useful materials [45]. Recently, our group used glycine to produce praseodymium-doped bismuth potassium titanate and praseodymium-doped bismuth sodium titanate [46, 47]. There also a study on praseodymium-doped bismuth titanate, however, the fuel agent was not introduced in synthesis process [48]. In the present study, Nd was partially doped in BIT using a novelty low combustion synthesis temperature without calcination process. The prepared samples were investigated in terms of phase formation, thermal behavior, structure, grain morphology, dielectric and ferroelectric properties

EXPERIMENTAL PROCEDURE

Nd-doped BIT ($Bi_{4-x}Nd_xTi_3O_{12}$) were prepared according to the Nd content x= 0, 0.25, 0.50, 0.75 and 1, the samples are denoted as BIT, BNT025, BNT050, BNT075 and BNT100, respectively. Firstly, bismuth nitrate (Bi $(NO_3)_3.5H_2O$, Sigma-Aldrich, 98 %) was dissolved at 40°C in distilled water. Separately, neodymium nitrate (Nd $(NO_3)_3.6H_2O$, Sigma-Aldrich, 99.9 %) was dissolved in distilled water and citric acid ($C_6H_8O_7$, Sigma-Aldrich, 99.5 %) was used as a fuel agent. The neodymium solution together with citric aqueous were added into the bismuth solution with continuous stirring. The titanium solution was prepared from titanium isopropoxide (Ti $[OCH(CH_3)_2]_4$, Aldrich Chemistry, 97 %) which was initially dissolved in 2-methaoxyethanol (Sigma-Aldrich, ≥99). Finally, the titanium solution was slowly added into the bismuth neodymium solution to obtain the precursor solution. This solution was adjusted to pH7 with NH_4OH (29 % solution). The prepared solution was stirred at 60°C for additional 24 h to obtain a homogeneous solution. After that, the temperature was increased to 80°C to form a dried precipitates. The precipitates were gently crushed using an agate mortar pestle. The crushed powder was heated on a hot plate attached with thermocouple for the soft combustion process to take place, and the temperature was recorded ~450°C. The reaction lasted less than 5 min and produced yellowish and greenish powders for BIT and BNT powders, respectively.

Thermal behavior of the dried powder was investigated using Thermogravimetry-Differential Thermal Analysis, TG-DTA (Linesis). Phase identification was investigated by X-Ray Diffraction with Cu-Kα radiation, X-ray diffraction (XRD) (Bruker D8 Advanced). Raman spectrometer (Horiba Jobin-Yvon

HR800UV) and FTIR spectrophotometer (Perkin Elmer) were used to investigate the phonon mode and adsorption band, respectively. The microstructure of the prepared samples was examined using a field emission scanning electron microscopy, FESEM [Zeiss Supra 55VP PGT/HKL]. To investigate the dielectric and ferroelectric properties, the sintered pellet was coated with silver conductive paint and fired at 700°C for 15 min. The capacitance and loss tangent were measured using an Impedance analyzer (Hewlett Packard 4192A LF). The ferroelectric P-E hysteresis loop was investigated using Sawyer-Tower circuit.

RESULT AND DISCUSSION

Fig. 1 shows the XRD patterns of the BIT powder prepared at different synthesis temperatures. The XRD patterns were compared with standard BIT data (JCPDS 73-2181). It was found that a stable phase BIT with layered perovskite structure could be obtained at temperatures between 40 and 60°C. Additionally, the stability of phase formation was also achieved in calcined powder at 500°C. This indicates that the synthesis temperature is sufficient to obtain the single phase of BIT without further calcination process.

Fig. 2 shows the TG and DTA of BIT powder derived at 60°C. As shown in Fig. 2, the TG curve can be divided into two distinct stages. The first weight loss took place at temperature range of 100 - 355°C and second weight loss at temperature range of 480 – 505°C. Above 505°C, the reaction was completed as indicated by linear curve. The total weight loss of about 42.4 % was obtained for BIT powder. The DTA curve showed the endothermic peaks at approximate 60, 130 and 170°C, while exothermic peak at approximate 252, 280, 307 and 501°C. The corresponding endothermic peaks could be ascribed to the vaporization of residual water and organic substances, which correspond to a small weight loss. The exothermic peaks between 183 and 347°C could be explained by decomposition of the nitrate and combustion/pyrolysis of the Bi-Ti organic chelating agent [49]. This is supported by massive weight loss of about 39.8% on the TG curve. A small exothermic peak at final weight loss could be due to phase transition from amorphous oxides to BIT compound.

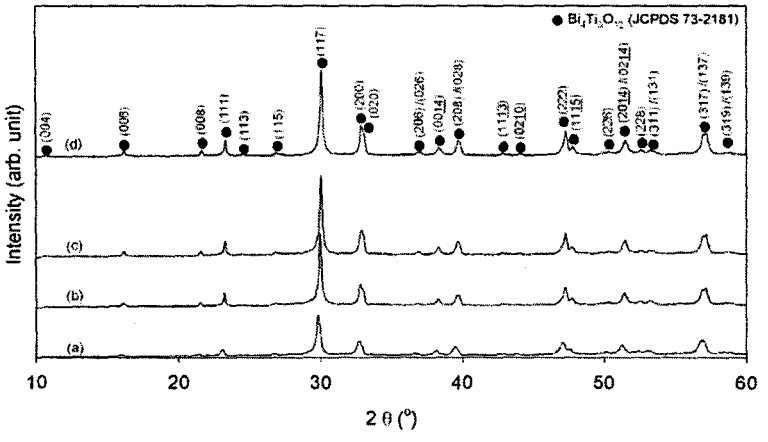

Figure 1. XRD patterns of BIT powder at different synthesis temperatures: (a) 40°C, (b) 50°C, (c) 60°C and (d) calcination at 500°C for (c) samples.

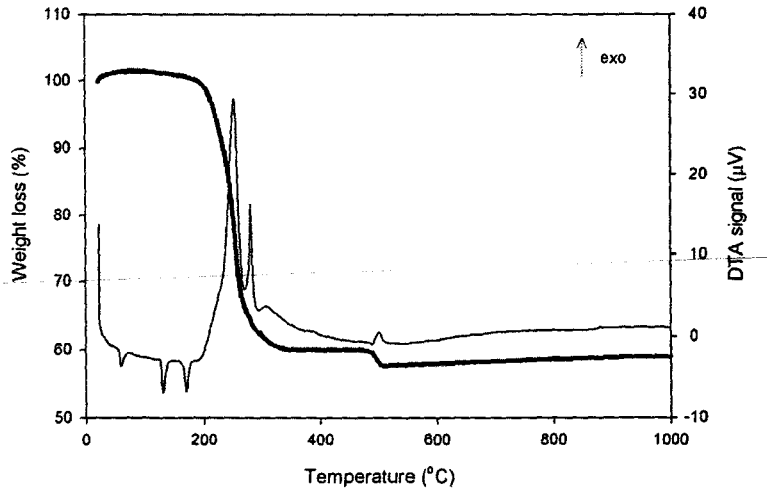

Figure 2. TG and DTA of BIT powder derived from 60°C.

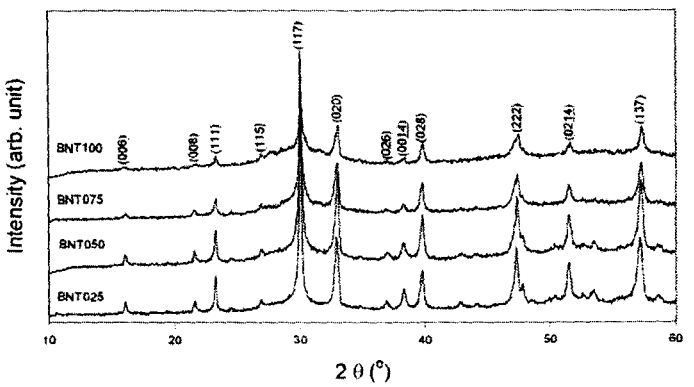

Figure 3. XRD patterns of BNT powders.

Fig. 3 shows the XRD patterns of BNT powders with various contents. The diffraction peaks are indexed using the standard data of BIT phase (JCPDS 73-2181). It was found that a single phase was obtained for all compositions that indicates Nd^{3+} ions were fully dissolved in the BIT solid solution. Additionally, the intensity of diffraction peaks were found to decrease and to have a broaden peak with Nd doping. Broadening of the peak indicates the decrease of crystallite size [47].

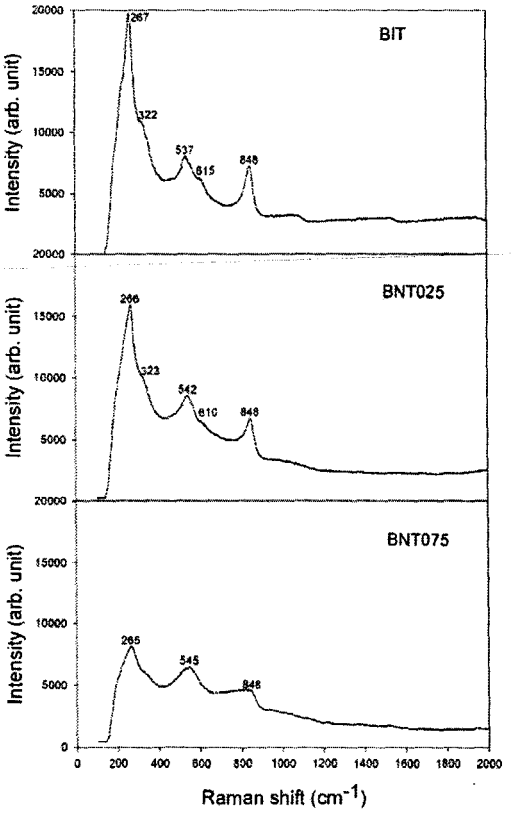

Figure 4. Raman spectrum of BIT, BNT025 and BNT075 at room temperature.

Fig. 4 shows the Raman spectra of BIT, BNT025 and BNT075 at room temperature from 100 to 2000 cm-1. The BIT exhibits a sharp and narrow peak with high intensity in five Raman modes at 267, 322, 537, 615 and 848 cm^{-1}. These modes characteristic changed with Nd content, which corresponded to the decrease in intensity and the increase in peak width. The peaks became broader and only showed three Raman modes as shown in BNT075. The interaction of internal mode of TiO_6 octahedra appeared above 200 cm-1 due to large intragroup binding energy in the octahedra and the much smaller mass of Ti^{4+} ions [50, 51]. In the case of BIT, the mode at 267 cm^{-1} ascribed from the torsional bending of TiO_6 and those at 615 and 848 cm^{-1} assigned to the stretching vibration. The mode at 322 cm^{-1} was from a combination of the stretching and bending vibrations. The mode at 537 cm^{-1} was ascribed to the O-Ti-O stretching vibrations.

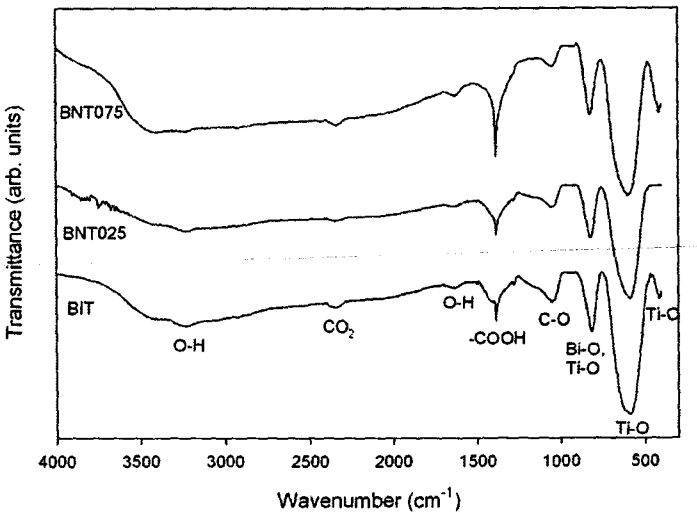

Figure 5. FTIR spectra of BIT, BNT025 and BNT075 at room temperature.

The FTIR spectra of BIT, BNT025 and BNT075 are shown in Fig. 5. Three adsorption bands appeared at 815, 587 and 418 cm^{-1} were ascribed the perovskite-layered structure of BIT. The band at 815 and 587 cm^{-1} belong to the Ti-O stretching vibrations while the peak around 418 cm^{-1} corresponded to the Ti-O bending vibration. The broad peak above 3000 cm^{-1} and a small peak at 1645 cm^{-1} were attributed to the stretching vibration of O-H groups and the bending vibrations of absorbed molecular water and 2-methaoxyethanol, respectively. The weak peak at 2365 cm^{-1} belonged to the stretching vibrations of CO_2, while the stretching vibration for carboxylic group (-COOH) was indicated by the presence of band at 1385 cm^{-1}. The bending vibrations of C-O were detected at 1052 cm^{-1}, indicating that a few organic groups were absorbed on the surface of the powders.

Fig. 6 shows the XRD patterns of BIT and BNT ceramics sintered at 900°C for 3 h. Regardless of the Nd contents, all the ceramic samples were pure phase with no secondary phase. This indicates that the stability of BIT phase with Nd doping at high sintering temperature. Additionally, the intensity of diffraction peaks was found to decrease with increasing Nd content. It also suggested that Nd doping has a significance effect on the crystallite size and lattice parameter of BIT.

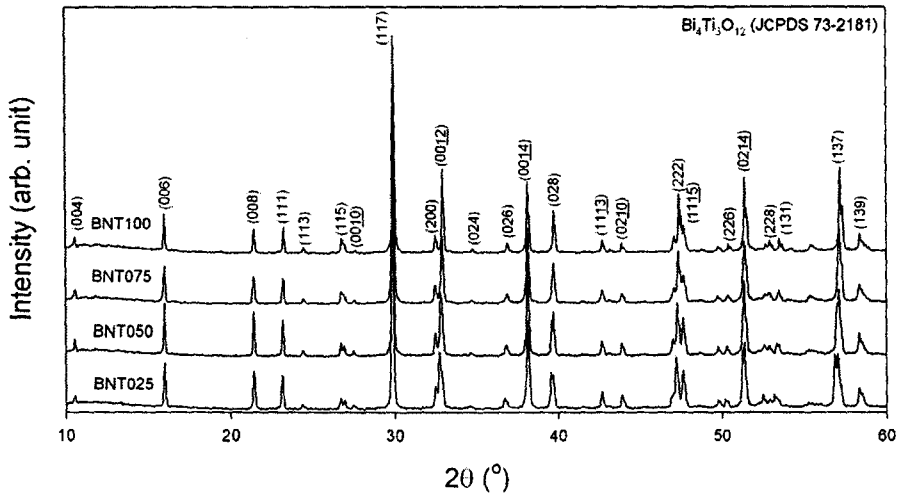

Figure 6. XRD patterns of BNT ceramics sintered at 900°C for 3 h.

Table 1. Average grain length and width of BIT and BNT ceramics.

Compositions	Average length (μm)	Average width (μm)
BIT	10.66	1.57
BNT025	8.14	1.33
BNT050	6.88	1.10
BNT075	6.37	0.90
BNT100	5.19	0.78

Fig. 7 shows the SEM micrographs of BIT and BNT ceramics. All the ceramics with different Nd content exhibited rod-like grains. The grain size of BIT was larger than that of BNT, both in terms of grain length and width. Additionally, the grain size of BNT ceramics decreased with increasing Nd content. The calculated average grain length and thickness is presented in Table 1. This indicates that Nd could act as grain growth inhibitor.

Fig. 8 shows the temperature dependence of the dielectric properties of BIT and BNT075 ceramics, measured at 1 MHz. With increasing temperature, the dielectric constant increases and has a maximum peak at the Curie temperature T_c. The T_c of BIT is 675°C. On the other hand, BNT075 has lower T_c value of 434°C. This indicates that the T_c decreased with Nd doping. Additionally, the dielectric peak broadens with Nd doping, indicating the diffusing of the ferro-paraelectric phase transition. The partial substitution of Nd for Bi in BNT significantly reduced the loss tangent as shown in Fig. 8.

The ferroelectric hysteresis loops of BIT and BNT ceramic measured at the applied field of 75 kV/cm are illustrated in Fig. 9(a). The remanent polarization, $2P_r$ and coercive field, $2E_c$ were plotted in Fig. 9(b). As shown in both figures, the $2P_r$ and $2E_c$ are strongly dependent on Nd content. The $2P_r$ and $2E_c$ increase from 0 to 0.75 and decrease beyond that. Then, the BNT075 ceramics shows the maximum $2P_r$ and $2E_c$ values of 18.4 $\mu C/cm^2$ and 100.6 kV/cm, respectively. These values are higher than that of BIT ceramic of 10.9 $\mu C/cm^2$ and 50.6 kV/cm. This indicates that Nd doping improved ferroelectricity.

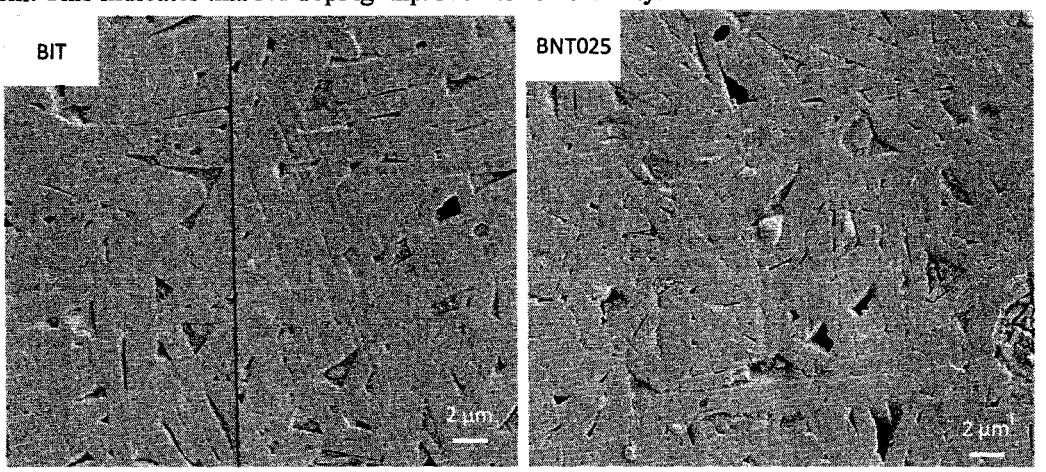

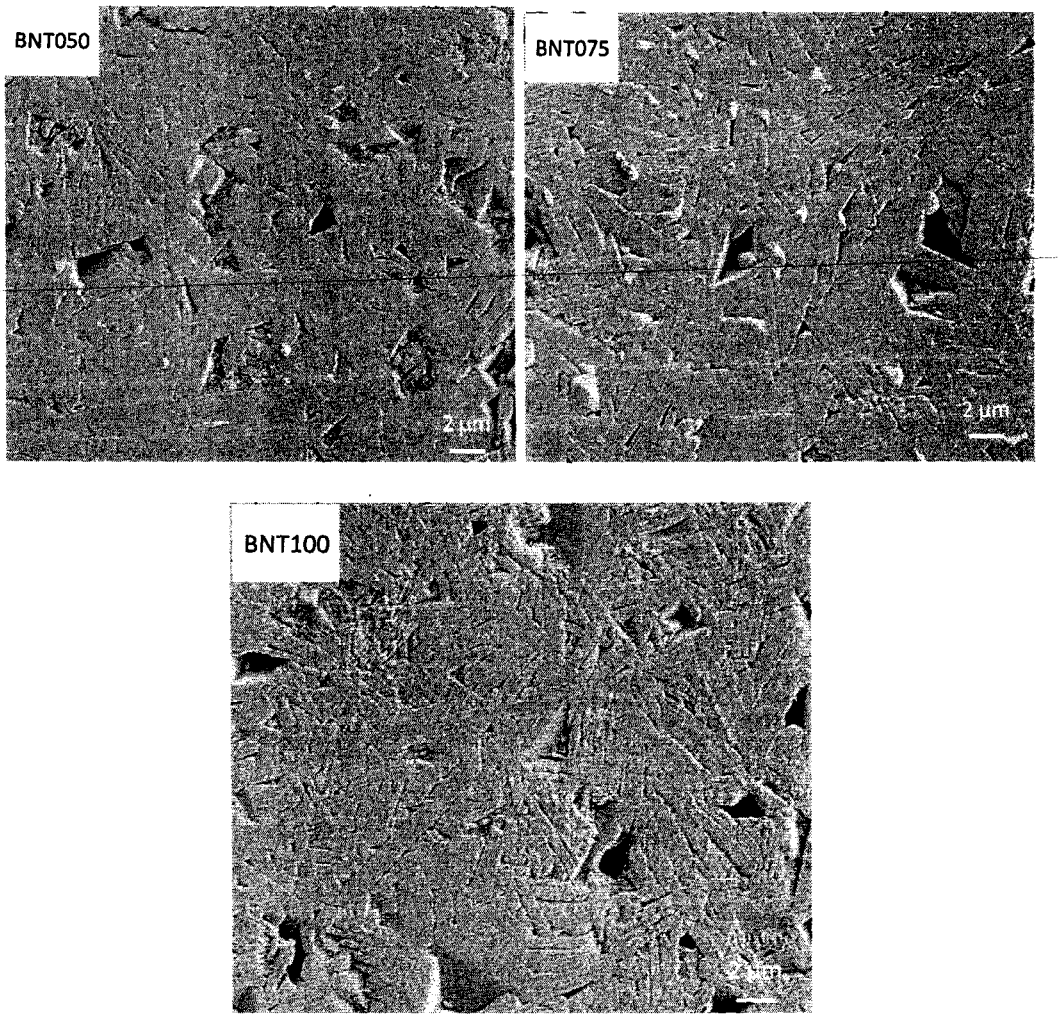

Figure 7. SEM micrographs of BIT and BNT ceramics.

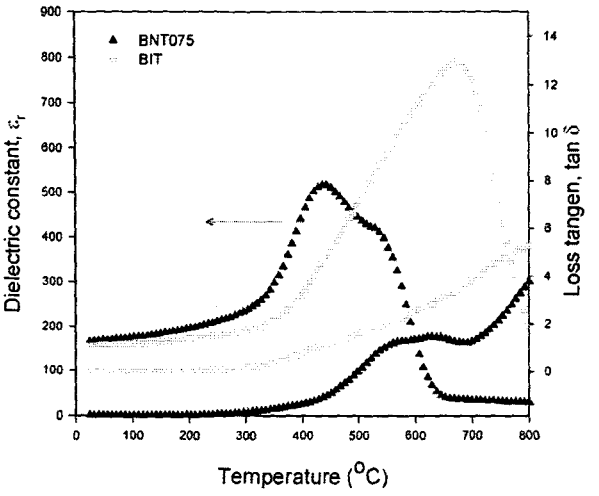

Figure 8. Dielectric properties of BIT and BNT075 as a function of temperature.

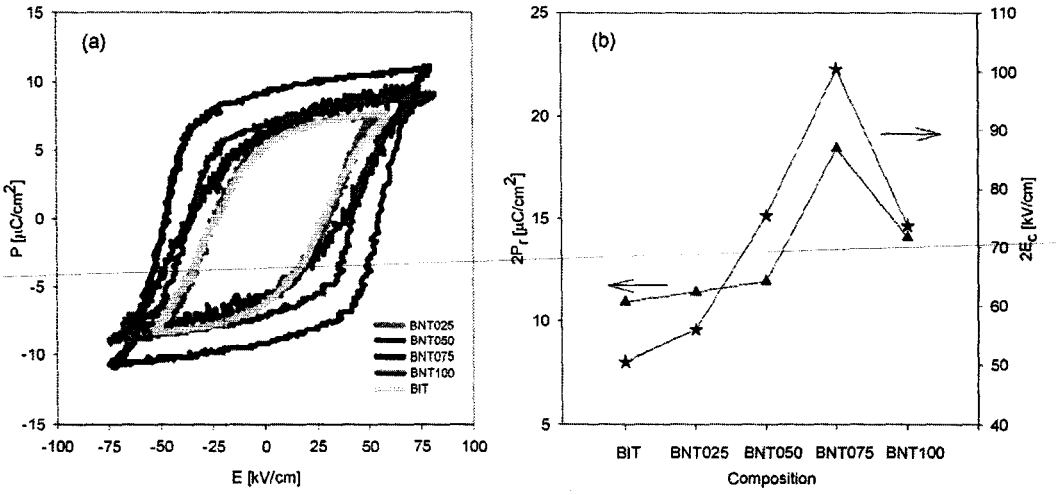

Figure 9. Ferroelectric hysteresis loops of BIT and BNT ceramics.

CONCLUSION

The single phase of BIT was obtained at different synthesis temperatures using the soft combustion technique. Nd-doped $Bi_4Ti_3O_{12}$ was successfully investigated in terms of phase formation, structure, thermal behavior, grain morphology, dielectric and ferroelectric properties. Thermal analysis showed the reaction was highly exothermic and completed at 500°C. The influence of Nd doping on Raman mode and FTIR spectra was clearly observed in both analysis. Additionally, the grain size both the length and width exhibited in small size at higher Nd content. The maximum dielectric peak was found to be broaden and to have a reduced Curie temperature, T_c with Nd doping. The ferroelectric properties was also improved with Nd content.

ACKNOWLEDGMENT

The authors appreciate the technical support provided by School of Materials and Mineral Resources Engineering, Universiti Sains Malaysia, Prof. Uematsu Keizo and Assoc. Prof. Tanaka Satoshi of Nagaoka University of Technology, Japan. This research was supported by USM-RU grant 1001/PBahan/8042018 and 1001/PBahan/811069.

REFERENCES

[1] Sedlar, M., Sayer, M., *Ceramics International,* 22, 3, 1996.
[2] Yamaguchi, M., Kawanabe, K., Nagatomo, T., Omoto, O., *Materials Science and Engineering* B, 41, 1, 1996.
[3] Madeswaran, S., Giridharan, N. V., Jayavel, R., *Materials Chemistry and Physics*, 80, 1, 2003.
[4] Park, B. H., Kang, B. S., Bu, S. D., Noh, T. W., Lee, J., Jo, W., *Nature,* 401, 6754, 1999.
[5] Kojima, T., Sakai, T., Watanabe, T., Funakubo, H., Saito, K., Osada, M., *Applied Physics Letters,* 80, 15, 2002.
[6] Chon, U., Kim, K. B., Jang, H. M., Yi, G. C., *Applied Physics Letters,* 79, 2001.
[7] Yao, Y. Y., Song, C. H., Bao, P., Su, D., Lu, X. M., Zhu, J. S., Wang, Y. N., *Journal of Applied Physics,* 95, 6, 2004.

[8] Kim, J. S., Lee, S. Y., Lee, H. J., Ahn, C. W., Kim, I. W., Jang, M. S., *Journal of Electroceramics,* 21, 1-4 SPEC. ISS., 2008.
[9] Chen, M., Liu, Z. L., Wang, Y., Wang, C. C., Yang, X. S., Yao, K. L., *Physica Status Solidi (A) Applied Research,* 200, 2, 2003.
[10] Chen, M., Liu, Z. L., Wang, Y., Wang, C. C., Yang, X. S., Yao, K. L., *Physica B: Condensed Matter,* 352, 1-4, 2004.
[11] Mao, X. Y., Mao, F. W., Chen, X. B., *Integrated Ferroelectrics,* 79, 1, 2006.
[12] Tang, Q. Y., Kan, Y. M., Li, Y. G., Zhang, G. J., Wang, P. L., *Solid State Communications,* 142, 1-2, 2007.
[13] Wang, W., Zhu, J., Mao, X. Y., Chen, X. B., *Journal of Physics D: Applied Physics,* 39, 2, 2006.
[14] Pineda-Flores, J. L., Chavira, E., Reyes-Gasga, J., Gonzalì□lez, A. M., Huanosta-Tera, A., *Journal of the European Ceramic Society,* 23, 6, 2003.
[15] Chen, X. Q., Qi, H. Y., Qi, Y. J., Lu, C. J., *Physics Letters, Section A: General, Atomic and Solid State Physics,* 346, 1-3, 2005.
[16] Cui, L.,Hu, Y. J., *Physica B: Condensed Matter,* 404, 1, 2009.
[17] Fan, S., Zhang, F., Wang, P., Ren, Y., *Journal of Rare Earths,* 26, 4, 2008.
[18] Kim, J., Kim, J. K., Heo, S., Lee, H. S., *Thin Solid Films,* 503, 1-2, 2006.
[19] Ke, H., Wang, W., Chen, L., Xu, J., Jia, D., Lu, Z., Zhou, Y., *Journal of Sol-Gel Science and Technology,* 53, 1,
[20] Guo, D. Y., Li, M. Y., Liu, J., Fu, L., Wang, J., Yu, B. F., Yang, B., *Materials Science and Engineering B: Solid-State Materials for Advanced Technology,* 142, 2-3, 2007.
[21] Bae, J. C., Kim, S. S., Choi, E. K., Song, T. K., Kim, W. J., Lee, Y. I., *Thin Solid Films,* 472, 1-2, 2005.
[22] Tajiri, T., Sumitani, K., Haruki, R., Kohno, A., *IEEE Transactions on Ultrasonics, Ferroelectrics, and Frequency Control,* 54, 12, 2007.
[23] Lu, C. J., Qiao, Y., Qi, Y. J., Chen, X. Q., Zhu, J. S., *Applied Physics Letters,* 87, 22, 2005.
[24] Tomar, M. S., Melgarejo, R. E., Singh, S. P., *Microelectronics Journal,* 36, 3-6, 2005.
[25] Bae, J. C., Kim, S. S., Park, M. H., Jang, K. W., Lee, Y. I., Song, J. S., *Journal of Crystal Growth,* 268, 1-2, 2004.
[26] Kan, Y. M., Zhang, G. J., Wang, P. L., Cheng, Y. B., *Journal of the European Ceramic Society,* 28, 8, 2008.
[27] Kan, Y., Jin, X., Zhang, G., Wang, P., Cheng, Y. B., Yan, D., *Journal of Materials Chemistry,* 14, 24, 2004.
[28] SimÃµes, A. Z., Quinelato, C., Ries, A., Stojanovic, B. D., Longo, E., Varela, J. A., *Materials Chemistry and Physics,* 98, 2-3, 2006.
[29] SimÃµes, A. Z., Stojanovic, B. D., Zaghete, M. A., Riccardi, C. S., Ries, A., Moura, F., Longo, E., Varela, J. A., *Integrated Ferroelectrics,* 60, 2004.
[30] Yang, B., Zhang, D. M., Zhou, B., Huang, L. H., Zheng, C. D., Wu, Y. Y., Guo, D. Y., Yu, J., *Journal of Crystal Growth,* 310, 21, 2008.
[31] Chen, Y. C., Hsiung, C. P., Chen, C. Y., Gan, J. Y., Sun, Y. M., Lin, C. P., *Thin Solid Films,* 513, 1-2, 2006.
[32] Chen, Y. C., Sun, Y. M., Lin, C. P., Gan, J. Y., *Journal of Crystal Growth,* 268, 1-2, 2004.
[33] Hu, X., Garg, A., Barber, Z. H., *Thin Solid Films,* 484, 1-2, 2005.
[34] Giridharan, N.,Supriya, S., *Thin Solid Films,* 516, 16, 2008.
[35] He, H., Huang, J., Cao, L., Wang, L., *Microelectronic Engineering,* 85, 3, 2008.
[36] Liu, W. L., Xia, H. R., Han, H., Wang, X. Q., *Materials Research Bulletin,* 39, 9, 2004.
[37] Liu, W. L., Xia, H. R., Han, H., Wang, X. Q., *Journal of Crystal Growth,* 264, 1-3, 2004.
[38] Liu, W. L., Xia, H. R., Han, H., Wang, X. Q., *Materials Letters,* 58, 24, 2004.
[39] Liu, W. L., Xia, H. R., Han, H., Wang, X. Q., *Journal of Solid State Chemistry,* 177, 9, 2004.

[40] Zhang, S. T., Zhang, X. J., Cheng, H. W., Chen, Y. F., Liu, Z. G., Ming, N. B., Hu, X. B., Wang, J. Y., *Applied Physics Letters,* 83, 21, 2003.
[41] Kojima, T., Sakai, T., Watanabe, T., Funakubo, H., Saito, K., Osada, M., *Applied Physics Letters,* 80, 2002.
[42] Patil, K. C., Aruna, S. T., Mimani, T., *Current Opinion in Solid State and Materials Science*, 6, 6, 2002.
[43] Luo, S., Tang, Z., Yao, W., Zhang, Z., *Microelectronic Engineering,* 66, 1-4, 2003.
[44] Berger, D., Matei, C., Papa, F., Voicu, G., Fruth, V., *Progress in Solid State Chemistry,* 35, 2-4 SPEC. ISS., 2007.
[45] Patil, K. C., *Bulletin of Materials Science,* 16, 6, 1993.
[46] Ng, C. Y.,Razak, K. A., *Journal of Alloys and Compounds*, 509, 3,
[47] Razak, K. A., Yip, C. J., Sreekantan, S., *Journal of Alloys and Compounds,* 509, 6,
[48] Goh, P. Y., Razak, K. A., Sreekantan, S., *Journal of Alloys and Compounds*, 475, 1-2, 2009.
[49] Du, X., Xu, Y., Ma, H., Wang, J., Li, X., *Journal of the American Ceramic Society*, 90, 5, 2007.
[50] Kojima, S., *Ferroelectrics,* 239, 1-4, 2000.
[51] Zhu, J., Chen, X. B., He, J. H., Shen, J. C., *Journal of Solid State Chemistry*, 178, 9, 2005.

Sintering and Characterization of Rare Earth Doped Bismuth Titanate Ceramics Prepared by Soft Combustion Synthesis

By Umar Al-Amani Azlan, Wanapong Krengpituk, Ahmad Fauzi Mohd Noor, Khairunisak Abd. Razak and Sivarain Seetharan

16

Sintering and Characterization of Rare Earth Doped Bismuth Titanate Ceramics Prepared by Soft Combustion Synthesis

Umar Al-Amani Azlan, Warapong Krengvirat, Ahmad Fauzi Mohd Noor, Khairunisak Abd. Razak and Srimala Sreekantan
Universiti Sains Malaysia, USM, Pulau Pinang
Malaysia

1. Introduction

Nowadays, ferroelectric ceramics and thin films have attracted much attention for various studies which are generally used for numerous potential applications in ferroelectric random access memory (FRAM), in microelectronic mechanical system (MEMS), non-linear optical devices, surface acoustic wave devices, tunable capacitors, sensing applications or pyroelectric detectors (Besland et al., 2006, Yang et al., 2008). The main focus to develop the ferroelectric thin films has started in 1980s (Besland et al., 2006). Several methods were initially used for deposition of thin films such as conventional dipping, sputtering and spin coating techniques. Typically, the deposition of thin films will be more complex to obtain a good layer that consists of several ferroelectric compounds on substrate. Furthermore, high precision deposition technique is essential to control the desired thickness and surface layer of ferroelectric compounds. As far as our concern, the up to date technique such as physical vapor deposition (PVD), RF sputtering, chemical vapor deposition (CVD) and metal-organic chemical vapor deposition have been frequently used in many studies to obtain a better ferroelectric thin films condition. Nevertheless, a major concern on expensive equipment and experience user limit this technique in many studies. In order to develop the ferroelectric materials, the preparation in the form of bulk ceramics has been extensively studied. Up to now, several methods, including solid state reaction, hydrothermal synthesis, mechanical activation technique, sol-gel method, co-precipitation method were used for the preparation of bulk ceramics. Recently, the soft combustion synthesis is used as alternative route since it offers several beneficial points to the processing element and the properties of ceramics (Yan ,Razak, 2010). Bismuth titanate, $Bi_4Ti_3O_{12}$ or BTO has received a lot of attention as dielectric and ferroelectric materials. Many studies have been conducted in various processing route to improve the microstructure that has a significance effect on dielectric and ferroelectric properties (Hardy et al., 2004, Pookmanee et al., 2004, Zhi-hui et al., 2010). In addition, a modification on basic compound is essential to enhance those properties. Since BTO is also sought as a potential material for dielectric application, in this chapter the effect of Sm^{3+} and Pr^{3+} doped-BTO was prepared and characterized by soft combustion technique. In order to investigate a possible application as wireless dielectric antenna, the dielectric study at different frequencies was carried out.

2. Bismuth titanate and other properties

Considerable attention has recently been paid to bismuth layer-structured ferroelectric (BLSF) as ferroelectric materials instead of unfriendly lead (Pb)-based ferroelectrics because of its excellent fatigue resistance and Pb-free chemical composition (AlguerÃ³ et al., 2006, Subbarao, 1961, Xue et al., 2009, Yang et al., 2003). The general formula is given by $(Bi_2O_2)^{2+}$ $(A_{m-1}B_mO_{3m-1})^{2-}$ where A = Bi^{3+}, Pb^{2+} Sr^{2+}, Ba^{2+}, etc. and B = Nb^{5+}, Ta^{5+}, Ti^{4+}, etc. m = 1, 2, 3, 4, 5, etc. $(Bi_2O_2)^{2+}$ is the bismuth oxide layer and $(A_{m-1}B_mO_{3m+1})^{2-}$ is the pseudo perovskite layer (Armstrong ,Newnham, 1972, Newnham et al., 1971, Yan et al., 2006). BLSF is expected to have various numbers of pseudo perovskite blocks in unit cells. BLSF, bismuth titanate, $Bi_4Ti_3O_{12}$ (m = 3) or BTO has three pseudo perovskite blocks in half-unit cells. In simple words, its structure can be described as formed by three unit cells of $(Bi_2Ti_3O_{10})^{2-}$ with perovskite like structure interleaved with $(Bi_2O_2)^{2+}$ layers (Ng et al., 2002). BTO is an attractive material that has low processing temperature (700-750°C) than other BLSF (e.g. $SrBi_2Ta_2O_9$) and strong anisotropy of the spontaneous polarization (P_s) along the *a*-axis (~ 50 μC/cm²) and *c*-axis (~ 4 μC/cm²) (Wang et al., 1999, Zhi-hui et al., 2010). However, the low remanent polarization (P_r = 5 μC/cm²), low fatigue resistance and high dielectric loss of BTO would limits its application in FRAM applications. The reduction in remanent polarization and fatigue with high dielectric losses become more serious issues due to defects in perovskite structure whereby the Bi ions volatile during sintering process and create the Bi vacancies accompanied by oxygen vacancies. Nevertheless, there are advantages on BTO whereby it has high Curie temperature at 675°C and high dielectric permittivity (~ 200), making this material for other possible applications such as capacitors, antennas, sensors and piezoelectric (Golda et al., 2011).

3. Rare-earth doping and other properties

Recent studies revealed that ion substitution in perovskite BTO structure is an efficient technique for improving the drawbacks of BTO as ferroelectric ceramics (Cui ,Hu, 2009, Santos et al., 2009, SimÃµes et al., 2008). It was reported that the fatigue free films with excellent ferroelectric properties are obtained by substitution of Bi-site ions in BTO films for La^{3+} ions using a pulsed laser deposition (Park et al., 1999). This ion substitution resulted in large remanent polarization value over 20μC/cm², which was considerably higher than that of BTO films. Furthermore, it has good fatigue resistance, low leakage current at 10^{-7} A/cm² at 5V and low processing temperature approximately in the range of 650 to 700°C. Recently, it has been reported that the substitution of Nd^{3+} in BTO thin films was more effective for improving the ferroelectric properties than La substitution (Kim ,Kim, 2005). This result can be explained by the fact that the substitution of Bi^{3+} by rare-earth ions with a smaller ionic radius for the Bi^{3+} site is effective in improving the ferroelectric properties. In this case, the ionic radius of Nd^{3+} is much smaller than those of Bi^{3+} and La^{3+}. According to both studies, it is necessary to find out more rare-earth elements with smaller ionic radius in other to enhance the ferroelectric properties of BTO ceramics. Besides that, a small amount of rare-earth elements is important to tailor the microstructures of BTO. Recently, it was reported that Nd doping into BTO ceramics act as a grain-growth inhibitor whereby a remarkable decrease in the grain size with fine and homogeneous microstructure (Kan et al., 2008). It is well known that typical BTO powders

are attributed to high anisotropic grains, in which the ferroelectric properties are grain orientation dependent. Thus, it can be said that the homogeneity in microstructure is strongly influenced by rare-earth content. In addition, the corresponding microstructure can produce better ferroelectric properties. The summary of doping studies in BTO and their properties are listed in **Table 1.** Based on this summary, the selection of processing route is important to determine the grain orientation and microstructure as well as dielectric and ferroelectric properties. Besides that, the doping studies can improve the dielectric and ferroelectric properties of BTO.

Rare-earth	Process	XRD	Microstructure	Dopant content	ε_r	tan δ	P_r	E_c
La^{3+} (47)	Polymeric precursor method			0	86	0.008	15.1	1.45
				0.25	104	0.0011	20.2	1.09
				0.5	112	0.0068	20.2	0.66
				0.75	148 at 1 MHz	0.0018	20.3	0.99
La^{3+} (38)	Sol-gel	Randomly oriented at 700°C for 30 minute		0			12.5	2.8
				0.85			18.6	2.8
La^{3+} (18)	Conventional solid state reaction			0	130	0.022		
				0.5	145	0.023		
				0.75	147	0.024		
				1	186	0.022		
				1.5	168	0.017		
				2	101 at 100 kHz	0.014		
Nd^{3+} (50)	Pulsed laser deposition	Highly *c*-axis oriented		0	103	0.063	4.5	142
				0.85	177 at 500 kHz	0.068	8.6	88
Nd^{3+} (24)	Solid state reaction			0.75	174	0.0603		
				0.80	143	0.0055		
				0.85	158	0.0044	11.1	
				0.90	179	0.0070		
Nd^{3+} (52)	Solid state reaction		Plate-like grains	0	108	0.0078	5.2	27
				0.25	128	0.0045	5.5	35.2
				0.5	132	0.0044	9.3	45.2
				0.75	148	0.0040	11.1	42
				1	160	0.0039	9.8	34
Nd^{3+} (53)	Metal organic solution decomposition	Highly *c*-axis oriented grains	Plate-like grains	0.5	172		17	150
				0.75	156		19	98
Sm^{3+} (56)	Solid state reaction	Randomly oriented	Plate-like grains	0.8	270	0.003	16	70

Table 1. Summary of doping studies in BTO and their properties.

4. Processing route for preparation the BTO and rare-earth doping

As is known, synthesis process plays a crucial role to determine the microstructure of the ceramics as well as the control purity and stoichiometry. Different synthesis methods have been developed for the production of perovskite powders, like solid state reaction, sol-gel technique, hydrothermal synthesis, co-precipitation and combustion synthesis (Hardy et al., 2004, Kim, 2006, Kojima et al., 2009, Macedo et al., 2004, Pookmanee ,Phanichphant, 2009). It was reported that the ferroelectric properties of BTO can also be improved with a specific control in terms of microstructure, chemical homogeneity and its purity (Lu et al., 2005, Yang et al., 2008). Nevertheless, there are several merits and drawbacks of each synthesis process in order to control the ferroelectric domains through the preferred microstructure as well as crystal structure. Thus, the description of each synthesis process is discussed in the following subsection.

4.1 Conventional solid state reaction

The conventional solid state reaction is mostly used for preparation of bulk ceramics. It is an endothermic reaction used to produce simple oxide from carbonates, hydroxides and other metal salts. Such conventional reaction often results in high agglomeration and compositional inhomogeneity of powders because of high calcination temperature and repeated grinding. As a result, the sinterability of ceramics is fairly low subsequently a higher sintering temperature is required to enhance their properties. Subbarao (Subbarao, 1961, Subbarao, 1962) prepared the BTO ceramics using the solid state reaction and sintered from 1000 to 1250°C to achieve the theoretical density of about 80 %. In some cases, the sintering condition with longer soaking time is needed to enhance other properties. Watcharapasorn et al. (Watcharapasorn et al., 2010) studied the grain growth behavior of BTO ceramics using different sintering conditions. It was reported that the sintering of ceramics for longer time could render a material with more isotropic microstructure with reduced preferred orientation. Nevertheless, the increase in relative density (91 - 94 %) was very small with increasing soaking time.

4.2 Mechanical activation technique

Mechanical activation technique was initially derived from mechanical alloying for synthesizing alloys and intermetallics. The corresponding technique is a common part of the powder preparation route in the field of ceramics where high-energy ball milling has become a conventional method for producing nanocrystalline materials. This technique uses low-cost and widely available oxides as starting materials and skips the calcination step at an intermediate temperature, leading to a simplified process (StojanoviÄ‡ et al., 2008). Furthermore, the mechanically derived powders have higher sinterability than those powders synthesized by the conventional ball milling. Kong et al. (Kong et al., 2001) obtained the large P_r (24 μC/cm²) and low E_c (11 kV/cm) for BTO ceramics with better density of 98 % after low temperature sintering at 850°C for the powder derived from mechanical activation technique. Stojanovic et al. (Stojanovic et al., 2006, Stojanovic et al., 2006) reported that the BTO powder can be directly synthesized using high impact milling for about 3 to 12 hours and then sintered at 1000°C for 2 h. Han et al. (Han ,Ko, 2009) stated the formation of BTO phase is highly dependent on the processing parameters particularly

the impact energy or milling intensity. Zdujic et al. (ZdujiÄ‡ et al., 2006) reported that a mixture of α-Bi_2O_3 transformed to $Bi_2O_2CO_3$ at a milling intensity of ~ 0.49 W/g, which in turn was converted directly into a nanocrystalline BTO phase when the intensity was increased to ~ 2.68 W/g. Thus, it can be concluded that the parameter of mechanical milling has a significance result on the particle morphology and sinterability.

4.3 Sol-gel synthesis

The most popular wet chemical technique like sol-gel synthesis is widely used since it offers excellent uniformity over a large area, easy composition control, short fabrication time, as well as a low temperature process at comparatively a low cost (Du et al., 2007). This technique can be used to prepare the samples in the form of bulk ceramics and thin films. Several factors that need to be considered in a sol-gel synthesis are solvent, precursors, catalyst, pH, additives and mechanical agitation (Du et al., 2007, Guo et al., 2007, Ke et al., 2010). These factors greatly influence the powder size and other properties. Du et al. (Du et al., 2007, Du et al., 2008) reported that a highly stable and homogeneous BTO powders was produced at calcination temperature as low as 550°C, which is fairly low in wet chemical technique.

4.4 Hydrothermal synthesis

Another wet chemical technique is known as hydrothermal synthesis. In hydrothermal synthesis, the reaction mixture is heated above the boiling point of water in an autoclave or other closed system and the sample is exposed to steam at high pressures (Pookmanee et al., 2004, Shi et al., 2000, Yang et al., 2003). In addition, the parameter of Teflon-lined vessel such as temperature and reaction time are mainly important factor to determine the phase structure and particle morphology (Pookmanee et al., 2004). It was also reported that the hydrothermally powder was significantly influenced by different mineralizer KOH content and molar ratio of Bi/Ti (Shi et al., 2000). Recently, Xie et al. (Xie et al., 2007) reported that the concentration of KOH, reaction time and temperature had a significant effect on the phase composition and morphology of the resultant single crystals. Many authors reported that hydrothermal synthesis has several advantages including narrow particle size distribution, highly purity with fine powder, and low degree of agglomeration. In processing stand point, the hydrothermal synthesis is able to synthesize powder at a much lower temperature compared to other methods. Nevertheless, the synthesis in an aqueous environment causes water to be incorporated into the powder, thus causing deterioration in the electrical properties (Yan ,Razak, 2010).

4.5 Co-precipitation method

In order to prepare the controlled morphology, narrow particle size distribution, high purity and high degree of crystallinity as well as possible reduction in sintering temperature, the co-precipitation method might be a promising route instead of other wet chemical route. Precipitation is the formation of a solid product or powder from a liquid solution which initiated by either changing the solution temperature, pressure, pH or using a chemical precipitation agent so as to exceed the solubility limit of the desired species (Pookmanee, Phanichphant, 2009, Thongtem ,Thongtem, 2004). In general, co-precipitation reaction relies

on dissolving the metal salts, commonly metal chlorides, nitrates and hydroxides followed by a rapid pH change to form precipitate. The precipitate must be thoroughly washed to get rid of the impurities from the solutions prior to calcination. It was reported that the well-dispersed particles of about 10 nm began to form a BTO phase at 470°C. The phase formation was complete after a 550°C for 30 minute heat treatment. It was finally sintered at 750°C for 1 hour to achieve a sample of high density of 97.2% (Kan et al., 2002).

4.6 Soft combustion synthesis

The synthesis of BTO powders using combustion reactions, which provides good compositional control, is an alternative synthesis method which worth pursuing. The combustion synthesis enables synthesis at low temperatures and the products obtained are in a finely divided state with large surface areas. Furthermore, the nature of combustion synthesis is characterized by simple experimental set-up, short reaction time between the preparation of the reactants and the availability of the final product and less in external energy consumption (Aruna ,Mukasyan, 2008, Patil et al., 2002). Typically, the mixture of reactants consists of metal nitrate and a suitable organic fuel such as urea, glycine and citric acid. Additionally, the temperature is essential to boil the mixture until the ignition and self-sustaining reaction takes off. The large amount of gases formed can result in the appearance of a flame, which can reach temperatures in excess of 1000°C. In some cases, the external source like simple calcination is necessary to accomplish the synthesis of the appropriate phase. This is because the energy released from the exothermic reaction between the nitrate and the fuel is usually ignited at a temperature much lower than the actual phase formation. Thus, the single phase formation is not ease to produce. Recently, our group had performed a modification on soft combustion synthesis, whereby nitrate salts, Bismuth (Bi) and organic Titanium (IV) isopropoxide (Ti) were dissolved into 2-methaoxyethanol and acetylacetone. In addition, the organic fuel was not used in this work. To introduce the doping content, the Sm^{3+} and Pr^{3+} from nitrate salts were also used. The observation of the soft combustion will be discussed in the following section.

5. Observation during the combustion process

Figure 1 shows the actual condition before and after combustion on BTO and Pr^{3+} doping. The Bi-Ti precursor was observed in clear-yellowish solution (**Figure 1a**) whereas the Pr^{3+} precursor was found in clear-greenish solution (**Figure 1b**). The Sm^{3+} precursor was observed in transparent solution (not shown here). The Bi-Ti precursor was then stirred at 40°C for 2 hours and the colour of the solution changed slightly milky-yellowish as shown in **Figure 1c**. The solution was then continuously evaporated and temperature maintained at ~90°C. The colour of the solution changed. It was found that higher Pr^{3+} doping tends to prolong hydrolysis process. After that, the temperature increased rapidly to ~120°C and the solution completely evaporated, resulting dark-yellowish gel (**Figure 1e**). The gel started to induced ignition at ~150°C. Metal nitrates were decomposed to form metal oxides and nitrogen. The compound was eventually acting as an oxidizer to continue the combustion synthesis, which was accompanied by the releasing of voluminous gases. At the end of this stage, flaming occurred and resulted foamy-like structure as shown in **Figure 1f**. The flaming temperature was found to be approximate 230°C. In order to remove the carbon

content in as-combusted powders, the calcination is necessary to enhance the degree of crystallinity with high purity of BTO content.

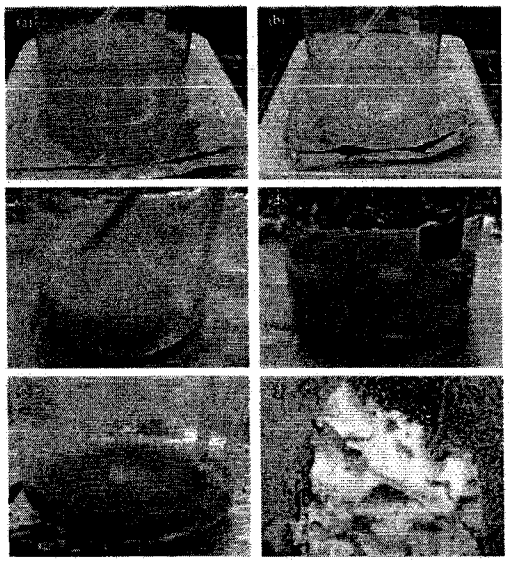

Fig. 1. Evolution of (a) Bi-Ti precursor (b) Pr precursor (c) Bi-Ti precursor stirred at 40°C for 2 hour (d) Bi-Ti precursor heated at 90°C (e) viscous gel and (f) as-combusted powder.

6. Powder characterization

6.1 Effect of calcination temperature on BTO

X-ray diffraction (XRD) was conducted on the as-combusted powders which calcined at different temperatures and the result is shown in **Figure 2.** The study on different calcination temperature is essential in this work. The main reason is to determine the optimum calcination temperature, which will be used for the following characterization in particular dielectric study. As seen in **Figure 2,** the BTO phase was observed in as-combusted powder. The main peak corresponding to BTO was found at ~29°. However, the presence other intermediate phases such as BTO7.7 and BTO2 were also identified and marked in XRD pattern. At calcination temperature of 600°C, there was a tremendous increase at the main peak (~29°). This inedicates that the presence more BTO phase was observed after calcination process. In addition, the peaks corresponding to intermediate phases were decreased. Further increase calcination temperature, the intermediate phases were gradually eliminated. The intermediate phases completely disappeared at 750 and 800°C. In other words, the BTO phase was successfully formed as single phase at temperature as low as 750°C. It also suggest that the optimum calcination temperature for BTO is 750°C. This temperature is probably lower than other processing route such as conventional solid state reaction and some other wet chemical synthesis (Kan et al., 2003, Pookmanee, 2008). Moreover, as the calcination temperature was increased, the XRD peaks were sharper and the stable phase BTO powders with higher crystallinity could be obtained. **Table 2** presents the variation of lattice parameters and

crystallite sizes of BTO calcined at different temperatures. As can be seen in **Table 2**, the corresponding lattice *a*-, *b*-, and *c*-parameters as well as volume cell units, V were observed to exhibit in various values as a result of calcination temperature. In addition, the crystal structure of calcined powder was confirmed to belong orthrhombic, in which it is a typical structure for BTO (Hervoches ,Lightfoot, 1999, Kim ,Jeon, 2004). Besides that, the crystallite size of calcined powder was increased with increasing calcination temperature. The increase in a such way was observed in many studies (Hou et al., 2010, Pookmanee ,Phanichphant, 2009, Umar Al-Amani et al., 2010).

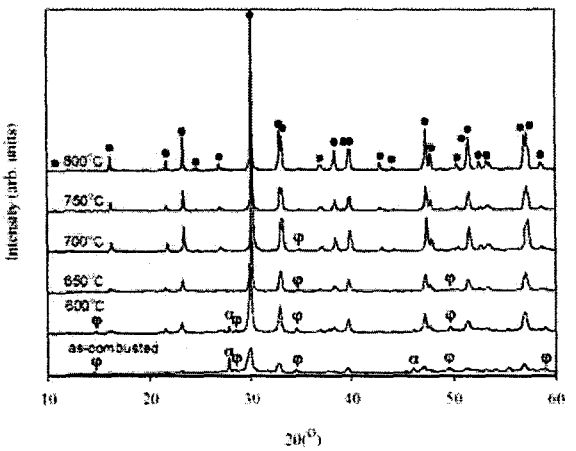

Fig. 2. XRD patterns of BTO powders calcined at different temperatures for 3 hour. •:$Bi_4Ti_3O_{12}$ or BTO; α:$Bi_{7.7}Ti_{0.3}O_{12.16}$ or BTO7.7; φ:$Bi_2Ti_2O_7$ or BTO2.

Calcination, °C	600	650	700	750	800
a/ Å	5.418(2)	5.4138(6)	5.4110(6)	5.4093(2)	5.4066(2)
b/ Å	5.433(2)	5.4385(6)	5.4438(6)	5.4418(2)	5.4429(2)
c/ Å	32.765(6)	32.810(3)	32.853(4)	32.830(1)	32.817(1)
V/Å^3	964.4709	966.0297	967.7028	966.4148	965.7186
Crystallite Size/ nm	24.87	37.19	50.54	71.34	98.07

Table 2. Lattice parameters and crystallite sizes of BTO.

6.2 Effect of Sm^{3+} and Pr^{3+} doping on crystal structure and lattice parameter

The introduction of Sm^{3+} and Pr^{3+} to form $Bi_{4-x}Sm_xTi_3O_{12}$ (BSmT) and $Bi_{4-x}Pr_xTi_3O_{12}$ (BPrT) was expected to have a major changes on calcination temperature, crystal structure, lattice parameter and crystallite size. Based on previous studies, the ionic radii of Sm^{3+} and Pr^{3+} were reported around 0.108 nm and 0.113 nm, respectively, whereas the ionic radii of Bi^{3+} was about 0.117 nm (Garg et al., 2005, Hu et al., 2005). In general, the substitution of Sm^{3+} or Pr^{3+} for Bi^{3+} with larger difference in ionic radii size would lead to larger structure distortion of BTO lattice

(Hu et al., 2005). In addition, the increase in dopant contents would also result in difference in structure distortion (Kan et al., 2004, Kan et al., 2008). In order to determine the effect of Sm^{3+} and Pr^{3+} doping on crystal structure and lattice parameter, the calcined powder for respective contents were analyzed by XRD. Interestingly, the calcination temperature was successfully reduced from 750°C (for BTO) to 650°C (for BSmT and BPrT). According to **Figure 3**, the XRD patterns of BSmT and BPrT powders calcined at 650°C for 3 hour with different Sm^{3+} and Pr^{3+} contents were presented. Regardless of Sm^{3+} and Pr^{3+} contents, the formation of a single phase BTO was observed in **Figure 3(a)** and **Figure 3(b)** for both doping powders. This indicates that the perovskite phase was fully formed in calcined powders and all of them have a bismuth-layered structure. In comparison to the BTO calcined powder at 650°C for 3 hour (see **Figure 2**), the intermediate phases such as BTO2 and BTO7.7 were eliminated as a result of Sm^{3+} and Pr^{3+} doping. This result indicates that the Sm^{3+} and Pr^{3+} ions in the BSmT and BPrT, respectively, are incorporated into the pseudo-perovskite structure, substituting for the Bi^{3+} ions. Besides that, the lattice parameters and crystallite size of BSmT and BPrT were greatly influenced by Sm^{3+} and Pr^{3+} doping, as shown in **Table 3** and **Table 4**, respectively. Based on both tables, the *a*-parameter rapidly approached the *b*-parameter with increasing Sm^{3+} and Pr^{3+} content. The closed value of the *a*- and *b*-parameters was obtained at 1.0 mole of Sm^{3+} and Pr^{3+}, corresponding to the increment in the symmetry of the crystal structure. This also suggested that the orthorhombic structure was formed when doping content was equivalent to 0.25, 0.5 and 0.75 whereas the tetragonal structure was formed doping content was equivalent to 1.0. Further observation shows that the *c*-parameter slightly changed with increasing Sm^{3+} and Pr^{3+} content. It was reported that the variation of *c*-parameter is attributed to the rotation of the TiO_6 octahedron and the reduction in the oxygen deficient (Yoneda et al., 2006). It is evident that Sm^{3+} and Pr^{3+} had substituted in $(Bi_2Ti_3O_{10})^{2-}$ perovskite-type layers and O vacancies in the TiO_6 octahedron; these would eventually result in the shrinkage of unit cell. The crystallite size of BTO was found to be 37.19 nm and decreased continuously to 24.69 nm and 24.56 nm with 1.0 of Sm^{3+} and Pr^{3+}, respectively. It is attributed to the reduction of space charge density and oxygen vacancies with increasing Pr^{3+} content, which act as grain growth inhibiter. This is supported by the finding of Xiang et al. (Xiang et al., 2006). Based on XRD studies, it can conclude that the optimum calcination temperature for BTO was determined at 750°C, whereas the BSmT and BPrT were around 650°C.

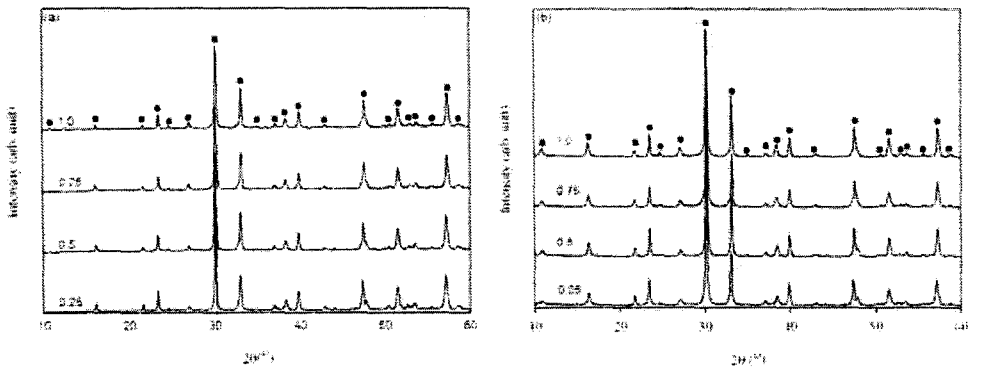

Fig. 3. XRD patterns of (a) BSmT and (b) BPrT powders calcined at 650°C for 3 hour with different Sm^{3+} and Pr^{3+} contents. •:$Bi_4Ti_3O_{12}$ or BTO.

Sm^{3+} content	0.25	0.5	0.75	1.0
a/ Å	5.4076(3)	5.4018(4)	5.3952(5)	5.3910(1)
b/ Å	5.4283(3)	5.4155(4)	5.4059(5)	5.3940(1)
c/ Å	32.798(2)	32.803(2)	32.800(2)	32.777(2)
V/Å^3	962.74	959.6153	956.6382	953.0192
Crystallite size/nm	54.89	48.47	45.27	24.69

Table 3. Lattice parameters and crystallite sizes of BSmT.

Pr^{3+} content	0.25	0.5	0.75	1.0
a/ Å	5.4210(9)	5.4157(8)	5.4099(1)	5.4067(8)
b/ Å	5.4306(9)	5.4213(8)	5.4161(1)	5.4054(8)
c/ Å	32.783(3)	32.810(2)	32.816(3)	32.817(3)
V/Å^3	965.0938	963.3097	961.527	959.0734
Crystallite size/ nm	36.44	32.86	28.55	24.56

Table 4. Lattice parameters and crystallite sizes of BPrT.

6.3 Grain morphology of BSmT and BPrT powders

To gain an insight into the formation of BTO prepared using different doping content, the calcined powders were monitored by taking field emission scanning electron microscopy (FESEM) micrographs. **Figure 4** shows the morphology of BTO, BSmT and BPrT powders. In order to observe the increase in particle size of BTO, the morphology at 650°C and 750°C were displayed in **Figure 4a** and **Figure 4b**, respectively. It was found that the particle size is relatively expanded with increasing temperature. It was also determined that the particle size in range of 0.1 - 0.2 μm and 0.3 - 0.5 μm were found at 650°C and 750°C, respectively. It clearly observed that plate-like morphology was formed at 750°C instead of 650°C. The formation of such morphology was observed in many studies in which the plate-like structure with highly anisotropic properties is one of typical shape for pure BTO (Chen et al., 2006). In addition, the variation in particle size is also attributed to a greater distortion of perovskite-layer along *ab*-plane (particle length) as compared with *c*-axis (particle thickness). The morphology of BSmT and BPrT powders with different doping contents were observed and depicted in **Figure 4c - 4f**. In this section, the selected micrographs for each dopant with doping content of 0.25 and 1.0 were presented. The selection of the minimum and maximum doping contents is necessary to determine the variation size and shape of resultant particles. It was found that the particle size decreased with increasing doping content, corresponding to the lower diffusivity of both doping content compared to Bi^{3+}, resulting to the suppression of the grain growth (Goh et al., 2009). It was determined that the particle size in range of 0.2 - 0.4 μm and 0.1 - 0.2 μm were observed when Sm^{3+} contents were equivalent to 0.25 and 1.0, respectively. Meanwhile, the average particle size in range of 0.1 - 0.2 μm and 0.05 - 0.1 μm were found when Pr^{3+} contents were equivalent to 0.25 and 1.0, respectively. It is also noticed that the

size of plate-like particle decreased relatively with increasing Sm^{3+} and Pr^{3+}, corresponding to the greater relaxation in the perovskite-layer. In order to see the difference of the particle size between Sm^{3+} and Pr^{3+}, the doping content was fixed at 0.25. As can be seen in **Figure 4c** and **Figure 4e** for Sm^{3+} and Pr^{3+}, respectively, the particle size of Sm^{3+} doping was found to substantially larger than Pr^{3+} doping. This might be attributed to the difference in ionic radii which also resulted in different diffusivity.

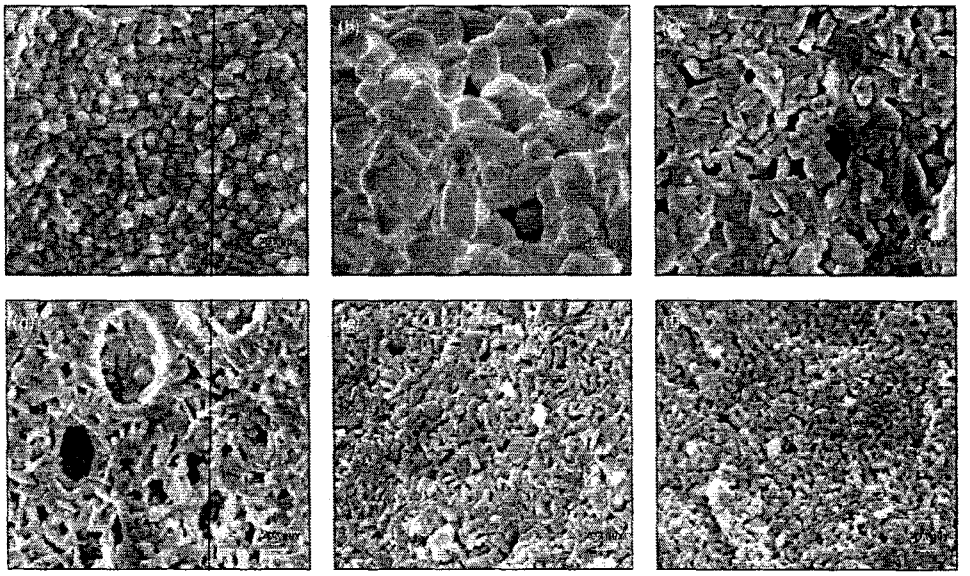

Fig. 4. Morphologies of (a) BTO:650°C, (b) BTO:750°C, (c) BSmT:0.25, (d) BSmT:1.0, (e) BPrT:0.25 and (f) BPrT:1.0.

6.4 Comparison of lattice vibration BTO and Sm^{3+} doping

In order to enhance the understanding of the doping effect from the structural point of view, Raman scattering study is a very useful tool for investigating the lattice vibrational modes, which can provide details of lattice vibrations changes. **Figure 5** shows the Raman spectra of BTO and BSmT powders at room temperature from 100 to 2000 cm^{-1}. Theoretically, the Raman selection rules allow 24 Raman active modes for orthorhombic BTO. (Kojima, 2000, Kojima ,Shimada, 1996). However, as shown in **Figure 5a**, the Raman spectrum of BTO less than 9 active modes were observed which is partially due to the possible overlap of the same symmetry vibrations or the weak features of some Raman bands (Liang et al., 2009). As can be seen in **Figure 5a**, the Raman modes at 193, 228, 267, 330, 353, 537, 563, 614 and 850 cm^{-1} were observed in BTO. All the Raman modes are also characterized as the vibrational modes of BTO which can be classified as internal modes of TiO_6 octahedra. According to Kojima et al. (Kojima ,Shimada, 1996), the internal modes of TiO_6 octahedra appear above 200 cm^{-1}. The mode at 850 cm^{-1} is attributed to the symmetric Ti - O stretching vibration of atom inside the TiO_6 octahedron whereas the mode at 614 cm^{-1} corresponds to the symmetry one. The two modes at 537 and 563 cm^{-1} correspond to the opposing excursions of the external apical oxygen (O) atoms of the TiO_6 octahedron. The 228 and 267 cm^{-1} modes are ascribed to the O - Ti - O

bending vibration. Although the mode at 228 cm^{-1} is Raman inactive according to the Oh symmetry of TiO_6, it is often observed because of the distortion of octahedron. The mode at 330 cm^{-1} was from a combination of the stretching and bending vibrations of the TiO_6 octahedron. In addition, the formation of BTO with orthorhombic structure is identified by the splitting mode at 193 and 228 cm^{-1}, and 537 and 563cm^{-1}. Nevertheless, the Raman modes of the lower wavenumber at 116 cm^{-1} was not found in this spectrum, to show the vibrations between Bi and O atoms. However, the reason of missing mode is still not clear. The effect of Sm^{3+} doping on the structure change of BTO on the basis of the Raman modes is presented in **Figure 5b**. It was clearly observed that the peak intensity decreased with increasing Sm^{3+} contents from 0.25 to 0.75. It is believed to be associated with strong interactions between the ionic bonds; corresponding to the smaller ionic radius of Sm^{3+} (0.108 nm) compared with Bi^{3+} (0.117 nm). With the increase of Sm content, the distortion structure would be more and the grain size would be smaller. This finding is in line with the XRD pattern and FESEM micrograph. It was reported that the duplet peaks observed in Raman spectra tend to merge into one mode when the Bi^{3+} is substituted by rare-earth elements (Wu et al., 2005). Similar observation was discovered in BST. In the present work, the duplet peaks at 228-267 cm^{-1}, 330-353 cm^{-1} and 537-563 cm^{-1} were found to merged into a single peak at 264 cm^{-1}, 322 cm^{-1} and 542 cm^{-1} for x= 0.25 and 264 cm^{-1}, 330 cm^{-1} and 553 cm^{-1} for x= 0.75.

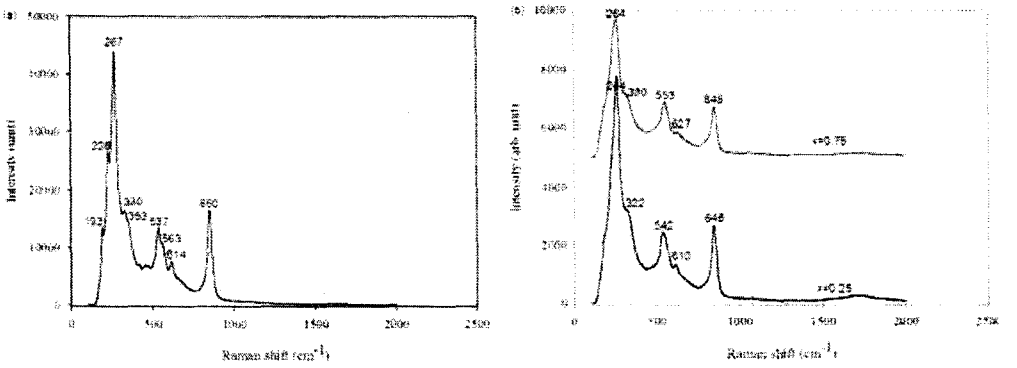

Fig. 5. Raman spectra of (a) BTO and (b) BSmT at different Sm^{3+} content.

7. Bulk ceramic characterization

7.1 Effect of sintering temperature of BTO

Figure 6 shows the XRD patterns of BTO ceramics sintered at different temperature for 3 hour. As can be seen from this figure, the BTO was formed with random oriented grains in which the strongest peak was found at (117) instead of (001). Besides that, the increase in calcination temperature also implies the improvement of crystallinity and the enhancement of crystallite size. This can be explained by the width of the diffraction lines, which decreased, whilst the intensity increased. The crystallite sizes for ceramics sintered at 900, 1000 and 1100oC were calculated to be approximately 104.66, 126.52 and 130.22 nm, respectively.

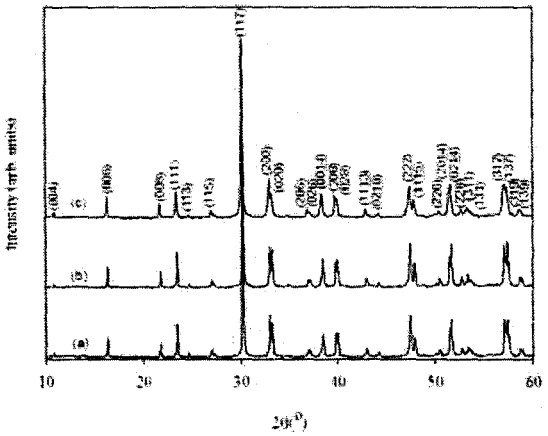

Fig. 6. XRD patterns of BTO ceramics sintered at different temperatures for 3 hour: (a) 900°C, (b) 1000°C and (c) 1100°C.

7.2 Effect of Sm^{3+} and Pr^{3+} doping on grain orientation

The preferred grain orientation was obviously affected by rare-earth doping in BTO particularly after sintering. Kannan et al. (Kannan et al., 2006) reported the reflections corresponding to (00*l*) plane along the *c*-axis was observed with increasing Nd^{3+} content from 0 to 0.25. It can give us another hint that preferred grain orientation would be different when rare-earth was introduced into BTO lattice. As discussed in **Figure 6**, the pure BTO was formed with no preferred grain orientation. In **Figure 7**, the XRD patterns of BST and BPT ceramics sintered at 1100°C for 3 hour were presented. As seen from this figure, the Sm^{3+} and Pr^{3+} doping show a highly *c*-axis oriented growth with increasing Sm^{3+} and Pr^{3+} contents. The XRD peak corresponding to (00*l*) plane was clearly observed with higher intensity as compared to (117) plane. To simplify the discussion, the peak at (00$\underline{14}$) and (117) are taken into consideration to determine the degree of *c*-axis orientation, α_c by Lotgering factor (Yang et al., 2008):

$$\alpha_c = I(00\underline{14})/[I(00\underline{14}) + I(117)]$$

The values of α_c calculated for the Sm^{3+} and Pr^{3+} doping with various contents are listed in **Table 5**. It was found that the degree of *c*-axis orientation increased with increasing Sm^{3+} and Pr^{3+} content. This indicates that the doping content has a significance result on grain orientation.

Sm^{3+} content	α_c (%)	Pr^{3+} content	α_c (%)
0.25	41.40	0.25	48.34
0.5	58.12	0.5	86.61
0.75	58.89	0.75	96.78
1.0	86.17	1.0	98.79

Table 5. Lotgering factor of the degree of *c*-axis orientation.

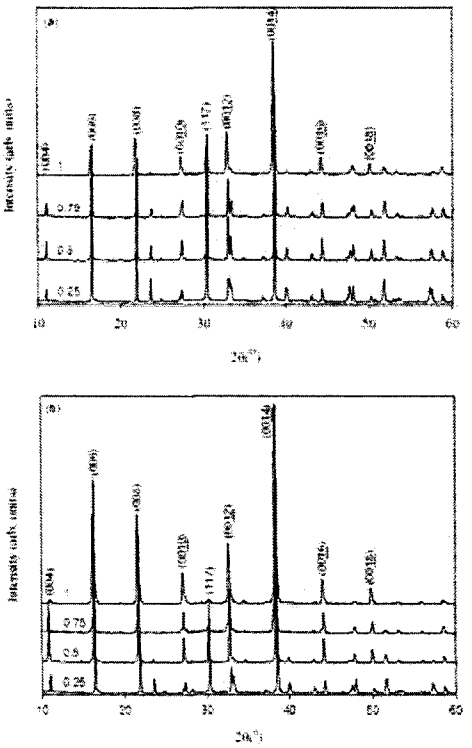

Fig. 7. XRD patterns of (a) BSmT and (b) BPrT ceramics sintered at 1100°C for 3 hour.

7.3 Microstructure of bulk ceramics after sintering

It is more interesting to observe the microstructure of bulk ceramics after sintering, as shown in **Figure 8.** Prior to view the micrograph using field emission scanning electron microscopy (FESEM), the surface of ceramics were polished on SiC papers grit 1000 followed by finer grit 2000. The polished ceramics were placed into ultrasonic for 10 minute to remove contaminants. The polished ceramics were thermally etched with temperature of 100°C lower than the sintering temperature for 30 minute. As can be seen in **Figure 8a**, the microstructure of the BTO ceramic shows a random arrangement of elongated-like grains, several of which are highly elongated. On the other hand, the microstructure of the BSmT and BPrT ceramics show a random arrangement of plate-like grains, as observed in **Figure 8b-8e**. It was also noticed that the average grain size relatively decrease with increasing Sm^{3+} and Pr^{3+} contents, indicating a strong influence of doping concentration which resulted in less amount of Bi^{3+} in BTO. The micrographs also revealed that the plate-like grains were not homogeneously distributed when Sm^{3+} and Pr^{3+} are equivalent to 0.25. Nevertheless, homogeneous microstructures with small grain size were found from the BSmT and BPrT ceramics with 1.0. The resultant micrographs was mainly attributed to a greater suppresion of the Bi^{3+} volatility by substitution of low diffusivity of Sm^{3+} and Pr^{3+}, which eventually inhibits the grain growth.

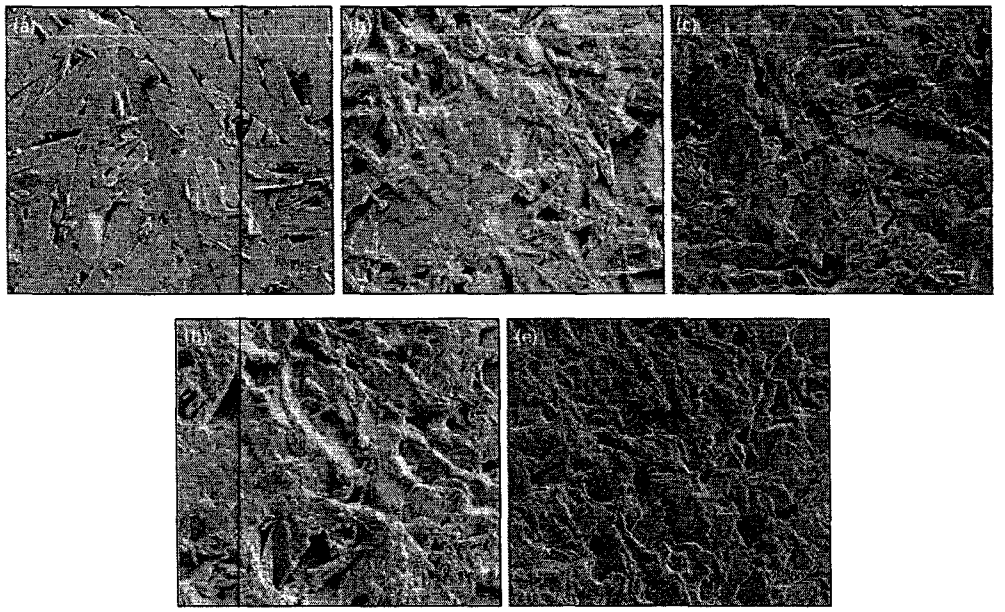

Fig. 8. FESEM micrograph of (a) BTO, (b) BSmT:025, (c) BSmT:1.0, (d) BPrT:025 and (e) BPrT:1.0, sintered at 1100°C for 3 hour.

7.4 Effect of sintering temperature and Sm^{3+}, Pr^{3+} content on relative density

The effect of sintering temperature on relative density of BTO ceramics was studied and depicted in **Figure 9a**. With increasing temperature, the relative density of ceramics was also increased up to 93% at 1100°C. This indicates that the densification behavior of BTO ceramics is temperature dependent. Thus, the sintering temperature at 1100°C was used for densification process with doping content. **Figure 9b** and **Figure 9c** show the relative density of Sm^{3+} and Pr^{3+} doping, respectively. As seen, the densities of BTO with doping content are different from one to another. It was determined that the densities was in range of 92 - 95%, indicating that a slight improvement as compared to pure BTO. The increase in relative density is associated to the decrease in Bi-loss during sintering resulting from the substitution effect by Sm^{3+} and Pr^{3+}. It can be said the small difference in relative density is another indicator to show the improvement of densification behavior in a such way.

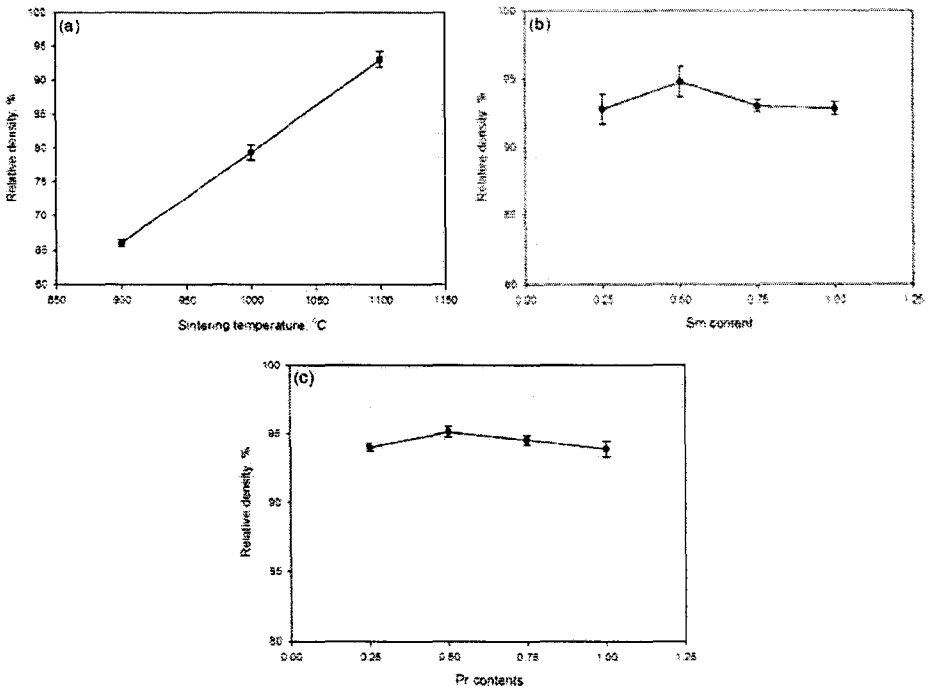

Fig. 9. Relative density of (a) BTO at different sintering temperatures, (b) BSmT with different Sm^{3+} contents and (c) BPrT with different Pr^{3+} contents; sintered at 1100°C.

7.5 Effect of Sm^{3+} and Pr^{3+} doping on dielectric properties

The effect of Sm^{3+} and Pr^{3+} contents in BSmT and BPrT on dielectric properties were studied. In this study, the measurement of dielectric constant, ε_r and dielectric loss, tan δ were performed at 1 kHz and at room temperature, 25°C and the results were presented in **Figure 10**. The variation of ε_r and tan δ were clearly observed in **Figure 10a** and **Figure 10b** for the BSmT and BPrT ceramics, respectively. The ε_r of the BSmT ceramics were in the range between 78 and 95, whereas the ε_r of the BPrT ceramics were in the range between 75 an 105. This indicates that the ε_r of the BPrT ceramics was slightly larger than the BSmT ceramics. This is associated to the larger ionic radii of Pr^{3+} than that of Sm^{3+}. This result can be explained by a shift of TiO_6 octahedra in a layered structure due to the substitution of larger ionic radii than that of Bi^{3+}. It was also noticed that the tan δ abruptly decreased with increasing Sm^{3+} and Pr^{3+} contents from 0.25 to 0.5. The decrement in the tan δ was attributed to a better electric flux caused by the reduction of grain imperfection. It was also supported by the increase in relative density, in which the ceramics appeared to be dense. Above 0.5, the tan δ were almost consistent with small difference in its value, corresponding to the reduction of the defects such as bismuth and oxygen vacancies. In order to see possible application as dielectric antenna, the dielectric study at different frequencies was performed. It was reported that the development of wireless technologies application requires very stringent criteria for dielectric ceramics materials. Typically, the dielectric ceramic materials must have a high dielectric constant, low dielectric loss and a a thermally

stable resonant frequency coefficient (LazareviÄ‡ et al., 2005). Thus, this study is essential to determine the potential application of such a field for the BTO, BSmT and BPrT ceramics.

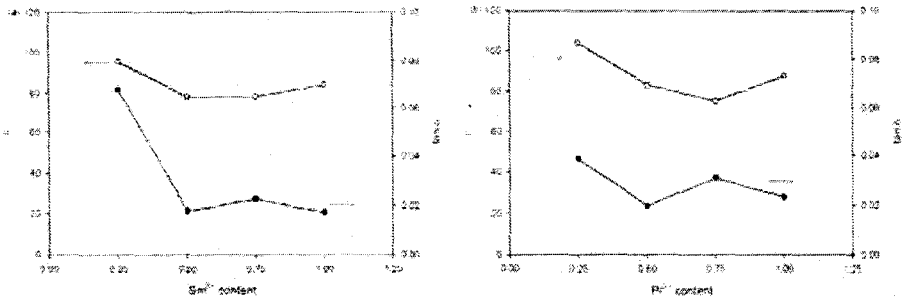

Fig. 10. Dielectric constant, ε_r and dielectric loss, tan δ at different doping contents: (a) BSmT and (b) BPrT.

7.6 Effect of various frequencies on the dielectric properties of the BTO, BSmT and BPrT ceramics

As reported in previous studies, the dielectric constant, ε_r and dielectric loss, tan δ were strongly dependent on frequency (Rachna et al., 2010, SimÃµes et al., 2008). In this work, the dielectric poperties were measured at different frequency ranges from 1 MHz to 1 GHz. As it can be seen from **Figure 11**, the ε_r of the BTO ceramic shows very obvious dispersion with

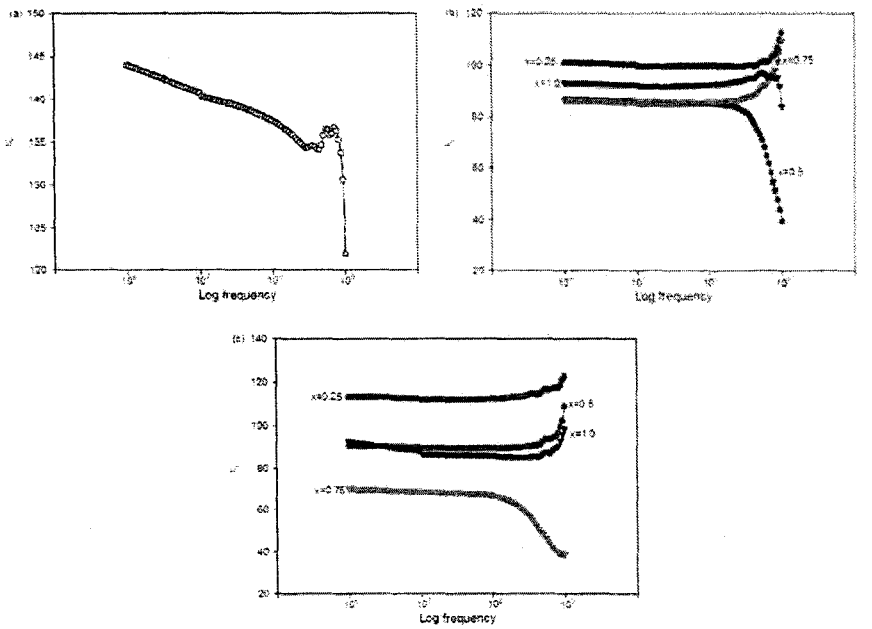

Fig. 11. Dielectric constant, ε_r of (a) BTO, (b) BSmT and (c) BPrT measured at high frequency range at room temperature.

frequency, indicating that the corresponding ceramic possess high defect concentration such as bismuth and oxygen vacancies. On the other hand, the ε_r of the BSmT and BPrT ceramics show very little dispersion from 1 MHz to 100 MHz. However, the ε_r shows very obvious dispersion above 100 MHz. This indicates the ε_r will be more complex at higher frequency range between 100 MHz and 1 GHz. The dielectric loss, tan δ at different frequencies was depicted in **Figure 12.** It was found that the tan δ of was slowly increased from 1 MHz to 10 MHz and abruptly increased from 10 MHz to 1 GHz, as shown in **Figure 12a.** In addition, the presence of relaxation peak in the tan δ was observed, as shown in inset **Figure 12a.** This indicates that the relaxation peak was observed approximately 700 MHz. It can be said that the increase trend in tan δ was also found in the BSmT and BPrT ceramics, as shown in **Figure 12b** and **Figure 12c,** respectively. Furthermore, the relaxation peaks in the tan δ was also observed around 700 MHz, which is almost comparable to BTO ceramic. The dielectric loss relaxation peak phenomenon can be explained by the Debye-like model for relaxation effects. The dielectric loss peak is maximal at the resonant frequency, which is the reciprocal of the relaxation time (Sulaiman et al., 2010). The dielectric loss relaxation may be generated by several possible factors such as surface roughness, distribution grain sizes and many more (Sulaiman et al., 2010, Wang et al., 2010). From the FESEM micrographs (see **Figure 8c to Figure 8e**) revealed that BSmT and BPrT with 1.0 have homogeneous distribution of grain sizes compared to 0.25.

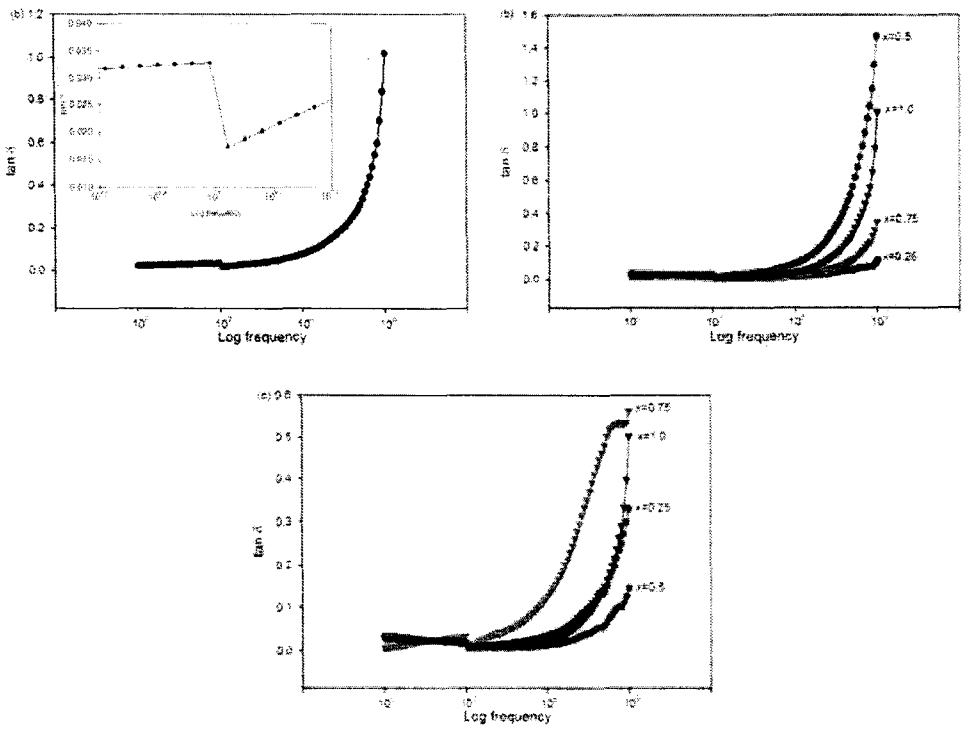

Fig. 12. Dielectric loss, tan δ of (a) BTO, inset showing the Debye relaxation effect, (b) BSmT and (c) BPrT measured at high frequency range at room temperature.

Therefore, the BSmT and BPrT with 1.0 gave a lower dielectric loss at relaxation frequency due to the above reason. Besides that, the improved ε_r with little dispersion and small variation in tan δ (or almost constant) can also suggest that the BSmT and BPrT ceramics are possible to be applied for wireless dielectric antenna applications instead of the BTO ceramic. However, a detail study is necessary to focus on return loss with a specific design of ceramic.

8. Conclusion

Based on this work, the rare-earth doping i.e. Sm^{3+} and Pr^{3+} had successfully improved the processing and properties of pure BTO ceramics. The calcination temperature was greatly reduced from 750°C to 650°C in order to form a single phase structure. The particle size of plate-like structure decreased continuously with increasing Sm^{3+} and Pr^{3+} content. The peak intensity and peak width in Raman spectrum were apparently low and broaden with increasing Sm^{3+} content. The Lotgering factor showed the enhancement in degree of *c*-axis orientation. The microstructure of the Sm^{3+} and Pr^{3+} doping showed a random arrangement of plate-like grains in which the grain size was relatively decrease at higher doping content. A great in densification behavior was also observed with Sm^{3+} and Pr^{3+} doping which resulted in the relative density of about 92-95% at 1100°C. The dielectric constant, ε_r of the BPrT ceramics was slightly larger than the BSmT ceramics, which can be explained in terms of larger ionic radii of Pr^{3+} than that of Sm^{3+}. The dielectric loss, tan δ of the BSmT and BPrT ceramics were greatly improved when dopant content above 0.5. For frequency study, the the ε_r of the BSmT and BPrT ceramics show very little dispersion from 1 MHz to 100 MHz instead of above 100 MHz. The relaxation peak in tan δ was observed approximately 700 MHz for all ceramics with different dopant contents. Based of frequency study, the BSmT and BPrT can be used as potential wireless dielectric antenna applications.

9. Acknowledgment

The authors appreciate the technical support from the School of Materials and Mineral Resources Engineering, Universiti Sains Malaysia. This research was supported by the USM Short term grant 6035276, USM-RU grant 1001/PBahan/8042018 and 811069.

10. References

Alguerό, M., Ferrer, P., Vila, E., Iglesias, J. E. & Castro, A., Journal of the American Ceramic Society, 89 (2006) 3340.

Armstrong, R. A. & Newnham, R. E., Materials Research Bulletin, 7 (1972) 1025.

Aruna, S. T. & Mukasyan, A. S., Current Opinion in Solid State and Materials Science, 12 (2008) 44.

Besland, M. P., Djani-Ait Aissa, H., Barroy, P. R. J., Lafane, S., Tessier, P. Y., Angleraud, B., Richard-Plouet, M., Brohan, L. & Djouadi, M. A., Thin Solid Films, 495 (2006) 86.

Chen, W., Kinemuchi, Y., Watari, K., Tamura, T. & Miwa, K., Journal of the American Ceramic Society, 89 (2006) 490.

Cui, L. & Hu, Y. J., Physica B: Condensed Matter, 404 (2009) 150.
Du, X., Xu, Y., Ma, H., Wang, J. & Li, X., Journal of the American Ceramic Society, 90 (2007) 1382.
Du, X., Xu, Y., Ma, H., Wang, J. & Li, X., Journal of the American Ceramic Society, 91 (2008) 2079.
Garg, A., Hu, X. & Barber, Z. H., Ferroelectrics, 328 (2005) 93.
Goh, P. Y., Razak, K. A. & Sreekantan, S., Journal of Alloys and Compounds, 475 (2009) 758.
Golda, R. A., Marikani, A. & Padiyan, D. P., Ceramics International, (2011)
Guo, D. Y., Li, M. Y., Liu, J., Fu, L., Wang, J., Yu, B. F. & Yang, B., Materials Science and Engineering B: Solid-State Materials for Advanced Technology, 142 (2007) 135.
Han, K. & Ko, T., Journal of Alloys and Compounds, 473 (2009) 490.
Hardy, A., Mondelaers, D., Van Bael, M. K., Mullens, J., Van Poucke, L. C., Vanhoyland, G. & D'Haen, J., Journal of the European Ceramic Society, 24 (2004) 905.
Hervoches, C. H. & Lightfoot, P., Chemistry of Materials, 11 (1999) 3359.
Hou, J., Kumar, R., Qu, Y. & Krsmanovic, D., Journal of Nanoparticle Research, 12 (2010) 563.
Hu, X., Garg, A. & Barber, Z. H., Thin Solid Films, 484 (2005) 188.
Kan, Y. M., Zhang, G. J., Wang, P. L. & Cheng, Y. B., Journal of the European Ceramic Society, 28 (2008) 1641.
Kan, Y., Jin, X., Wang, P., Li, Y., Cheng, Y.-B. & Yan, D., Materials Research Bulletin, 38 (2003) 567.
Kan, Y., Jin, X., Zhang, G., Wang, P., Cheng, Y. B. & Yan, D., Journal of Materials Chemistry, 14 (2004) 3566.
Kan, Y., Wang, P., Li, Y., Cheng, Y. B. & Yan, D., Materials Letters, 56 (2002) 910.
Kannan, C. V., Cheng, Z. X., Kimura, H., Shimamura, K., Miyazaki, A. & Kitamura, K., Journal of Crystal Growth, 292 (2006) 485.
Ke, H., Wang, W., Chen, L., Xu, J., Jia, D., Lu, Z. & Zhou, Y., Journal of Sol-Gel Science and Technology, 53 (2010) 135.
Kim, J. S. & Kim, S. S., Applied Physics A: Materials Science and Processing, 81 (2005) 1427.
Kim, J. S., Integrated Ferroelectrics, 79 (2006) 139.
Kim, Y. I. & Jeon, M. K., Materials Letters, 58 (2004) 1889.
Kojima, S. & Shimada, S., Physica B: Condensed Matter, 219-220 (1996) 617.
Kojima, S., Ferroelectrics, 239 (2000) 55.
Kojima, T., Yoshida, I., Uekawa, N. & Kakegawa, K., Journal of the European Ceramic Society, 29 (2009) 431.
Kong, L. B., Ma, J., Zhu, W. & Tan, O. K., Materials Letters, 51 (2001) 108.
Lazarevic, Z. Stojanovic, B. D. & Varela J. A., Science of Sintering, 37 (2005) 199.
Liang, K., Qi, Y. & Lu, C., Journal of Raman Spectroscopy, 40 (2009) 2088.
Lu, C. J., Qiao, Y., Qi, Y. J., Chen, X. Q. & Zhu, J. S., Applied Physics Letters, 87 (2005) 1.
Macedo, Z. S., Ferrari, C. R. & Hernandes, A. C., Powder Technology, 139 (2004) 175.
Newnham, R. E., Wolfe, R. W. & Dorrian, J. F., Materials Research Bulletin, 6 (1971) 1029.
Ng, S. H., Xue, J. & Wang, J., Journal of the American Ceramic Society, 85 (2002) 2660.
Park, B. H., Kang, B. S., Bu, S. D., Noh, T. W., Lee, J. & Jo, W., Nature, 401 (1999) 682.
Patil, K. C., Aruna, S. T. & Mimani, T., Current Opinion in Solid State and Materials Science, 6 (2002) 507.

Pookmanee, P. & Phanichphant, S., Journal of Ceramic Processing Research, 10 (2009) 448.
Pookmanee, P., Journal of Ceramic Processing Research, 9 (2008) 30.
Pookmanee, P., Uriwilast, P. & Phanichpant, S., Ceramics International, 30 (2004) 1913.
Rachna, S., Bhattacharyya, S. & Gupta, S. M., Materials Science and Engineering B: Solid-State Materials for Advanced Technology, 175 (2010) 207.
Santos, V. B., M'Peko, J. C., Mir, M., Mastelaro, V. R. & Hernandes, A. C., Journal of the European Ceramic Society, 29 (2009) 751.
Shi, Y., Cao, C. & Feng, S., Materials Letters, 46 (2000) 270.
Simões, A. Z., Stojanovic, B. D., Ramirez, M. A., Cavalheiro, A. A., Longo, E. & Varela, J. A., Ceramics International, 34 (2008) 257.
Stojanovic, B. D., Paiva-Santos, C. O., Cilense, M., Jovalekic, C. & Lazarevic, Z. Z., Materials Research Bulletin, 43 (2008) 1743.
Stojanovic, B. D., Paiva-Santos, C. O., Jovalekic, C., Simoes, A. Z., Filho, F. M., Lazarevic, Z. & Varela, J. A., Materials Chemistry and Physics, 96 (2006) 471.
Stojanovic, B. D., Simoes, A. Z., Paiva-Santos, C. O., Quinelato, C., Longo, E. & Varela, J. A., Ceramics International, 32 (2006) 707.
Subbarao, E. C., Journal of Physics and Chemistry of Solids, 23 (1962) 665.
Subbarao, E. C., Physical Review, 122 (1961) 804.
Sulaiman, M. A., Hutagalung, S. D., Ain, M. F. & Ahmad, Z. A., Journal of Alloys and Compounds, 493 (2010) 486.
Thongtem, T. & Thongtem, S., Ceramics International, 30 (2004) 1463.
Umar Al-Amani, A., Srimala, S., Ahmad Fauzi, M. N. & Khairunisak, A. R., Malaysian Journal of Microscopy, 6 (2010) 69.
Wang, C. M., Lin, S. Y., Kao, K. S., Chen, Y. C. & Weng, S. C., Journal of Alloys and Compounds, 491 (2010) 423.
Wang, X. S., Zhang, Y. J., Zhang, L. Y. & Yao, X., Applied Physics A: Materials Science and Processing, 68 (1999) 547.
Watcharapasorn, A., Siriprapa P. & Jiansirisomboon S., Journal of the European Ceramic Society, 30 (2010) 87.
Wu, D., Deng, Y., Mak, C. L., Wong, K. H., Li A. D., Zhang M. S. & Ming N. B., Applied Physics A: Materials Science and Processing, 80 (2005) 607.
Xiang, P. H., Kinemuchi, Y. & Watari, K., Materials Letters, 60 (2006) 2837.
Xie, L., Ma, J., Wu, P., Tian, H., Zhao, Z., Zhou, J., Hu, Y., Wang, Y., Tao, J. & Zhu, X., Materials Research Bulletin, 42 (2007) 389.
Xue, K. H., Celinska, J. & Paz De Araujo, C. A., Applied Physics Letters, 95 (2009)
Yan, H., Zhang, H., Zhang, Z., Ubic, R. & Reece, M. J., Journal of the European Ceramic Society, 26 (2006) 2785.
Yan, N. C. & Razak, K. A., Journal of Alloys and Compounds, 509 (2011) 942-947
Yang, B., Zhang, D. M., Zhou, B., Huang, L. H., Zheng, C. D., Wu, Y. Y., Guo, D. Y. & Yu, J., Journal of Crystal Growth, 310 (2008) 4511.
Yang, Q., Li, Y., Yin, Q., Wang, P. & Cheng, Y. B., Journal of the European Ceramic Society, 23 (2003) 161.
Yoneda, Y., Kohara, S. & Mizuki, J., Japanese Journal of Applied Physics, Part 1: Regular Papers and Short Notes and Review Papers, 45 (2006) 7556.

Zdujić, M., Jovalekić, Č., Poleti, D., Veljković, I. & Karanović, L., Journal of Non-Crystalline Solids, 352 (2006) 3058.

Zhi-hui, C., Jun-fu, Q., Cheng, L., Jian-ning, D. & Yuan-yuan, Z., Ceramics International, 36 (2010) 241.

Journal of Alloys and Compounds 509 (2011) 2936–2941

Contents lists available at ScienceDirect

Journal of Alloys and Compounds

journal homepage: www.elsevier.com/locate/jallcom

Synthesis of $(Bi_{0.5}Na_{0.5})TiO_3$ (BNT) and Pr doped BNT using the soft combustion technique and its properties

Khairunisak Abdul Razak*, Chiah Jun Yip, Srimala Sreekantan

School of Materials and Mineral Resources Engineering, Engineering Campus, Universiti Sains Malaysia, 14300 Nibong Tebal, Penang, Malaysia

ARTICLE INFO

Article history:
Received 28 September 2010
Received in revised form
11 November 2010
Accepted 19 November 2010
Available online 30 November 2010

Keywords:
Chemical synthesis
Ceramics
Dielectric response
Microstructure

ABSTRACT

In this work, bismuth sodium titanate $(Bi_{0.5}Na_{0.5})TiO_3$ (BNT) and praseodymium (Pr)-doped BNT were successfully produced using the soft combustion technique. The effects of Pr doping on stoichiometry, microstructure, density and dielectric properties were studied. Pure Pr-doped BNT was obtained in all samples containing 5, 10 and 20 mol% Pr after calcination at 800 °C for 3 h. The produced powders were then pressed into pellets and sintered at 1100 °C for 3 h. The very similar ionic radii of Pr^{3+} with Bi^{3+} and Na^+ made it possible to substitute both Bi and Na. The crystallite size and grain size decreased with increasing Pr amount because Pr acted as grain growth inhibitor, both for calcined powders and for sintered pellets. Maximum density was obtained in 5 mol% Pr-doped BNT, beyond which density decreased. The maximum dielectric constant of 756 was obtained in 5 mol% Pr-doped BNT and decreased at higher levels of Pr doping. Pr doped into BNT also caused a decrease in dielectric loss.

1. Introduction

Piezoelectric ceramics are important in many electronic applications due to their unique properties. Their ability to convert mechanical stress to electrical output and vice versa makes them attractive for use in electronic and mechanical devices such as capacitors, sensors, and ultrasonic detectors. However, most current piezoelectric ceramics are lead-based (e.g. PZT, PLZT), making them environmentally unfriendly and hazardous to health. Moreover, volatilization of the lead components at temperatures as low as 800 °C also causes degradation of their dielectric properties [1–3]. In order to overcome these problems, research widely seeks candidates for lead-free piezoelectric ceramics.

$Bi_{0.5}Na_{0.5}TiO_3$ (BNT) is a promising perovskite-structure lead-free piezoelectric material. This compound has a large remnant polarization of 38 $\mu C/cm^2$ with a coercive field (E_c) of 73 kV/cm at room temperature. It also has a high Curie temperature of 320 °C [4]. However, a pure BNT system has many problems. Sintered pure BNT shows significant grain growth as well as non-uniform grain size distribution and shape. The large coercive field of pure BNT causes difficulty during poling [5–7]. Furthermore, some researchers have found that the piezoelectric properties of a pure BNT system are not very good. The surface of BNT often becomes conductive, causing high loss. BNT also has been widely studied with the addition of K, $BiNa_xK_{1-x}TiO_3$ (BNKT) as piezoelectric material because this compound has better dielectric properties than BNT alone [8,9]. However, the electrical properties are still not comparable to those of Pb-based piezoelectrics.

Therefore, research pursues its search for a suitable dopant for BNT that would enhance its desirable properties. Dopant segregated cation vacancies as well as acceptor solutes at the grain boundaries are used to induce the space-charge region [7], thereby inhibiting grain growth. In addition, some electrical properties such as dielectric properties, piezoelectric coefficient, and loss tangent can be enhanced by tuning the concentration of dopant. Very little information on the effects of dopants on BNT exists. However, the considerable research that has been carried out on doping of other lead-free compounds can provide useful guidance. CuO, MnO, MnO_2 and ZnO have been doped into piezoelectric compounds to reduce sintering temperature and improve electrical properties of the compounds [1,2]. CuO doping has proven beneficial to improve densification of the product [2]. Mn doping in BNT has been found to decrease phase transition temperature and to increase the values of electromechanical coupling factors and the piezoelectric constant d_{33}.

Doping of some rare earth elements in lead-free piezoelectrics has also been studied. Nd_2O_3-doped 0.82BNT–0.18BKT showed an improved piezoelectric constant [10]. Doping of 0.3 wt.% Sm_2O_3 in $0.82Bi_{0.5}Na_{0.5}TiO_3$–$0.18Bi_{0.5}K_{0.5}TiO_3$ exhibited the optimum properties with high piezoelectric constant (d_{33} = 147 pC/N) and high planar coupling factor (k_p = 22.4%) [11]. Doping of rare earth elements in $(Na_{0.5}Bi_{0.5})_{0.93}Ba_{0.07}TiO_3$ resulted in an increase in diffuseness in phase transition and a decrease in depolarization temperature (T_d). The doping of La_2O_3 or Pr_2O_3 resulted in electrical

* Corresponding author. Tel.: +60 4 5996126; fax: +60 4 5941011.
E-mail address: khairunisak@eng.usm.my (K.A. Razak).

0925-8388/$ – see front matter © 2010 Elsevier B.V. All rights reserved.
doi:10.1016/j.jallcom.2010.11.163

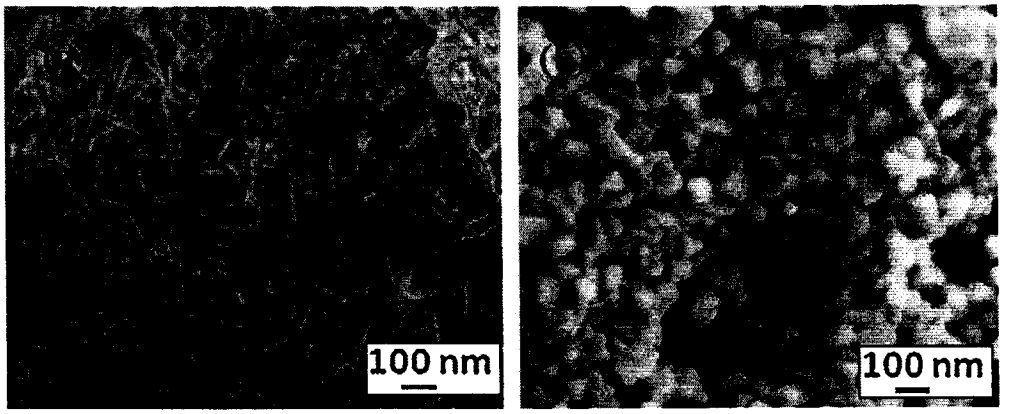

Fig. 1. SEM micrographs of BNT (a) as synthesized powders and (b) after calcination at 800 °C for 3 h.

properties following a soft doping effect. On the other hand, doping with Eu_2O_3 or Gd_2O_3 led to an abnormal change in the electrical properties, which was qualitatively interpreted as an internal stress effect [3]. Previous work has shown that Pr doping was beneficial in improving the dielectric properties of BIT [12].

BNT ceramic powder can be synthesized using a number of methods such as the solid state technique, the sol–gel technique, and the hydrothermal method [8,9,13–15]. The solid state method is limited by its requirement for a high sintering temperature (>1400 °C), causing Bi ion volatilization, which occurs at temperatures above 1130 °C [15]. Moreover, the solid state technique produces a powder with large particle size and a wide range particle size distribution. The sol–gel technique has been widely used to produce nanoparticles. However, the technique requires a long processing period and repeated heat treatment to obtain the desired products. The hydrothermal technique has the advantage of producing fine particle size. However, the stoichiometry of the products is dependent on the kinetics and thermodynamics of the elements during hydrothermal reaction. The soft combustion technique, in contrast, has the advantages of lower formation temperature, better homogeneity, a simple experimental set-up, relative inexpensiveness and production of fine size powders with a narrow particle size distribution range [12,16].

This work focused on the properties of BNT and praseodymium (Pr)-doped BNT synthesized using the soft combustion technique. BNT, a lead-free piezoelectric ceramic, was chosen for its environmental friendliness. The use of Pr as dopant was expected to improve the dielectric constant and reduce the grain size. Moreover, doping BNT with Pr was expected to result in homogenous grain growth and a narrower grain size distribution and shape. The soft combustion technique was selected for its low synthesis temperature, which minimizes volatilization of Bi.

2. Experimental details

BNT powder was prepared using the soft combustion technique. Bismuth nitrate and sodium nitrate were mixed and dissolved at 40 °C in 2-methoxyethanol. For Pr-doped BNT synthesis, praseodymium nitrate (5, 10, or 20 mol%) was mixed with bismuth nitrate and sodium nitrate. 1 mol of glycine was added into the solution to aid the combustion process. In parallel, 1 mol of titanium isopropoxide was dissolved separately in 2-methoxyethanol and acetylacetone. The acetylacetone functions as a chelating agent in the reaction. Next, the prepared titanium solution was continuously stirred into the prepared bismuth and sodium solution or Pr-doped bismuth sodium solution for 2 h, producing a yellowish homogeneous solution. The mixture was then heated to 130 °C on a hot plate with continuous stirring. Evaporation transformed the mixture into a viscous brownish solution. Continued heating at 130 °C led to combustion and the formation of foam. Next, the foam was ground using an agate mortar to form fine powder. The resulting powder was calcined at 800 °C for 3 h. The calcined powder was then pressed into pellets using 52.2 bar of pressure. The pellets were then sintered at 1100 °C for 3 h at a heating rate of 5 °C/min.

The microstructure of the samples was observed using scanning electron microscopy (FESEM; Zeiss SUPRA 35). Phase presence and stoichiometry of the samples were analyzed using X-ray diffractometer (XRD; Bruker AXS D8 Advance). Density of the samples was measured using Archimedes' method. For measurement of dielectric properties, silver paste was applied on both major surfaces of the sintered pellet, and capacitance and dielectric constant were measured using LCR meter (Agilent HP4284).

3. Results and discussion

In this work, $(Bi_{0.5}Na_{0.5})TiO_3$ (BNT) and Pr-doped BNT were produced using the soft combustion technique. Fig. 1(a) shows the SEM

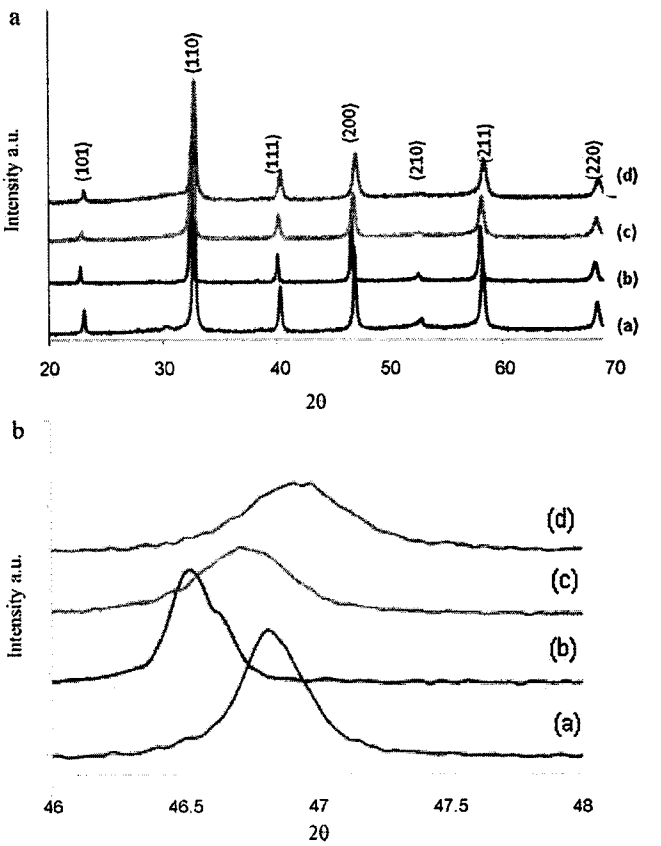

Fig. 2. XRD spectra of samples after calcination at 800 °C of (a) BNT, (b) 5 mol% Pr-doped BNT, (c) 10 mol% Pr-doped BNT and (d) 20 mol% Pr-doped BNT. [a] Wide scan XRD spectra and [b] XRD spectra of (2 0 0) peak position.

micrograph of BNT powder before calcination, showing the plate-like and pin-shaped BNT particles, indicating the lack of mutual solubility between the bismuth layer structure phase and the perovskite phase. The plate-like particles are the bismuth-layered phase whereas the smaller cubic or round particles with a size of 100 nm are regarded as perovskite. In Fig. 1(b), the SEM micrograph of BNT powder after calcination shows a distribution of nearly cubical or round particles. No plate-like particles appeared after calcination, indicating that calcination process fully transformed all bismuth layered phase into perovskite structure. A similar phenomenon was observed by Ma et al. [17]. They found that during the calcination process, some unwanted compounds such as water and carbon phases decomposed. At the same time, diffusion of ions occurred that led to the formation of pure compound with stable crystal structure. In this study, ions in the unstable bismuth-layered phase diffused and formed a more stable cubic or round particle with perovskite structure. The average particle size was around 140 nm.

The XRD spectra of BNT and BNT doped with varying amounts of Pr calcined in air at 800 °C for 3 h are shown in Fig. 2. A single perovskite phase was obtained for all Pr-doped BNT (JCPDS No. 36-340). At room temperature, pure BNT and Pr-doped BNT powders have rhombohedral symmetry. However, in the XRD spectra, rhombohedral structure is hard to distinguish due to the overlapping of peaks that could be due to nearly cubic lattice parameters. Although the crystal structure of BNT was rhombohedral, the diffraction lines were indexed based on the pseudocubic unit cell because of the small degree of rhombohedral distortion [18]. In BNT compound, the ionic radius of Bi is close to Na (1.03 Å and 1.02 Å, respectively), which causes a slight distortion of lattices [19]. Doping with Pr with ionic radius 1.013 Å in BNT caused a local lattice contraction that further distorts the lattices. However, since the ionic radii of those

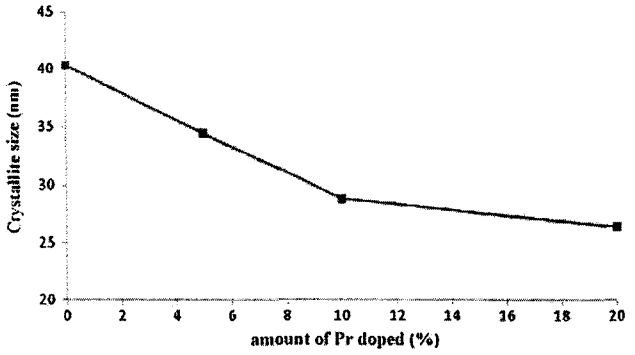

Fig. 3. Crystallite size of BNT doped with various levels of Pr after calcination at 800 °C for 3 h.

ions are very close, the changes in degree of lattice distortion are not obvious.

XRD spectra of Pr-doped BNT powders in Fig. 2[a] did not show any peak belonging to praseodymium oxide, which is taken to indicate the substitution of praseodymium ions into the perovskite lattice. The closeness of the ionic radii of the three elements enabled the ready substitution of Pr^{3+} ions for Bi^{3+} ions or Na^{+} ions into the perovskite lattice. Since the charge of Pr ions can be 2+ or 3+, Pr ions can substitute into the A-site in the BNT perovskite structure [7].

The XRD spectra of calcined BNT and Pr-doped BNT powders at the peak position (2 0 0) are shown in Fig. 2[b]. The peak position shift to the left was proportional to the level of Pr added. The result shows the change in the unit cell size that is caused by lattice distortion of BNT [4,19]. Some micro-strain occurred with the

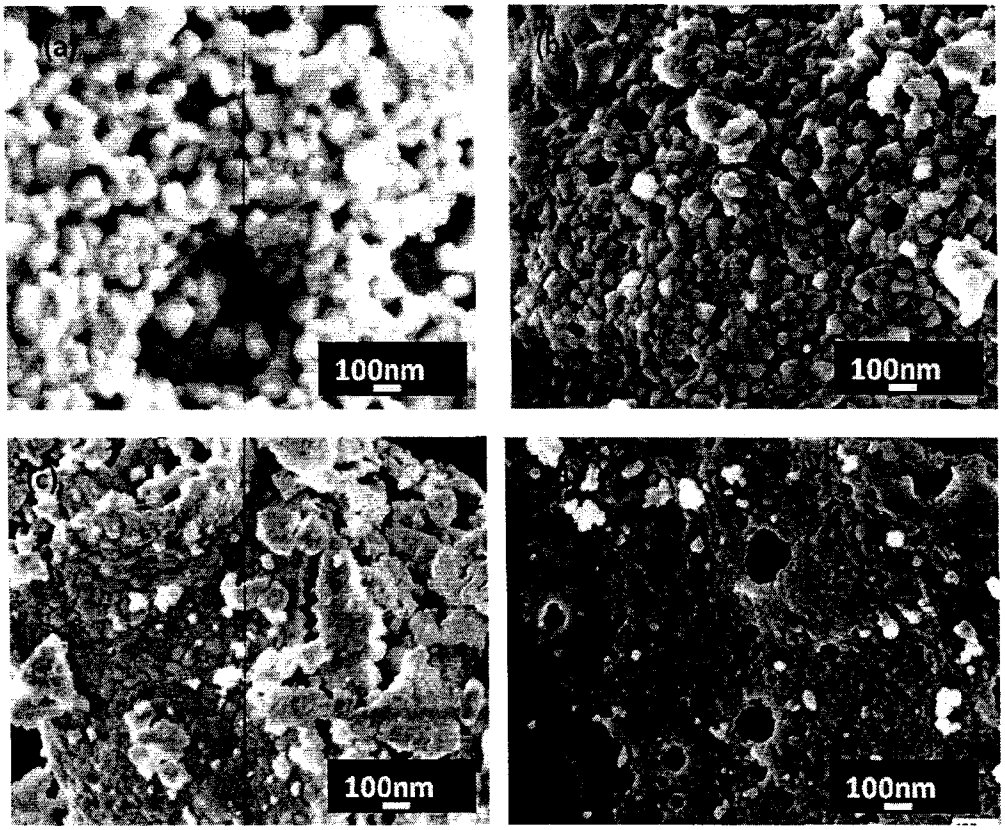

Fig. 4. SEM micrographs of (a) BNT, (b) 5 mol% Pr doping, (c) 10 mol% Pr doping and (d) 20 mol% Pr doping after calcination at 800 °C.

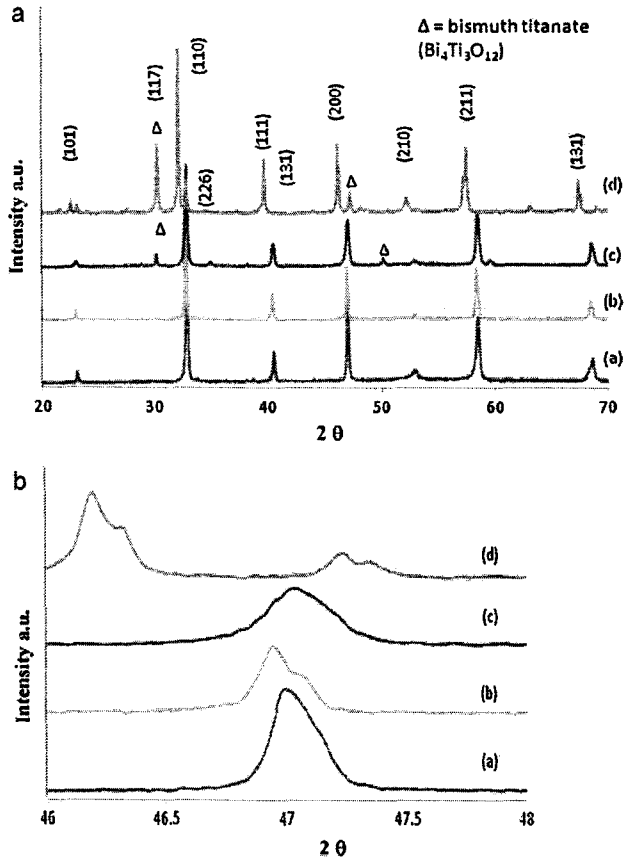

Fig. 5. XRD spectra of (a) BNT, (b) 5 mol% Pr doping, (c) 10 mol% Pr doping and (d) with 20 mol% Pr doping after sintering at 1100 °C. [a] Wide scan XRD spectra, [b] splitting of (*h* 0 *l*)- and (0 *k l*)-type reflections of (2 0 0) peak position.

doping of Pr to BNT. This micro-strain can be explained by Vegard's law, which suggests a linear relationship between the crystal lattice parameter and the concentration of the Pr dopant added. The increase of ion shift results in an increase of lattice energy to stabilize the structure. However, this increasing trend stopped at the 5 mol% level of Pr doping of BNT and started to shift to the right side with further addition of Pr. This result is in agreement with those of Lee et al. [16] and Liu et al. [14].

Fig. 2[b] shows that the intensity of the peak position (2 0 0) decreases with increasing concentration of Pr dopant. Pr-doped BNT was found to have a broader peak than that of undoped BNT, mainly because of compositional fluctuation or substitution disordering in the arrangement of cations at crystallographic sites in the lattice structure. Broadening of the peak indicates a decrease of crystallite size, which is confirmed by calculation using Scherrer's equation [$k = (0.9 \times \lambda)/(B \cos\theta)$], showing that crystallite size decreases with increasing amount of Pr, as shown in Fig. 3.

Fig. 4 shows the SEM micrographs of doped and undoped BNT after calcination at 800 °C. The grain size decreased gradually with increasing level of Pr doping. The SEM micrograph of undoped BNT shows the largest average grain size, around 215.86 nm. As levels of Pr dopant increased to 5, 10, 20 mol%, grain size decreased to 157.12 nm, 76.47 nm and 70.77 nm, respectively. In Pr-doped BNT, Pr acted as an inhibitor during the growth process. The slower diffusion rate of Pr ions than that of Bi ions caused Pr to inhibit the growth of grains [14].

The XRD spectra of BNT and Pr-doped BNT pellets sintered in air at 1100 °C for 3 h are shown in Fig. 5[a]. A single phase Pr-doped BNT was obtained up to the 5 mol% level of Pr doping (JCPDS No. 36-340). The secondary phase that was present in 10 mol% and 20 mol% Pr-doped BNT was bismuth titanate ($Bi_4Ti_3O_{12}$; BIT) (JCPDS No. 00-047-0398). When the amount of Pr dopant increased, the intensities of the BIT peaks became stronger, indicating that the secondary BIT phase became more dominant (with higher crystallinity) as the amount of dopant increased. When the amount of Pr dopant increased, more Pr^{3+} ions substituted Bi^{3+} ions, thus more bondless Bi^{3+} ions were available to react with Ti^{4+} and O^{2-} ions to form a greater amount of BIT phase.

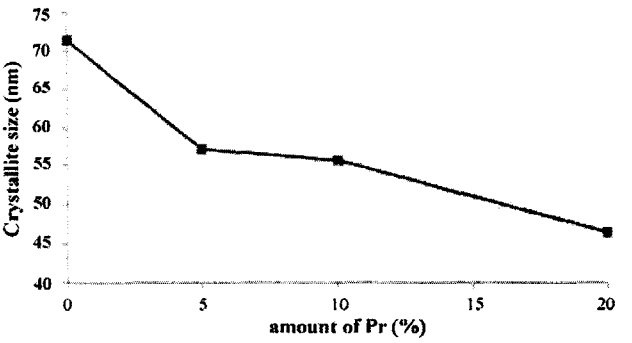

Fig. 6. Crystallite size of BNT and Pr-doped BNT after sintering at 1100 °C for 3 h.

Fig. 5[b] shows the XRD spectra of the splitting of (*h* 0 *l*)- and (0 *k l*) of BNT and Pr-doped BNT at $2\theta \sim 47°$. BNT and BNT doped with Pr at $x = 0.10$ do not show any peak splitting caused by (*h* 0 *l*)- and (0 *k l*)-type reflections. Normally, splitting is caused by lattice distortion [20]. The peaks can be assigned to a (2 0 0/0 2 0) peak splitting following a rhombohedral symmetry and a tetragonal symmetry. The splitting shows that Pr doping tends to change the lattice parameter and distort the position of ions in the lattice. The result indicates the coexistence of rhombohedral and tetragonal phases, which is consistent with the nature of the specimen with its morphotropic phase boundary composition [21].

Fig. 6 shows the crystallite sizes of BNT with different levels of Pr doping after sintering at 1100 °C. In general, crystallite size of BNT increased after sintering, as it did in powder after calcination. For each composition, crystallite size decreased with increasing Pr doping in BNT. Crystallite size of undoped BNT was 71.4 nm whereas crystallite size of 5 mol% Pr-doped BNT was 57.2 nm. As the level of Pr doping in BNT increased to 10 mol% and 20 mol%, crystallite size continued to decrease, to 55.6 nm and 46.5 nm, respectively. Similarly, Watcharapasorn and Jiansirisomboon [7] have reported that dysprosium doped into BNT can cause grains of BNT to become smaller. McLaughlin [21] has reported that grain growth during sintering was suppressed with small levels of additives, but larger levels of additives increased grain size. However, this study found that BNT doped with Pr up to 20 mol% still suppressed crystallite size.

Fig. 7 shows SEM micrographs of BNT doped with different levels of Pr after sintering at 1100 °C for 3 h. The grain size of Pr-doped BNT was found to be clearly smaller than that of undoped BNT. Undoped BNT had a large grain size of greater than 10 μm whereas BNT at the 5 mol% level of Pr doping showed a much smaller grain size (683.152 nm). Pr appears to have acted as a grain growth inhibitor that influences the diffusion process during sintering. This finding is in agreement with that of Watcharapasorn and Jiansirisomboon [7]. By doping with a small amount of Pr, grain size can be reduced as the diffusivity of Pr becomes lower than that of Bi. Although grain size decreased with increasing Pr level, the highest density was obtained in 10 mol% Pr doping (Fig. 8). The result could be due to the closely packed structure of the grains at that level of doping.

The relative dielectric constant and loss tangent were measured at 25 °C with an electric field of 1 V, as shown in Fig. 9. BNT showed

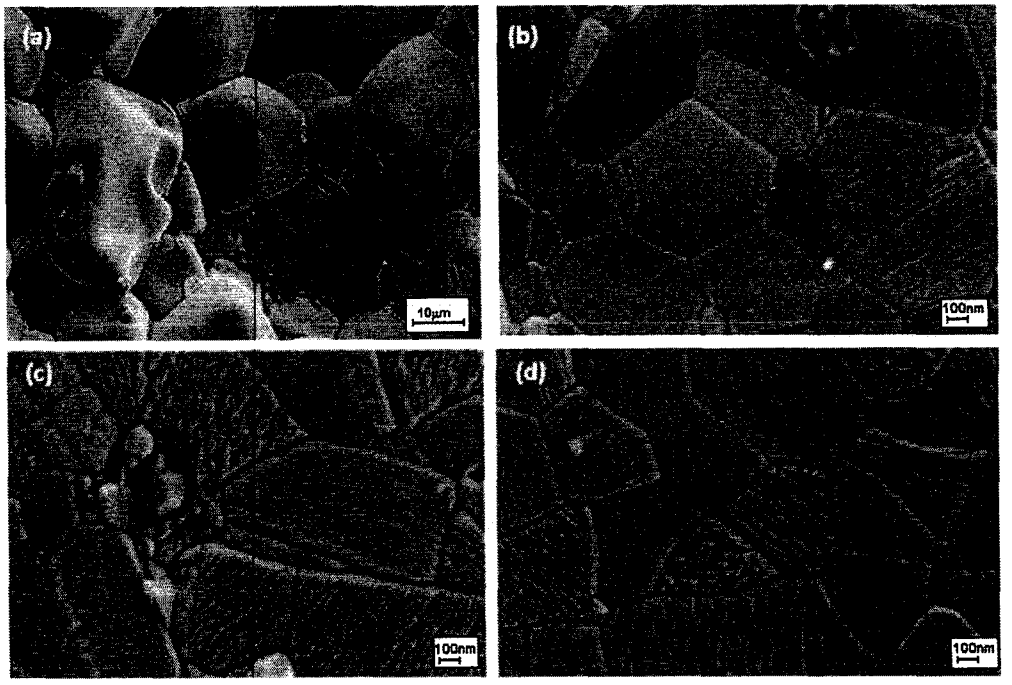

Fig. 7. SEM micrographs of (a) BNT, (b) 5 mol% Pr doping, (c) 10 mol% Pr doping and (d) 20 mol% Pr doping after sintering at 1100 °C for 3 h.

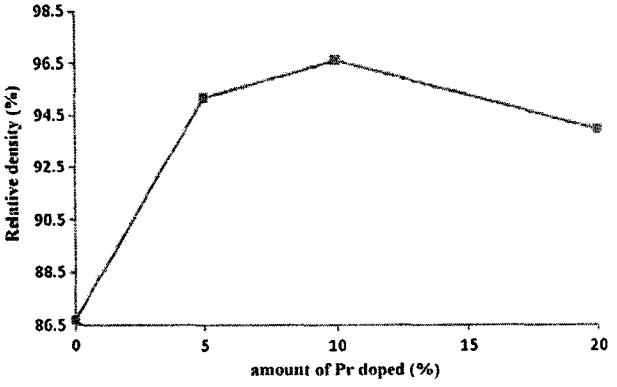

Fig. 8. Relative density of various amounts of Pr doped BNT after sintering at 1100 °C for 3 h.

the lowest dielectric constant value at only 347, whereas 5 mol% Pr-doped BNT had the highest dielectric constant value of 756. With Pr doping at a level higher than 5 mol%, the dielectric constant decreased. Pr-doped BNT improved the dielectric constant and reduced the loss tangent. The result could be explained by

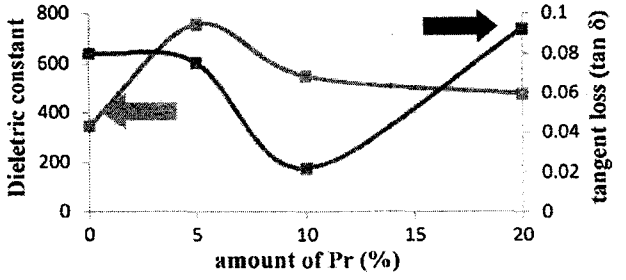

Fig. 9. Relative dielectric constant and loss tangent (tan δ) of (a) BNT, (b) 5 mol% Pr doping, (c) 10 mol% Pr doping and (d) 20 mol% Pr doping after sintering at 1100 °C for 3 h.

the presence of domains in the grains of the samples, influencing the dielectric properties. In BNT, large grains cause the presence of many 90° and 180° domains [19]. The presence of many domains in various directions suppressed the dielectric properties of the sample. At 5 mol% Pr doping, grain size was smaller than in BNT, causing lower domains presence in grains (Fig. 7). Therefore, dielectric properties of Pr-doped BNT were better than in BNT. However, further increase of Pr doping up to 20 mol% in BNT caused degradation of dielectric properties. This phenomenon was caused by the presence of stress in fine grains in ferroelectric region [19,22–25]. In large grains stress can be reduced by the arrangement of 90° domains. However, 90° domains are not present when grain size is fine. The absence of 90° domains in fine grains suppresses dielectric properties of whole samples due to the presence of unrelieved stress in the grains.

Pr doped BNT produced using soft combustion technique showed comparable dielectric constant value with other piezoelectric compounds such as $(K_{0.5}Na_{0.5})_{0.97}(Nb_{0.9}Ta_{0.1})O_3$ (ε_r = 890), $(PbMg_{1/3}Nb_{2/3})O_3$–$PbTiO_3$ (ε_r = 797) and $PbTiO_3$ (ε_r = 200) [26–28]. BNT produced in this work has lower dielectric constant compared to BNT produced using other techniques. The low dielectric constant value was caused by the small (submicron) grain size of the samples. In most research the grain size was larger than 5 μm [14,17,21]. The fine grains even after sintering could be beneficial in device miniaturization since the produced powders could be used as thick film instead of bulk pellets. Comparing with our previous work [12], BNT has a lower dielectric constant than that of BIT as a result of the substitution of Na for Bi. Up to 5 mol% Pr doped BNT enhanced the dielectric constant, but beyond that the dielectric constant decreased because Pr acted as grain growth inhibitor. On the other hand, the dielectric constant of Pr-doped BIT initially decreased up to 5 mol%, beyond which it increased. The result was due to increasing of grain size with increasing Pr doped BIT.

4. Conclusion

Pure BNT and Pr-doped BNT ceramic powders were successfully synthesized using the soft combustion technique after calcination

at 800 °C. However, after sintering at 1100 °C for 3 h, only 5 mol% Pr-doped BNT showed only a single phase while 10 and 20 mol% Pr-doped BNT showed the presence of secondary phase $Bi_4Ti_3O_{12}$. Grain size and crystallite size decreased with increasing Pr doping level because Pr acted at grain growth inhibitor. Optimum density was obtained with 10% Pr doping. The highest dielectric constant was obtained for 5 mol% Pr-doped BNT. The result could be due to the optimum grain size of the sample and the presence of a single phase in the compound.

Acknowledgments

The authors express sincere appreciation to the technical support of the School of Materials and Mineral Resources Engineering, Universiti Sains Malaysia. This research was supported by a Malaysian Research University grant 1001/PBahan/811069.

References

[1] X.P. Jiang, Y. Chen, K.H. Lam, S.H. Choy, J. Wang, J. Alloys Compd. 501 (2010) 323.
[2] D. Lin, K.W. Kwok, H.L.W. Chan, J. Alloys Compd. 461 (2008) 273.
[3] Q. Xu, M. Chen, W. Chen, H.-X. Liu, B.-H. Kim, B.-K. Ahn, J. Alloys Compd. 463 (2008) 275.
[4] L.F. Gao, Y.Q. Huang, Y. Hu, H.Y. Du, Ceram. Int. (2007) 1041.
[5] L. Huidong, F.F. Chude, Y. Wenlong, Mater. Lett. 58 (2004) 1194.
[6] X.X. Wang, K.W. Kwok, X.G. Tang, Solid State Commun. 129 (2004) 319.
[7] A. Watcharapasorn, S. Jiansirisomboon, Ceram. Int. 34 (2008) 769.
[8] Y. Hou, L. Hou, M. Zhu, H. Wang, H. Yan, Mater. Lett. 61 (2007) 3371.
[9] A. Ullah, C.W. Ahn, A. Hussain, I.W. Kim, Curr. Appl. Phys. 10 (2010) 1367.
[10] Y. Hou, B. Liu, L. Wei, Ceram. Int. 35 (2009) 1423.
[11] Y. Zhang, R. Chu, Z. Xu, J. Hao, Q. Chen, F. Peng, W. Li, G. Li, Q. Yin, J. Alloys Compd. 502 (2010) 341.
[12] P.Y. Goh, K.A. Razak, S. Sreekantan, J. Alloys Compd. 475 (2009) 758.
[13] M. Cernea, E. Andronescu, R. Radu, F. Fochi, C. Galassi, J. Alloys Compd. 490 (2009) 690.
[14] Y.F. Liu, Y.N. Lu, S.H. Dai, J. Alloys Compd. 484 (2009) 801.
[15] M. Raghavender, G.S. Kumar, G. Prasad, J. Phys. Chem. Solids 67 (2006) 1803.
[16] W.C. Lee, C.Y. Huang, L.K. Tsao, Y.C. Wu, J. Eur. Ceram. Soc. (2009) 1443.
[17] L. Ma, K. Zhao, J. Li, Q. Wu, M. Zhao, C. Wang, J. Rare Earth (2009) 496.
[18] E. Fukuchi, T. Kimura, J. Am. Ceram. Soc. (2002) 1461.
[19] N.N. Greenwood, A. Earnshaw, Chemistry of Elements, second ed., Butterworth Heinemann, 1998.
[20] Y.G. Wang, G. Xu, L.L. Yang, Z.H. Ren, X. Wei, W.J. Weng, P.Y. Du, G. Shen, G.R. Han, Ceram. Int. (2009) 1657.
[21] S.R. McLaughlin, PhD thesis, Queen's University Kingston, Ontario, 2008.
[22] C.R. Zhou, X.Y. Liu, Mater. Chem. Phys. (2008) 413.
[23] W. Cao, C.A. Randall, J. Phys. Chem. Solids 57 (1996) 1499.
[24] U. Helbig, J. Eur. Ceram. Soc. 27 (2007) 2567.
[25] M.-S. Yoon, N.H. Khansur, B.-K. Choi, Y.G. Lee, S.C. Ur, Ceram. Int. 35 (2009) 3027.
[26] D.W. Wua, R.M. Chen, Q.F. Zhou, K.K. Shung, D.M. Lin, H.L.W. Chan, Ultrasonics 49 (2009) 395.
[27] Q.F. Zhou, X.C. Xu, E.J. Gottlieb, L. Sun, J.M. Cannata, H. Ameri, M.S. Humayun, P.D. Han, K.K. Shung, IEEE Trans. Ultrason. Ferr. 54 (2007) 668–675.
[28] K.A. Snook, J.Z. Zhao, C.F. Alves, J.M. Cannata, W.H. Chen, R.J. Meyer, T.A. Ritter, K.K. Shung, IEEE Trans. Ultrason. Ferr. 49 (2002) 169.

Advanced Materials Research Vols. 148-149 (2011) pp 1619-1622
Online available since 2010/Oct/27 at www.scientific.net

doi:10.4028/www.scientific.net/AMR.148-149.1619

Synthesis and properties study of Pr doped $(Bi_{0.5}Na_{0.5})TiO_3$ produced using the soft combustion technique

Cheah Jun Yip[1,a], Khairunisak Abdul Razak[1,b], Srimala Sreekantan[1,c]

[1]School of Materials and Mineral Resources Engineering, Engineering Campus,
Universiti Sains Malaysia, 14300 Nibong Tebal, Penang, Malaysia
[a]jychiah@gmail.com, [b]khairunisak@eng.usm.my, [c]srimala@eng.usm.my

Keywords: bismuth sodium titanate, doping, soft combustion, dielectric

Abstract. In this work, Praseodymium (Pr) doped bismuth sodium titanate, $(Bi_{0.5}Na_{0.5})TiO_3$ (BNT) is successfully produced using the soft combustion technique. The effects of Pr doping on stoichiometry, microstructure, density and dielectric properties are studied. Pure phase can be obtained in all samples containing 0, 5, 10 and 20% Pr after calcination at 800°C for three hours. The powders are then pressed into pellets and sintered at 1050°C for three hours. The crystallite size and grain size decrease with increasing Pr amount because Pr acts as grain growth inhibitor. Maximum density is obtained in 5% Pr doped BNT, beyond which density decreasing. Maximum dielectric constant of 756 was obtained in 5% Pr doped BNT and decreases beyond that. Pr doped in BNT also causes dielectric loss to decrease. The result is in agreement with structural, microstructure and density analysis.

Introduction

Piezoelectric ceramics are important in many electronic applications due to its unique properties which can convert mechanical stress to electrical output and vice versa. However, most of piezoelectric ceramic materials nowadays are lead-based ceramics (e.g. PZT, PLZT) that are environmental unfriendly and hazardous to health. $Bi_{0.5}Na_{0.5}TiO_3$ (BNT) is a promising perovskite structure lead-free piezoelectric material [1]. A pure BNT is hard to be poled for it has large coercive field and relatively large conductivity. Therefore investigation on suitable dopant on BNT has been widely studied by many researchers [2]. BNT ceramic powder can be synthesized using various methods such as solid state technique, sol gel technique, and hydrothermal method [3, 4]. The solid state method has limitations such as requires high sintering temperature (>1400°C) that causes Bi ions volatilization occurs above 1130°C [5].

To solve this problem, the soft combustion technique is used in this work to produce BNT and Pr doped BNT. This technique has advantages of lower sintering temperature, better homogeneity, requires a simple experimental set up, relatively cheap, and capable to produce fine size powders with narrow particle size distribution range [6]. The soft combustion technique can reduce the synthesis temperature and hence minimize volatilization of Bi. The use of Pr dopant into BNT enhances dielectric properties and reduces the grain size.

Experimental details:

BNT powder was prepared using the soft combustion technique. A certain amount of praseodymium nitrate (0, 5, 10, 20 mol %), bismuth nitrate, sodium nitrate were mixed and dissolved at 40°C in 2-Methoxyethanol. Titanium isopropoxide was dissolved separately in 2-Methoxyethanol and acetylacetone. Both solutions were mixed and stirred for two hours. The mixture was then heated to 130°C on a hot plate with continuous stirring until combustion occurred and formed foam. The obtained powder was calcined at 800°C for 3 hours. The calcined powder was then pressed into pellets and sintered at 1100°C for 3 hours. Microstructures of the samples were observed using scanning electron microscopy (SEM). Phases presence and stoichiometry of the samples were analyzed using X-Ray Diffractometer (XRD). Density of the samples was

measured using Archimedes's method while capacitance and dielectric loss were measured using LCR meter.

Results and discussion

In this work, $(Bi_{0.5}Na_{0.5})TiO_3$ (BNT) and Pr doped BNT were produced using the soft combustion technique. Figure 1 (a) shows the SEM micrograph of BNT powder before calcination whereby BNT particle is in plate-like and pin shaped that shows lack of mutual solubility between bismuth layer structure phase and perovskite phase. The plate-like shape is the bismuth-layered phase whereas the smaller cubic or round particles with a size of 100 nm are regarded as the perovskite structure [7]. SEM micrograph of BNT powder after calcination shows nearly cubical or round shaped particle distribution (Figure 1(b)). There is no plate-like shaped particle appears which shows all bismuth layered phases are fully transformed into the perovskite structure. The average particles size is around 140 nm.

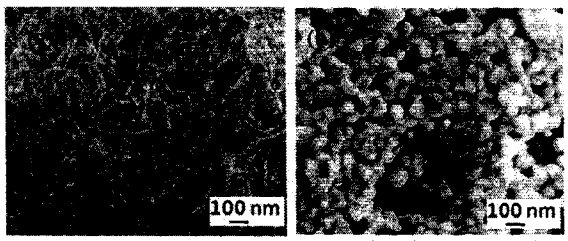

Figure 1: SEM micrographs of BNT; (a) as synthesized powders and (b) after calcination at 800°C.

The XRD spectra of BNT and Pr doped BNT powders calcined in air at 800°C for 3 hours are shown in Figure 2. Generally, a single perovskite phase without secondary phase is observed for Pr doped BNT. At room temperature, BNT and Pr doped BNT powders have rhombohedral symmetry. The diffraction lines were indexed based on the pseudocubic unit cell because of the small degree of rhombohedral distortion [8]. BNT powders did not show any peak which belong to Pr oxide. This observation proved that the Pr ions were substituted inside the perovskite lattice. The ionic radii of Pr^{3+}, Bi^{3+}, and Na^{+} were very close; 0.99 nm, 0.96 nm and 0.99 nm, respectively [9]. The close values of ionic radii made Pr^{3+} ions are readily substituted Bi^{3+} ions or Na^{+} ions in the perovskite lattice.

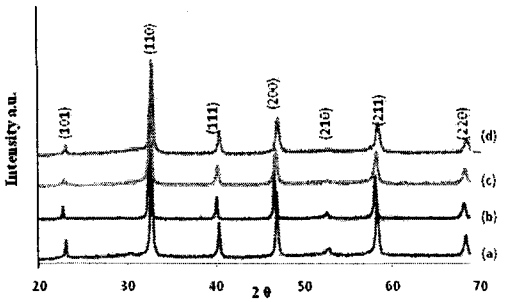

Figure 2: XRD spectra of samples after calcination at 800°C, (a) BNT, (b) 5% of Pr doped BNT, (c) 10% of Pr doped BNT, (d) 20% of Pr doped BNT.

Figure 3 shows the SEM micrographs of BNT and Pr doped BNT after calcination at 800°C. The grain size decreases gradually with increasing the amount of Pr. Undoped BNT has the largest average grain size of 215.86 nm. With increasing Pr dopant to 5, 10, 20 mol %, grain size decreases to 157.12 nm, 76.47 nm and 70.77 nm, respectively. The result proved that grain size decreased by doping with Pr. In Pr dope BNT, Pr acts as an inhibitor during the growth process. Slower diffusion rate of Pr than Bi ions cause Pr to inhibit the growth of grains [3].

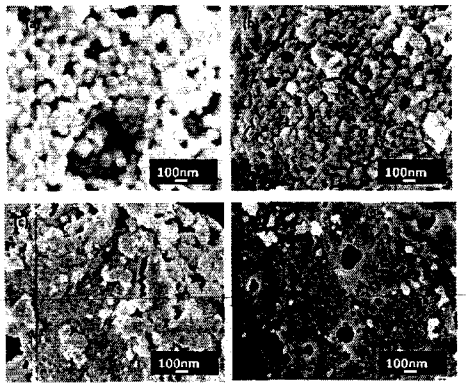

Figure 3: SEM micrographs of Pr doped BNT after calcination at 800°C, (a) BNT, (b) 5% Pr, (c) 10% Pr, and (d) 20% Pr.

Figure 4 shows the SEM micrographs of different amount of Pr doped on BNT after sintering at 1100°C. It is obvious that the grain size of Pr doped BNT is smaller compared to undoped BNT. BNT had a large grain size > 10μm whereas 5% of Pr doped showed smaller grain size (683.152 nm) compared to BNT. The result is in agreement with literature [2]. The effects of dopant are attributed to segregation of cation vacancies as well as acceptor solutes at the grain boundaries in which the space charge region is induced and this limits the movement of grain boundaries. By doping a small amount of Pr, the grain size can be reduced due to the diffusivity of Pr become lower compared to Bi.

The relative density results shows that 10% of Pr doped shows the highest relative density value which is 96.64% whereas undoped BNT sample shows the lowest relative density value of 86.69%. This indicates that Pr doped has improved the density of BNT. Above 10% of Pr doped BNT, density starts to decrease. 20% of Pr doped BNT has 93.92% relative density.

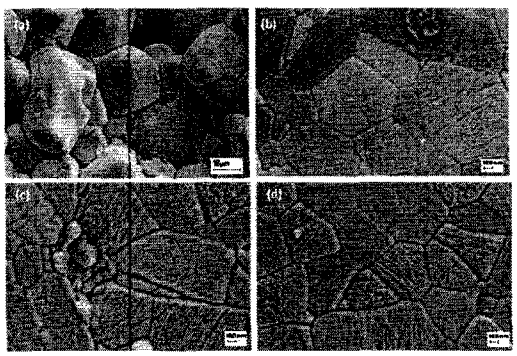

Figure 4: SEM micrographs of samples sintered at 1100°C, (a) BNT, (b) 5% of Pr doped BNT, (c) 10% of Pr doped BNT, and (d) 20% of Pr doped BNT.

The relative dielectric constant and tangent loss are shown in Figure 5. BNT shows the lowest dielectric constant value which is only 347, whereas 5% of Pr doped BNT has the highest dielectric constant value of 756. Beyond 5% Pr doping, dielectric constant decreases. Pr doped BNT improved the dielectric constant and reduced the loss tangent that are influenced by domains and the grain size of the samples. In general, a domain is proportional to the grain size. When grain size increases, more domains could exist and tangent loss could be influenced by domain wall [10]. However, increasing until 20% of Pr doped BNT the degradation of dielectric constant suddenly happen and loss tangent also increase that is due to unrelieved stress in the grains.

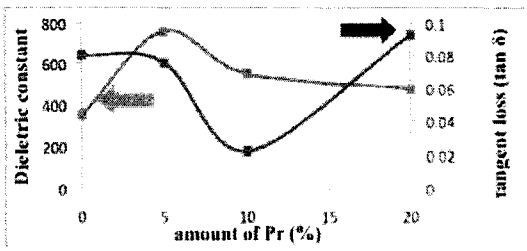

Figure 5: Relative dielectric constant and loss tangent (tan δ) of a) BNTS, b) 5% of Pr doped BNT, c) 10% of Pr doped BNT, d) 20% of Pr doped BNT after sintering at 1100°C.

Conclusion

Pure Pr doped BNT ceramic powders were successfully synthesized using the soft combustion technique after calcination at 800°C. Grain size and crystallite size decreased with increasing Pr amount because Pr acted at grain growth inhibitor. The highest dielectric constant was obtained for 5% Pr doped BNT that was in good agreement with structural, density and microstructure observation.

Acknowledgments

The authors appreciate technical support from School of Materials and Mineral Resources Engineering, Universiti Sains Malaysia. The research was supported by Research University grant 1001/PBahan/811069.

References:

[1] L.F. Gao, Y.Q. Huang, Y. Hu , H.Y. Du, Ceram. Int. (2007) p. 1041

[2] A. Watcharapasorn, S. Jiansirisomboon, Ceram. Int. Vol. 34 (2008) p.769

[3] Y.F.Liu, Y.N. Lu, S.H. Dai, J. Alloy. Compd. Vol. 484 (2009) p. 801

[4] M. Raghavender, G.S.Kumar, G. Prasad, J. Phys. Chem. Solids Vol. 67(2006) p. 1803

[5] M.Cernea, E.Andronescu, R.Radu, F.Fochi, C.Galassi, J. Alloy. Compd. Vol. 490(2009) p.690

[6] P.Y.Goh, K.A.Razak, S.Sreekantan, J. Alloy. Compd. Vol. 475 (2009) p. 758

[7] W.C.Lee, C.Y. Huang, L.K.Tsao, Y.C. Wu, J. Eur. Ceram. Soc. (2009) p. 1443

[8] E.Fukuchi, T.Kimura, J. Am. Ceram. Soc. (2002) p. 1461

[9] Y.G.Wang, G.Xu, L.L.Yang, Z.H. Ren, X.Wei, W.J.Weng, P.Y.Du, G.Shen, G.R. Han, Ceram. Int. Vol. 35 (2009) p. 1657

[10] S. R. McLaughlin (2008), Fabrication and Properties of Bi ½Na ½TiO$_3$ Based Ferroelectric Ceramics with Low Levels of B-site Additives, Queen's University Kingston, Ontario, Canada

Manufacturing Processes and Systems
doi:10.4028/www.scientific.net/AMR.148-149

Synthesis and Properties Study of Pr Doped(Bi_{0.5}Na_{0.5})TiO₃ Produced Using the Soft Combustion Technique

doi:10.4028/www.scientific.net/AMR.148-149.1619

Journal of Alloys and Compounds 509 (2011) 942–947

Contents lists available at ScienceDirect

Journal of Alloys and Compounds

journal homepage: www.elsevier.com/locate/jallcom

Properties of praseodymium-doped bismuth potassium titanate ($Bi_{0.5}K_{0.5}TiO_3$) synthesised using the soft combustion technique

Chai Yan Ng, Khairunisak Abdul Razak*

School of Materials and Mineral Resources Engineering, Universiti Sains Malaysia, 14300 Nibong Tebal, Penang, Malaysia

ARTICLE INFO

Article history:
Received 19 July 2010
Received in revised form
22 September 2010
Accepted 23 September 2010
Available online 1 October 2010

Keywords:
Ceramics
Chemical synthesis
Dielectric response
Microstructure

ABSTRACT

Bismuth potassium titanate ($Bi_{0.5}K_{0.5}TiO_3$; BKT) and praseodymium-doped BKT ($Bi_{0.5(1-x)}Pr_xK_{0.5}TiO_3$; BPKT) powders were synthesised using the soft combustion technique. Fine particles of 10–100 nm of BKT and BPKT were produced. A single phase BKT was obtained with a minimum of 0.5 mol of glycine. Various compounds of $Bi_{0.5(1-x)}Pr_xK_{0.5}TiO_3$ where $x = 0.01$, 0.03, 0.05, 0.10, 0.15 and 0.20 were prepared. Pure BKT and BPKT powders were obtained after calcination at 800 °C for 3 h. After sintering at 1050 °C for 5 h, pure BKT and BPKT pellets were obtained for $x = 0$ and 0.01. However, for BPKT with $x = 0.03$, 0.05, 0.10, 0.15 and 0.20, a minor amount of $Bi_4Ti_3O_{12}$ (BIT) secondary phase was present after sintering at 1050 °C for 5 h. The crystallite size and grain size of all the samples followed similar trends, first increasing from $x = 0$ (undoped BKT) to $x = 0.05$ and then decreasing above $x = 0.05$. Among the undoped and doped samples, BPKT with $x = 0.05$ had the highest dielectric properties ($\varepsilon_r = 713.87$) due to its large crystallite size (68.66 nm), large grain size (~435 nm) and high relative density (93.39%).

1. Introduction

Lead-based piezoelectric materials are known for their hazards to health and negative environmental impact. Moreover, because lead is volatile above 800 °C and thus can be more hazardous as it is released into the environment, researchers are actively seeking to replace lead with lead-free materials. Potassium sodium niobates ($K_{0.5}Na_{0.5}NbO_3$; KNN) and bismuth sodium titanate ($Bi_{0.5}Na_{0.5}TiO_3$; BNT) are among the most studied lead-free piezoelectric materials [1]. In addition, bismuth potassium titanate ($Bi_{0.5}K_{0.5}TiO_3$; BKT), a well-known Bi-based perovskite piezoelectric ceramic, is also one of the candidates for lead-free piezoelectrics due to its excellent electrical properties and high Curie temperature (T_c) of 380 °C. However, only a few studies on BKT ceramics have been reported. This lack of information may be due to the difficulty of producing a high density BKT ceramic because Bi and K are volatile at high sintering temperatures [2,3].

BKT powders have been prepared typically by common methods of solid state reaction [2,4,5], sol–gel technique [6,7] and hydrothermal technique [8]. The solid state reaction method has the advantages of ease of implementation and its ability to synthesise compounds in large amounts. However, the powders usually tend to agglomerate and have inhomogeneous particle size [6,9,10]. The sol–gel technique has excellent compositional control and homogeneity on the molecular level, yet the derived precipitates are amorphous in nature [6]. On the other hand, the hydrothermal technique is capable of yielding high-purity, fine crystalline powders [8]. Nevertheless, this synthesis in an aqueous environment causes water to be incorporated into the powder, thus causing deterioration in the electrical properties [11]. The soft combustion technique can produce fine particle size powder from the nanometre to the submicron scale and requires a low sintering temperature (1050 °C). Sintering at this lower temperature can minimise the volatilisation of Bi and K ions. Furthermore, this soft combustion technique requires only simple equipment, has a low cost and allows better control of stoichiometry [12]. Hence, the current work used the soft combustion technique to prepare the samples.

Furthermore, to improve the electrical properties of BKT, praseodymium (Pr) was doped in BKT to produce $Bi_{0.5(1-x)}Pr_xK_{0.5}TiO_3$ (BPKT). Pr is a lanthanide element that has a tendency to reduce the Bi and O vacancies in the BKT. In addition, Pr^{3+} has a six-coordinated ionic radius (0.99 Å), which is close to the ionic radius of Bi^{3+} (1.03 Å), suggesting that Pr ions may easily replace the Bi ions with a small lattice distortion [13]. In this paper, the morphologies, structural and dielectric properties of the BKT and BPKT are reported.

2. Experimental details

The $Bi_{0.5}K_{0.5}TiO_3$ (with 0.1, 0.3, 0.5, 1.0 and 1.5 mol of glycine) and $Bi_{0.5-x}Pr_xK_{0.5}TiO_3$ (with $x = 0.01$, 0.03, 0.05, 0.10, 0.15 and 0.20) powders were synthesised using the soft combustion technique. For preparation of the BKT powder, bismuth (III) nitrate pentahydrate [$Bi(NO_3)_3{\cdot}5H_2O$], potassium nitrate (KNO_3) and titanium (IV) isopropoxide {$Ti[OCH(CH_3)_2]_4$} were used as the starting materials

* Corresponding author.
E-mail address: khairunisak@eng.usm.my (K.A. Razak).

0925-8388/$ – see front matter © 2010 Elsevier B.V. All rights reserved.
doi:10.1016/j.jallcom.2010.09.136

for Bi, K and Ti, respectively. First, KNO_3 and $Bi(NO_3)_3{\cdot}5H_2O$ were dissolved in 25 ml of 2-methoxyethanol ($CH_3OCH_2CH_2OH$) at 40 °C. However, KNO_3 could not be fully dissolved in the solution. Thus, KNO_3 was first dissolved in 5 ml of deionised water before mixing with $Bi(NO_3)_3{\cdot}5H_2O$. In addition, to aid in the combustion process, glycine (H_2NCH_2COOH), which acts as a combustion fuel, was added into $Bi(NO_3)_3{\cdot}5H_2O$. On the other hand, $Ti[OCH(CH_3)_2]_4$ was dissolved separately in 25 ml of $CH_3OCH_2CH_2OH$, with 5 ml of acetylacetone ($CH_3COCH_2COCH_3$) as the chelating agent to stabilise the mixture. Then the $Ti[OCH(CH_3)_2]_4$ solution was added to the Bi–K solution with continuous stirring, and the final mixture was stirred for 2 h.

Next, the mixture was heated to 130 °C on a hot plate with continuous stirring. Evaporation occurred, and a sticky gel was formed, followed by a soft combustion process (exothermic chemical reaction that resulted in the production of flame) that formed foam. This foam was then crushed in a mortar to obtain a fine powder. This synthesised powder was calcined at 800 °C for 3 h with a heating rate of 5 °C min^{-1} and a cooling rate of 10 °C min^{-1}. After calcination, the powder was pressed at a pressure of 55 bar into pellets 12 mm in diameter. Finally, the pellets were sintered at 1050 °C for 5 h at a heating rate of 5 °C min^{-1} and a cooling rate of 10 °C min^{-1} in a closed alumina crucible. For the preparation of BPKT powder, praseodymium (III) nitrate hexahydrate [$Pr(NO_3)_3{\cdot}6H_2O$] was dissolved together with the $Bi(NO_3)_3{\cdot}5H_2O$ and H_2NCH_2COOH in the beginning, and the remaining steps were similar to those for the preparation of the BKT.

The powders and sintered pellets were analysed for the presence of phases using an X-ray diffractometer (Bruker AXS D8 ADVANCE) equipped with Cu Kα radiation from 20° to 70°. The morphology of powders and sintered pellets was observed using a field emission scanning electron microscope (Zeiss SUPRA 35) and transmission electron microscope (Philips CM 12). Crystallite size was measured using Rietveld refinement, and the density of sintered pellets was measured using the Archimedes method. The dielectric properties of the pellets were measured using a LCR meter (Agilent HP4284) at 1 MHz and 1 V. Prior to dielectric measurement, silver paste was applied on both surfaces of the pellets for ohmic contact.

3. Results and discussion

First, the BKT powder was produced without dissolving KNO_3 in deionised water. Fig. 1(a) shows the XRD pattern of the powder after calcination at 800 °C. This XRD spectrum shows the presence of a secondary phase in the compounds, indicating that the process did not form a single phase BKT. The BKT phase matched the ICDD number of 36-0339, whereas the secondary phase matched the ICDD number (72-1019) of bismuth titanate ($Bi_4Ti_3O_{12}$; BIT). It could have been that KNO_3 had not been fully dissolved in the solution, causing the formation of the secondary phase, so thereafter, KNO_3 was first dissolved in 5 ml of deionised water.

The XRD spectrum of the calcined powder is shown in Fig. 1(b). Like the powder that had not been dissolved in deionised water, the BKT dissolved in 5 ml of deionised water also contained the secondary phase of BIT. However, the BIT peaks were not obvious in the spectrum. The most obvious peak was (1 1 7). It could be that the low intensity XRD peak reflects the presence of only a very small amount of the BIT phase. Thereafter, to minimise the presence of the secondary phase, all subsequent powders were produced by

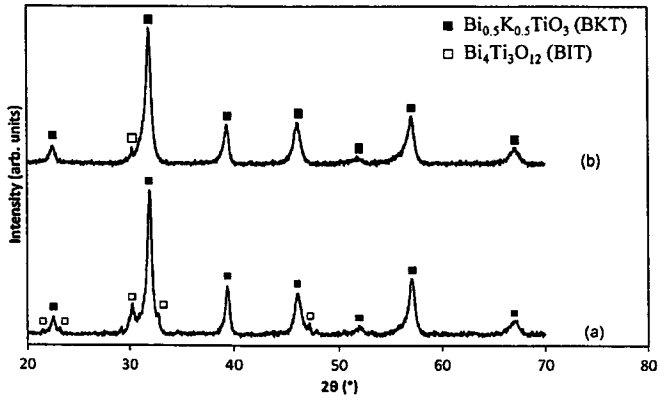

Fig. 1. XRD spectra of the BKT powders: (a) without dissolution in deionised water and (b) dissolved in 5 ml deionised water calcined at 800 °C.

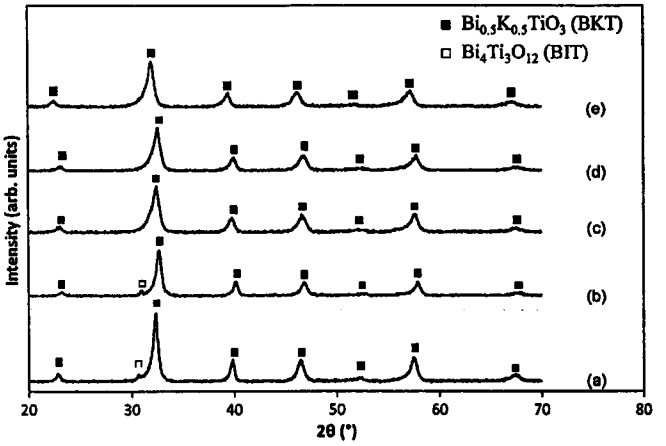

Fig. 2. XRD spectra of the BKT powders with: (a) 0.1 mol, (b) 0.3 mol, (c) 0.5 mol, (d) 1.0 mol and (e) 1.5 mol of glycine. All samples were calcined at 800 °C.

dissolving KNO_3 in 5 ml of deionised water during the preparation of BKT.

At this point, the calcined powder containing only a single phase BKT had not been obtained yet. It was thought that the presence of the secondary phase that remained even after dissolving KNO_3 in water could be due to incomplete combustion of the starting materials. Therefore, glycine (H_2NCH_2COOH) was added into the starting materials. Glycine is one of the most popular and attractive fuels for producing uniform composition and precisely controlled stoichiometry of complex oxide ceramic powders [14]. From the XRD spectra of BKT produced using various molar fractions of glycine (Fig. 2), it can be observed that the BKT synthesised with the addition of 0.1 and 0.3 mol of glycine, like the BKT synthesised without glycine, showed the presence of the secondary BIT phase. However, the BKT with 0.5, 1.0 and 1.5 mol of glycine showed the presence of only single phase BKT. The result indicates that the addition of a small amount of glycine (0.1 and 0.3 mol) was insufficient to enhance the combustion process, whereas a higher amount of glycine (0.5 mol and above) was sufficient to yield pure phase BKT. Thereafter, 0.5 mol of glycine was used to prepare the subsequent powders.

Fig. 3 shows the thermogravimetric analysis (TGA) curve of BKT powder with 0.5 mol of glycine. Weight losses were observed at 100–120 °C, 320–380 °C, 380–550 °C and 550–700 °C. Because water vaporises in the lowest temperature range, weight loss in this range was likely due to the loss of moisture from the sample. At 320–380 °C, the weight loss was likely due to the decomposition of organic substances. A gradual weight loss also occurred in the temperature range of 380–550 °C, also attributable

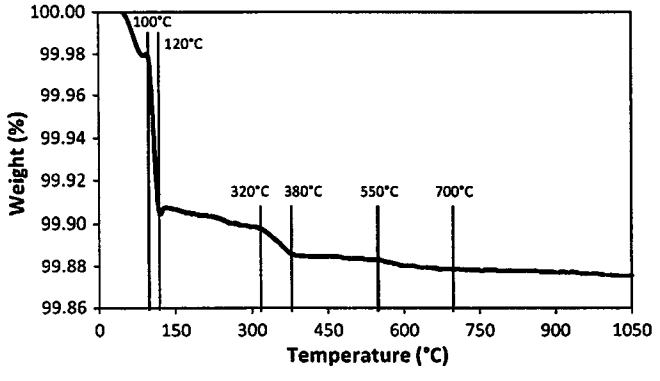

Fig. 3. TGA curve of the BKT powder with 0.5 mol of glycine.

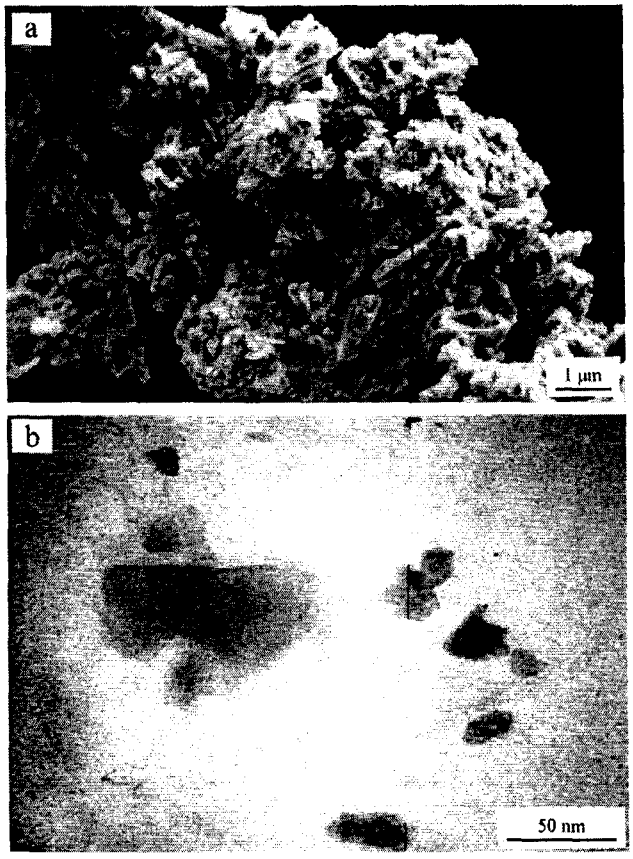

Fig. 4. (a) FESEM and (b) TEM micrographs of the calcined BKT powders produced using 0.5 mol of glycine.

to decomposition of physically and chemically absorbed water. Moreover, the decomposition of nitrate materials of $Bi(NO_3)_3{\cdot}5H_2O$ and KNO_3 also took place at this temperature [15]. In addition, weight loss was also observed at 550–700 °C. This weight loss could be due to the solid state reaction of the starting materials to

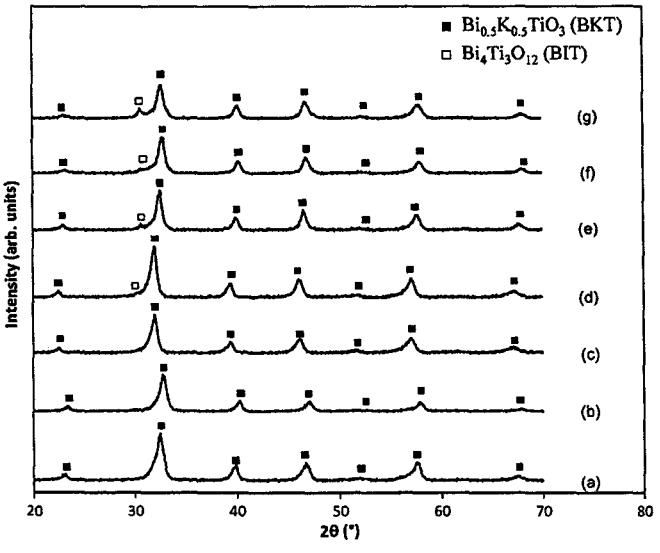

Fig. 5. XRD spectra of the BPKT powders with varying x calcined at 800 °C: (a) 0 (BKT), (b) 0.01, (c) 0.03, (d) 0.05, (e) 0.10, (f) 0.15 and (g) 0.20.

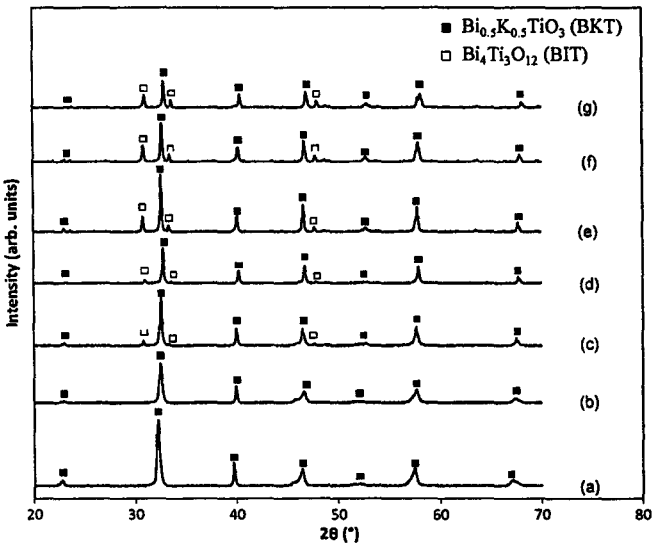

Fig. 6. XRD spectra of the BPKT pellets with varying x sintered at 1050 °C: (a) 0, (b) 0.01, (c) 0.03, (d) 0.05, (e) 0.10, (f) 0.15 and (g) 0.20.

form BKT powder. Above 700 °C, there was no measurable weight change of the powder. This finding implies that complete reaction occurred at this temperature and formed BKT [15,16]. Hence, in this research the calcination temperature of BKT powder was set above 700 °C. The FESEM and TEM micrographs of the BKT powders (with 0.5 mol of glycine) after calcination at 800 °C are shown in Fig. 4. The BKT powders have flake-like particles in the range of 10–100 nm.

In this study, various amounts of Pr (x = 0.01, 0.03, 0.05, 0.10, 0.15, 0.20) were added to BKT to obtain $Bi_{0.5-x}Pr_xK_{0.5}TiO_3$ (BPKT). Fig. 5 shows the XRD spectra of the undoped BKT and various BPKT powders calcined at 800 °C. The BPKT with x = 0.01 and 0.03 show only single phase BPKT, indicating that the Pr^{3+} in the BPKT did not form a secondary phase or separate from the interior grain but instead dissolved into the perovskite lattice [17]. However, as the x increased (x = 0.05, 0.10, 0.15, 0.20), the secondary phase of BIT appeared. For the BPKT (x = 0.01) and BPKT (x = 0.03), the amount of Pr added was lower, and thus the secondary phase of BIT was not formed, whereas for the BPKT with x = 0.05, 0.10, 0.15 and 0.20, a small amount of the secondary phase was formed. The formation of the secondary BIT phase was due to the high level of Pr doping. When Pr was added to BKT, the Pr^{3+} substituted the Bi^{3+}, and these bondless Bi^{3+} ions then reacted with Ti^{4+} and O^{2-} to form

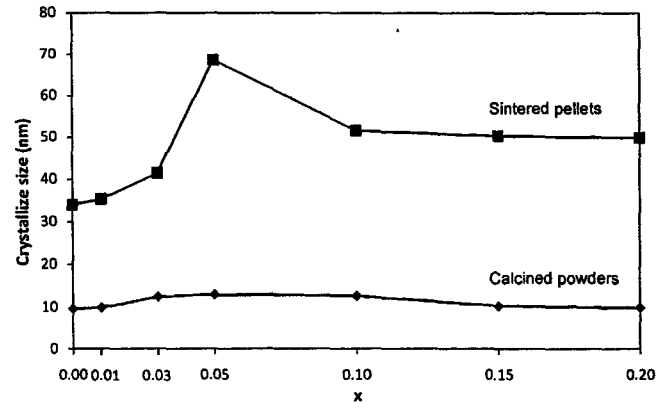

Fig. 7. Crystallite size of the calcined powders and sintered pellets of BKT and BPKT.

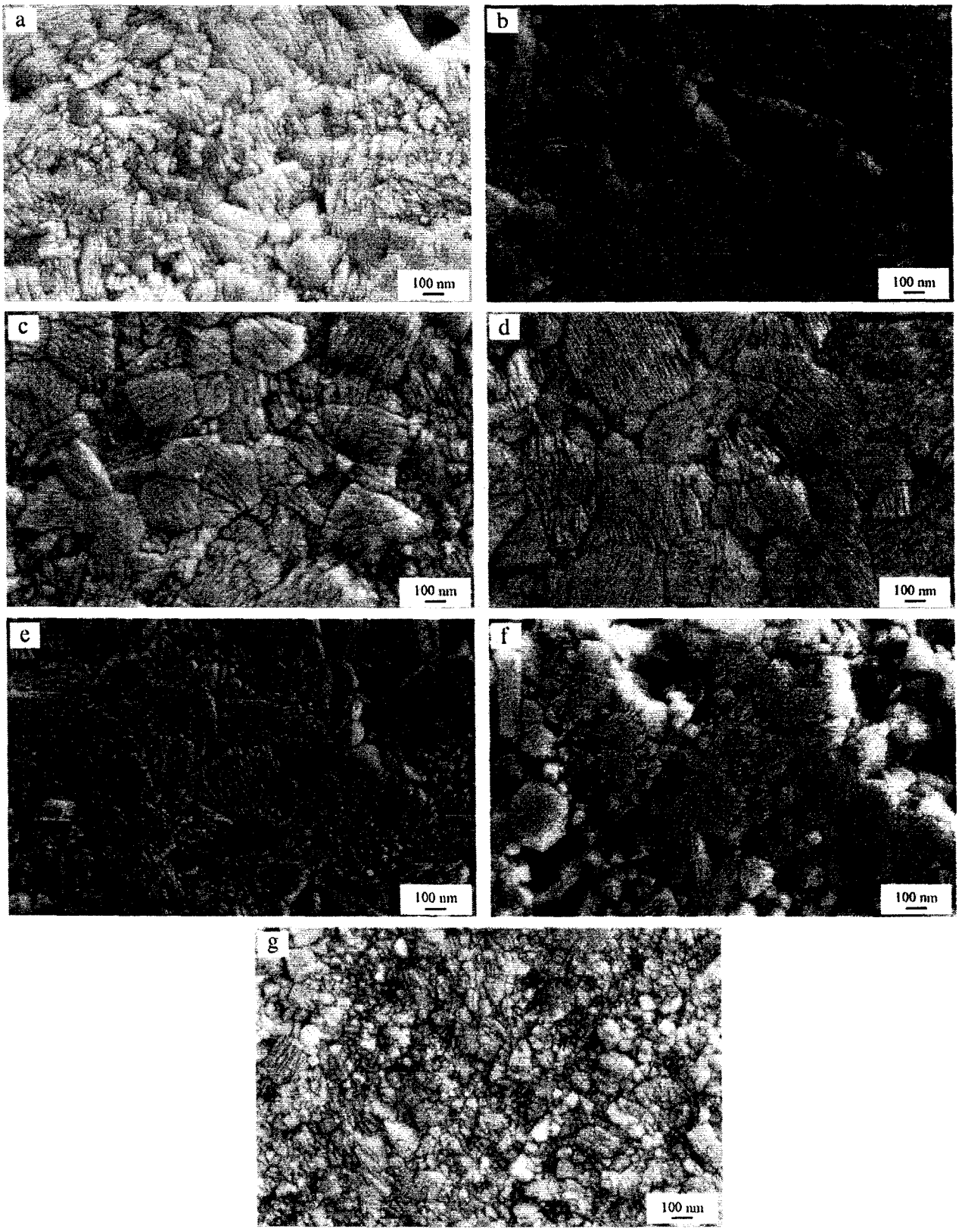

Fig. 8. FESEM micrographs of the BPKT with varying x: (a) 0, (b) 0.01, (c) 0.03, (d) 0.05, (e) 0.10, (f) 0.15 and (g) 0.20.

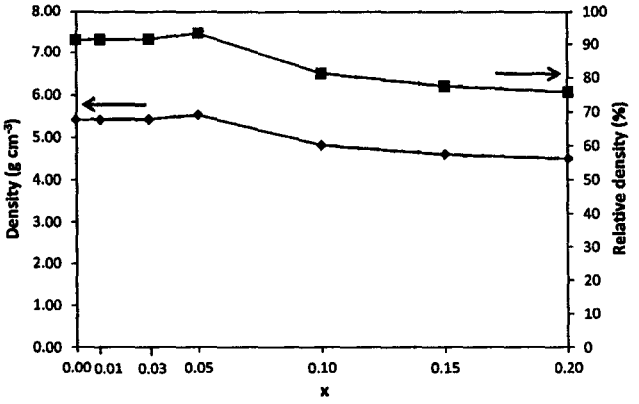

Fig. 9. Density and relative density of the sintered pellets.

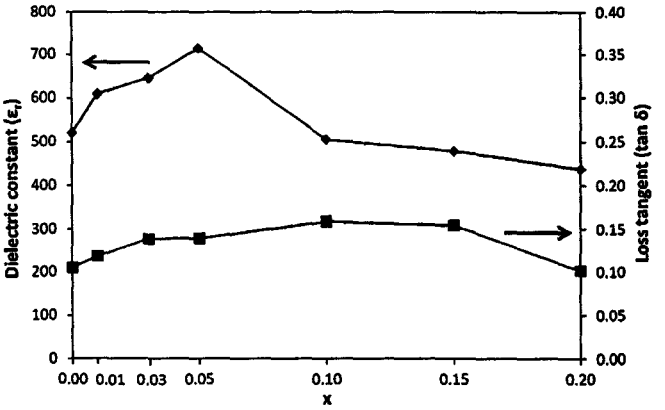

Fig. 10. Dielectric properties of BPKT with varying x.

BIT. The formation of the secondary BIT phase is not typical in BKT formation. Previous studies found the formation of BKT contained secondary phases of $Bi_2Ti_2O_7$ [18], $K_4Ti_3O_8$ [4], $K_2Ti_4O_9$ [2] and $K_2Ti_6O_{13}$ [2]. The presence of the BIT secondary phase could be explained by the volatilisation of K^+ and Bi^{3+} during the sintering process.

These calcined powders were then pressed into pellets and sintered at 1050 °C for 5 h. Fig. 6 shows the XRD spectra of the sintered BKT and BPKT pellets. These XRD spectra show that only the BKT and BPKT ($x = 0.01$) contained pure phase BKT and BPKT with no evidence of the presence of the secondary phase. For the BPKT pellets with $x = 0.03$, 0.05, 0.10, 0.15 and 0.20, the secondary phase of BIT was present. As the amount of Pr dopant increased, the intensities of the peaks for the BIT phase became stronger, indicating that the secondary BIT phase became more dominant (with higher crystallinity) as the amount of dopant increased. As the amount of Pr dopant increased, more Pr^{3+} were substituted for the Bi^{3+}; thus, more bondless Bi^{3+} were available to react with Ti^{4+} and O^{2-}, resulting in the formation of more BIT. Moreover, K also evaporates at the sintering temperature used. Hence, lower levels of K can lead to the formation of a more stable BIT.

The crystallite size of the calcined powders and sintered pellets was in the range of 9.66–13.01 nm and 33.98–68.66 nm, respectively. The plots of the crystallite size of calcined powders and sintered pellets against the amount of Pr (x) are shown in Fig. 7. It can be observed that the crystallite size of both calcined powders and sintered pellets increased from $x = 0$ to $x = 0.05$ and then decreased from $x = 0.05$ to $x = 0.20$. Because the BKT was doped with small amounts of Pr ($x = 0.01$–0.05), the Pr ions diffused into the BKT and assisted the growth of the grains. However, when the amount of Pr increased to $x = 0.10$, an obvious secondary BIT phase was formed. It is believed that this BIT phase acted as a grain growth inhibitor, thus suppressing the crystallite growth of the BPKT phase [12,19,20]. In addition, it can be seen that the crystallite size in the sintered pellets was larger than that in the calcined powders, probably because ion diffusion during the sintering process caused crystallite growth.

The FESEM micrographs of the sintered BKT and BPKT pellets are presented in Fig. 8. The grains showed no particular shape. The grain sizes of the BPKT increased when $x = 0$ (100–300 nm) to $x = 0.05$ and decreased between $x = 0.05$ and $x = 0.20$. The BPKT with $x = 0.05$ had the largest grain sizes, averaging 435 nm. This trend toward changing grain sizes aligns with the trend toward changing crystallite size that was observed in XRD analysis. This similarity is expected because crystallite size normally increases as grain size increases [12,21].

Fig. 9 shows the plots of density and relative density of the sintered pellets against x. The densities of the pellets increased from $x = 0$ to $x = 0.05$ and then decreased from $x = 0.05$ to $x = 0.20$. It could be that the addition of Pr caused the formation of close-packed microstructures with increasing grain size. The decrease in density was likely due to the decreasing grain size from $x = 0.05$. In addition, the decreasing density could be caused by the presence of more secondary phase.

The dielectric constant (ε_r) and loss tangent ($\tan\delta$) of the sintered pellets were found to be in the range of 437.19–713.87 and 0.1014–0.1589, respectively (Fig. 10). The ε_r increased up to $x = 0.05$ and decreased beyond $x = 0.05$. The undoped BKT had an ε_r of 520.1, while the BPKT ($x = 0.05$) had the highest ε_r of 713.87. This ε_r trend aligns with the trends of crystallite sizes and grain sizes, which is expected because the ε_r always increases with increasing grain sizes [5]. It is known that the electrical properties of ferroelectric ceramics are highly dependent on the grain size and microstructure of the samples [12]. As the ferroelectric ceramic was cooled through the T_c, stress appeared in the system. These stresses within the grains can be released or reduced by the formation of an appropriate arrangement of 90° domains. For larger grains, most of the stresses can be relieved with this mechanism. On the other hand, as the grain size decreases, the domains also become smaller. This domain width is roughly proportional to the square root of the grain size. The number of domains in a grain decreases as the square root of the grain size, and thus the smaller the grain, the larger the unrelieved stress [21–23]. Furthermore, the decrease of ε_r between $x = 0.05$ and $x = 0.20$ could also be due to the poor density. It is well known that low density ceramics have low ε_r as well. The values of $\tan\delta$ increased from $x = 0$ to $x = 0.10$ and then decreased from $x = 0.10$ to $x = 0.20$. The BPKT ($x = 0.05$) had the highest ε_r and an acceptable $\tan\delta$ of 0.1391, indicating that this BPKT can be used as a capacitor and in ferroelectric and piezoelectric devices.

4. Conclusions

BKT and BPKT were successfully produced using the soft combustion technique. The optimum amount of glycine added to aid the combustion reaction was found to be 0.5 M. Pure BPKT was obtained up to $x = 0.01$. Above that level, the ferroelectric compound BIT was formed. BPKT with $x = 0.05$ showed the optimum dielectric properties with a dielectric constant of 713.87 and $\tan\delta$ of 0.1391. The result was in agreement with the largest crystallite size and grain size, and the highest density was observed for BPKT with $x = 0.05$.

Acknowledgements

The authors express their sincere appreciation to the technical support of the School of Materials and Mineral Resources Engineering, Universiti Sains Malaysia. This research was supported by Research University grant 1001/PBahan/811069.

References

[1] L. Chen, H. Fan, M. Zhang, C. Yang, X. Chen, J. Alloys Compd. 492 (2010) 313–319.
[2] J. Konig, M. Spreitzer, B. Jancar, D. Suvorov, Z. Samardzija, A. Popovic, J. Eur. Ceram. Soc. 29 (2009) 1695–1701.
[3] T. Wada, A. Fukui, Y. Matsuo, Jpn. J. Appl. Phys. 41 (2002) 7025–7028.
[4] P.V.B. Rao, E.V. Ramana, T.B. Sankaram, J. Alloys Compd. 467 (2009) 293–298.
[5] Y. Hiruma, H. Nagata, T. Takenaka, Jpn. J. Appl. Phys. 46 (2007) 1081–1084.
[6] Y.D. Hou, L. Hou, S.Y. Huang, M.K. Zhu, H. Wang, H. Yan, Solid State Commun. 137 (2006) 658–661.
[7] X. Huang, Z. Yang, L. Sun, Q. Xie, B. Li, J. Zhou, L. Li, Mater. Chem. Phys. 114 (2009) 23–25.
[8] M.M. Lencka, M. Oledzka, R.E. Riman, Chem. Mater. 12 (2000) 1323–1330.
[9] X. Chen, Y. Liao, H. Wang, L. Mao, D. Xiao, J. Zhu, Q. Chen, J. Alloys Compd. 493 (2010) 368–371.
[10] H. Zhang, S. Jiang, K. Kajiyoshi, J. Alloys Compd. 495 (2010) 173–180.
[11] J.G. Lisoni, F.J. Piera, M. Sanchez, C.F. Soto, V.M. Fuenzalida, Appl. Surf. Sci. 134 (1998) 225–228.
[12] P.Y. Goh, K.A. Razak, S. Sreekantan, J. Alloys Compd. 475 (2009) 758–761.
[13] S.S. Kim, W.J. Kim, Thin Solid Films 484 (2005) 303–309.
[14] S.T. Aruna, A.S. Mukasyan, Curr. Opin. Solid State Mater. Sci. 12 (2008) 44–50.
[15] J. Hao, X. Wang, R. Chen, L. Li, Mater. Chem. Phys. 90 (2005) 282–285.
[16] C.S. Chou, J.H. Chen, R.Y. Yang, S.W. Chou, Powder Technol. 202 (2010) 39–45.
[17] U. Chon, J.S. Shim, H.M. Jang, J. Appl. Phys. 93 (2003) 4769–4775.
[18] Y. Zhang, X. Zheng, T. Zhang, L. Gong, S. Dai, Y. Chen, Sens. Actuators B: Chem. 147 (2010) 180–184.
[19] S. Kuharuangrong, J. Mater. Sci. 36 (2001) 1727–1733.
[20] H. Zhang, S. Jiang, K. Kajiyoshi, J. Xiao, J. Am. Ceram. Soc. 93 (2010) 750–757.
[21] V. Buscaglia, M.T. Buscaglia, M. Viviani, L. Mitoseriu, P. Nanni, V. Trefiletti, P. Piaggio, I. Gregora, T. Ostapchuk, J. Pokorny, J. Petzelt, J. Eur. Ceram. Soc. 26 (2006) 2889–2898.
[22] A.J. Moulson, J.M. Herbert, Electroceramics: Materials, Properties, Applications, 2nd edition, John Wiley & Sons, 2003.
[23] Z. Zhao, V. Buscaglia, M. Viviani, M.T. Buscaglia, L. Mitoseriu, A. Testino, M. Nygren, M. Johnsson, P. Nanni, Phys. Rev. B 70 (2004) 024107-1–124107-8.

The effects of combustion agent on the formation of Bi-based compounds synthesized using the soft combustion technique

Khairunisak Abdul Razak*, Mohamad Afifi Anuar

School of Materials and Mineral Resources Engineering, Engineering Campus, Universiti Sains Malaysia, 14300 Nibong Tebal, Penang, Malaysia

*Email: khairunisak@eng.usm.my

ABSTRACT

In this work, 20 % Pr doped bismuth sodium titanate (PBNT) powders were synthesized using the soft combustion technique. Various combustion agents such as polyethylene glycol 200, citric acid and glycine with 0.2, 2 and 5 mol, respectively, were used to prepare PBNT samples. A single phase PBNT could be obtained with the addition of 5 mol % citric acid. In general, crystallite size increased with increasing sintering temperature. Dielectric properties increased with increasing densities. The optimum properties were obtained for PBNT with 5 mol % citric acid sintered at 1100°C for 3 hours which gave high dielectric constant (1153.20), acceptable loss tangent (0.1074) and high relative density (95.03).

Introduction

Lead-based ceramics have been widely used for many electronic and industrial applications. However, the toxicity of lead-based ceramics which is hazardous to health and environment causes a new material is sought after. Bismuth sodium titanate, $Bi_{0.5}Na_{0.5}TiO_3$ (BNT) is an excellent candidate as a key lead-free piezoelectric material [1,2]. BNT ceramic powder has been synthesized using various methods such as conventional solid-state reaction, sol gel and hydrothermal methods. Those methods have limitations such as high temperature processing, none homogeneous, and large particles size distribution. To overcome these problems, in this work a soft combustion technique was used [3,4]. The effects of three types of combustion agents which are Polyethylene

The $(Bi_{0.5}Na_{0.5})_{(1-x)}Pr_xTiO_3$ (x=0.2) with 0.2, 2 and 5 mol of PEG 200, citric acid and glycine, respectively, were synthesized using the soft combustion technique. The details of synthesis details were as our previous works [3, 4]. The as- synthesized powders were then calcined at 800°C. After calcination process, the powder was pressed into pellets and sintered at 1100°C.

Results and discussion

In this work, PBNT with varying combustion agent concentrations were produced using the soft combustion technique. Fig. 1 shows the XRD spectra of PBNT after calcination in air at 800°C. A pure phase PBNT was obtained for the sample synthesized using 5 mol citric acid.

For samples synthesized using PEG, the secondary phase exists which is $Bi_4Ti_3O_{12}$ (JCPDS No. 47-0398) but the intensity of the $Bi_4Ti_3O_{12}$ decreased with increasing PEG concentration. When Pr was added into BNT, the Pr^{3+} substituted the Bi^{3+}. These bondless Bi^{3+} were then reacted with Ti^{4+} and O^{2-}, and formed the BIT phase [4]. Similar results was obtained for glycine and citric acid combustion agents.

The crystallite size of the calcined powders and sintered pellets for all the combustion agents are in the range of 17.20-33.73 nm and 36.98-68.92 nm, respectively (Fig. 2). Crystallite size of PBNT after sintering increased compared to powder after calcination process due to crystal growth. For calcined powders, it can be observed that 0.2 mol% PEG combustion agent produced smaller crystallite size compared to citric acid and

vapor pressure of bismuth and that of praseodymium near 670°C are 10^{-2} and 10^{-10} Torr, respectively. Hence, the substitution of Pr ions with Bi ions suppress the grain growth of PBNT. This phenomenon occurred due to the lower diffusivity of Pr.

The dielectric constant (ε_r) and loss tangent (tan δ) of the sintered pellets were found to be in the range of 379.72 to 1280.51 and 0.0226 to 0.1074, respectively. For samples produced using PEG and glycine, the dielectric constant increased as the combustion agents concentration increased. The result could be due to the homogeneity of grains. While for citric acid, it shows that the dielectric constant decreased as the combustion agents concentration increased.

For loss tangent, it shows that the value increasing for samples produced using citric acid and glycine, and decreasing for sample produced using PEG. Hence, it indicates that combustion agents had improved the dielectric constant and reduced the loss tangent.

Conclusion

PBNT was successfully synthesized using the soft combustion technique. The optimum properties was obtained for sample synthesized using 5 mol of citric acid with optimum crystallite size (40.04 nm), dielectric constant (1153.20) and acceptable tan δ of 0.1074.

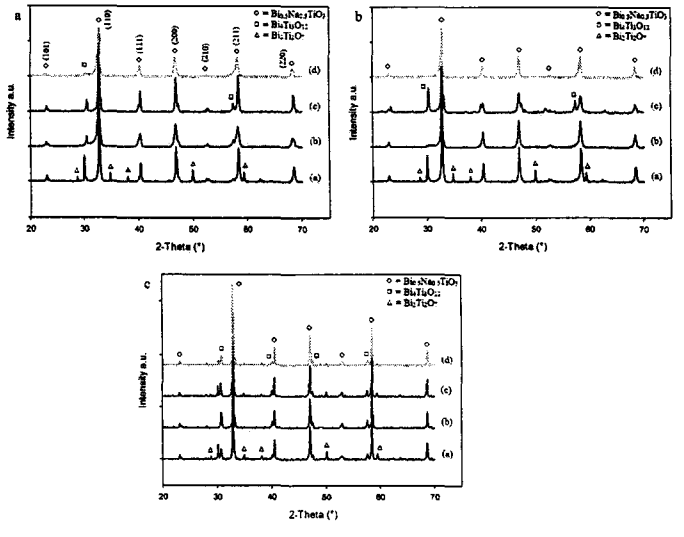

Fig. 1. XRD spectra of PBNT powders after calcination at 800°C with varying concentration of fuel agent: (a) PEG 200, (b) citric acid and (c) glycine.

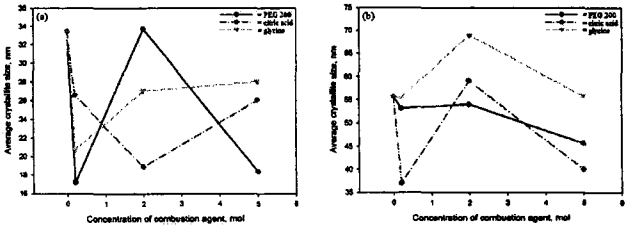

Fig. 2. Crystallite size of the PBNT with varying of combustion agent: (a) after calcination at 800°C and (b) after sintering at 1100°C.

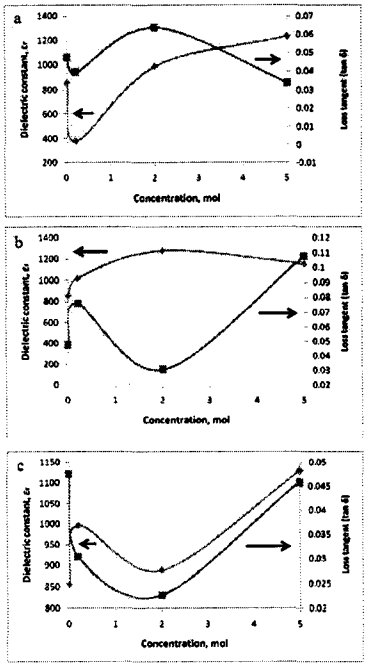

Fig. 3. Dielectric properties of PBNT with varying concentration of fuel agent: (a) PEG 200, (b) citric acid and (c) glycine.

References

1. Gao, L., Y. Huang, Y. Hu, and H. Du, Ceramics International, 2007. 33(6): p. 1041
2. Zhang, H., S. Jiang, J. Xiao, and K. Kajiyoshi, Journal of the European Ceramic Society, 2010a. 30(15): p. 3157
3. Goh, P.Y., K.A. Razak, and S. Sreekantan, Journal of Alloys and Compounds, 2009. 475(1-2): p. 758-761.
4. Razak, K.A., C.J. Yip, and S. Sreekantan,. Journal of Alloys and Compounds. 2011, **509**(6): p. 2936-29

PROCEEDINGS OF

The 3rd Regional Conference

Interdisciplinary on

Natural Resources and Materials Engineering

25-26 October 2010

Bayview Hotel, Langkawi, Malaysia

ISBN 978-967-0167-00-8

Proceedings

3rd RC-NRM

Regional Conference Interdisciplinary on Natural Resources and Materials Engineering

BAYVIEW HOTEL, LANGKAWI, MALAYSIA
OCTOBER, 25-26 , 2010

"SUSTAINABLE DEVELOPMENT IN ASEAN THROUGH NETWORKING IN NATURAL RESOURCES AND MATERIALS"

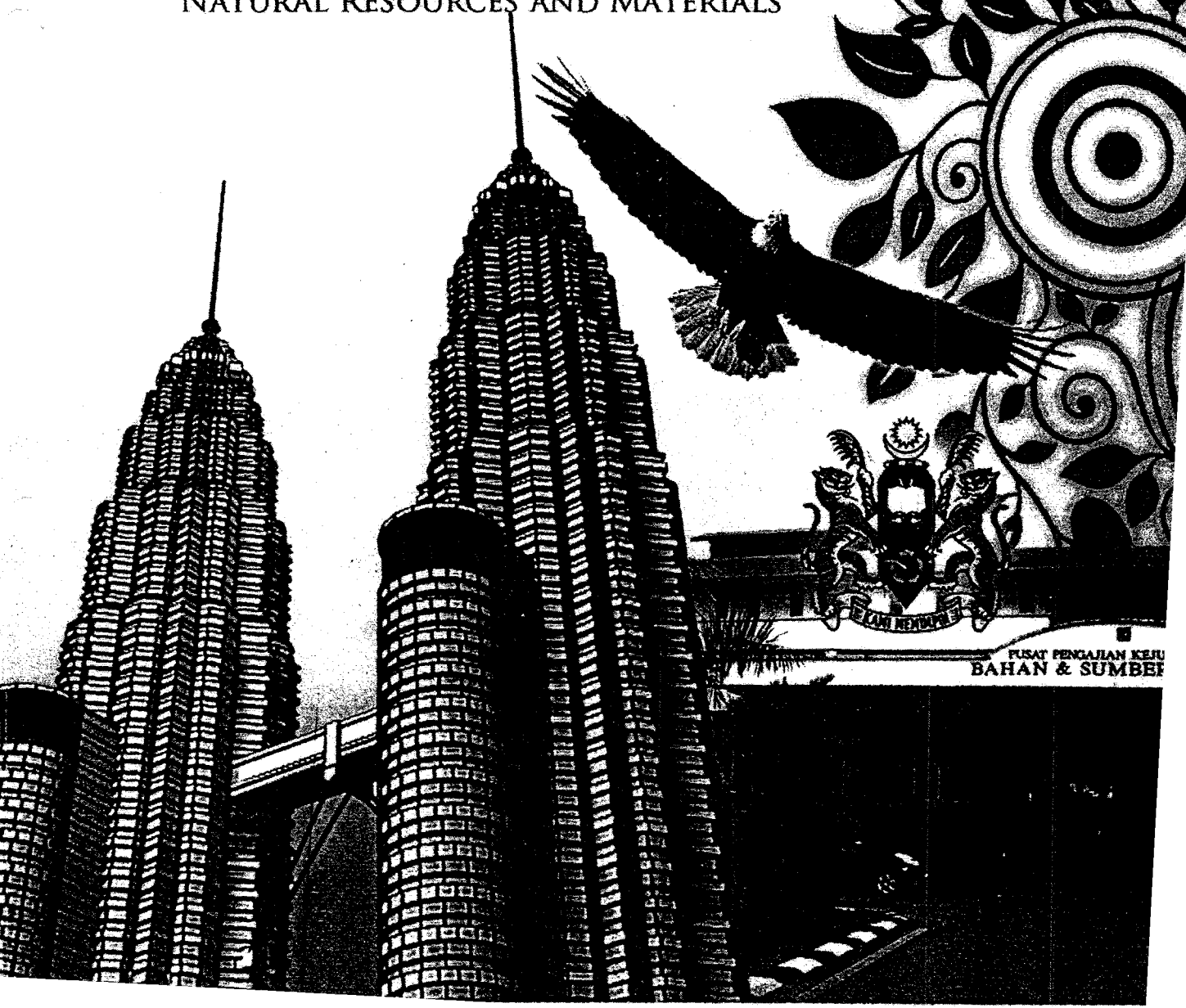

Praseodymium-doped Bismuth Potassium Titanate ($Bi_{0.5}K_{0.5}TiO_3$) Synthesised Using the Glycine-assisted Soft Combustion Technique

Ng Chai Yan and Khairunisak Abdul Razak

School of Materials and Mineral Resources Engineering,
Universiti Sains Malaysia, 14300 Nibong Tebal, Penang, Malaysia
E-mail: khairunisak@eng.usm.my

ABSTRACT

In the current work, soft combustion technique was used to prepare bismuth potassium titanate ($Bi_{0.5}K_{0.5}TiO_3$; BKT) and praseodymium-doped BKT ($Bi_{0.5(1-x)}Pr_xK_{0.5}TiO_3$; BPKT) powders. Fine particle sizes (10-100 nm) of BKT and BPKT powders were able to produce using this technique. A single phase BKT was obtained with the addition of at least 0.5 mol glycine (combustion fuel). Various $Bi_{0.5(1-x)}Pr_xK_{0.5}TiO_3$ compounds with x = 0.01, 0.03, 0.05, 0.10, 0.15 and 0.20 were prepared. These powders were calcined at 800°C for 3 hours and pure BKT and BPKT were obtained. After sintering at 1050°C for 5 hours, pure BKT and BPKT pellets were obtained for x = 0 and 0.01. However, for other BPKT compounds, a small amount of $Bi_4Ti_3O_{12}$ (BIT) secondary phase formed after sintering. The undoped BKT possessed crystallite size of 33.98 nm, grain size of 100-300 nm, relative density of 91.37 % and dielectric constant (ε_r) of 520.21 (at 1 MHz). Among all of the samples, BPKT with x = 0.05 had the highest dielectric properties (ε_r = 713.87) due to its large crystallite size (68.66 nm), large grain size (~ 435 nm) and high relative density (93.39 %).

KEYWORDS

Bismuth potassium titanate; Soft Combustion; Dielectric

1. INTRODUCTION

Lead-based piezoelectric materials are known for their hazardous and negative environmental impact. Besides that, lead is volatile above 800°C and makes it more dangerous when it is released into the environment. Therefore, researchers are actively seeking for lead-free materials for replacement. Bismuth potassium titanate ($Bi_{0.5}K_{0.5}TiO_3$; BKT) is a well-known Bi-based perovskite piezoelectric material due to its excellent electrical properties and high Curie temperature (T_c) of 380°C. However, only a few studies on BKT have been reported. This may be due to the difficulty of producing a high density BKT ceramic because Bi and K are volatile at high sintering temperatures [1,2].

BKT powder is traditionally prepared using a solid state reaction [1,3,4]. However, this technique can only produce micron-sized powder and requires high sintering temperature. In addition, the powders usually tend to agglomerate and contain inhomogeneous particle size. The soft combustion technique can produce fine particle size powder ranging from nanometre to submicron scale and requires a low sintering temperature (1050°C). The volatilisation of Bi and K ions can be minimised with this lower sintering temperature. Moreover, this soft combustion technique requires simple equipment, allows better stoichiometry control and is cost effective [5]. Thus, the current work uses the soft combustion technique to prepare the samples.

In order to improve the electrical properties of BKT, praseodymium (Pr) was doped in BKT to produce $Bi_{0.5(1-x)}Pr_xK_{0.5}TiO_3$ (BPKT) compounds. Pr is a lanthanide element that has a tendency to lessen the Bi and O vacancies in the BKT. Also, Pr^{3+} has a six-coordinated ionic radius (0.99 Å), which is close to the ionic radius of Bi^{3+} (1.03 Å) and suggests that the replacement of Pr in Bi is easy with a small lattice distortion [6]. The morphologies, structural and dielectric properties of the BKT and BPKT are reported.

2. EXPERIMENTAL DETAILS

The $Bi_{0.5}K_{0.5}TiO_3$ (with 0.1, 0.3, 0.5, 1.0 and 1.5 mol of glycine) and $Bi_{0.5-x}Pr_xK_{0.5}TiO_3$ (with x = 0.01, 0.03, 0.05, 0.10, 0.15 and 0.20) powders were produced using the soft combustion technique. For BKT powders preparation, bismuth (III) nitrate pentahydrate [$Bi(NO_3)_3.5\ H_2O$], potassium nitrate (KNO_3) and titanium (IV) isopropoxide {$Ti[OCH(CH_3)_2]_4$} were used as the starting materials for Bi, K and Ti, respectively. First, KNO_3 was dissolved in 5 ml deionised water, while $Bi(NO_3)_3.5H_2O$ and glycine (H_2NCH_2COOH) were dissolved in 25 ml 2-methoxyethanol

($CH_3OCH_2CH_2OH$) at 40°C. This KNO_3 solution was then added into $Bi(NO_3)_3.5H_2O$ solution. On the other hand, $Ti[OCH(CH_3)_2]_4$ was dissolved separately in 25 ml of $CH_3OCH_2CH_2OH$, with 5 ml acetylacetone ($CH_3COCH_2COCH_3$) as the chelating agent. Then, this $Ti[OCH(CH_3)_2]_4$ solution was added to the Bi-K solution with continuous stirring, and the final mixture was stirred for 2 h.

Next, the mixture was heated to 130°C with continuous stirring. After evaporation a sticky gel was formed followed by a soft combustion process that formed a foam. This foam was then crushed to obtain a fine powder. This powder was calcined at 800°C for 3 h with a heating rate of 5°C min^{-1} and a cooling rate of 10°C min^{-1}. After that, the powder was pressed into 12 mm diameter pellets with a pressure of 55 bar. Finally, the pellets were sintered at 1050°C for 5 h in a closed alumina crucible. For the preparation of BPKT powder, praseodymium (III) nitrate hexahydrate [$Pr(NO_3)_3.6\ H_2O$] was dissolved together with the $Bi(NO_3)_3.5\ H_2O$ and H_2NCH_2COOH in the beginning, and the other steps were similar to those for the preparation of the BKT.

The phases in the powders and sintered pellets were analysed using an X-ray diffractometer (Bruker AXS D8 ADVANCE) equipped with CuKα radiation from 20-70°. Whereas, the morphology were observed using a field emission scanning electron microscope (Zeiss SUPRA 35) and transmission electron microscope (Philips CM 12). The crystallite size was analysed using Rietveld refinement, and the density of sintered pellets was measured using the Archimedes technique. The dielectric properties of the pellets were measured using LCR meter (Agilent HP4284) at 1 MHz and 1 V. Prior to dielectric measurement, silver paste was applied on both surfaces of the pellets as ohmic contact.

3. RESULTS AND DISCUSSION

Firstly, the BKT powder was synthesised without the addition of glycine. Fig. 1 shows the XRD pattern of the powder after calcination. This XRD spectrum shows the presence of a secondary phase in the compounds. The BKT phase matched the ICDD number of 36-0339, whereas the secondary phase matched the bismuth titanate ($Bi_4Ti_3O_{12}$; BIT) phase with ICDD number of 72-1019. The formation of this secondary phase could be due to incomplete combustion of the initial precursors. Consequently, glycine was added into the starting materials. Glycine is one of the most popular fuels for producing uniform composition and precisely controlled stoichiometry of complex oxide ceramic powders [7].

From the XRD spectra of BKT synthesised using various molar fractions of glycine (Fig. 2), it can be observed that the BKT produced with the addition of 0.1and 0.3 mol of glycine showed the presence of the secondary phase BIT as in the BKT produced without glycine. However, the BKT with 0.5, 1.0 and 1.5 mol of glycine contained only single phase BKT. The results indicate that the addition of a small amount of glycine (0.1 and 0.3 mol) was insufficient to aid in the combustion process, whereas a higher amount of glycine (0.5 mol and above) was sufficient and able to obtain the pure phase BKT. Thereafter, 0.5 mol of glycine was used to synthesis the subsequent powders. Fig. 3 shows the FESEM and TEM micrographs of the BKT powders (with 0.5 mol of glycine) after calcination at 800°C. The BKT powders have flake-like particles in the range of 10 nm to 100nm.

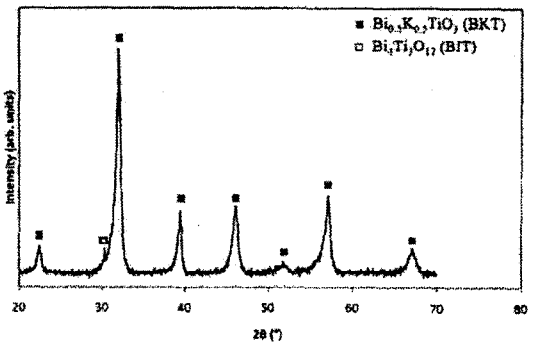

Fig. 1. XRD spectrum of the calcined BKT powder without adding of glycine.

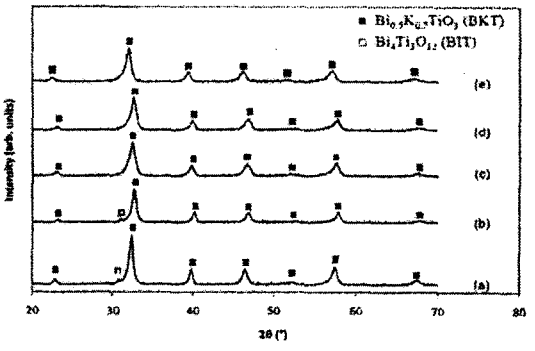

Fig. 2. XRD spectra of the calcined BKT powders with: (a) 0.1, (b) 0.3, (c) 0.5, (d) 1.0 and (e) 1.5 mol of glycine.

Various amounts of Pr (x = 0.01, 0.03, 0.05, 0.10, 0.15, 0.20) were added to BKT to form $Bi_{0.5-x}Pr_xK_{0.5}TiO_3$ (BPKT). XRD spectra of the undoped

BKT and various BPKT powders calcined at 800°C are shown in Fig. 4. The BPKT with x = 0.01 and 0.03 show only the presence of single phase BPKT, indicating that the Pr^{3+} in the BPKT were diffused into the perovskite lattice and
did not form a secondary phase or separate from the interior grain [8]. However, when the amount of x was increased (x = 0.05 and above), the secondary phase BIT appeared. For the BPKT (x = 0.01 and 0.03), the amount of Pr added was lower, and thus the secondary phase BIT was not formed, whereas, for the BPKT with x = 0.05 and above, a small amount of the secondary phase was formed. The formation of the secondary phase BIT was due to the high amount of Pr doping. When Pr was added to BKT, the Pr^{3+} substituted the Bi^{3+}, and these bondless Bi^{3+} ions were then reacted with Ti^{4+} and O^{2-} to form BIT. The formation of the secondary phase BIT was not common in BKT formation. Previous studies found the formation of BKT contained secondary phases of $Bi_2Ti_2O_7$ [9], $K_2Ti_4O_9$ [1], $K_2Ti_6O_{13}$ [1] and $K_4Ti_3O_8$ [3]. The presence of the secondary phase BIT could be explained by the volatilisation of Bi^{3+} and K^+ during the sintering process.

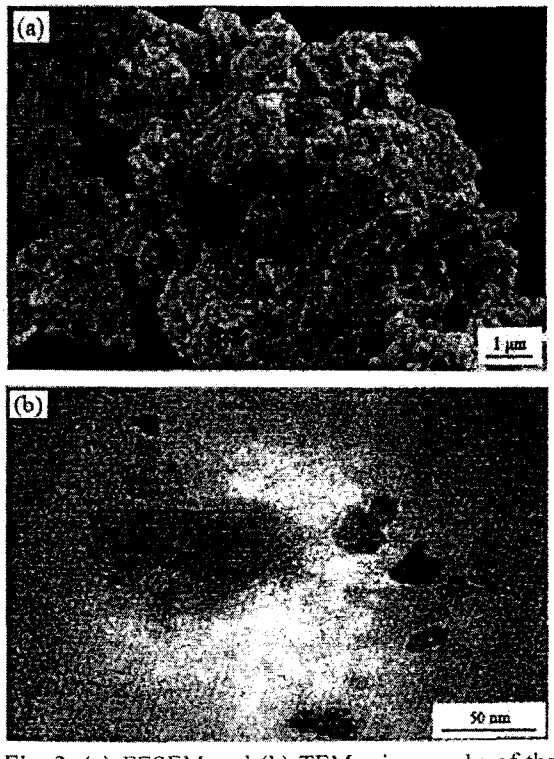

Fig. 3. (a) FESEM and (b) TEM micrographs of the calcined BKT powders synthesised using 0.5 mol of glycine.

These calcined powders were subsequently pressed into pellets and sintered at 1050°C for 5 h. The XRD spectra of the sintered BKT and BPKT pellets are shown in Fig. 5. These XRD spectra show that only BKT and BPKT (x = 0.01) contained pure phase BKT and BPKT with no evidence of the presence of secondary phase. For the BPKT pellets with x = 0.03 and above, the secondary phase BIT was present. As the amount of Pr dopant increased, the intensities of the BIT peaks became stronger, indicating that the secondary BIT phase became more dominant (with higher crystallinity) as the amount of dopant increased. As the amount of Pr dopant increased, more Pr^{3+} were substituted for the Bi^{3+}; hence, more bondless Bi^{3+} were available to react with Ti^{4+} and O^{2-}, resulting in the formation of more BIT. Moreover, K also evaporates at the sintering temperature used. Hence, lower levels of K can lead to the formation of a more stable BIT.

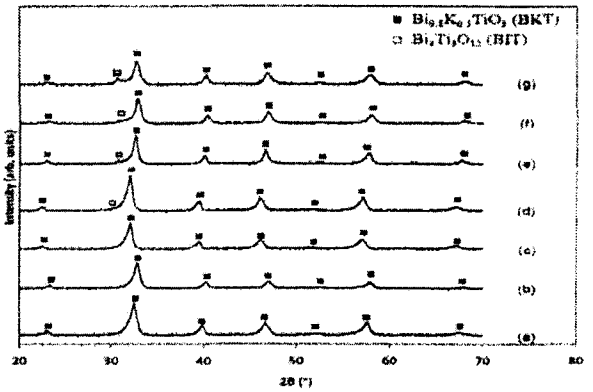

Fig.4. XRD spectra of the calcined BPKT powders with varying x: (a) 0 (BKT), (b) 0.01, (c) 0.03, (d) 0.05, (e) 0.10, (f) 0.15 and (g) 0.20.

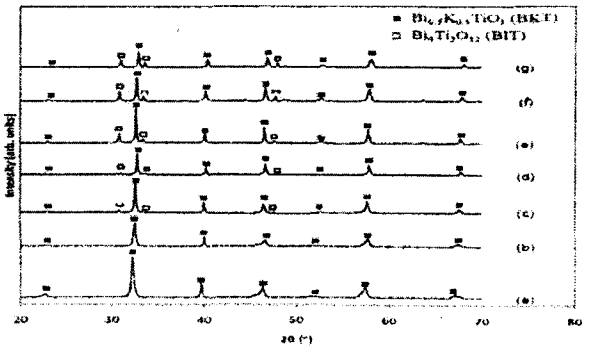

Fig.5. XRD spectra of the sintered BPKT pellets with varying x: (a) 0, (b) 0.01, (c) 0.03, (d) 0.05, (e) 0.10, (f) 0.15 and (g) 0.20.

The crystallite size of the calcined powders and sintered pellets were in the range of 9.66-13.01 nm and 33.98-68.66 nm, respectively. Fig. 6 shows the plots of the crystallite size of calcined powders and sintered pellets against the amount of Pr (x). The crystallite size of both calcined powders and sintered pellets increased from x = 0 to x = 0.05 and then decreased from x = 0.05 to x = 0.20. When the BKT was doped with small amounts of Pr (x = 0.01 to 0.05), the Pr ions diffused into the BKT and assisted the growth of the grains. However, when the amount of Pr increased to x = 0.10, an obvious secondary phase BIT was formed. It is thought that this BIT phase acted as a grain growth inhibitor, thus suppressed the crystallite growth of the BPKT phase [5,10,11]. Moreover, it can be observed that the crystallite size of the sintered pellets was larger than that in the calcined powders because ion diffusion occurs during the sintering process and caused crystallite growth.

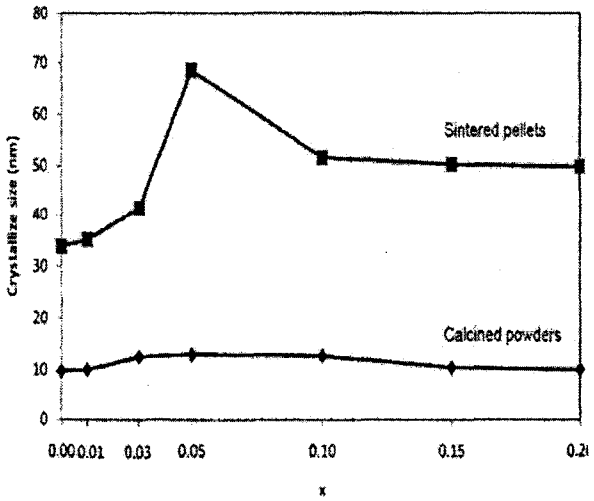

Fig. 6. Crystallite size of the calcined powders and sintered pellets of BKT and BPKT.

Fig. 7 shows the FESEM micrographs of the sintered BKT and BPKT pellets. The grains had no particular shape. The grain sizes of the pellets increased when x = 0 (100-300 nm) to x = 0.05 and decreased between x = 0.05 and x = 0.20. The BPKT with x = 0.05 had the largest grain size, averaging 435 nm. This trend toward changing grain sizes in agreement with the trend toward changing crystallite size that was observed in XRD analysis. This likeness is expected because crystallite size normally increases as grain size increases [5,12].

The plots of density and relative density of the sintered pellets against x are shown in Fig. 8. The densities of the pellets increased from x = 0 to x = 0.05 and started to decrease from x = 0.05 to x = 0.20. It could be the addition of Pr caused the formation of close-packed microstructures with increasing grain size. The decrease in density was probably due to the decreasing grain size from x = 0.05. Besides that, the decreasing density could be caused by the presence of more secondary phase.

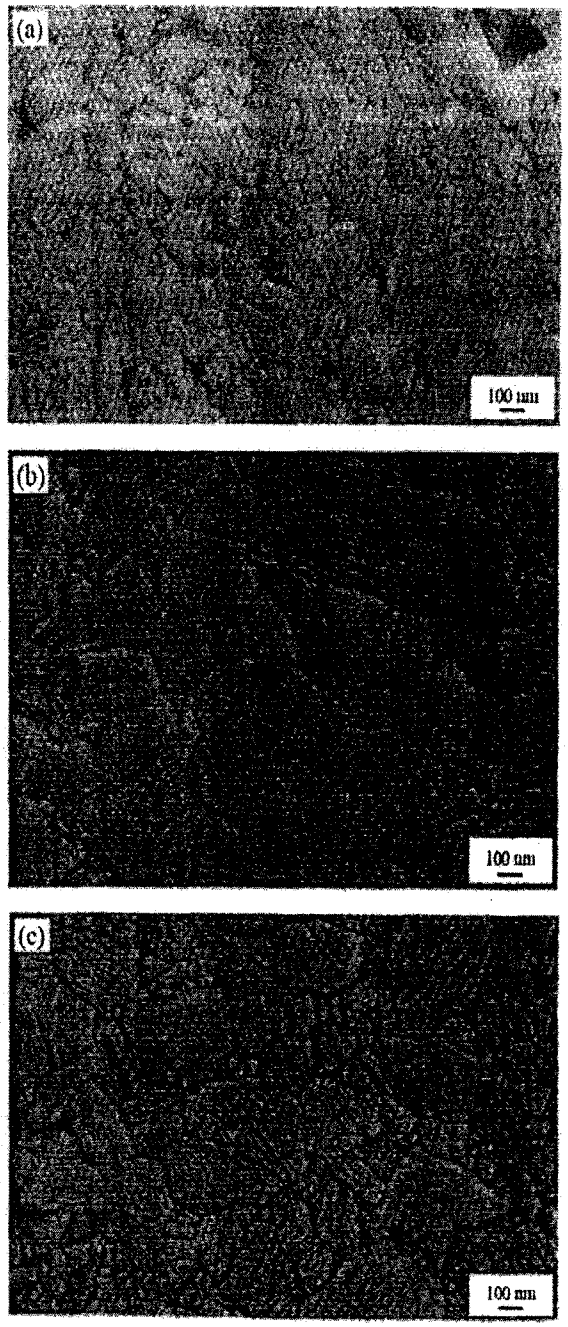

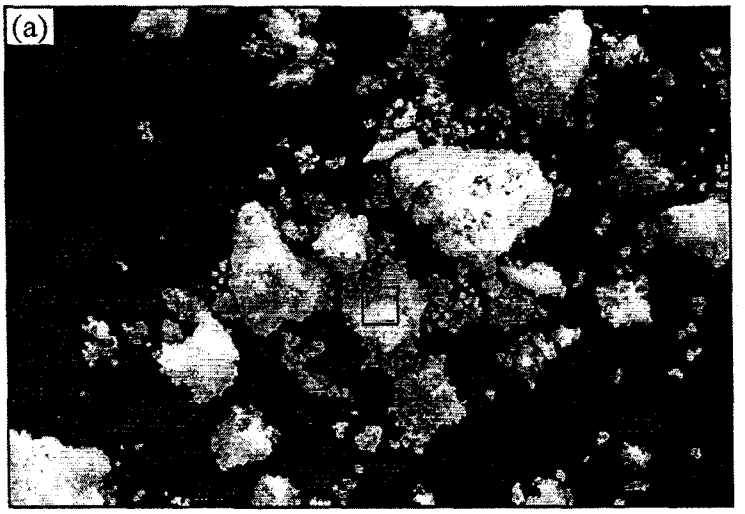

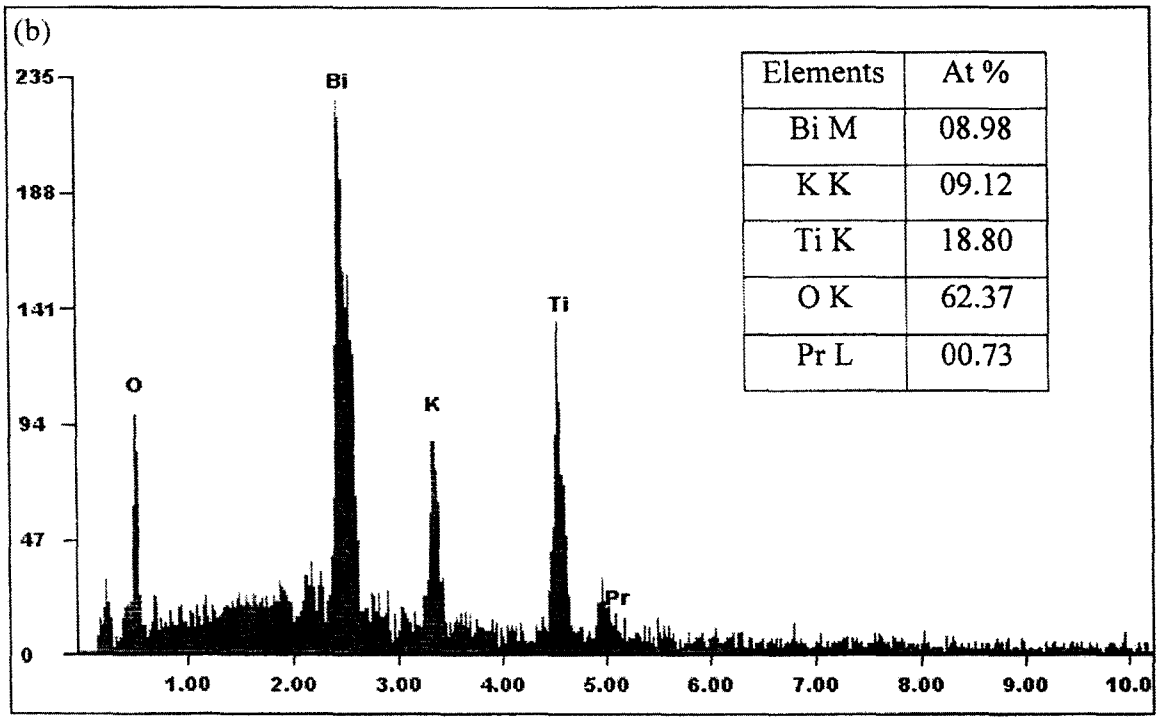

Elements	At %
Bi M	08.98
K K	09.12
Ti K	18.80
O K	62.37
Pr L	00.73

Figure 4.23: (a) SEM micrograph and (b) EDX spectrum of the calcined BPKT powder with x = 0.01.

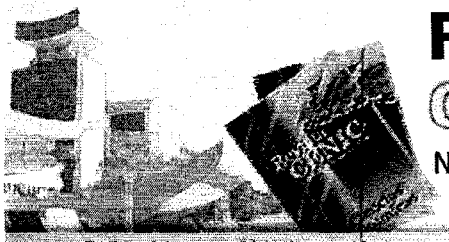

Revista CENIC

Ciencias Químicas

Número Especial 2010

Volumen 41, 2010
ISSN: 1015-8553

Ciencias B

Ciencias Biológicas
EDITORIAL CENIC
Ciencias Químicas

Servicios que ofrece:
Edición general: otras publicaciones, cubiertas CD ROM, plegables, tarjetas postales y personales, boletines, folletos, sueltos, etcétera. Diseño y edición de microcarteles (microposters). Encuadernación de trabajos de especialidad, maestrías, doctorados y de publicaciones menores. Fotografía científica y general. Investigación y elaboración de guiones para videos, documentales y multimedia. Diferentes productos y publicaciones multimedia, etcétera.

Productos que ofrece la Editorial CENIC:
Revista CENIC Ciencias Químicas y Revista CENIC Ciencias Biológicas (revistas científicas primarias arbitradas, indizadas por 9 Directorios Internacionales y 2 Nacionales). Colecciones electrónicas de sus revistas científicas. Videos científicos y promocionales.

Crecimiento de núcleos de nanovarillas de oro para aplicaciones de diagnóstico

Seed-mediated Growth of Gold Nanorods for Diagnostic Applications

Khoo Khai Ling[1], Khairunisak Abdul Razak[1,3], Azlan Abdul Aziz[2,3]

[1] School of Materials and Mineral Resources Engineering, Engineering Campus, Universiti Sains Malaysia, 14300 Nibong Tebal, Penang, Malaysia.

[2] School of Physics, Universiti Sains Malaysia, 11800 USM, Penang, Malaysia

[3] NanoBiotechnology Research and Innovation (NanoBRI), Institute for Research in Molecular Medicine, Universiti Sains Malaysia, 11800 USM, Penang, Malaysia

khairunisak@eng.usm.my

Seed-mediated Growth of Gold Nanorods for Diagnostic Applications

RESUMEN

En el siguiente trabajo se describen las propiedades de nanovarillas de oro sintetizadas utilizando un método de semillas. La sal de oro primero se reduce empleando un agente reductor fuerte, el $NaBH_4$, para producir las partículas de semillas. En presencia de bromuro de cetiltrimetilamonio (CTAB), empleado como surfactante, se produce una reducción de la sal del metal con un agente reductor más débil (ácido ascórbico) para formar las nanovarillas de oro. Se investigan varios parámetros: concentración de oro, concentración de CTAB y concentración de $AgNO_3$. La morfología y distribución de las partículas se caracterizó mediante microscopia electrónica de transmisión (TEM) y mediante dispersión dinámica de luz (DLS). Se empleó un espectrofotómetro UV-Visible (UV-Vis) para observar las propiedades de dispersión de las muestras. El resultado muestra que la concentración de oro no tiene un impacto significativo en la formación de nanovarillas. Además, se forman nanoesferas de oro con desigual tamaño y distribución para todos los casos, como muestran los ensayos mediante TEM y DLS. Por otra parte, la forma alargada de algunos de ellos podría ser causada por una insuficiencia en la concentración de CTAB para ayudar en la formación de nanovarillas de oro y por tanto favorecen la formación de nanoesferas de oro. El papel de CTAB es dirigir el crecimiento mediante el bloqueo del eje más extenso de la cara del cristal y promover el crecimiento de oro en el eje corto para formar las nanovarillas. Se observa que se requiere CTAB 1,0 M para formar las nanovarillas. Cuando la cantidad de CTAB es mayor, las partículas se transforman hacia la formación de rectángulos. El análisis mediante UV-Vis muestra que las nanovarillas presentan señales alrededor de los 540 nm y 720. El estudio sobre el efecto del $AgNO_3$ muestra que al aumentar la concentración de $AgNO_3$ aumenta el largo de las partículas. Sin embargo, la forma de bastón se transforma en una forma rectangular utilizando una concentración elevada de $AgNO_3$. La formación de nanovarillas es altamente dependiente del CTAB y de la concentración de $AgNO_3$ a temperatura ambiente, pero también depende de la concentración de los precursores de oro en la solución de crecimiento. El largo de las nanovarillas de oro puede ajustarse variando los parámetros de la síntesis.

Palabras claves: Nanopartículas de oro; Nanovarillas; Crecimiento por semillas; Diagnóstico.

ABSTRACT

This work describes properties of gold nanorods synthesized using a seed-mediated method. Gold salt is first reduced using a strong reducing agent which is $NaBH_4$ to produce seed particles. In the presence of cetyltrimethylammonium bromide (CTAB) as a surfactant, subsequent reduction of more metal salt with a weak reducing agent (ascorbic acid) formed gold nanorods. Several parameters are investigated; gold concentration, CTAB concentration and $AgNO_3$ concentration. Morphology and distribution of particles are characterized using transmission electron microscope (TEM) and dynamic light scattering (DLS). UV-Visible (UV-Vis) spectrophotometer is used to observe scattering properties of the samples. The result shows that the amount of gold concentration does not have significant impact on nanorods formation. Gold nanospheres with uneven size and shape distribution are formed for all cases as observes using TEM and further proves using DLS. Moreover, some of them have elongated shape that could be caused by insufficient CTAB concentration to aid in the formation of gold nanorods and thus favour the formation of gold nanospheres. The role of CTAB is to direct the growth by blocking the long axis crystal faces and promoting gold growth on the short-axis faces to form nanorods. It is observed 1.0 M

CTAB is required to form nanorods. When the amount of CTAB is further increased, the shapes transform into rectangle shape. UV-Vis analysis shows that nanorods have peaks at around 540 nm and 720 nm. The study on the effect of $AgNO_3$ shows that the aspect ratio increases with increasing $AgNO_3$ amount. However, the rod shape transform into rectangle shape at high concentration of $AgNO_3$. The formation of nanorods is highly dependent on CTAB and $AgNO_3$ concentration at room temperature, but least dependent on the gold precursor concentration in the growth solution. The aspect ratio of gold nanorods can be tuned by changing synthesis parameters.

Keywords: Gold nanoparticles; Nanorods; Seed-mediated growth; Diagnostic.

INTRODUCTION

The field of nanotechnology is undergoing speedy developments in many fronts. It is a field of science that deals with the control and manipulation of particles at the length scale between 1 to 100 nm and the exploitation of novel properties and phenomena developed at that scale. The creation of new properties in nano-scale is resulted from three size-related factors which are quantum confinement, large surface to volume ratio and force or energy changes landscape with the shrinking scale (1). In addition, a wide variety of materials have been formed into nanoparticles (AuNPs). Besides the most common spherical shape (AuNS), various shapes such as cube, rod, ring, wire, tetrapod, and triangular prism type of nanoparticles have been synthesized. As the nanoparticle synthesis technology has been advanced, the application of nanoparticle has been extended further into various fields especially in biomedical applications such as X-ray contrast agents, diagnosis of diseases, photothermal therapy, drug delivery and biological sensors (2).

Gold nanoparticles (AuNPs) have attracted significant interest among scientists for generations as a novel platform for biotechnology and biomedicine due to their amazing chemical and physical properties at nanoscale level. In this work, gold nanorods (AuNRs) were synthesized using seed-mediated approach. AuNRs differ from spheres since they have a particular aspect ratio in which the material is elongated along a single dimension, keeping the other two dimensions approximately equal. It is essential to limit growth direction to a single axis by using surfactant in order to synthesize AuNRs (3). AuNRs have two peaks in their absorbance spectra that correspond to plasmon resonances: one at approximately 520 nm from plasmon oscillations in the shorter transverse direction and a second at longer wavelengths (typically between 700 nm and 1300 nm) from longitudinal oscillations (4). Apart from the obvious advantages of AuNP that do not photobleach or blink, chemically inert and biologically compatible, AuNRs added extra dimension as an attractive candidates for biomedical applications since their position of the longer wavelength plasmon peak can now be tuned to near infrared wavelengths which penetrate deep into cells and tissue by varying the AuNRs aspect ratio.

In this work, AuNRs have been synthesized using a seed-mediated approach. The effect of synthesis parameters on the properties of AuNRs formation was studied. It was observed that the formation of AuNRs were highly dependent on CTAB and silver nitrate concentrations at room temperature, but least dependent on concentration of gold in the growth solution.

MATERIALS AND METHODS

Seed mediated approach was used to synthesis gold nanorods (AuNRs). Seed solution was prepared by mixing Hexadecyltrimethylammonium bromide solution (CTAB) (5 mL, 0.20 M) with 5.0 mL of 0.00050 M gold (III) chloride. 30 mL of ice-cold 0.010 M sodium borohdyride was added to the stirred solution which resulted in the formation of a brownish yellow solution. The seed solution was vigorously stirred for 2 min and kept at

25°C. The growth solution was prepared by dissolving CTAB (5 mL, 0.20 M) in 20 mL of 0.0040 M silver nitrate solution at 25°C. To this solution, 5.0 mL of 0.0010 M gold (III) chloride was added followed by the addition of 10mL 0.0788 M ascorbic acid. Ascorbic acid as a mild reducing agent changed the growth solution from dark yellow to colorless. After that, 50mL of the seed solution was added into the growth solution. This solution was maintained at 25°C without stirring overnight. The color of the solution gradually changed within 10-20 min. AuNPs were then washed three times by centrifugation at 10000 rpm with deionised water (DI) to remove excess CTAB and re-dispersed in DI water. Several parameters were studied including the effect of gold concentration in the growth solution (0.0005M-0.003M), CTAB concentration (1.0M-1.5M), silver concentration (0.003M-0.007M) and reaction temperature (25-70°C).

Shape, size and distribution of the AuNPs were observed using Philips 420T transmission electron microscope (TEM). Absorbance properties of AuNPs were analyzed using the ultraviolet-visible spectrophotometer (UV-Vis). Particle size distribution AuNPs was determined by using Zetasizer NanoZS.

RESULTS AND DISCUSSION

Gold chloride concentration of growth solutions was varied; 0.0005M, 0.001M, and 0.002 M and 0.003 M. From the result of UV-visible absorbance spectra (Fig.1), obviously there was only one absorbance peak at ~540 nm for all cases indicates AuNSs were formed because AuNRs should exhibit two absorbance peaks as opposed to only one peak at ~520 nm for AuNSs. However, for 0.003 M $HAuCl_4$, the absorbance peak cannot be seen clearly because the concentration of solution is too dilute and hence affect the absorption of light.

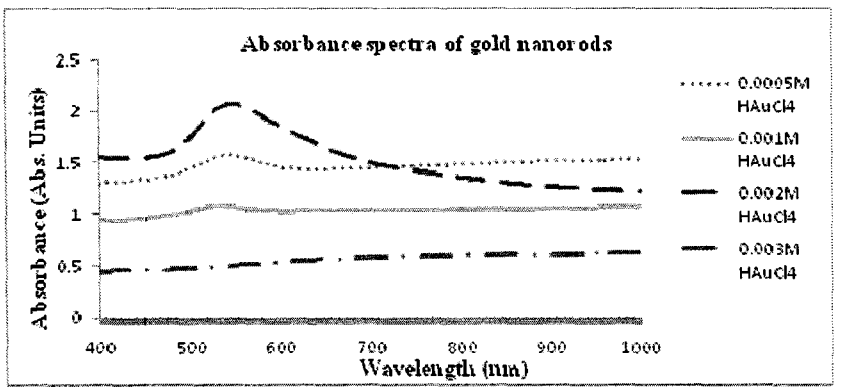

Fig.1. UV-Vis spectra of AuNRs synthesized using different gold chloride concentration.

Transmission electron microscopy (TEM) images (Fig. 2) further confirmed that all gold concentration did not form AuNRs. Also, the shapes of AuNSs were found to be slightly elongated rather than entirely spheres. Therefore, the amount of CTAB added was expected to be insufficient in inducing AuNRs formation. Moreover, bromide or silver bromide could be the initial species that deposit on the seed through chemisorb on gold crystal faces. However, the affinity of bromide or silver bromide for gold is modest. Hence, high concentrations of bromide will be required to drive the ions onto the gold surface. The low amount of CTAB will lower the Br concentration and hence favor spheres (5). Hence, the effect of CTAB concentration was subsequently studied.

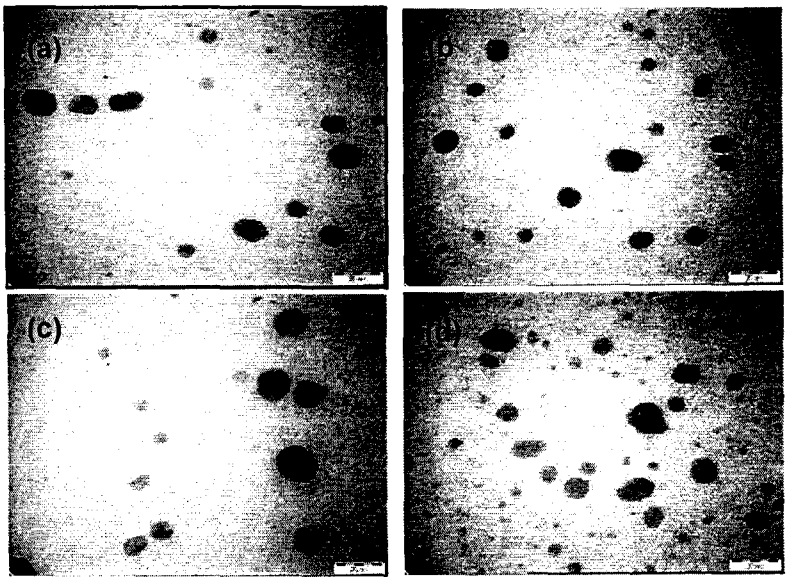

Fig.2. TEM images of AuNPs synthesized with varying $HAuCl_4$ concentration in growth solution; (a) 0.0005 M, (b) 0.001 M, (c) 0.002 M and (d) 0.003 M.

CTAB concentration was studied from 1.0 M, 1.5 M and 2.0 M. From UV-Vis absorbance spectra (Fig. 3), two absorbance peaks were observed for all cases, which was the characteristic of AuNRs. One of the absorbance peaks is at ~520 nm and the other at ~700-1300 nm. Besides, it can be seen that longitudinal peaks and transverse peaks shifted to longer wavelength first and then followed by shifting to shorter wavelength. Longitudinal peak was attributed to the length of AuNRs, while transverse peak represented the width of AuNRs. In other words, length and width of AuNRs increased when CTAB concentration increased from 1 M to 1.5 M. However, as CTAB concentration increased to 2 M, both length and width of AuNRs decreased. This was due to the shape changes of the rod shape. Additionally, the intensities of absorbance increased with increasing CTAB concentration since the concentration of AuNRs solution to absorb light increased.

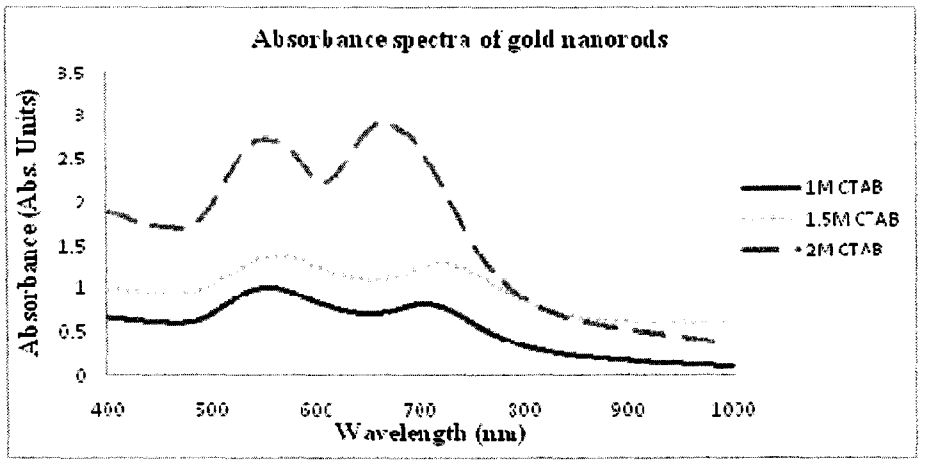

Fig.3. Absorbance spectra of AuNRs with various CTAB concentrations.

Formations of AuNRs for all cases were confirmed by TEM observation (Fig.4). This proved that a high concentration of CTAB was required for AuNRs formation. Nonetheless, a small amount of AuNSs was present as a byproduct. The role of CTAB

was to aid in anisotropic growth of AuNRs by preferentially bound to {110} side face of gold. As a result, gold could only grow along front face {100} direction since side face was blocked by CTAB. From the TEM images in Fig. 4, it was observed that the shape of AuNRs formed with 1.5 M and 2 M CTAB were slightly different compared to AuNRs formed using 1 M CTAB. With 1 M CTAB, well-shaped of AuNRs were produced (Fig. 4 (a)). While with 1.5 M and 2 M CTAB, the ends of AuNRs becomes flattened rather than rounded. In other words, the shapes of rods had transformed into dogbones. Also, a large number of amorphous and unshape particles are present (Figs. 4 (b) and (c)). The result could be caused by the excessive amount of CTAB on the {110} side face that prevented more gold atoms from depositing on this plane, and more gold atoms deposited on the {100} front face with some preference. This could lead to gold nanodogbones formation. This condition was also observed in the studies conducted by Wang et al. (6) and Gou and Murphy (7).

Fig. 5 shows the particles size distribution of AuNRs with different CTAB concentration using Zetasizer. It can be seen that, size distribution for all samples have two distinct peaks. The first peak attributes to the width of AuNRs while the second peak represents the length of AuNRs. These results further confirmed that width and length of AuNRs increase with increasing CTAB concentration from 1 M to 1.5 M. On the other hand, width and length of AuNRs decrease as concentration of CTAB increase to 2 M.

Fig.4. TEM images of AuNRs synthesized with varying CTAB concentration; (a) 1 M, (b) 1.5 M and (c) 2 M CTAB.

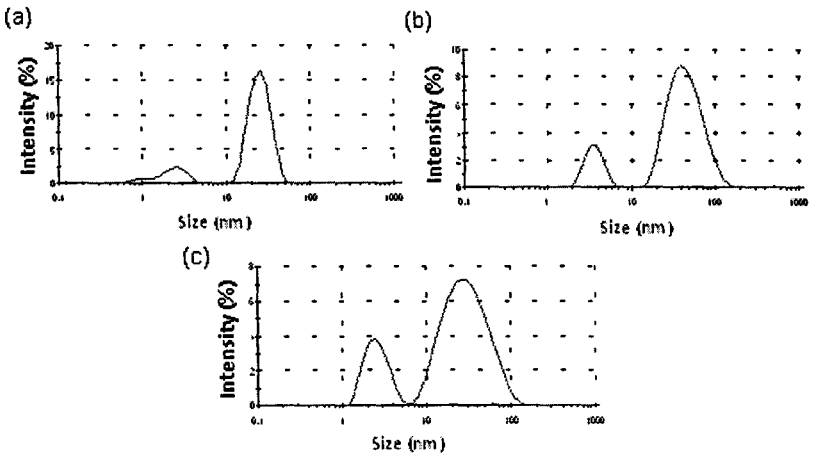

Fig.5. Size distribution by intensity for (a) 1 M, (b) 1.5 M and (c) 2 M CTAB.

The effect of silver concentration was studied by varying the concentration of silver nitrate; 0.003 M, 0.004 M, 0.005 M and 0.007 M. UV-Vis spectra for these four samples showed the presence of AuNRs with two absorbance peaks (Fig. 6). It can be seen that, both longitudinal and transverse peaks shifted to longer wavelength first, subsequently shifted to shorter wavelength and finally shifted to longer wavelength. This indicates that both length and width of AuNRs increase with increasing concentration of silver nitrate except at 0.0005 M of silver nitrate due to the shape changes and causes length and width of AuNRs reduce. The role played by silver nitrate is quite similar with CTAB molecule. Both of them have preferential binding on {110} side face of rods. Thus, the addition of silver content was used to grow and stabilize AuNRs to a desired aspect ratio. When silver nitrate concentration increases, more silver deposited on AuNRs {110} side face, resulted in AuNRs with higher aspect ratio (8).

Fig. 7 shows the TEM images of AuNRs synthesized by using different silver nitrate concentration. Well-shaped of AuNRs were produced with 0.004 M silver nitrate (Fig. 7 (b)). Meanwhile, AuNRs with 0.003 M, 0.005 M and 0.007 M of silver nitrate exhibit dogbones shape (Figs. 7 (a), (c) and (d)). Also, a higher concentration of silver nitrate resulted in lower rod yield.

Fig. 8 shows the particles size distribution of AuNRs with different silver nitrate concentration using Zetasizer. It can be seen that both peaks that represent width and length of AuNRs increased when silver nitrate concentration increased except at 0.005 M of silver nitrate, both length and width of AuNRs decreased.

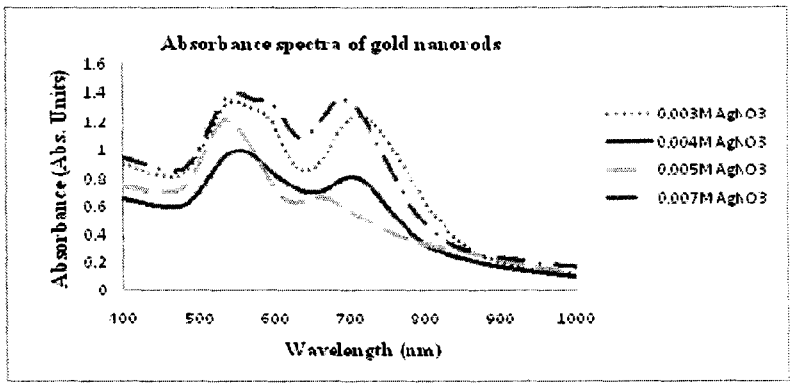

Fig.6. UV-Vis spectra of AuNRs synthesized with various silver nitrate concentrations.

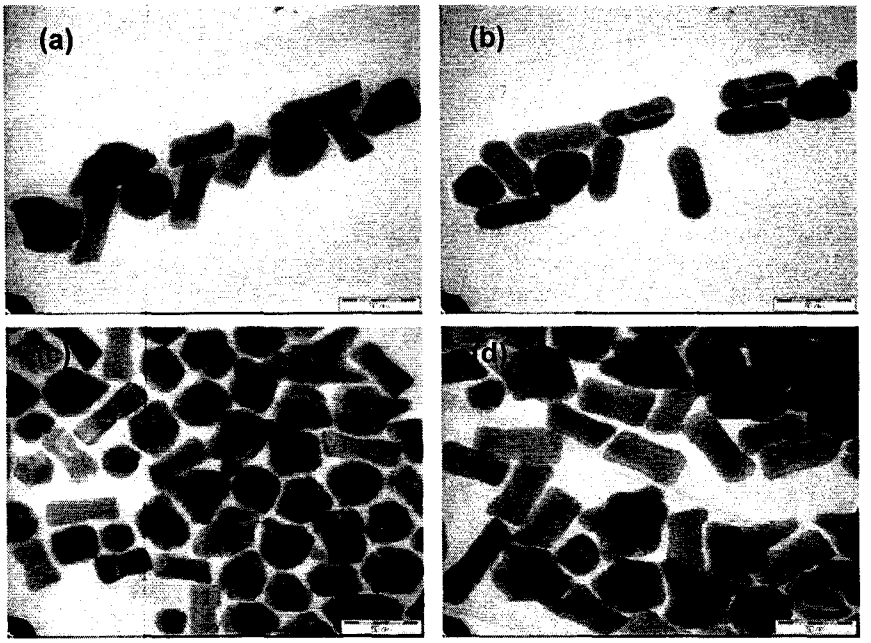

Fig.7. TEM images of AuNRs synthesized with varying silver nitrate concentration; (a) 0.003 M, (b) 0.004 M (c) 0.005 M and (d) 0.007 M.

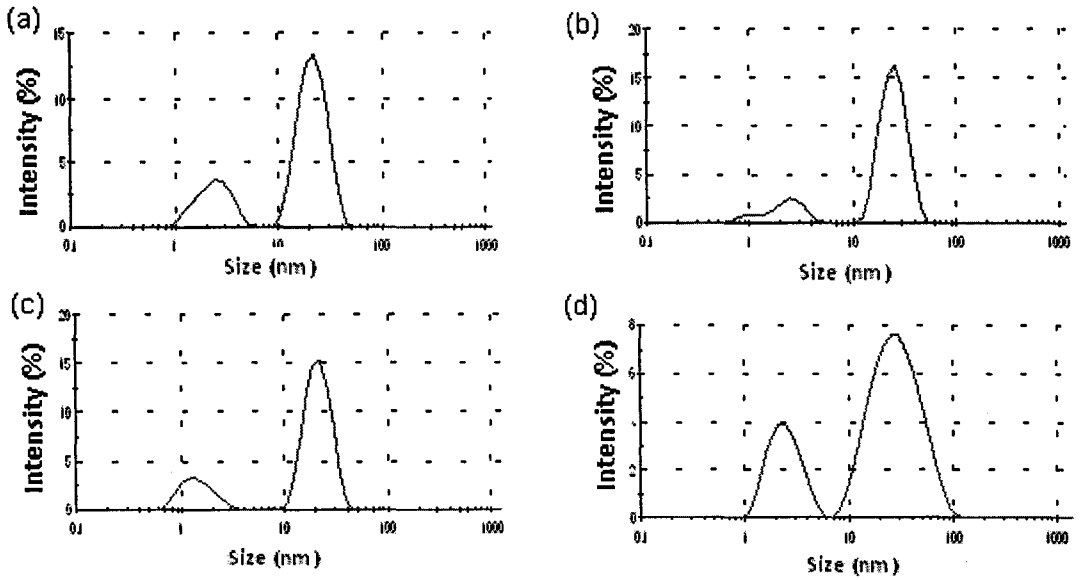

Fig.8. Size distribution by intensity for AuNRs synthesized with varying silver nitrate concentration; (a) 0.003 M, (b) 0.004 M, (c) 0.005 M and (d) 0.007 M.

The effect of temperature was studied at 25°C, 35°C and 70°C. UV-Vis spectra exhibited two absorbance peaks for samples synthesized at 25°C and 35°C but only one peak for 70°C (Fig. 9). The result suggested that AuNRs was formed up to 35°C. When temperature increased to 70°C, only AuNSs were produced. Furthermore, longitudinal and transverse peaks shifted to shorter wavelength as temperature increased from 25 C to 35°C. This indicated that both length and width of AuNRs

decreased with increasing temperature. Besides, the intensity for AuNRs at 35°C was lower than 25°C, indicated that lower rods yield.

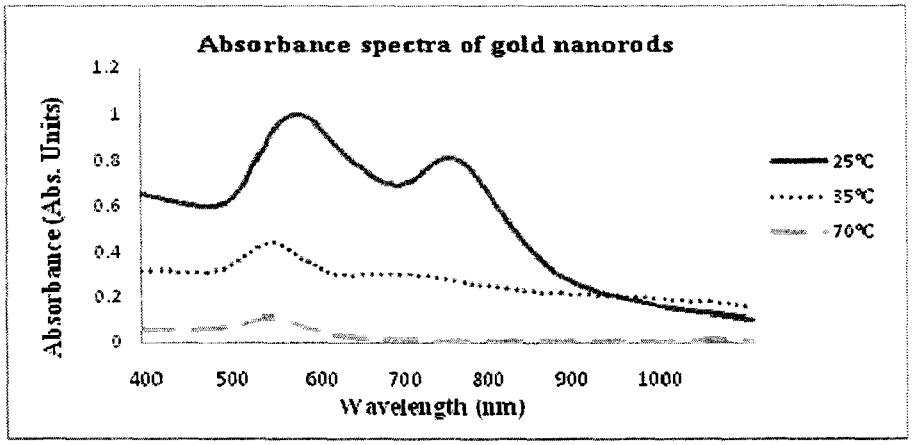

Fig.9. UV-Vis spectra of AuNRs synthesized at various temperatures.

TEM images in Fig.10 further confirmed AuNRs were produced at 25°C and 35°C whereas only AuNSs were formed at 70°C. When the solution temperature decreased, the growth rate of gold particles also decreased. Consequently, the gold intermediates remained in the solution for a relatively long time. Thus, the probability that CTAB adsorbed onto unstable facets of the gold intermediate increased at low temperature. Meanwhile, the growth rate of gold increased as the temperature increased hence the intermediate rapidly disappeared. As a result, intermediates did not adsorb by CTAB and formed spheres [9].

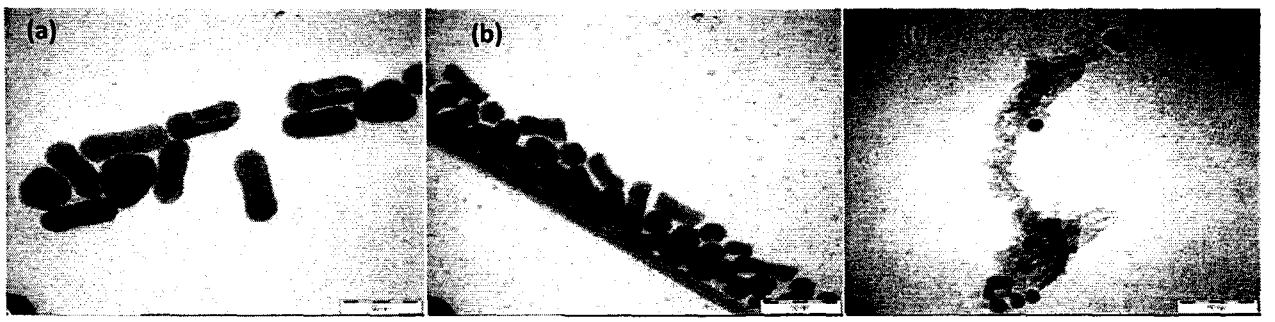

Fig.10. TEM images of AuNRs synthesized with varying temp: (A) 25°C (B) 35°C and (C) 70°C

Fig. 11 shows the particles size distribution of AuNRs with different temperature using Zetasizer. It can be seen that, both peaks that represented width and length of AuNRs decreased when temperature increased. The formation of shorter length AuNRs at higher temperature might be related to the number of nuclei with the addition of sodium borohydride. More nuclei were present when temperature increased caused less gold monomer available per nuclei. Consequently, shorter length of nanorods was formed [10]. AuNSs formed at 70°C shows well size distribution and indicated that AuNSs were almost similar in size. The Z-average size for samples synthesized at 70°C was 60.66 nm.

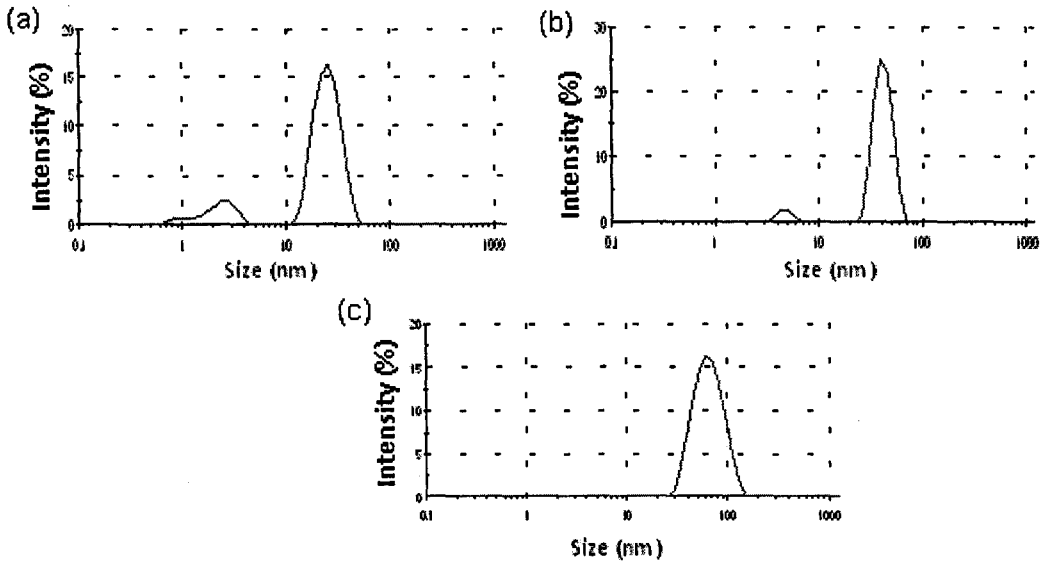

Fig.11. Size distribution of AUNRs synthesized with varying temperature, (a) 25°C, (b) 35°C and (c) 70°C.

CONCLUSIONS

Gold nanorods (AuNRs) have been successfully synthesized using the seed mediated approach. The formation of AuNRs is highly dependent on CTAB concentration and concentration of silver nitrate at room temperature and least dependent on gold concentration in the growth solution.

ACKNOWLEDGMENTS

The authors acknowledge technical support from School of Materials and Mineral Resources Engineering and INFORMM, Universiti Sains Malaysia. The research was supported by research university grant 1001/PBahan/811069 and 1001/JNC/AUPRM001.

REFERENCES

1. Mei, B. Functionalized Nanoparticles for Biological Imaging and Detection Applications. Ph.D. diss., University of Massachusetts Amherst. 2009; 75-104.
2. Dornhaus, R., Benner, R. E., Chang, R.K. and Chabay, I. Surface Plasmon Contribution to SERS. Surface Science. 1980; 101: 367-373.
3. Travis, J and Geoffrey,S. Past, Present, and Future of Gold Nanoparticles. In Bio-Applications of Nanoparticles. Warren, C.W. Chan. eds. Landes Bioscience and Springer Science+Business Media, 2007; 34-46.
4. Brown, K.R., Walter, D.G. and Natan, M.J. Seeding of Colloidal Au Nanoparticle Solutions. Chem. Mater. 2008; 12 (2): 306-313.
5. Murphy, C.J., Sau, T.K. and Gole, A.M.. Anisotropic Metal Nanoparticles: Synthesis, Assembly, and Optical Applications. Journal of Physical Chemistry. 2005; 109: 13857-13870.
6. Wang, C., Wang, T., Ma, Z. and Su, Z..tuned synthesis of gold nanostructures from gold nanorods with different aspect ratios. Nanotechnology. 2005; 16: 2555-2560.

7. Gou, L. and Murphy, C.J. Fine-Tuning the Shape of Gold Nanorods. Journal of Chem. Mater. 2005; 12: 3668-3672.
8. Sau, T.K. and Murphy, C.J.. Seeded High Yield Synthesis of Short Au Nanorods in Aqueous Solution. Journal of Langmuir. 2004; 20: 6414-6420.
9. Sung, K.K., Soonwoo, C. and Chang, C.Y. Aspect Ratio Controlled Synthesis of Gold Nanorods. Korean Journal of Chemistry Engineering. 2003; 20(6): 1145-1148.
10. Zijlstra, P., Bullen, C. and James, W.M.. High Temperature Seedless of Gold Nanorods. Journal of Physical Chemistry. 2006;110: 19315-19318.
11. Orendorff, C.J. and Murphy, C.J. Quantitation of Metal Content in the Silver-Assisted Growth of Gold Nanorods. Journal of Physical Chemistry, 2006; 110: 3990-3994.

PROPERTIES OF SILICA NANOCOLLOIDS SYNTHESIZED VIA MICELLE FORMATION APPROACH

Khairunisak Abdul Razak[1,2*], Azlan Abdul Aziz[1,3] , Shaharum Shamsuddin[1,4]

[1]NanoBiotechnology Research and Innovation

Institute for Research in Molecular Medicine (NanoBRI@INFORMM)

Universiti Sains Malaysia, 11800 USM, Penang, Malaysia

[2]School of Materials and Mineral Resources Engineering

Engineering Campus, Universiti Sains Malaysia

14300 Nibong Tebal, Penang, Malaysia.

[3]School of Physics, Universiti Sains Malaysia,

11800 USM, Penang, Malaysia

[4]School of Health Sciences, Health Campus,

Universiti Sains Malaysia, 16150 Kubang Kerian, Kelantan, Malaysia

***(khairunisak@eng.usm.my)**

ABSTRACT: Silica nanoparticles have been widely studied for their potential application as molecules and drugs carriers. In this paper, the effects of temperature and BuOH additive on physical properties of silica nanoparticles produced using micelle formation approach are discussed. It is observed that the increase of temperature and BuOH amount causes the increasing in particle size. Both parameters have significant impact in reducing critical micelle concentration (CMC), and hence allow particle size growth due to aggregation and Olswald ripening. Fluorescent tracing agent 1,1'-dioctadecyl-3,3,3',3'-tetramethylindodicarbocyanine 4-chlorobenzenesulfonate salt (DiD) is encapsulated inside silica. The toxicity *in vitro* of plain silica and DiD encapsulated silica with DiD control is studied using HCT116 cell line whereby it is observed that DiD encapsulated silica shows different behavior compared to plain silica. Biodistribution *in vivo* shows that DiD encapsulated silica exhibits excellent distribution, high contrast, and prolonged life cycle in the blood circulation.

KEYWORDS : silica, nanoparticle, molecules delivery, nanocarrie

INTRODUCTION

Silica nanoparticles has been widely used in biomedical applications owing to non-toxicity and biocompatibility, high chemical and mechanical stability, hydrophilic properties, and porous structure that can be tuned to control the diffusion of an adsorbed or encapsulated molecules. Silica nanoparticles can be produced using various methods including solgel, hydrothermal, hydrolysis and micelles formation approach. In this study, micelles formation approach is used since the method is capable to produce silica with tunable size, shape and porosity (Barbe *et al.*, 2004, Kortesuo *et al.*, 1999, Lin *et al.*, 2006, Slowing *et al.*, 2008,

Stromme *et al.*, 2009, Tan *et al.*, 2004, Wang *et al.*, 2008, Yilmaz and Bengisu, 2005). Silica nanocarriers can be used as fluorescent carrier, whereby fluorescent tracing agent can be encapsulated inside silica. This approach can eliminate the problem of photostability of tracing agent as well as toxicity (Sokolov *et al.*, 2007).

In this study, silica nanocarriers were prepared using micelle formation approach. The effects of temperature and BuOH as additive were systematically studied. Fluorescent tracing agent 1, 1'-dioctadecyl-3,3,3',3'-tetramethylindodicarbocyanine 4-chlorobenzenesulfonate salt (DiD) was entrapped inside the silica shells. The samples were tested for toxicity in vitro and biodistribution in vivo. It was observed that the particles size increased with increasing temperature. Toxicity in vitro showed that a low amount of DiD encapsulated silica can be tolerated by cells. Biodistribution in vivo showed that DiD encapsulated silica exhibited long circulation in blood with excellent contrast. Hence, DiD encapsulated silica is a potential candidate for imaging applications.

EXPERIMENTAL DETAILS

Silica nanocarriers were prepared using micelle formation approach. Tween80 surfactant was diluted in distilled water and pH value of the solution was adjusted to pH 9-10 using NH_3. BuOH was added into the solution for the formation of micelles. The solution was then transferred into a thermostated reactor set at various temperatures.

In this work, 1, 1'-dioctadecyl-3,3,3',3'-tetramethylindodicarbocyanine 4-chlorobenzenesulfonate salt (DiD) was first dissolved using ethanol. The concentration of DiD was determined using UV-Vis following Beer's law as shown in Figure 1. 300 µL of DiD solution was then added into the prepared micelle suspension in the thermostated reactor. The mixture was left for an hour to stabilize the solution. A certain amount of silica precursor,

triethoxyvinylsilane was then added into the micelle suspension. The suspension was then continuously stirred for 20 hours. The suspension was transferred into a cellulose membrane tube and subjected to dialysis process at 8°C for 5 days to remove the surfactant.

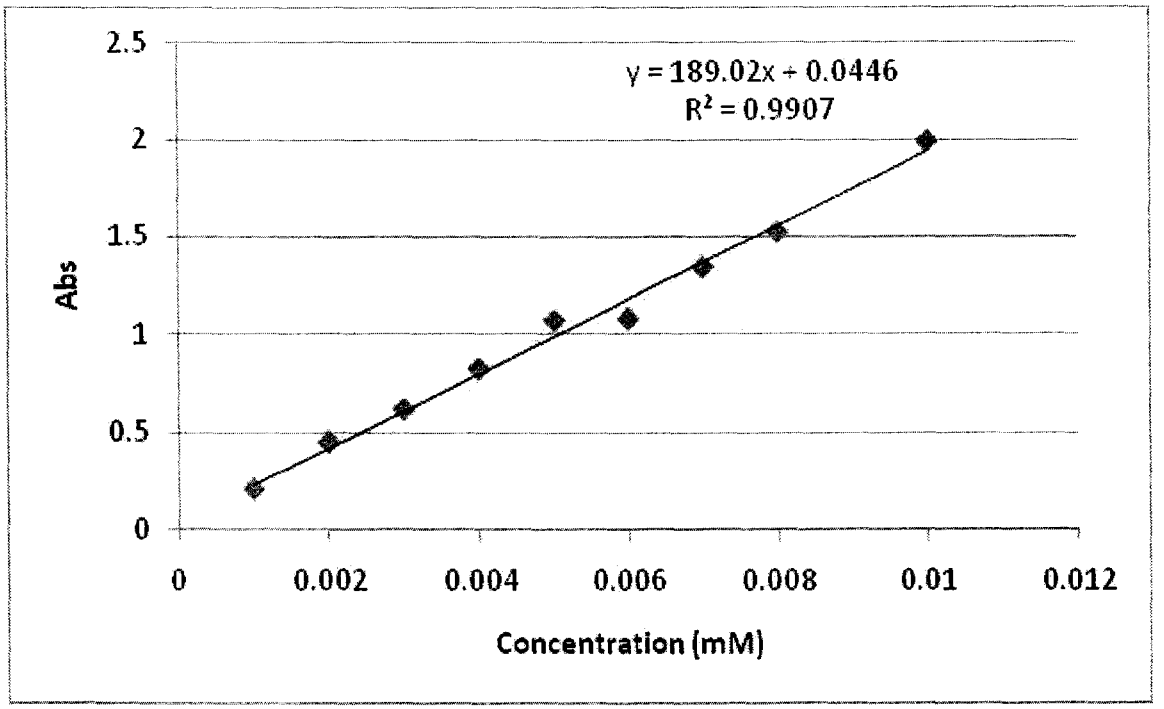

Figure 1. *Calibration curve to determine concentration of DiD using UV-Vis spectrophotometer.*

DiD encapsulated silica with 50 nm size was tested for toxicity *in vitro* and biodistribution *in vivo*. Prior to *in vitro* and *in vivo* analysis, the suspension was concentrated to 0.036 mM, and mixed with 5% glucose and trisodium trimetaphosphate.

In vitro toxicity analysis

In vitro toxicity was carried out using HCT 116 human colon cancer cell line in 96 well microplate. 200 µL of the calculated amount of freshly prepared cell suspension was prepared to obtain 5000 cells/well next day. The dispensed cells were cultured overnight in a CO_2 incubator at 37 °C.

The overnight medium of cultured cells was removed and filled with 100 µL complete medium. Three replicates of 200 µL sterile samples with known concentration and control were transferred into column 11 of 96-well microplates. Dilution was carried out throughout the column, mixed well and re-incubated at 37°C for 3 hours. After 3 hours, the 96-well microplates were taken out from the incubator. The complete medium was removed and rinsed with 200 µl sterile PBS (1X). The wells were then filled with 200 µl new complete medium and incubated for another two days in the CO_2 incubator. After two days of incubation, the plate was checked for contamination and proceeds with the WST-1 toxicity test.

10% (v/v) Fresh WST-1 solution (Roche) was prepared using the respective medium without serum. After 2 days incubation, the medium was removed. Without washing the wells, 100 µl of pre-prepared 10% WST-1 solution was added into each of the wells followed by incubation at 37°C for two hours in the CO_2 incubator. After the reaction has completed, the absorbance of the samples was analysed at 630 nm using automated ELISA reader.

Biodistribution *in vivo*

The test was carried out at certified laboratory. Anesthetized mice (isoflurane/oxygen 3.5 % for induction and 1.5 % thereafter) was subjected intravenous injection (tail vein) of 10 ml/kg of DiD encapsulated silica in 5 % glucose solution. Mice were imaged with varying time of post-injection, after 15 min, 1 hour, and 5 hours using Fluorescence reflectance imaging. At the end of in vivo imaging experiment, the animals were sacrificed (Dolethal, 1 µL/g intracardiac); main organs such as heart, lungs, brain, skin, thigh muscle, adrenals, bladder, intestine, spleen, pancreas, fat, stomach, womb, ovaries and liver were removed and analysed using the same system.

RESULTS AND DISCUSSION

In this work, silica nanocarriers were successfully produced via micelle formation approach. The size of silica nanocariers was dependent on synthesis parameters such as concentration amount of BuOH, silica precursor and temperature. In general, the properties of nanocarriers synthesized using micelle formation approach were highly dependent on critical micelle concentration (CMC), aggregation number and degree of dissociation of the micelles (Husseini and Pitt, 2008, Lo *et al.*, 2009). At low concentration of surfactant, the surfactant molecules exist as unassociated monomers. The increase of concentration causes the self aggregation of molecules and forms micelles. The concentration at which the micelles formed was called CMC. Aggregation number of a micelle was a number of surfactant molecules per micelles that was dependent on the dispersant conditions.

In this study, although non-ionic surfactant Tween 80 was used in this study, ionic charged was developed due to the addition of NH_3 in the solution. Figure 2 shows that the particle size of silica nanocarriers increased with increasing temperature. The increase of temperature causes CMC decreases due to an increase of hydrophobicity, that is caused by destruction of hydrogen bond between water molecules and hydrophilic groups (Kang *et al.*, 2001). In the formation of silica nanocarriers through micelle approach, nucleation of silica layer occurred upon the addition of silica precursor in the micelles suspension. Particle growth occurred through aggregation of nuclei during intermicellar collision (F.J. and K., 2006). The increase of temperature caused increasing degree of dissociation, hence the micelles template expands. Therefore, the particle size of silica nanocarriers increased. Moreover, when temperature increased more energy was supplied to the micelles. Hence, diffusion of small particles on large particles occurred and resulted in larger particles following Ostwald ripening (Chen *et al.*, 1998, Chiang *et al.*, 2004, Kang *et al.*, 2001).

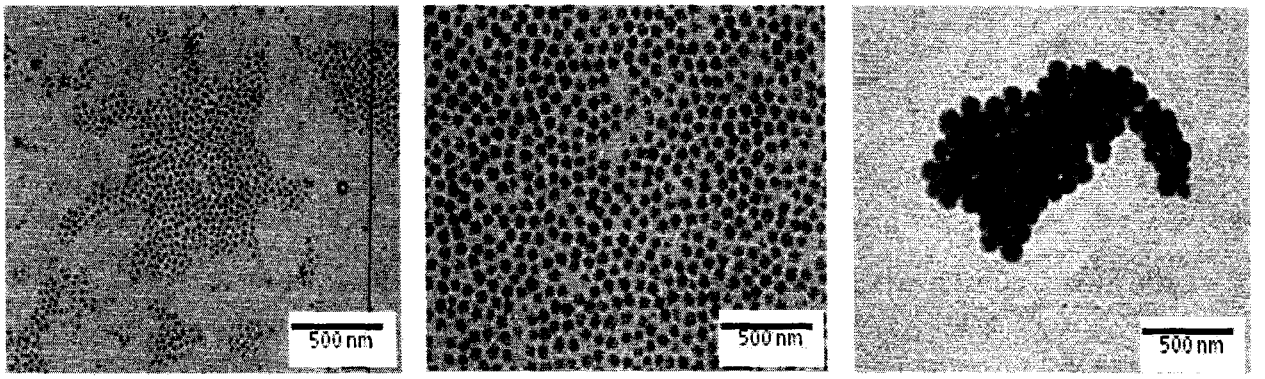

(a) (b) (c)

Figure 2. *TEM micrographs of silica nanocarriers with varying synthesis temperature; (a) 27℃ (b) 38℃ and (c) 50℃.*

It was observed that the increase of BuOH resulted in increasing particle size of silica (Figure 3). BuOH is an alcohol additive that binds to the micelle and caused intercalation between the surfactant ionic head groups to decrease the micelle surface area per head group and increase of ionization. Moreover, it is known that in micellar system, the effects of alcohol on micellar system were dependent on hydrophobicity of the alcohol (Akhter and Alawi, 2000, Attwood et al., 2000). BuOH which is a medium chain length alcohol caused decreasing in CMC, decreasing micelle aggregation number and increasing the degree of dissociation of micelles (Attwood *et al.*, 2000, Akhter and Alawi, 2000). The modification using BuOH allows faster nucleation of silica nanocarriers followed by particle growth. Higher degree of dissociation of micelles, promotes the growth of silica nanocarriers.

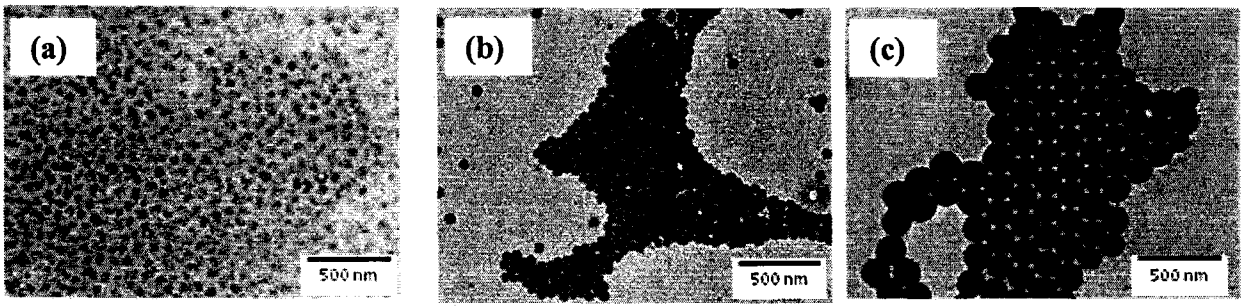

Figure 3. *TEM micrographs of silica nancarriers with varying the amount of BuOH; (a) 4 ml, (b) 6 ml, and (c) 8 ml. Temperature was fixed at 50°C and amount of silica precursor 2 ml.*

DiD encapsulated silica was also prepared using micelle formation approach. Figure 4 shows UV-Vis spectra of plain DiD and DiD encapsulated silica. It can be seen that the maximum peak was at similar wavelength which indicated that the properties of DiD was still maintained although it was encapsulated inside silica. In this case, the absorbance value was different due to different concentration of DiD. UV-Vis analysis was also performed on DiD encapsulated silica; as-synthesized and after dialysis in cellulose membrane whereby the concentration of DiD was calculated using Beer's law (as in Figure 1). It was observed that more than 99% DiD was remained in the samples after dialysis, suggesting an excellent entrapment of DiD in silica shells.

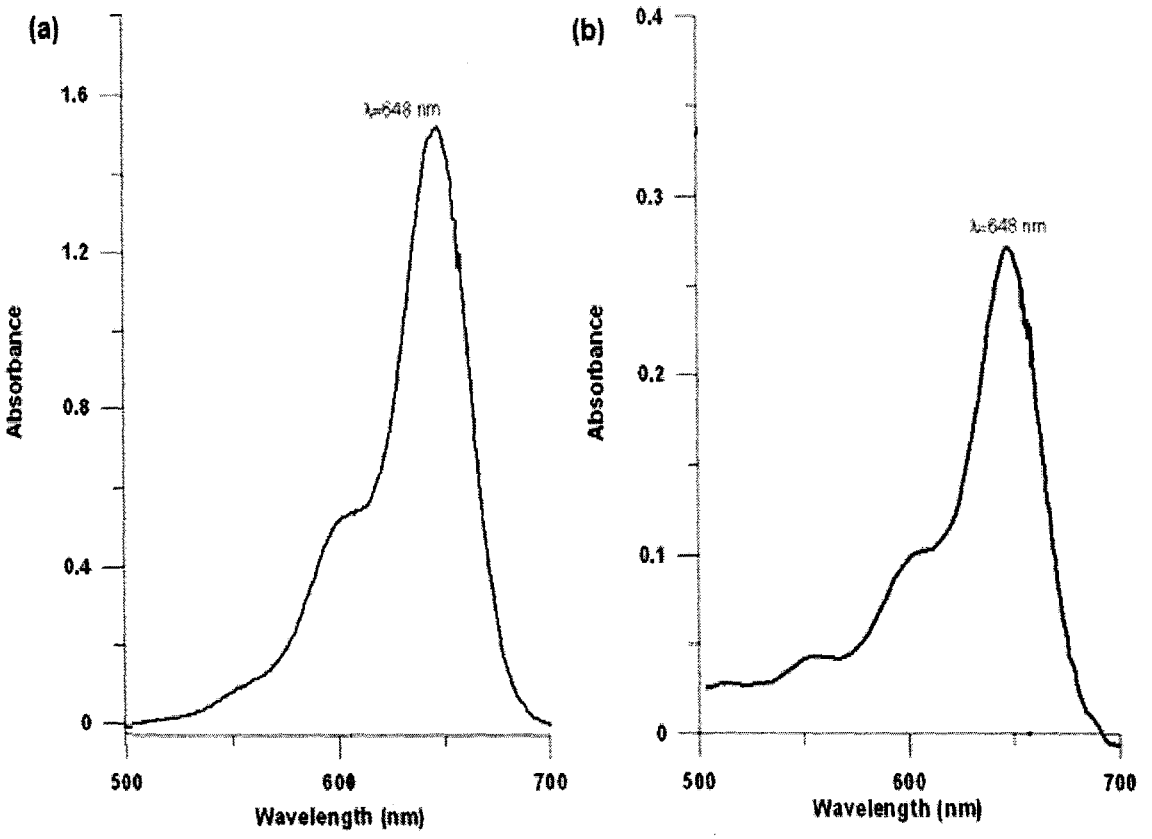

Figure 4. Typical UV-Vis spectra, (a) plain DiD and (b) DiD encapsulated silica.

Toxicity *in vitro* was carried out on plain silica, DiD encapsulated silica with plain DiD control was shown in Figure 5. It can be seen that plain silica was toxic to cells at high concentration (above 50 μM). However, the combination of DiD encapsulated silica resulted in toxicity at a lower concentration. The result could be due to the reaction of DiD with silica molecules. It is also worth to note that in this in vitro toxicity work was carried on cancer cells, hence the cells properties could be different from normal cells.

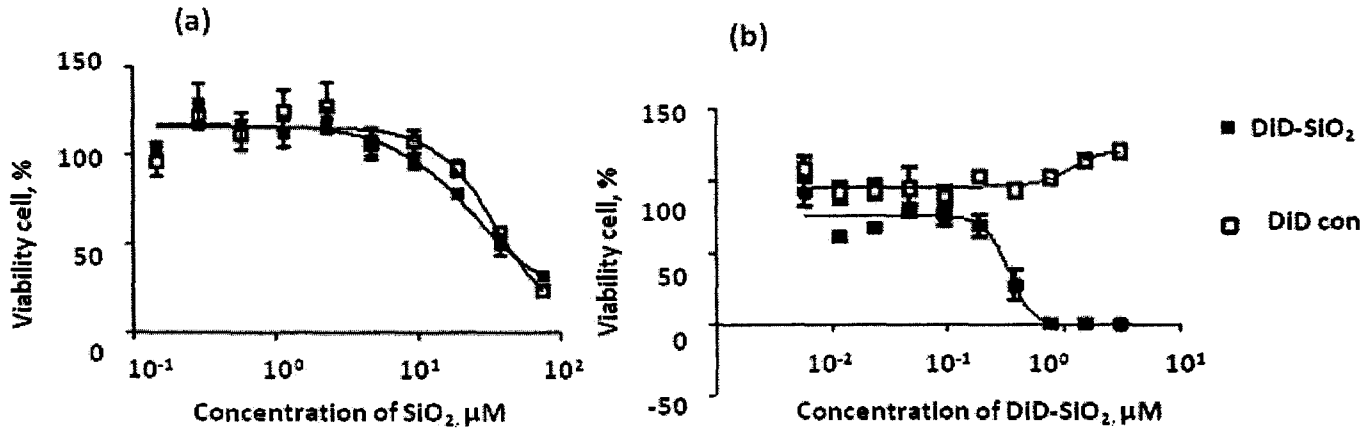

Figure 5 . Toxicity in vitro of, (a) plain silica, (b) DiD encapsulated silica with DiD control.

Figure 6 shows the biodistribution of DiD encapsulated silica with varying time. Excellent circulation in blood was evidenced by the strong contrast of blood vessels on the images. A very weak accumulation was observed in the liver.

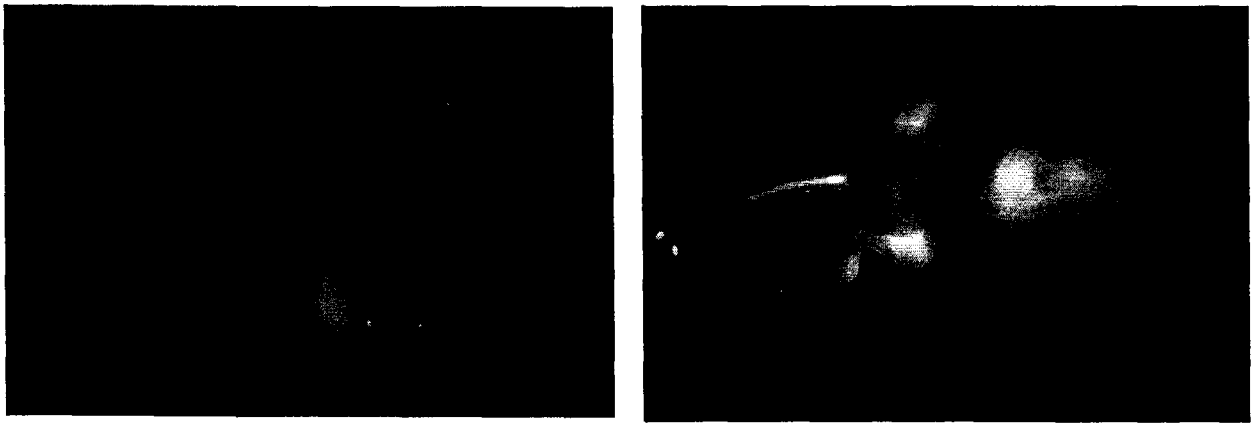

Figure 6. Biodistribution in vivo, (a) bare DiD and (b) DiD encapsulated silica.

Figure 7 shows biodistribution of DiD encapsulated silica with varying time. Excellent circulation in blood was observed even after 1 hour injection. The sample displayed weak signals in suprarenal glands after 1 hour, which indicated that a small amount of sample was accumulated. After 5 hours injection, signal decreased progressively which was related to decaying of luminescence signal with time. Figure 7d shows fluorescence imaging of organs after 5 hours injection. Some signal was observed in some of the organs e.g. liver, suprarenal glands, ovaries and lungs. From the results obtained in this study, it can be concluded that silica produced by micelle formation approach is a potential candidate for imaging applications.

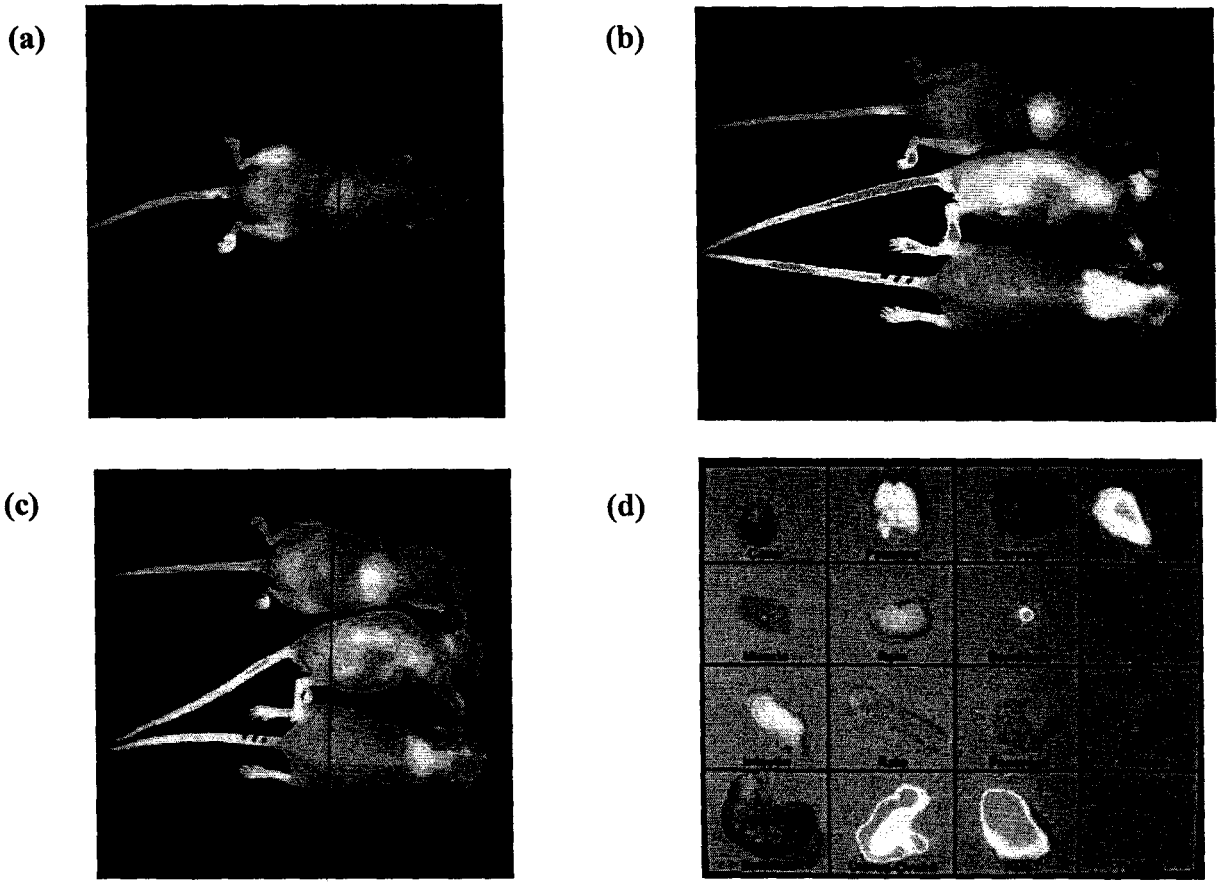

Figure 7: Biodistribution of DiD encapsulated silica nancarriers in vivo; (a) 15 min, (b) 1 hour, (c) 5 hours, and (d) organs-necropsy after 5 hours (Read from Left to Right:1st row: heart, lungs, brain, skin; 2nd row: muscle, kidney, adrenal, bladder; 3rd row: intestine,

spleen, pancreas, fat; 4th row: stomach, uterus-ovary, liver, tumor. The different result in 3 mice was due to viability of one animal to another.

CONCLUSION

The effects of synthesis parameters; temperature, BuOH and silica precursor on properties of silica nanocarriers were systematically studied. Particle size of silica nanocarriers increased with increasing temperature, amount of BuOH additive and silica precursor that could be explained by decreasing CMC and micelles aggregation number, and increasing in degree of micelles dissociation. Hence, these factors promote nucleation and growth of nanocarriers. Toxicity *in vitro* studies showed that silica and DiD encapsulated silica were toxic up to a certain concentration. Biodistribution *in vivo* showed that DiD encapsulated silica is a promising candidate for imaging applications.

ACKNOWLEDGMENT

The authors acknowledged financial supports from Malaysian Biotechnology Corporation and technical support from Nanobiotix S.A. Paris. The work was also supported by research grant 1001/PBahan/811069.

REFERENCES

Akhter, M. S. and Alawi, S. M. (2000). The effect of organic additives on critical micelle concentration of non-aqueous micellar solutions. *Colloids and Surfaces A: Physicochemical and Engineering Aspects,* **175**: pp 311-320.

Attwood, D., Terreros, A., Lopez-Cabarcos, E. and Galera-Gomez, P. A. (2000). Light Scattering Study of the Effect of n-Butanol on the Micellar Properties of Undecylammonium Chloride in Aqueous Electrolyte Solutions. *Journal of Colloid and Interface Science,* **225**: pp 25-31.

Barbe, C., Bartlett, J., Kong, L., Finnie, K., Lin, H. Q., Larkin, M., Calleja, S., Bush, A. and Calleja, G. (2004). Silica particles: a novel drug-delivery system. *Advanced Materials,* **16**: pp 1959-1965.

Chen, L.-J., Lin, S.-Y., Huang, C.-C. and Chen, E.-M. (1998). Temperature dependence of critical micelle concentration of polyoxyethylenated non-ionic surfactants. *Colloids and Surfaces A: Physicochemical and Engineering Aspects,* **135**: pp 175-181.

Chiang, C.-L., Hsu, M.-B. & Lai, L.-B. (2004). Control of nucleation and growth of gold nanoparticles in AOT/Span80/isooctane mixed reverse micelles. *Journal of Solid State Chemistry,* **177**: pp 3891-3895.

F.J., A. and K., O.-A. (2006) *Colloidal silica fundamentals and applications,* New York, Taylor & Francis Group.

Husseini, G. A. and Pitt, W. G. (2008) Micelles and nanoparticles for ultrasonic drug and gene delivery. *Advanced Drug Delivery Reviews,* **60**: pp 1137-1152.

Kang, K.-H., Kim, H.-U. & Lim, K.-H. (2001). Effect of temperature on critical micelle concentration and thermodynamic potentials of micellization of anionic ammonium dodecyl sulfate and cationic octadecyl trimethyl ammonium chloride. *Colloids and Surfaces A: Physicochemical and Engineering Aspects,* **189**: pp 113-121.

Kortesuo, P., Ahola, M., Karlsson, S., Kangasniemi, I., Kiesvaaral, J. and Yli-Urpo, A. (1999). Sol-gel-processed sintered silica xerogel as a carrier in controlled drug delivery. *Silica Xerogel as a carrier*, pp 162-167.

Lin, W., Huang, Y.-W., Zhou, X.-D. and Ma, Y. (2006). In vitro toxicity of silica nanoparticles in human lung cancer cells. *Toxicology and applied pharmacology,* **217**: pp 252-259.

Lo, C.-L., Lin, S.-J., Tsai, H.-C., Chan, W.-H., Tsai, C.-H., Cheng, C.-H. D. and Hsiue, G.-H. (2009). Mixed micelle systems formed from critical micelle concentration and temperature-sensitive diblock copolymers for doxorubicin delivery. *Biomaterials,* **30**: pp 3961-3970.

Slowing, I. I., Vivero-Escoto, J. L., Wu, C.-W. & Lin, S. Y. (2008) Mesoporous silica nanoparticles as controlled release drug delivery and gene transfection carriers. *Advanced Drug Delivery Reviews,* **60**: pp 1278-1288.

Sokolov, I., Kievsky, Y. Y. & Kaszpurenko, J. M. (2007) Self-assembly of ultrabright fluorescent silica particles. *Small,* **3**: pp 419-423.

Stromme, M., Brohede, U., Atluri, R. & Garcia-Bennett, A. E. (2009). Mesoporous silica-based nanomaterials for drug delivery: evaluation of structural properties associated with release rate. *Nanomedicine and nanobiotechnology,* **1**: pp 140-148.

Tan, W., Wang, K., He, X., Zhao, X. J., Drake, T., Wang, L. & Bagwe, R. P. (2004). Bionanotechnology based on silica nanoparticles. *Medicinal Research Reviews,* **24**: pp 621-638.

Wang, L., Zhao, W. and Tan, W. (2008). Bioconjugated silica nanoparticles: development and applications. *Nano Res,* **1**: pp 99-115.

Yilmaz, E. and Bengisu, M. (2005). Drug entrapment in silica microspheres through a single step sol-gel process and in vitro release behavior. Journal of biomedical Materials Research, **77B**, pp 149-155